

**Design and Characterisation of Metallic Bipolar Plates for
Proton Exchange Membrane Fuel Cells**

by

ATINUKE MODESOLA OLADOYE

[B.Sc., M.Sc.]

A thesis submitted in fulfilment of the requirement for the degree of

Doctor of Philosophy

Supervisors:

Dr Joseph Stokes

School of Mechanical and Manufacturing Engineering

Faculty of Engineering and Computing

Dublin City University, Ireland.

Prof Abdul-Ghani Olabi

Institute of Engineering and Energy Technologies

University of the West of Scotland, United Kingdom

August 2016



DECLARATION

I hereby certify that this material, which I now submit for assessment on the programme of study leading to the award of PhD is entirely my own work, that I have exercised reasonable care to ensure that the work is original, and does not to the best of my knowledge breach any law of copyright, and has not been taken from the work of others save and to the extent that such work has been cited and acknowledged within the text of my work.

Signed: M.A. Oladoye

ID No.10113240

Date 24/08/2016

PUBLICATIONS

Journals:

1. **A.M. Oladoye**, J.G. Carton, K. Benyounis, J. Stokes and A. G. Olabi, Optimisation of pack chromised stainless steel for proton exchange membrane fuel cells using response surface methodology. *Surface and Coatings Technology* 2016; 304: pp. 384-392.
2. **A.M. Oladoye**, J.G. Carton, and A.G. Olabi, Characterization of Graphite Coatings Produced by CoBlast™ Technology, *Journal of Materials (JOM)*, Vol. 66, No. 4, 2014, DOI: 10.1007/s11837-014-0941-z,2014. The Minerals, Metals & Materials Society.
3. **A.M. Oladoye**, J.G. Carton, and A.G. Olabi, Evaluation of CoBlast™ coated Titanium Alloy as Proton Exchange Membrane fuel Cells Bipolar plates. *Journal of Materials*, Vol. 2014, Article ID 914817, 10 pages, 2014. doi:10.1155/2014/914817.

International conference paper:

1. **A.M. Oladoye**, J. G. Carton, K. Benyounis, J. Stokes and A.G. Olabi, Optimisation of pack chromised AISI 304 stainless steel for Proton exchange Membrane fuel cell bipolar plates using Box-Behnken Design. 8th International Conference on Sustainable Energy & Environmental Protection (SEEP 2015), August 11-14, 2015, Scotland, United Kingdom
2. **A.M. Oladoye**, J.G. Carton, and A.G. Olabi, Improvement on the Corrosion Behaviour and Surface Conductivity of CoBlast™ Coatings by Pack Cementation, International Conference on Metallurgical coatings and thin films (ICMCTF 2014), 28 April-3rd May 2014, San Diego, California.
3. **A.M. Oladoye**, J.G. Carton, and A.G. Olabi, Evaluation of Graphite coated metals as bipolar plates for Proton Exchange Membrane (PEM). 6th International Conference on

Sustainable Energy & Environmental Protection (SEEP 2013) 20 -23 August, 2013,
Maribor, Slovenia.

4. **A.M Oladoye**, J.G. Carton, and A.G. Olabi, The significance of the deposition method on coated metallic bipolar plates for proton exchange membrane fuel cells. 5th International Conference on Sustainable Energy & Environmental Protection (SEEP 2012), 5 – 8 June, 2012, Dublin, Ireland.

DEDICATION

This thesis is dedicated to the

God of Mountain of Fire and Miracles Ministries,

My present help in time of need,

He drew me out of the deep waters, placed my feet on a rock and established my goings.

ACKNOWLEDGEMENTS

My profound gratitude to the Almighty God, the giver of life and wisdom, knowledge and understanding, my source of inspiration, without whom this thesis would never have materialised.

I would like to express my deepest appreciation to my Supervisors; Dr Joseph Stokes and Prof Abdul Olabi for their academic support, guidance and encouragement throughout the programme.

My heartfelt gratitude goes to Dr James Carton - my third and unofficial supervisor. Thank you for all your support, I am eternally grateful. I would like to thank Prof S.M.J Hashmi for his academic support at the beginning of the programme.

I would also like to thank my sponsors: Tertiary Education Trust Fund, (TETFund), Nigeria. I also want to thank the Vice Chancellor and Management of the University of Lagos, Nigeria for granting me study leave throughout the programme.

Many thanks to EnBio Limited for providing the CoBlast™ samples and providing access to their facilities. I want to express my profound appreciation to Dr. Brendan Duffy of the FOCAS Institute, Dublin Institute of Technology, Dublin 8 for his help on accessing the potentiostat for the electrochemical polarisation test for the CoBlast™ samples. I also want to express my sincere appreciation to Dr. Anthony Betts of Dublin Institute of Technology, Dublin 8 for the tutorials on electrochemistry and corrosion.

Many thanks to the technical staff I worked with during my stay in DCU – Liam Dominican, Chris Crouch, Michael May, Michael Tyrell and Billy Roarty of the School of Electronic

Engineering. To my friends at DCU: Leonard, Asmaa, Rajani, Emmanuel, Hussam, Shadi, Richard and so on...too numerous to mention. The journey was not so smooth but you were there to gist with and exchange ideas.

My sincere appreciation to my Pastors: Pastor and Pastor (Mrs) Adekunle Daniel, Pastor Samuel Adekunle and Pastor & Mrs Godwin Abia for their spiritual support. I would also want to thank Mr & Mrs. Kehinde Adejumo and Mr. & Mrs Adeleye Olaiwola for their prayers and kind gestures. To my brethren at R.C.C.G Open heavens, Dublin and Mountain of Fire and Miracles Ministries, Dublin, Ireland... you were simply wonderful. My heartfelt gratitude to Mrs. Funmilayo Akingbade for making sure I did not go hungry while writing the thesis.

I want to specially thank Dr M.O.H Amuda, my lecturer and senior colleague at the University of Lagos, Nigeria for the role he played in making this dream come true.

My profound gratitude to my husband, Olayemi. Thank you for allowing me to fulfil my dreams and taking care of the children while I was away in another continent. My sincere gratitude to my children, FiyinfoLuwa and Anuoluwapo. Thank you for co-operating throughout the programme. I want to thank my extended family for their support to my husband and children while I was in Ireland especially my sister, Abisoeye for helping out with my children.

ABSTRACT

Design and Characterisation of Metallic Bipolar Plates for Proton Exchange Membrane Fuel Cells

Atinuke Modesola Oladoye (B.Sc., M.Sc.)

Metals are potential candidate materials for proton exchange membrane fuel cells (PEMFC) bipolar plates (BP). However, metals require surface coatings to enhance its corrosion resistance and interfacial contact resistance (ICR) in PEMFC environments. The present study investigated the performance of metals coated with: graphite based coatings deposited by the CoBlast™ process and chromised coatings deposited by pack cementation in PEMFC environments.

CoBlast™ coated metals exhibited high ICR and low corrosion resistance in 0.5 M H₂SO₄ + 2 ppm HF. Hence, it was unsuitable for PEMFC BP application. Post chromising of CoBlast™ coated stainless steel at 900°C for 3 hours reduced its ICR by ~72 % at 140 N/cm² but increased its susceptibility to corrosion. Therefore, Box–Behnken design was employed to optimise and investigate the influence of activator content, time and temperature on the corrosion current density of chromised 304 stainless steels exposed to aerated 0.5 M H₂SO₄ + 2 ppm HF at 70 °C. Temperature was found to be the most significant parameter, while the optimum process conditions were: activator content of 6.84 wt. %, time of 3 hours and temperature of 1040 °C.

The optimised coatings exhibited acceptable corrosion resistance in PEMFC environments and about six fold decrease in the ICR of the substrate at 150 N/cm². However, pack carburisation at 925 °C for 3 hours prior to chromising decreased its ICR by 55% at 150 N/cm². Consequently, the single fuel cell with the modified chromised stainless steel BP attained a peak power density of 18.20 mW/cm² at a current density of 53.2 mA/cm². This result represented a two-fold and three-fold increase in the peak power density of the single fuel cells with chromised stainless steel produced at the optimised process conditions and uncoated BP respectively. A similar trend was sustained in the ten-hour durability test. Surface characterisation of the plates after the test indicated the need to adopt low temperature carburisation techniques. The work presented herein demonstrated that both chromising and pre-carburisation prior to chromising are promising techniques for surface modification of metallic PEMFC bipolar plates.

Table of Contents

DESIGN AND CHARACTERISATION OF METALLIC BIPOLAR PLATES FOR PREOTON EXCHANGE MEMBRANE FUEL CELLS

DECLARATION	II
PUBLICATIONS	III
DEDICATION	V
ACKNOWLEDGEMENTS	VI
ABSTRACT	VIII
LIST OF FIGURES	XII
LIST OF TABLES	XXII
LIST OF ABBREVIATIONS	XXV
Chapter 1	1
Introduction	1
1.1 INTRODUCTION.....	1
1.2 FUEL CELLS	4
1.3 FUEL CELLS FOR ROAD TRANSPORTATION	10
1.4 RESEARCH GOALS AND APPROACH	11
1.5 THESIS OUTLINE	14
Chapter Two	15
Background and Literature review	15
2.1 INTRODUCTION.....	15
2.2 PROTON EXCHANGE MEMBRANE FUEL CELLS.....	15
2.3 CHALLENGES TO COMMERCIALISATION OF AUTOMOTIVE PEM FUEL CELLS.....	25
2.4 A SURVEY OF THE LITERATURE ON METALLIC BIPOLAR PLATES.....	36
2.5 SUMMARY AND INDICATION OF GAP WITHIN THE LITERATURE.....	81
CHAPTER THREE	83
Experimental Methodology	83
3.1 INTRODUCTION.....	83

3.2	MATERIAL AND COATING PROCESSES	83
3.3	SURFACE CHARACTERISATION	105
3.4	EVALUATION OF CORROSION PERFORMANCE OF COATED METALS IN SIMULATED PEM FUEL CELL ENVIRONMENT.	111
3.5	INTERFACIAL CONTACT RESISTANCE MEASUREMENT.....	125
3.6	SINGLE FUEL CELL PERFORMANCE EVALUATION.....	128
3.7	SUMMARY	131
CHAPTER 4.....		133
Graphite Coatings deposited by CoBlast™ Technology.....		133
4.1	INTRODUCTION.....	133
4.2	SURFACE CHARACTERISATION	133
4.2	EVALUATION OF GRAPHITE COATED TITANIUM (V) ALLOY AS PEM FUEL CELL BIPOLAR PLATES	146
4.3	EVALUATION OF GRAPHITE COATED STAINLESS STEEL AS PEM FUEL CELLS BIPOLAR PLATES	153
4.4	SUMMARY	160
Chapter 5.....		161
Post Modification Of Graphite Coated Stainless Steel.....		161
5.1	INTRODUCTION	161
5.2	SURFACE CHARACTERISATION	163
5.3	INTERFACIAL CONTACT RESISTANCE.....	170
5.4	CORROSION BEHAVIOUR IN SIMULATED PEM FUEL CELL ENVIRONMENT AT 70 °C.....	172
5.5	SUMMARY	177
Chapter 6.....		179
Chromium Diffusion Coatings.....		179
6.1	INTRODUCTION.....	179
6.2	EXPERIMENTAL RESULTS AND MATHEMATICAL MODELLING	179
6.3	EVALUATION OF OPTIMISED CHROMISED COATING.....	201
6.4	SUMMARY.....	221
Chapter 7.....		223
Pre-carburised And Chromised Coatings		223

7.1 INTRODUCTION	223
7.2 PRE-CARBURISATION AND CHROMISING PROCESSING OVERVIEW	223
7.3 SURFACE CHARACTERISATION	224
7.4 Interfacial contact resistance	235
7.5 CORROSION BEHAVIOUR EVALUATION	236
7.6 SINGLE FUEL CELL PERFORMANCE	241
7.7 SUMMARY	245
Chapter 8.....	247
Conclusions, Contributions and Future work.....	247
8.1 CONCLUSIONS	247
8.2 CONTRIBUTION TO KNOWLEDGE	250
8.3 FUTURE WORK	251
REFERENCES.....	252
APPENDIX I	286
APPENDIX II.....	292
APPENDIX III	296

LIST OF FIGURES

FIGURE 1 WORLD PRIMARY ENERGY CONSUMPTION FOR 2014	2
FIGURE 2 SCHEMATIC DIAGRAM OF A FUEL CELL, ADAPTED FROM	4
FIGURE 3 COMPONENTS OF A PEM FUEL CELL	16
FIGURE 4 SCHEMATIC DIAGRAM OF A PEM FUEL CELL	17
FIGURE 5 SCHEMATIC REPRESENTATION OF A PEM FUEL CELL STACKS	18
FIGURE 6 STRUCTURE OF PER FLUORINATED SULFONIC ACID (PFSA) MEMBRANES	19
FIGURE 7 STRUCTURE OF SULPHONATED POLY ETHER KETONE	20
FIGURE 8 (A) SCHEMATIC OF STRUCTURE OF FLOW CHANNELS AND MEMBRANE ELECTRODE ASSEMBLY SHOWING THE FLOW PATTERN (B) MICROGRAPHS OF CARBON CLOTH AND CARBON PAPER GDL MATERIALS	22
FIGURE 9 FEATURES OF A TYPICAL BIPOLAR PLATE	23
FIGURE 10 SCHEMATIC DIAGRAM OF TYPICAL FLOW FIELD DESIGN: (A) PIN-TYPE, (B) SERIES- PARALLEL, (C) SERPENTINE AND (D) INTERDIGITATED TYPE	24
FIGURE 11 SCHEMATIC DIAGRAM OF OXYGEN CROSSOVER THROUGH THE MEMBRANE IN A PEM FUEL CELL	31
FIGURE 12 ENERGY LOSSES IN PEM FUEL CELLS.	33
FIGURE 13 EFFECT OF PTFE LOADING ON CONTACT RESISTANCE.	35
FIGURE 14 CLASSIFICATION OF METALLIC MATERIALS FOR PEM FUEL CELLS BIPOLAR PLATE	37
FIGURE 15 (A) SEM IMAGE OF THE CROSS-SECTION OF Ni-50Cr ALLOY NITRIDED AT 1100 °C FOR 1 HOUR, (B) SEM IMAGE OF THE CROSS SECTION OF NITRIDED AT Fe-27Cr-6V STAINLESS STEEL NITRIDED AT 900 °C FOR 4 HOURS SHOWING INTERNAL AND EXTERNAL NITRIDES	53

FIGURE 16 (A) PRE-OXIDISED (900 °C FOR 10 HOURS) 446M STAINLESS STEEL NITRIDED AT 1100 °C FOR 2 HOURS (B) PRE-OXIDISED (900 °C FOR 5 HOURS) 430 STAINLESS STEEL NITRIDED AT 1040°C FOR 6 HOURS.....	54
FIGURE 17 (A) SEM IMAGE OF THE CROSS-SECTION OF PRE-OXIDISED NITRIDED Fe–27Cr–6V NITRIDED AT 850 °C FOR 24 HOURS IN N ₂ –4H ₂ ATMOSPHERE. (B) BRIGHT-FIELD CROSS-SECTION TEM OF SEM IMAGE IN (A)	55
FIGURE 18 SCHEMATIC ILLUSTRATION OF THE DESIGN CONCEPT OF THE GRAPHITE-COATED PLATES .	70
FIGURE 19 (A) NON- HOT PRESSED (B) HOT-PRESSED GRAPHITE COMPOSITE COATING	71
FIGURE 20 ATLAS CELL CONTAINING 3.5 WT.% SODIUM CHLORIDE SOLUTION	73
FIGURE 21 COMPARISON OF BIPOLAR PLATES MADE FROM (A) METAL FOAM (B) BULK STAINLESS STEEL	80
FIGURE 22 (A) SCHEMATIC REPRESENTATION OF THE CoBLAST™ PROCESS ADAPTED FROM , (B) PICTURE OF THE CoBLAST™ EQUIPMENT.....	86
FIGURE 23 SEM IMAGES OF (A) MICROFYNE GRAPHITE (B) ALUMINA POWDERS	87
FIGURE 24 SEM IMAGES OF (A) CHROMIUM POWDER (B) AMMONIUM CHLORIDE POWDER.....	88
FIGURE 25 CARBOLITE TUBE FURNACE USED IN THE STUDY.....	88
FIGURE 26 MAJOR STEPS INVOLVED IN PACK CEMENTATION	91
FIGURE 27 STRUCTURE OF ALLOYING ELEMENTS IN STAINLESS STEEL ALLOYS (A) FACE CENTERED CUBIC STRUCTURE (FCC) (B) BODY CENTRED STRUCTURE (BCC)	94
FIGURE 28 IRON –CARBON PHASE DIAGRAM	95
FIGURE 29 RELATIONSHIP BETWEEN M ₂₃ C ₆ PRECIPITATION AND INTERGRANULAR CORROSION IN TYPE 304 AUSTENITIC STAINLESS STEEL	97

FIGURE 30 PICTORIAL REPRESENTATION OF BOX-BEHNKEN DESIGN	99
FIGURE 31 PICTURE OF CRUCIBLE CONTAINING PACK POWDER MIXTURE OF CHROMIUM, AMMONIUM CHLORIDE AND ALUMINA AND SEALED WITH FIRE CLAY	103
FIGURE 32 PICTURE OF THE PACK CHROMISING PROCEDURE (A) LENTON TUBE FURNACE (B) SEALED CRUCIBLE IN TUBE FURNACE (C) TUBE FURNACE SEALED AND ARGON GAS IS PASSED THROUGH THE TUBE (D) END OF THE TUBE CONNECTED TO THE FUME HOOD.	103
FIGURE 33 MATERIALS FOR PACK CARBURISING.	104
FIGURE 34 SCHEMATIC REPRESENTATIONS OF (A) THE OPERATING PRINCIPLES OF THE SEM (B) SIGNALS PRODUCED WITHIN THE SEM AT DIFFERENT DEPTH OF PENETRATION.	106
FIGURE 35 SCHEMATIC REPRESENTATION OF XRD	107
FIGURE 36 OPERATING PRINCIPLES IN XPS	109
FIGURE 37 (A) TR200 SURFACE ROUGHNESS TESTER (B) CLOSE-UP VIEW	110
FIGURE 38 SCHEMATICS OF WATER CONTACT ANGLE SET UP	111
FIGURE 39 CORROSION CELL IN ACTION.....	112
FIGURE 40 (A) ANODIC AND CATHODIC HALF-CELL REACTIONS (B) EVANS DIAGRAM FOR A MIXED ELECTRODE STATE OF A METAL, M CORRODING IN AN ACIDIC ELECTROLYTE	114
FIGURE 41 TAFEL LINE EXTRAPOLATION METHOD	116
FIGURE 42 FLAT CORROSION CELL AND THE ELECTRODES USED IN THE STUDY.	119
FIGURE 43 SCHEMATIC REPRESENTATION OF EXPERIMENTAL SET UP FOR ELECTROCHEMICAL POLARISATION EXPERIMENTS. (AE: AUXILIARY ELECTRODE, WE – WORKING ELECTRODE, RE – REFERENCE ELECTRODE)	122
FIGURE 44 EXPERIMENTAL SET UP AT FOCAS INSTITUTE, DUBLIN INSTITUTE OF TECHNOLOGY, IRELAND.	123

FIGURE 45 EXPERIMENTAL SET UP AT DUBLIN CITY UNIVERSITY, IRELAND (1) EXTRACTION HOOD (2) POLYETHYLENE FRAME WITH DANGER SIGNS (3) H ₂ GAS CYLINDER (4) N ₂ GAS (5) AIR PUMP (6) REFERENCE ELECTRODE (7) WORKING ELECTRODE (8) COUNTER ELECTRODE (9) H ₂ LEAK SENSOR (10) GAMRY POTENTIOSTAT.	124
FIGURE 46 SCHEMATIC OF THE TEST ASSEMBLY FOR INTERFACIAL CONTACT RESISTANCE.	126
FIGURE 47 PICTURE OF EXPERIMENTAL SET UP FOR ICR (1) ZWICK ROELL UTM (2) POWER SOURCE (3) COMPUTER (4) COPPER ELECTRODES (5) MULTI-METER.	127
FIGURE 48 304 STAINLESS STEEL BIPOLAR PLATE WITH SERPENTINE FLOW FIELD DESIGN.	129
FIGURE 49 THE THREE SINGLE CELLS INVESTIGATED IN THIS STUDY.	130
FIGURE 50 EXPERIMENTAL SET UP FOR SINGLE CELL FUEL TESTING. HYDROGEN GAS CYLINDER (1), NITROGEN GAS CYLINDER (2), SINGLE FUEL CELL (3), POTENTIOSTAT (4), HUMIDIFIER (5)...	131
FIGURE 51 SUMMARY OF THE EXPERIMENTAL METHODOLOGY EMPLOYED IN THE STUDY.	132
FIGURE 52 SURFACE MORPHOLOGIES OF GR-SS AND GR-TiV.	133
FIGURE 53 CROSS SECTION OF COBLAST GRAPHITE COATED STAINLESS STEEL. SIMILAR THIN AND DISCONTINUOUS COATED LAYER WAS OBTAINED FOR GRAPHITE COATED TITANIUM GRADE (V) ALLOY.	134
FIGURE 54 SEM/ BSD OF GRAPHITE COATED AISI 316 STAINLESS STEEL.	135
FIGURE 55 SEM/ BSD VIEW OF THE SURFACE MORPHOLOGY OF GRAPHITE COATED TITANIUM GRADE (V) ALLOY.	136
FIGURE 56 CROSS SECTION OF COBLAST HA COATING ON Ti (V) ALLOY.	136
FIGURE 57 SURVEY SPECTRA OF COATED (GR-SS) AND UNCOATED 316 STAINLESS STEEL.	139
FIGURE 58 SURVEY SPECTRA OF COATED (GR-TiV) AND UNCOATED TITANIUM (V) ALLOYS.	140

FIGURE 59 XPS NARROW SCAN REGION FOR (A) C1S (B) AL 2P AND (C) O1S FOR GR-SS AND GR-TiV.....	142
FIGURE 60 XPS NARROW SCAN REGION FOR (A) CR2P (B) FE2P FOR GR-SS (C) Ti2P FOR GR-TiV.	143
FIGURE 61 XRD PATTERNS FOR (A) GR-SS (B) SS316 (C) GR-TiV (D) BARE-TiV.	145
FIGURE 62 PLOT OF INTERFACIAL CONTACT RESISTANCE VS. COMPACTION PRESSURE FOR GR-TiV, BARE TiV AND GRAPHITE.....	146
FIGURE 63 POTENTIODYNAMIC POLARISATION CURVES FOR GR- TiV AND BARE- TiV IN 0.5 M H ₂ SO ₄ + 2 PPM HF AT ROOM TEMPERATURE WITH (A) AIR BUBBLED (B) H ₂ GAS BUBBLED INTO THE ELECTROLYTE. SCAN RATE 1 MV/S.....	149
FIGURE 64 POTENTIOSTATIC POLARISATION OF GR-TiV AND BARE -TiV IN 0.5 M H ₂ SO ₄ + 2 PPM HF AT 70 °C (A) AIR BUBBLED (E = 0.6 V (AG/AGCL) AND (B) H ₂ GAS BUBBLED (E = -0.1 V (AG/AGCL) INTO THE SOLUTION.....	151
FIGURE 65 POTENTIODYNAMIC CURVES FOR GR-SS AND SS316 IN 0.5 M H ₂ SO ₄ + 2 PPM HF AT ROOM TEMPERATURE IN SIMULATED (A) CATHODE (AIR BUBBLED INTO THE SOLUTION) AND (B) ANODE ENVIRONMENTS (HYDROGEN GAS BUBBLED INTO THE SOLUTION). SCAN RATE = 1 MV/S.....	155
FIGURE 66 POTENTIOSTATIC POLARISATION OF GR-SS AND SS316 IN 0.5 M H ₂ SO ₄ +2 PPM HF AT	157
FIGURE 67 SEM IMAGES OF CHROMISED GR-SS (A) SECONDARY ELECTRON VIEW (B) BACKSCATTERED (BSD) VIEW (DARK PATCHES – GRAPHITE /ALUMINA COATINGS, LIGHT AREA –CHROMIUM RICH REGION).....	163

FIGURE 68 SEM IMAGES OF CHROMISED SS316 (A) SECONDARY ELECTRON VIEW (B) BACKSCATTERED VIEW. SURFACE MORPHOLOGIES PROVIDED AT HIGHER MAGNIFICATIONS THAN IN FIGURE 67 IN ORDER TO REVEAL THE GRANULAR MORPHOLOGY.	164
FIGURE 69 CROSS-SECTION OF (A) CHROMISED GR-SS AND (B) CHROMISED SS316 BOTH SAMPLES WERE PACK CHROMISED AT 900 °C FOR 3 HOURS.	165
FIGURE 70 XRD PATTERNS OF (A) CHROMISED GR-SS AND (B) CHROMISED SS316.	166
FIGURE 71 GLANCING XRD PATTERNS FOR CHROMISED GR-SS.	167
FIGURE 72 XPS SURVEY SPECTRA FOR CHROMISED GR-SS AFTER 10MINUTES OF ARGON SPUTTERING.	168
FIGURE 73 HIGH RESOLUTION SCAN FOR C1S IN CHROMISED GR-SS.	169
FIGURE 74 HIGH RESOLUTION SCAN FOR Cr2P IN CHROMISED GR-SS.	169
FIGURE 75 ICR OF CHROMISED GR-SS AND CHROMISED GR-SS COMPARED WITH THAT OF GRAPHITE AND GR-SS.	171
FIGURE 76 POTENTIODYNAMIC POLARISATION OF CHROMISED GR-SS, CHROMISED SS316, SS316 AND GR-SS IN 0.5 M H ₂ SO ₄ + 2 PPM HF AT 70 °C, SCAN RATE =1 mV/s.	173
FIGURE 77 POTENTIOSTATIC POLARISATION OF CHROMISED GR-SS AND CHROMISED SS316 AT 0.6 V vs. Ag/AgCl IN 0.5 M H ₂ SO ₄ + 2 PPM HF PURGED WITH AIR AT 70 °C, SCAN RATE =1 mV/s. THE INSET SHOWS THE OSCILLATORY BEHAVIOUR EXHIBITED BY CHROMISED GTR-SS.	176
FIGURE 78 SEM MICROGRAPHS OF (A) CHROMISED GR-SS (B) CHROMISED SS316 AFTER 4 HOURS OF POTENTIOSTATIC POLARISATION IN 0.5 M H ₂ SO ₄ + 2 PPM HF AT 70 °C.	177
FIGURE 79 NORMAL PROBABILITY PLOT OF THE STUDENTISED RESIDUAL FOR CORROSION CURRENT DENSITY.	184
FIGURE 80 PREDICTED VERSUS ACTUAL VALUES PLOT FOR CORROSION CURRENT DENSITY.	184

FIGURE 81 PERTURBATION PLOT FOR CORROSION CURRENT DENSITY.	186
FIGURE 82 SURFACE MORPHOLOGIES OF COATINGS PRODUCED AT (A) 1000 °C (R6) AND (B) 1100°C (R1) AT 3 WT.% ACTIVATOR CONTENT AND 6 HOURS. INSET SHOWS R6 AT MAGNIFICATION OF 2 μM.....	187
FIGURE 83 XRD OF CHROMISED COATING FORMED WITH PROCESS PARAMETERS SPECIFIED FOR R6 AND R1.....	188
FIGURE 84 SURFACE MORPHOLOGIES OF COATINGS FORMED AT PROCESS PARAMETERS INDICATED BY (A) R12 AND (B) R17.....	190
FIGURE 85 SURFACE MORPHOLOGIES OF COATINGS PRODUCED AT 1100°C FOR 3 HOURS WITH POWDER CONTAINING (A) 3 WT.% (R12) (B) 7WT% ACTIVATOR CONTENT (R13).	192
FIGURE 86 CONTONUR PLOT SHOWING THE INTERACTION BETWEEN TEMPERATURE AND ACTIVATOR CONTENT.	193
FIGURE 87 RESPONSE SURFACE PLOTS SHOWING THE INTERACTION BETWEEN TEMEPRTURE AND TIME.	194
FIGURE 88 INTERACTION PLOT SHOWING INTERACTION BETWEEN TEMPERATURE AND ACTIVATOR CONTENT.	195
FIGURE 89 SURFACE MORPHOLOGY OF (A) R1 AND (B) R9.....	196
FIGURE 90 SURFACE MORPHOLOGY OF R6 AND (B) R3.....	198
FIGURE 91 OPTIMUM CONDITIONS FOR MINIMUM CORROSION CURRENT DENSITY OF CHROMISED 304 STAINLESS STEEL IN 0.5 M H ₂ SO ₄ + 2 PPM HF AT 70 °C.....	200
FIGURE 92 TAFEL PLOT FOR COATING PRODUCED WITH OPTIMAL PROCESS PARAMETERS AND THE SUBSTRATE IN 0.5 M H ₂ SO ₄ + 2 PPM HF AT 70 °C. SCANNING RATE = 1mV/s.....	201

FIGURE 93 CHROMISED COATINGS PRODUCED AT OPTIMISED PROCESS PARAMETERS (A) SURFACE MORPHOLOGY OF THE OPTIMISED COATING (Cr-304) (B) EDX SPECTRUM AND AVERAGE COMPOSITION.....	203
FIGURE 94 CHROMISED COATINGS PRODUCED AT OPTIMISED PROCESS PARAMETERS (A) CROSS-SECTION SEM IMAGE (B) EDX LINE SCAN OF Cr-304.	204
FIGURE 95 SURVEY SPECTRUM OF Cr-304 BEFORE AND AFTER ARGON ION SPUTTERING.....	205
FIGURE 96 XPS SPECTRUM OF (A) CARBON (B) OXYGEN (C) NITROGEN AND (D) CHROMIUM IN Cr-304 AFTER 0s, 60s AND 120s OF SPUTTERING. INSET OF (D) SHOWS THE Cr2P BEFORE SPUTTERING.....	207
FIGURE 97 GLANCING INCIDENCE ANGLE XRD OF Cr-304.....	209
FIGURE 98 POTENTIODYNAMIC POLARISATION OF Cr-304 AND SS304 IN 0.5 M H ₂ SO ₄ + 2 PPM HF AT 70 °C (A) AIR BUBBLED (B) HYDROGEN BUBBLED INTO THE ELECTROLYTE,	211
FIGURE 99 POTENTIOSTATIC POLARISATION OF Cr-304 AND SS304 IN 0.5 M H ₂ SO ₄ + 2 PPM HF AT 70 °C IN SIMULATED PEM FUEL CELL (A) CATHODIC ENVIRONMENT (B) ANODIC ENVIRONMENT,	213
FIGURE 100 ICR OF Cr-304 AND SS304 AS A FUNCTION OF COMPACTION PRESSURE.	216
FIGURE 101 COMPARISON OF ICR OF SS316 IN FIGURE 75 AND SS304 IN FIGURE 100 IN ORDER TO SHOW THE INFLUENCE OF PTFE LOADING OF THE TORAY CARBON PAPER (T-GH-90) ON ICR.	219
FIGURE 102 SINGLE FUEL CELL PERFORMANCE OF Cr-304 AND SS304 BIPOLAR PLATES.....	220
FIGURE 103 XRD OF CPC-304-3 CARBURISED AT 925 °C FOR 3 HOURS.....	225
FIGURE 104 CROSS-SECTION OF 304 STAINLESS STEEL CARBURISED AT 925 °C FOR 3 HOURS....	226
FIGURE 105 SURFACE MORPHOLOGY OF (A) CPC-304-1(B) CPC-304-2 (C) CPC-304-3.....	227

FIGURE 106 SEM IMAGE AND EDX SPECTRUM OF CPC-304 (A) DISCRETE PARTICLES (B) MATRIX.	228
FIGURE 107 (A) CROSS-SECTION AND EDX COLOUR MAP OF (A) CPC-304-1(B) CPC-304-2 (C) CPC-304-3.....	229
FIGURE 108 GLANCING INCIDENCE XRD OF CPC-304 SAMPLES AT 5°	230
FIGURE 109 XPS SURVEY SPECTRUM FOR CPC-304 SAMPLES AFTER 150 SECONDS OF SPUTTERING.	232
FIGURE 110 XPS ANALYSIS OF CPC-304 SAMPLES (A) N1S (B) O1S SPECTRUM.....	233
FIGURE 111 FE2P CORE LEVEL SPECTRA FOR PRE-CARBURISED AND CHROMISED CPC-304 SAMPLES	235
FIGURE 112 INTERFACIAL CONTACT RESISTANCE OF CPC-304 STAINLESS STEELS AS A FUNCTION OF COMPACTION PRESSURE.....	236
FIGURE 113 POTENTIODYNAMIC CURVES FOR CPC-304 SAMPLES IN SIMULATED PEM FUEL CELL (A) ANODIC AND (B) CATHODIC ENVIRONMENT.....	237
FIGURE 114 POLARISATION CURVES AND POWER DENSITY CURVES FOR SINGLE FUEL CELLS WITH CPC-304, Cr-304 AND SS304 BIPOLAR PLATES.....	241
FIGURE 115 CURRENT DENSITY –TIME GRAPH FOR C-304-3, Cr-304 AND SS304 AT 0.6 V	243
FIGURE 116 CATHODE SIDE GDL OF SINGLE FUEL CELL WITH CPC-304-3 BIPOLAR PLATES AFTER 10 HOURS OF TESTING (A) SURFACE MORPHOLOGY (B) EDX SPECTRUM.....	244
FIGURE 117 CATHODE SIDE GDL OF SINGLE FUEL CELL WITH Cr-304 BIPOLAR PLATES AFTER 10 HOURS OF TESTING (A) SURFACE MORPHOLOGY (B) EDX SPECTRUM.....	244
FIGURE 118 (A) SEM IMAGE (B) EDX SPECTRUM OF THE CATHODE SIDE GDL OF SINGLE CELL WITH SS304 BIPOLAR PLATES AFTER 10 HOURS OF TESTING.....	245

FIGURE 119 SURFACE MORPHOLOGIES OF CHROMISED 304 STAINLESS STEEL PRODUCED AT (A)
1000 °C AND (B) 1100 °C FOR 3 HOURS 287

FIGURE 120 (A) HYDROGEN GAS REGULATOR B) HYDROGEN LEAK SENSOR AND EXTRACTION HOOD
..... 294

LIST OF TABLES

TABLE 1 COMPARISONS OF THE DIFFERENT TYPES OF HYDROGEN FUEL CELLS	7
TABLE 2 REPRESENTATIVE PHYSICAL VALUES FOR DIFFERENT BIPOLAR PLATE MATERIAL.....	30
TABLE 3 POSSIBLE OXYGEN REDUCTION REACTIONS AT THE PEM FUEL CELL CATHODE AND THE THERMODYNAMIC ELECTRODE POTENTIALS OF ELECTROCHEMICAL O ₂ REDUCTIONS	32
TABLE 4 DENSITIES OF METALS COMMONLY USED FOR BIPOLAR PLATE.....	42
TABLE 5 COMPARISON OF C-17200 CU-BE ALLOY BIPOLAR PLATE PERFORMANCE WITH 316L STAINLESS STEEL BIPOLAR PLATE.	44
TABLE 6 NOMINAL COMPOSITION OF SUBSTRATE USED FOR COBLAST™ PROCESS.....	85
TABLE 7 PROCESS FACTORS AND DESIGN LEVELS	100
TABLE 8 DESIGN MATRIX BASED ON THREE- LEVEL, THREE –FACTOR BOX–BEHNKEN DESIGN....	101
TABLE 9 PREPARATION METHODS FOR MATERIALS USED FOR THE BIPOLAR PLATES.....	129
TABLE 10 SURFACE ROUGHNESS AND CONTACT ANGLE OF COATED AND UNCOATED SURFACES..	137
TABLE 11 XPS CHEMICAL COMPOSITION OF THE OUTER LAYER FOR THE COATED AND UNCOATED METALS.....	141
TABLE 12 2 x ICR OF GR-TiV AND BARE-TiV AT 140 N/CM ²	147
TABLE 13 CORROSION PARAMETERS OF GR-TiV AND TiV IN 0.5 M H ₂ SO ₄ + 2 PPM AT ROOM TEMPERATURE.	148
TABLE 14 TOTAL METAL ION CONCENTRATION AFTER 14400 SECONDS OF POTENTIOSTATIC POLARISATION OF GR-TiV AND TiV IN SIMULATED PEM FUEL CELL ENVIRONMENT OF 0.5 M H ₂ SO ₄ +2 PPM HF AT 70 °C	153

TABLE 15 CORROSION POTENTIAL AND CORROSION CURRENT DENSITY OF GR-SS AND SS316 IN SIMULATED PEM FUEL CELL ENVIRONMENT OF 0.5 M + 2 PPM H ₂ SO ₄ AT ROOM TEMPERATURE WITH AIR BUBBLING (CATHODE) AND HYDROGEN GAS BUBBLING (ANODE)	156
TABLE 16 METALLIC ION CONCENTRATION (IN PPM) AFTER POTENTIOSTATIC POLARISATION IN PEM FUEL CELL CATHODE ENVIRONMENT AND WORKING POTENTIAL.....	158
TABLE 17 CORROSION PARAMETERS FOR CHROMISED GR-SS, CHROMISED SS316, SS316 AND GR- SS.....	174
TABLE 18 DESIGN MATRIX BASED ON THREE LEVEL-THREE FACTOR BOX-BEHNKEN DESIGN.	180
TABLE 19 SEQUENTIAL MODEL SUM OF SQUARES	181
TABLE 20 ANOVA FOR RESPONSE SURFACE QUADRATIC MODEL.....	182
TABLE 21 CONSTRAINTS FOR OPTIMISATION.....	200
TABLE 22 XPS PARAMETERS FOR COMPOSITION AND BINDING ENERGY OF CR-304 WITH THE SPUTTERING PROFILE.	206
TABLE 23 CORROSION PARAMETERS OF SS304 AND CR-304 IN SIMULATED PEM FUEL CELL ENVIRONMENTS.	212
TABLE 24 COMPARISON OF THE PERFORMANCE OF CR-304 WITH PUBLISHED WORKS ON CHROMISED STAINLESS STEELS FOR PEM FUEL CELL BIPOLAR PLATE APPLICATION.....	215
TABLE 25 ICR OF 304 STAINLESS STEEL IN THE LITREATURE.....	218
TABLE 26 ICR OF CHROMISED STAINLESS STEEL IN THE LITREATURE	218
TABLE 27 PEAK POWER DATA FOR THE SINGLE CELLS WITH COATED AND UNCOATED STAINLESS STEEL AND THE CORRESPONDING ICR AT 125 N/cm ²	220
TABLE 28 MASS GAIN BY SS304 AFTER CARBURISING FOR 1-3 HOURS AND SUBSEQUENTLY CHROMISING AT 1040 °C FOR ~ 3 HOURS	224

TABLE 29: CORROSION PARAMETERS OF CPC-304 SAMPLES IN 0.5 M H₂SO₄ + 2 PPM HF AT 70 °C

..... 238

TABLE 30 TIME RANGE REPORTED FOR PACK CHROMISING PROCESS IN THE LITERATURE. 288

LIST OF ABBREVIATIONS

PEM	Proton Exchange Membrane
AFC	Alkaline fuel cell
GHG	Greenhouse gases
MCFC	Molten Carbonate fuel cell
PAFC	Phosphoric acid fuel cell
SOFC	Solid oxide fuel cell
MEA	Membrane Electrode Assembly
GDL	Gas Diffusion Layer
ICR	Interfacial Contact Resistance
ORR	Oxygen Reduction Reaction
HRR	Hydrogen Reduction reaction
DoE	Design of Experiments
DOE	Department of Energy
RSM	Response of Surface Methodology
OCV	Open Circuit Voltage
SEM	Scanning Electron Microscopy
EDX	Energy-dispersive X-ray spectroscopy
MEA	Membrane Electrode Assembly
XPS	X-ray Photoelectron Spectroscopy
XRD	X-ray Diffraction
EDM	Electrical Discharge Machine
au	arbitrary unit

sccm	Standard Cubic Centimetre Per Minute
i_{corr}	Corrosion current density
E_{corr}	Corrosion potential

Chapter 1

Introduction

1.1 INTRODUCTION

Developing alternative fuels to reduce global dependence on fossil fuel and to meet the ever-growing global energy demand and consumption driven by an escalating population and an upsurge in human activities, is a key energy challenge of the 21st century. According to recent reports [1-3], more than 80% of the energy consumed globally is derived from fossil fuels, with crude oil accounting for about one third of the total fossil fuel consumption as shown in Figure 1. The combustion of fossil fuels within various energy-requiring activities releases anthropogenic greenhouse gases (GHG) such as carbon dioxide (CO₂), nitrous oxide (N₂O), and methane (CH₄) etc. into the atmosphere resulting in air pollution, global warming and affects climate change. Among these GHG gases, the concentration of CO₂ has been reported to increase annually with energy use in electricity and heat generation as well as the transport sector, accounting for over 50% of CO₂ emissions [3]. Besides the environmental challenges, the substantiality of fossil fuels, as the world's major energy source is doubtful, due to the finite nature of fossil fuels and instability of crude oil prices. Hence, it is imperative that alternatives to fossil fuels must not only be clean, but also renewable.

Hydrogen is one of the most promising alternative fuels being developed particularly for the transport sector, which accounted for over 60% of the world oil energy consumption and over 23% of global CO₂ emission in 2012 [4-6]. Hydrogen can generally be considered as a future energy supply to be utilised in the transport sector for the following reasons:

World consumption

Million tonnes oil equivalent

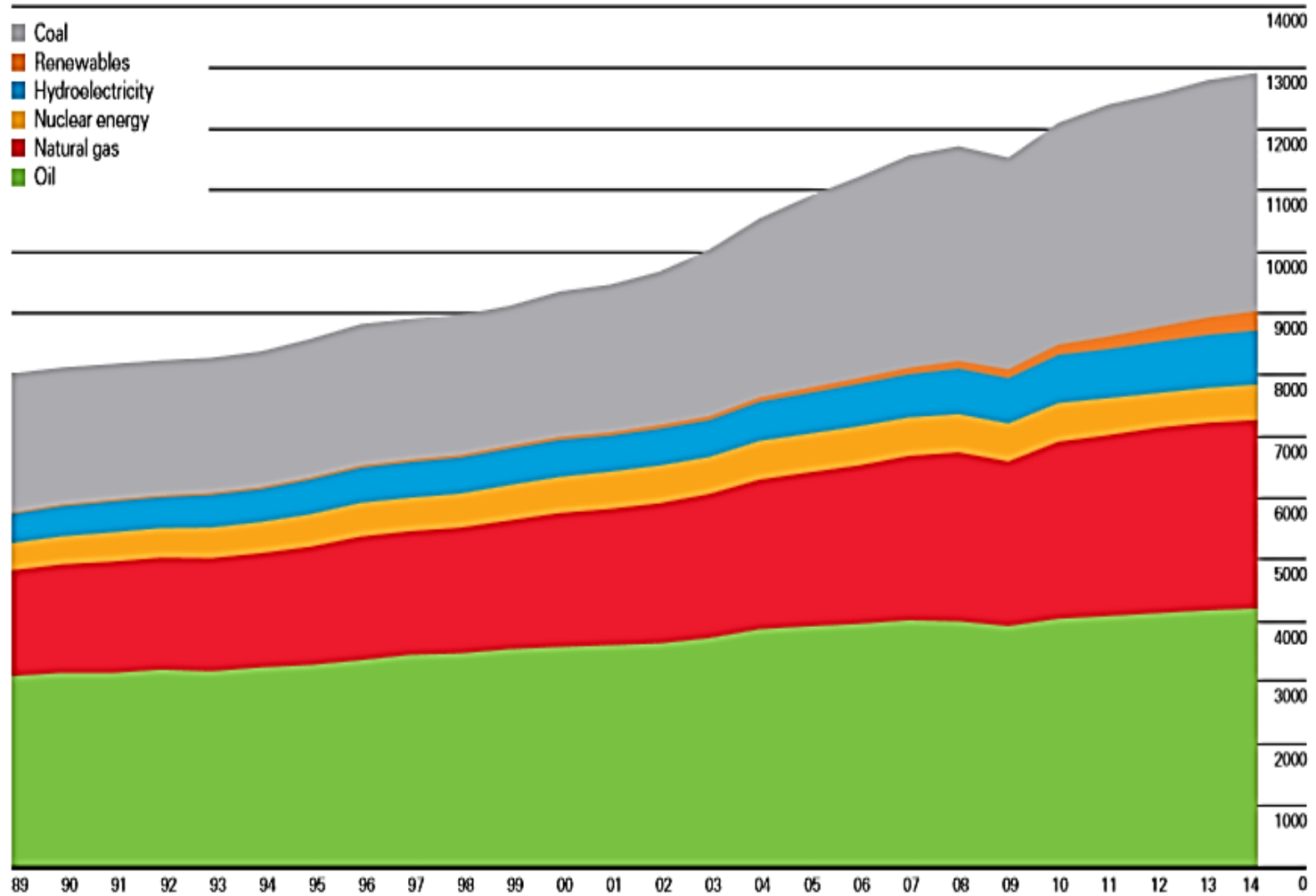


Figure 1 World Primary Energy Consumption for 2014 [1].

- (1) Hydrogen can be produced from diverse energy sources such as steam reforming of natural gas, gasification of coal, partial oxidation of hydrocarbon fuels, pyrolysis of biomass and electrolysis of water, which are powered by renewable energy sources such as wind, solar and nuclear energy.
- (2) The main by-product of the chemical reaction between hydrogen and oxygen/air is water depending on the source of hydrogen; hence, the use of hydrogen in automobiles and other transportation devices has the potential to reduce GHG gases emissions from conventional petroleum based fuels.
- (3) Hydrogen can be used in conventional internal combustion engines, although the combustion of hydrogen can generate small amounts of nitrous oxide.
- (4) Hydrogen has a higher specific energy (120 MJ/kg) than that of any other transport fuel. For instance, 1 kg of hydrogen can deliver about three times the energy of an equivalent weight of petrol with a specific energy of 43 MJ/kg. However, the volumetric density of hydrogen is lower than that of petrol, implying that a liter of petrol contains about six times more energy than an equivalent volume of hydrogen. The low volumetric density of hydrogen poses a challenge for on-board storage; hence, it has attracted considerable research attention.

Amongst the various modes of transport, road transport accounts for a considerable portion of the oil consumed and CO₂ emission globally [1-7]. In Europe, for instance, GHG emissions from road transport contributed about 60% of the total CO₂ emissions in 2012 with emissions from light duties vehicles such cars and vans accounting for three quarters of the emissions [7, 8]. Although, there are strict governmental policies and legations around the reduction of CO₂ emissions, especially in developed nations, notwithstanding, with increasing number of automobiles on our roads, the environmental impact of CO₂ emissions on life especially in our urban cities has become

more threatening. Hence, the need for the substitution of fossil fuel driven automobiles with hydrogen fuelled automobiles, built on fuel cell based technology, which generates only water and heat as by-products.

1.2 FUEL CELLS

Fuel cells are energy conversion devices that generate electricity from the electrochemical reaction of a hydrogen-rich fuel (hydrogen, methanol, natural gas etc.) and an oxidant (air or oxygen) to produce water and heat as the main by-products [9-13]. In other words, fuel cells convert the chemical energy of a fuel directly into electrical energy. A single fuel cell as diagrammatically represented in Figure 2, consists of an electrolyte sandwiched between two electrodes.

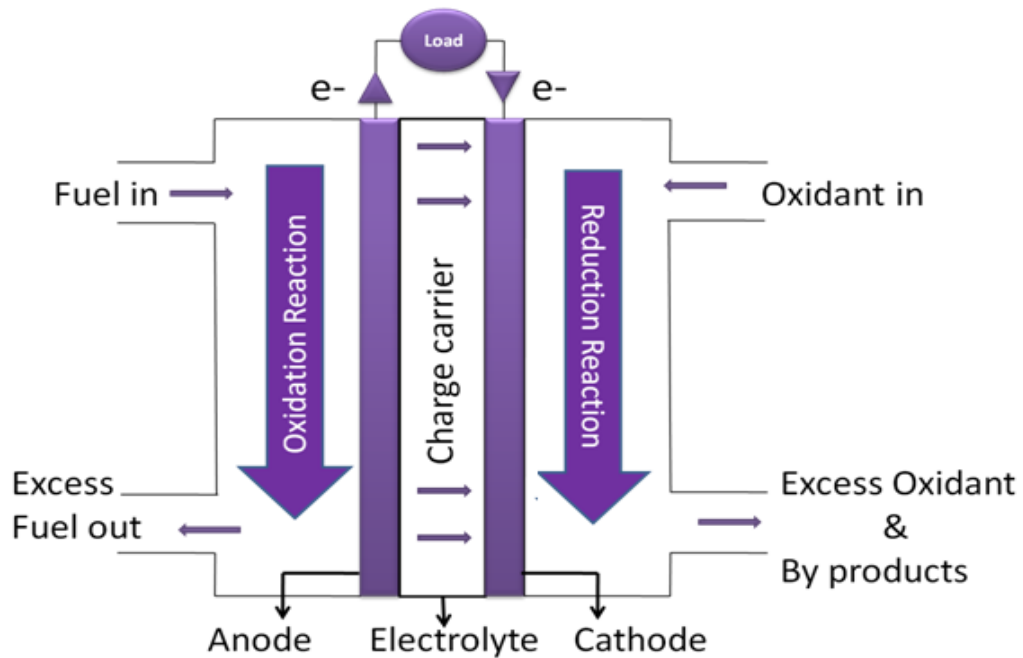


Figure 2 Schematic diagram of a fuel cell, adapted from [14]

At the anode, the hydrogen-rich fuel is oxidised into hydrogen or hydroxyl ions (depending on the type of fuel cells). The electrons travel through an external circuit to generate electricity while the hydrogen or hydroxyl ions migrate to the cathode via the electrolyte to react with oxygen forming water as a by-product.

1.2.1 Fuel cells and competing technologies

Fuel cells offer many advantages over conventional technologies such as the internal combustion engines and batteries which have gained widespread market acceptance. Compared to internal combustion engines (ICEs):

(1) Fuel cells directly convert the chemical energy in fuels to electricity without an intermediate step, thus they are not limited by Carnot cycle and can operate at efficiencies of more than 60%.

In contrast, ICEs convert chemical energy in fuels to electricity via intermediate steps of thermal and mechanical energy.

(2) Fuel cells are environmentally friendly devices which have near zero pollutant emissions while the water and heat by-products can be used for co-generation. Conversely, combustion of fossil fuels in ICEs generates CO₂ and other related GHG emissions.

(3) Fuel cells have no internal moving parts; hence they operate quieter than ICEs.

Fuel cells, however, operate similar energy conversion principle as batteries. Both devices convert chemical energy into electrical energy via electrochemical reactions. Also, both devices can achieve high efficiencies when partially loaded. The main difference between fuel cells and batteries is the need to recharge the latter due to the limited storage capacity of the electrode from which the energy for the electrochemical process is generated. Fuel cells, however, do not require

recharging as they can continuously produce direct current as long as the fuel/oxidant supply is maintained [9 -13, 15].

1.2.2 Types of Fuel Cells

Fuel cells dates back to the 19th century when Sir William Grove, a Welsh judge and scientist, demonstrated that the backward reaction of water electrolysis can generate electricity. Hence, he built the first fuel cells initially called a gas battery, which has gone through various developmental stages. At present, there are five main types of hydrogen fuel cells used in various applications including transportation, stationary power generation and portable devices. Fuel cells are fundamentally classified according to the type of electrolytes employed. They can also be further classified by their operating temperatures into low and high temperature fuel cells [9-12, 14, 15]. The basic characteristics of each fuel cell type is summarised in Table 1 and briefly described below:

1. Alkaline fuel cells

Alkaline fuel cell (AFC) was the first practical fuel cell to be developed. AFC utilises an aqueous electrolyte, potassium hydroxide (KOH), and operates at 90-100 °C. The first AFC was built by Francis Bacon, a British Engineer in 1939 and was later improved on by UTC, USA. The improved AFC was used to power the National Aeronautics and Space Administration (NASA) Apollo space craft in the 20th century. The advantages of AFC includes: (1) a less corrosive alkaline environment, which permits the use of cheaper component materials (2) the use of non-noble metal catalysts such as Nickel and Silver. (3) AFC can achieve higher electrical efficiency of up to 60% compared to other low temperature fuel cells. Nevertheless, the aqueous electrolyte in AFC is sensitive to carbon dioxide and the volume of the liquid used affects cell performance:

excess/insufficient liquid results in electrode flooding/drying. Recent advances in AFC include the replacement of KOH solution with an anion exchange membrane [9-13, 15].

Table 1 Comparisons of the different types of hydrogen fuel cells [9-13]

Type	Electrolyte	Operating temperature (°C)	Fuel	Efficiency (%)	Application
Alkaline fuel cells (AFC)	Aqueous solution of potassium hydroxide	90-100	Pure hydrogen	50	Military and space
Proton exchange (PEM) fuel cells	Solid polymer membrane	60-80	Pure hydrogen	40-60	Transportation, stationary-power back up, portable power
Phosphoric acid fuel cells (PAFC)	Phosphoric acid	150-200	Pure hydrogen	40	Distributed generation
Molten carbonate fuel cells (MCFC)	Lithium and potassium carbonate	600-700	Hydrogen, methane and other hydrocarbon	>50	Distributed power
Solid oxide fuel cells (SOFC)	Stabilised solid electrolyte	700-1000	Hydrogen, methane and other hydrocarbon	>50	Auxiliary power Distributed generation

2. Proton Exchange Membrane Fuel Cells

Proton exchange membrane (PEM) fuel cells are low temperature fuel cells which operate between 60-80 °C. They are typically based on a solid polymer electrolyte (also called the proton exchange membrane) and porous carbon electrodes containing a platinum or platinum alloy catalyst. The main advantages of PEM fuel cells are low operating temperatures, high power density and near zero emissions, which make their application in automobiles very attractive. On the other hand, the platinum based catalyst is very sensitive to carbon monoxide poisoning, hence, pure hydrogen must be used. If impure hydrogen is used, an additional reactor that reduces carbon monoxide (CO) is necessary. Other drawbacks of PEM fuel cells include cost and durability of other components [9-13, 16, 17].

3. Phosphoric Acid Fuel Cells

Phosphoric acid fuel cells (PAFC) were the first type of fuel cells to be commercially developed for stationary power generation. This type of fuel cells is currently in use for power generation in some office buildings and hotels in Europe, America and Japan. As the name suggests, the electrolyte in PAFC is concentrated phosphoric acid, in a Teflon-bonded silicon carbide matrix, while the electrodes are porous carbon containing platinum catalyst. They operate typically between 150 °C and 220 °C. Advantages of PAFC are (1) co-generation of electricity and heat making it to achieve high efficiency of up to 85%. However, the efficiency is lower (about 37-42%) when only electricity is generated. (2) Higher resistance to carbon monoxide poisoning compared to AFC and PEM fuel cells. Hence, PAFC can utilise hydrogen produced from fossil fuels, which often contain sulphur. The main drawback of PAFC is associated with the high cost of the catalyst [9-13, 18].

4. Molten Carbonate Fuel Cells

Molten carbonate fuel cells (MCFC) are high temperature fuel cells (600-700 °C) composed of a mixture of carbonate salt as electrolyte (e.g. $\text{Li}_2\text{CO}_3/\text{K}_2\text{CO}_3$ or $\text{Li}_2\text{CO}_3/\text{Na}_2\text{CO}_3$) and porous carbon electrodes. At 650 °C, the electrolyte melts into conductive carbonate ion at the cathode. MCFC are tolerant to CO poisoning, hence, they can use a wide variety of fuels such as biogas and natural gas. These high temperature fuel cells can achieve up to 60% efficiency when used for electricity generation alone and up to 85% efficiency when used for cogeneration of heat and electricity. Another advantage of MCFC is the possibility of using non-noble metal as catalyst; thereby reducing cost. However, slow start-up and limited durability as well as high operating temperature and corrosive electrolyte which promote material degradation are major demerits of the MCFC [9-13, 19].

5. Solid Oxide Fuel Cells

This type of fuel cells generate electricity at high temperatures between 800-1000 °C via a solid ceramic electrolyte (e.g. zirconium oxide stabilised with yttrium oxide (YSZ)) sandwiched between porous electrodes. At the cathode, oxygen from air is reduced to oxygen ions and thereafter migrates to the cathode to react with hydrogen producing electricity and heat. The high operating temperature in solid oxide fuel cells (SOFC) permits the use of a wide variety of fuels, eliminates the need for external fuel reformers and makes the use of non-precious metal catalysts possible. Durability as in the case of MCFC is one of the major challenges with SOFC [9-13, 20].

1.3 FUEL CELLS FOR ROAD TRANSPORTATION

Fuel cells find application in diverse energy requiring devices ranging from portable devices to stationary power distribution and transportation devices. Remarkable progress has been reported in recent times concerning the development of fuel cells for portable devices, stationary power generation and automobiles [9, 13, 16, 18]. In the transport sector, the successful deployment of fuel cells as power sources for automobiles could be promising for reduction of global GHG emissions.

Amongst the different types of fuel cells, PEM fuel cells are attractive for automotive propulsion due to its high power density, low operating temperatures and near zero emissions, all advantageous over conventional internal combustion engines (ICEs). Nevertheless, there are a number of economic and technical challenges that need to be addressed before PEM fuel cells powered automobiles can be fully commercialised. One of these challenges is the development of low cost and durable materials for key components of the PEM fuel cells stack.

A typical PEM fuel cells stack consists of a number of single fuel cells arranged in series. Each single fuel cell is made up of a membrane electrode assembly (MEA) sandwiched between two bipolar plates. The MEA consist of a solid polymer electrolyte, the catalyst layer and the gas diffusion layer (GDL). These components perform vital roles, which will be discussed later in Chapter 2, which dictate the performance of the PEM fuel cells. Hence, cost reduction and durability enhancement of materials used for these components, are considered necessary for commercialisation of PEM fuel cells.

The present research focuses on the bipolar plates, which constitute a significant proportion of the cost and weight of the stack. Bipolar plates are traditionally fabricated from non-porous graphite

due, to their high corrosion resistance and high surface conductivity in the warm and humid PEM fuel cells environment. Conversely, graphite is brittle and has to be made several millimetres thick (> 2-5mm) via resin impregnation to prevent gas leakage. The use of thick plates adversely affects the power density of the fuel cells. In addition, the processing and machining cost associated with graphite bipolar plates are too enormous for mass production consideration. Thus, alternative materials such as metals and carbon based composites are under investigation to replace graphite bipolar plates [16, 17, 21-24].

Metals such as stainless steels and aluminium generally offer advantages such as higher mechanical strength and lower cost of production, over carbon based composites and graphite. Metals are also better conductors of heat and electricity, impermeable to gases and amendable to low-cost production process like stamping and hydroforming. Metals are, however, susceptible to corrosion attack in PEM fuel cell environments and exhibit high interfacial contact resistance with the GDL. Metallic ions produced during corrosion can poison the proton exchange membrane and be detrimental to its efficiency. On the other hand, high contact resistance with the GDL can generate ohmic losses within the cell that degrade cell output power [21-23]. Consequently, surface modification of metals via coatings and treatments is necessary for metals to be a viable option for PEM fuel cells bipolar plate.

1.4 RESEARCH GOALS AND APPROACH

The primary aim of this research work is to explore the feasibility of developing surface coatings that can enhance the performance of metal bipolar plates in PEM fuel cells. This aim was accomplished through the following objectives:

1. Characterisation and evaluation of adopted coatings performance in simulated PEM fuel cells environments.
2. Optimisation of coating parameters via experimental design.
3. Evaluation of single fuel cell performance of selected coatings.

The research was conducted in two phases:

1. Evaluation and modification of novel CoBlast™ graphite coatings.
2. Optimisation of pack-cemented chromised coating via experimental designs, performance evaluation of the optimised chromised coating in simulated and real PEM fuel cell environments and modification of the optimised coatings.

The targets for each phase are as outlined below:

Phase I: Evaluation and modification of CoBlast™ deposited graphite coatings

- Preliminary investigations into the suitability of graphite coatings deposited by a room temperature surface enhancement technique known as CoBlast™ and subsequent modification of the coatings.
- Surface characterisation of the coated surfaces using scanning electron microscopy (SEM), energy dispersive X-ray (EDX) analysis and X-ray diffraction (XRD) and X-ray photoelectron spectroscopy (XPS).

Phase 2: Optimisation of pack-chromised coating via experimental designs

- Development of design matrix based on Box-Behnken experimental designs and implementation of the design matrix to deposit coatings. Accelerated corrosion testing and

surface characterisation using scanning electron microscopy (SEM), energy dispersive x-ray (EDX) analysis and X-ray diffraction (XRD) for chromised coatings

- Development of a mathematical model, optimisation of deposition process parameters and validation of model developed
- Surface characterisation of the optimised coating with scanning electron microscopy (SEM), energy dispersive x-ray (EDX) analysis and X-ray diffraction (XRD) and X-ray photoelectron spectroscopy (XPS)
- Simulative testing in PEM fuel cell cathodic and anodic working conditions and environments.
- Evaluation of single cell performance of optimised chromised coating using the substrate as reference.
- Attempts to improve single cell performance of the optimised chromised coatings via pack carburisation prior to chromising.

The application of chromised coatings for enhancing the surface conductivity and corrosion properties in PEM fuel cell environment has been reported in the literature. However, only comparatively few alloys have been investigated within limited process parameters [25-29]. Hence, in this work, a design of experiments (DoE) approach will be adopted to systemically investigate the effect of process parameters on the corrosion current density of pack-chromised AISI304 stainless steel exposed to a simulated PEM fuel cell environment of 0.5 M H₂SO₄ + 2 ppm HF at 70 °C for the first time. DoE will also be employed to establish optimum process parameters for depositing pack-chromised coating on AISI304 stainless steel with minimum corrosion current density in the selected simulated PEM fuel cell environment.

1.5 THESIS OUTLINE

This thesis is presented in eight chapters. Chapter one introduces the reader to the challenges and opportunities of fuel cell driven automobiles, as well as the research aims and objectives. In chapter two, a review of the literature on important aspects of PEM fuel cells is given, as well as a review of surface coatings and treatments employed in bipolar plate applications and their performances in real and simulated environments. Chapter three focuses on the materials, methods and equipment utilised for coating deposition, surface characterisation, and corrosion testing, as well as surface conductivities of coating and single cell performance along with the design of experiment (DoE) approach used. The results obtained for surface characterisation, electrochemical polarisation and contact resistance of CoBlast™ coatings and its subsequent modification by pack chromising are reported and discussed in Chapters 4 and 5 respectively. In chapter 6, the DoE results for the systematic investigation of the influence of the selected parameters on corrosion current density of chromised 304 stainless steel as well as optimisation of the process parameters were presented and discussed. In-situ and ex-situ performance of the chromised stainless steel produced at the optimised process parameters were also discussed. Chapter 7 presents and discusses the surface characterisation results obtained for the surface characterisation of the modified chromised coatings as well as its performance in real and simulated PEM fuel cell environments. The conclusions drawn from the study, contributions to knowledge and recommendations for future work are highlighted in the eighth chapter.

Chapter Two

Background and Literature review

2.1 INTRODUCTION

In this chapter, details of the operating principles and components of the PEM fuel cells as well as the challenges to commercialisation of PEM fuel cells are presented. A review of the literature on metallic bipolar plates is also presented.

2.2 PROTON EXCHANGE MEMBRANE FUEL CELLS

Proton exchange membrane (PEM) fuel cells are energy conversion devices that generate clean electrical energy from the electrochemical reaction between hydrogen and oxygen. These devices use an electro-catalyst and a solid polymer membrane and function at temperatures between 60 °C and 80 °C producing water and heat as the only by-products. Hence, these electrochemical devices are increasingly being targeted for automotive, stationary and portable power generation. Other advantages of PEM fuel cells include low operating temperature, high power density, quick start-up capacity, and rapid response to varying load. [9-13, 16, 17].

A single PEM fuel cell consists of the membrane electrode assembly (MEA), the flow fields plates (also called bipolar plates in stacks), current collector, backing/end plates, the gaskets and bolts arranged as shown in Figure 3. The basic operation of a typical PEM fuel cell involves oxidation of hydrogen at the anode and reduction of either oxygen or air at the cathode.

As illustrated in Figure 3, humidified reactant gases (H_2 and O_2 /air) are pumped in through the bipolar plates to the respective electrodes:

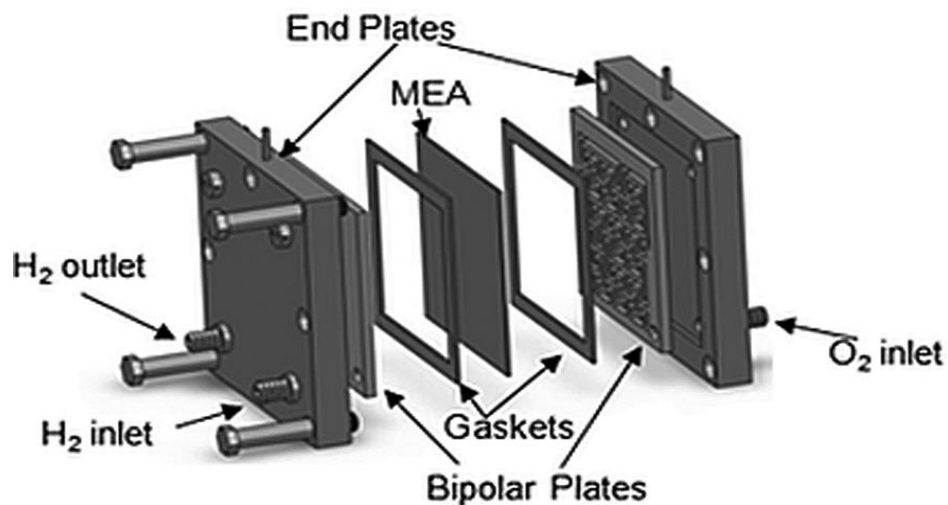
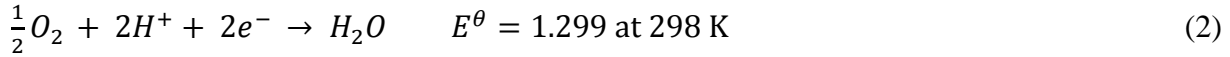


Figure 3 Components of a PEM fuel cell [30].

At the anode, hydrogen gas is oxidised to hydrogen protons by releasing its electrons as shown in Equation 1. The reaction is known as the hydrogen oxidation reactions (HOR).



The hydrogen ion produced at the anode travels through the solid polymer electrolyte, which only allows the passage of positively charged ions, to the cathode while the electrons are transported to the cathode through an external circuit. At the cathode, the hydrogen protons react with oxygen or air by a reaction known as the oxygen reduction reaction (ORR) (Equation 2)



The overall reaction is;

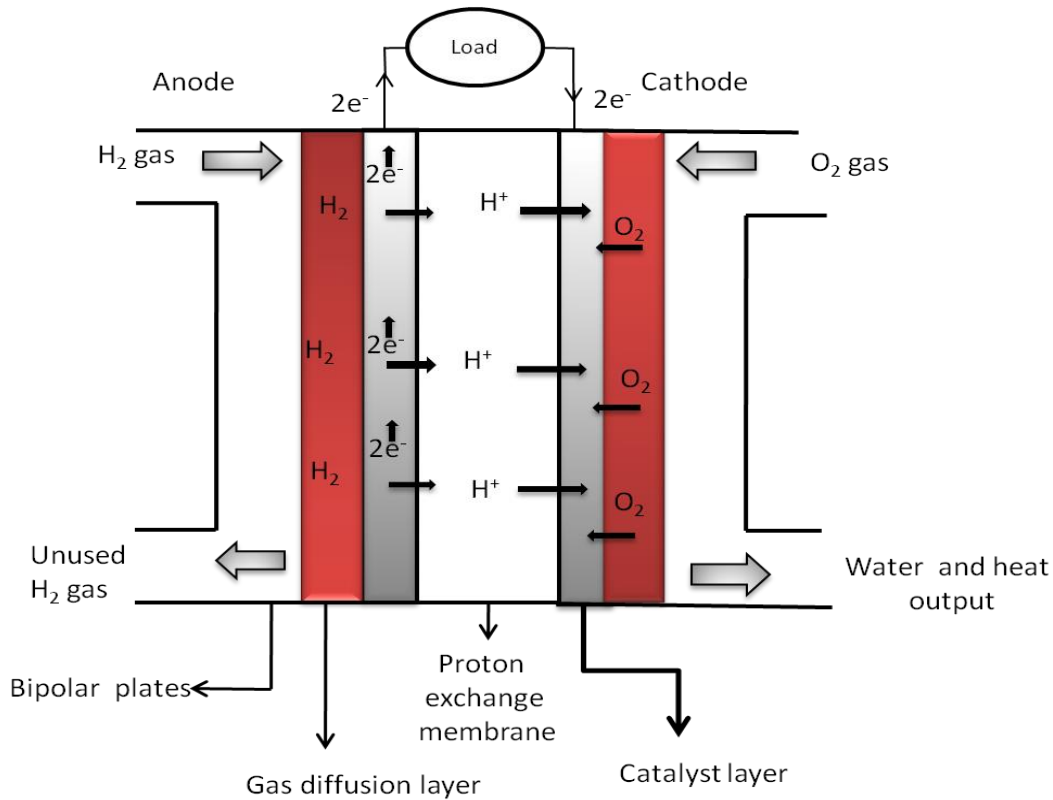
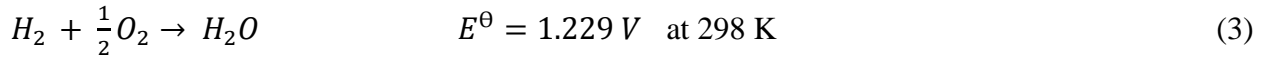


Figure 4 Schematic diagram of a PEM fuel cell.

2.1.1 PEM fuel cell stack

Single PEM fuel cells have little practical application due to the low voltage (0.6-0.7 V) produced. Therefore, in order to achieve higher voltage output for practical application, two or more single cells are arranged in series to form a stack, as shown in Figure 5.

PEM fuel stacks consist of the membrane electrode assembly, bipolar plates, end plate, current collectors and bolts. Among these components, the bipolar plates and the membrane electrode assembly (MEA) are key components that significantly influence the cost, performance and durability of the stack. These components and their functions are briefly discussed as follows:

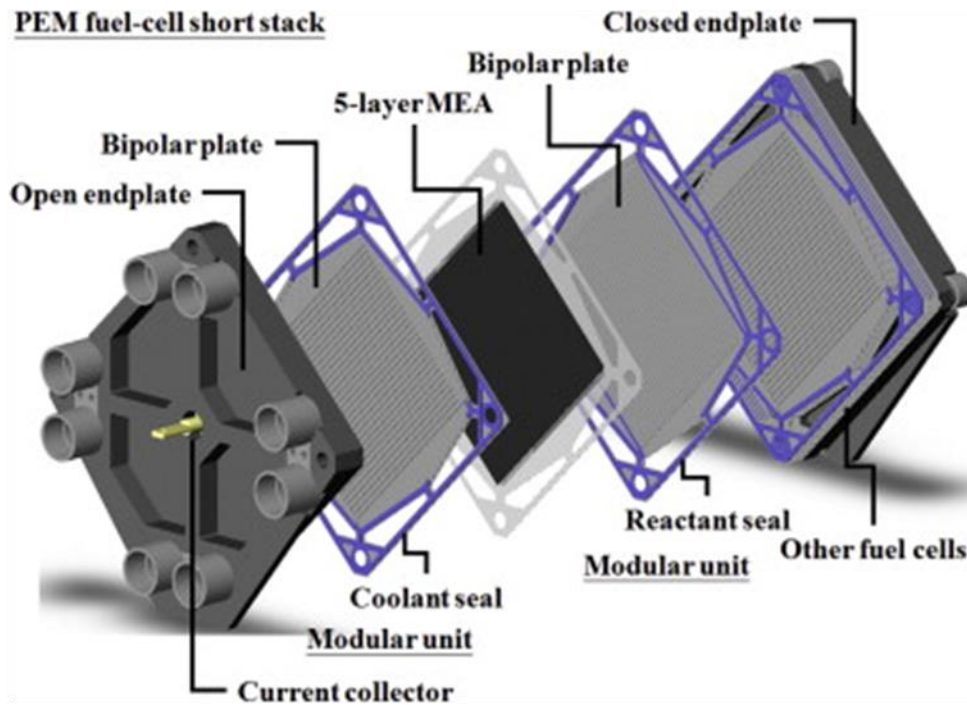


Figure 5 Schematic representation of a PEM fuel cell stacks [31].

(A) Proton Exchange Membrane

The membrane in a typical PEM fuel cell is a solid polymer which conducts only protons and is often referred to as ‘the heart’ of PEM fuel stacks, as its performs critical roles that determine cell performance. The primary roles of the membrane includes; (1) transportation of hydrogen proton produced at the anode to the cathode, (2) structural support for the MEA and (3) separation of the reactions at the cathode (ORR) and the anode (HOR). Hence, the basic requirements for PEMs are

high ionic and proton conductivity as well as high mechanical, chemical and thermal stability under PEM fuel cell working conditions. Other requirements include cost effectiveness, low gas impermeability and availability.

Perfluorinated sulfonic acid (PFSA) membranes with a polymer backbone with a basic chemical structure shown in Figure 6 are commonly used in conventional and commercially available PEM fuel cells. Examples of PSFA membranes include Nafion[®] Gore[®], Flemion[®] and Aciplex[®]. Among these membranes, Nafion[®] is the most widely used PSFA electrolyte, as it possesses high proton conductivity and high mechanical strength. However, Nafion[®] is expensive and requires that the reactant gases be humidified to prevent the membrane from drying out.

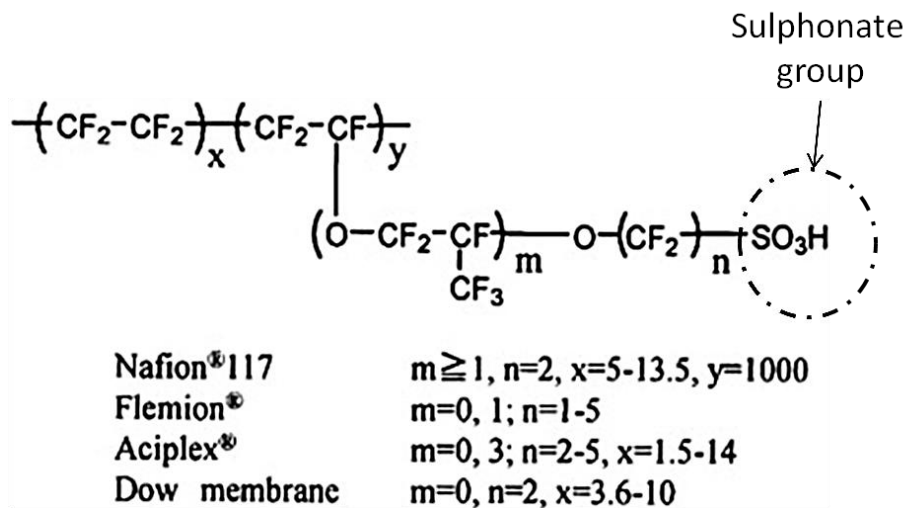


Figure 6 Structure of per fluorinated sulfonic acid (PFSA) membranes [32].

Alternative materials to Nafion[®] membranes include radiation grafted polymer electrolytes, modified Nafion membranes with porous support material or added organic/inorganic compounds and sulfonated aromatic polymeric such as sulphonated Polyetherketone (PEEK) with chemical structure as shown in Figure 7. PEMs are subject to mechanical degradation such pinholes, cracks,

tears, and chemical degradation by hydroperoxyl radicals (HO_2^\cdot), cationic contaminations etc. These failure modes have a profound effect on proton conductance and water transport within the membrane [10, 12, 16, 32-34].

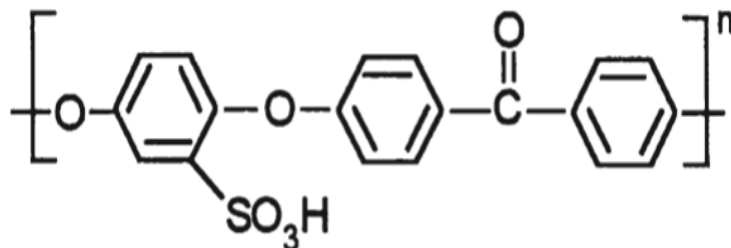


Figure 7 Structure of sulphonated Poly ether ketone [33].

(B) The Catalyst Layer

The catalyst layer consists of platinum or a platinum alloy supported on carbon materials such as Vulcan-XC 72 carbon black or a catalyst coated membrane. The platinum catalyst facilitates the electrochemical reactions within the fuel cells, such as hydrogen oxidation reactions (HOR) and oxygen reduction reactions (ORR). The latter is typically a very slow reaction and therefore determines the performance of the catalyst layer in PEM fuel cell working conditions. The rate of these reactions depends on factors such as the chemical composition and catalyst loading. A high catalyst loading facilitates faster electrochemical reactions at increased cost.

The catalyst layer, generally, constitutes the largest proportion of the cost of a PEM fuel cell stack due to the high price of platinum. However, in recent times, different approaches to cost reduction have been explored. These approaches includes: reduction of platinum loading, development of non-precious metal catalysts such as iron-based nanostructures on nitrogen functionalised mesoporous carbons (NMC), and the use of non-carboneous support. Nevertheless, achieving high

ORR activity and stability in PEM fuel cell environments is challenging. Apart from cost reduction, improving the durability of the catalyst layer is another research and development (R&D) focus, as the catalyst layer is subject to a couple of degradation processes such as; poisoning and contamination from impurities which originate from the fuel/oxidant supply or other fuel cell components, agglomeration of platinum particle (Ostwening ripening) and carbon support corrosion [10-12, 16, 17, 33, 34].

(C) The Gas Diffusion Layer

The gas diffusion layer (GDL) is a single or dual layer carbon based material with a porous structure which permits the diffusion of reactant gases (H_2 and O_2 /air) from the bipolar plates to the catalyst layer and conducts electrons between the two components. The GDL also provides mechanical support to the catalyst layer and facilitates water and heat transport from the catalyst layer to the bipolar plates as illustrated in Figure 8 (a). GDLs are required to be hydrophobic in order to effectively remove water produced at the cathode which can lead to blockage of the pores thereby preventing gas passage to the catalyst,

The single layered GDLs are made of a macro-porous substrate such as carbon paper, cloth (Figure 8 (b)) or foam treated with polytetrafluoroethylene (PTFE). The double layered GDLs, on the other hand, contain an additional thin microporous layer of carbon black powder mixed with PTFE which is positioned next to the catalyst layer to reduce the contact resistance and enhance water transport between the two components. The GDL is subject to degradation modes such as mechanical failure due to the thermal cycling nature of the PEM fuel cells and loss of hydrophobic material due to long term use [10, 12, 13, 17, 34, 35].

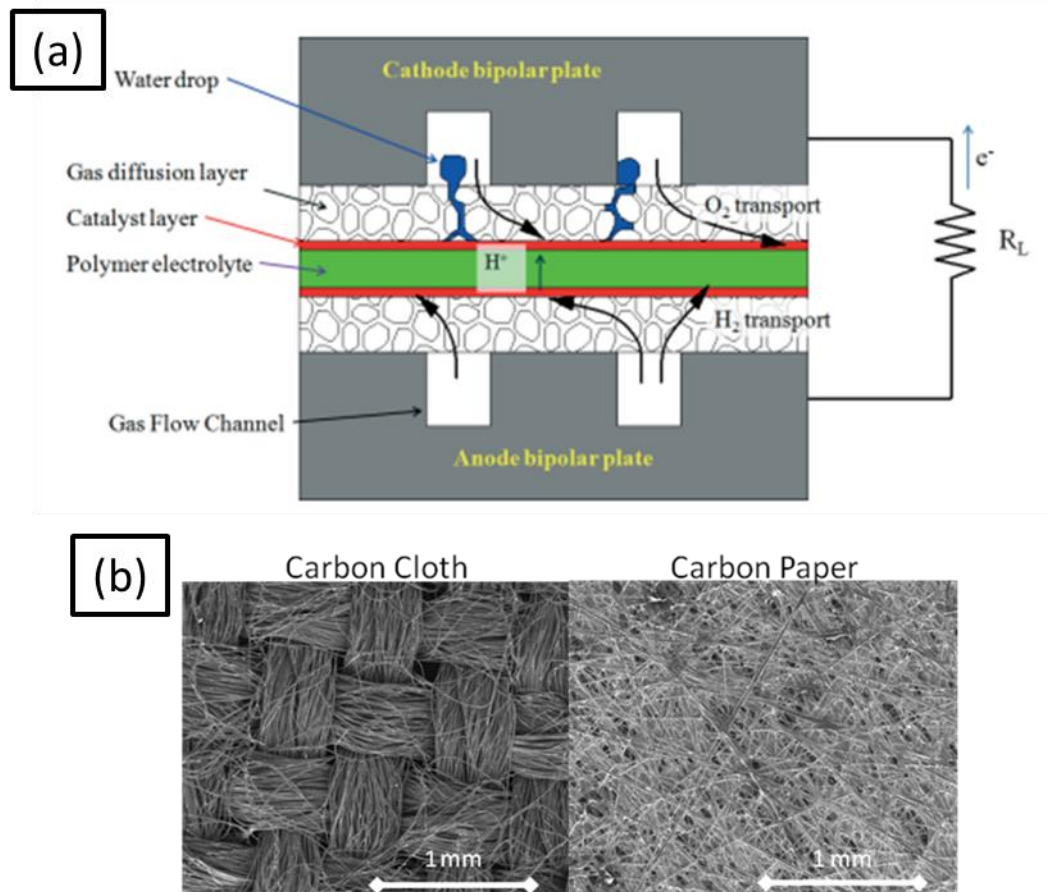


Figure 8 (a) Schematic of structure of the flow channels within the bipolar plate and the membrane electrode assembly (b) Micrographs of carbon cloth and carbon paper GDL materials [35].

(D) The Bipolar plates

The bipolar plates (also called the separator plates) are multi-functional components of the PEM fuel cells that perform critical functions that influence cell performance. The primary roles of the bipolar plates are;

- (1) Uniform distribution of reactant gases over the active electrode area,
- (2) Electrical connection between individual cells,
- (3) Facilitation of water and heat management within the cells,

(4) Provision of mechanical support and strength for the MEA [21-24, 31, 36].

In order to improve reactant gas transport and distribution, the bipolar plates are typically designed with flow field channels, land and manifolds as shown in Figure 9. These features provide pathway for reactant gases and uniform distribution over the active electrode area. The channels provide routes for reactant gases to flow to the catalyst layer via the GDL (Figure 8 (a)) while the lands facilitate electron transport to and from the GDL. On the other hand, the ‘manifolds’ carry reactant gases and by-products from and to the bipolar plates. The design of the flow channels significantly impacts the performance of PEM fuel cells. Hence, different types of flow field designs as shown in Figure 10 have been developed and the influence of such design on PEM fuel cells power output has been investigated [36].

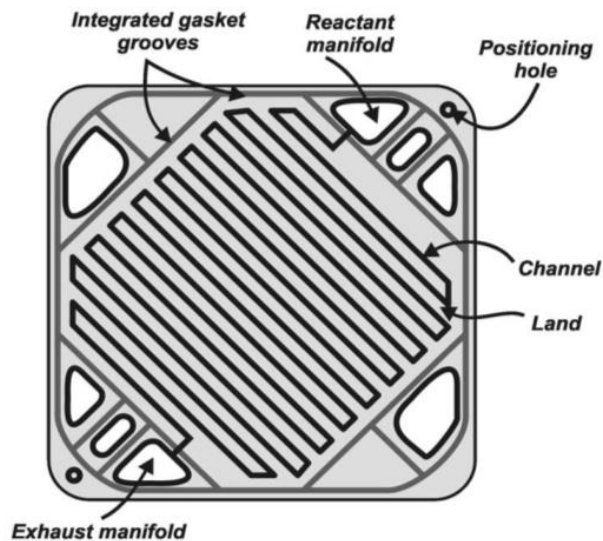


Figure 9 Features of a typical bipolar plate [21].

Materials requirements for bipolar plates includes: low cost, high corrosion resistance and high electrical and thermal conductivity. Graphite is the conventional material for PEM fuel cell bipolar plates. However, graphite is brittle and expensive for mass production purposes amongst other disadvantages. Hence, alternative materials such as metals and carbon/polymer composites have attracted considerable R&D attention as potential replacement for graphite bipolar plates. Bipolar plates are, however, subject to corrosion and increase in interfacial contact resistance with the GDL during operation irrespective of the material from which it was fabricated [19, 21, 22, 37-39].

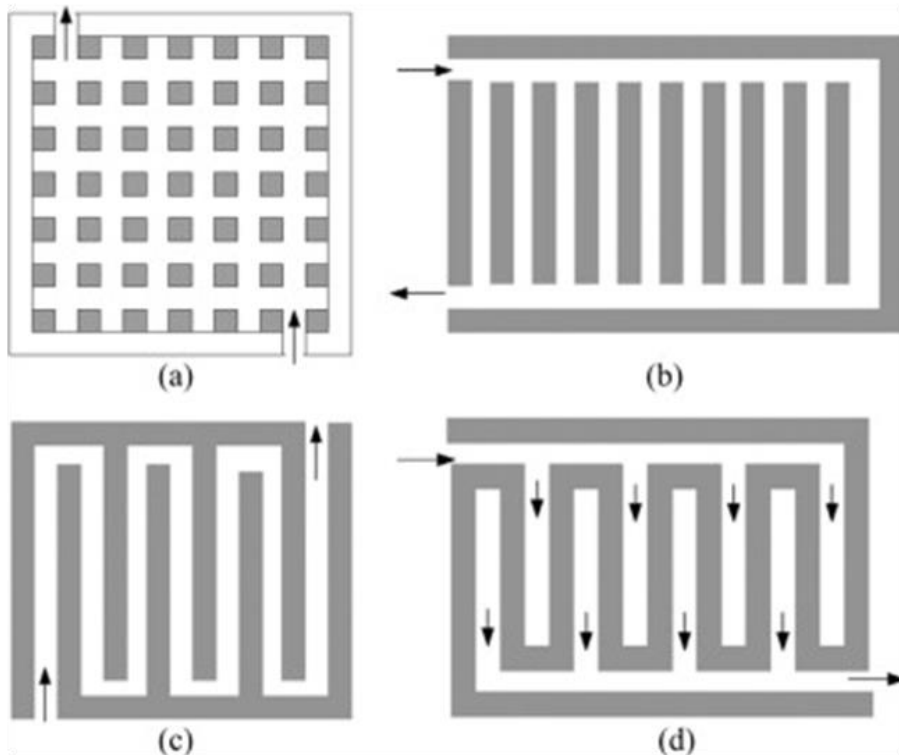


Figure 10 Schematic diagram of typical flow field design: (a) pin-type, (b) series-parallel, (c) serpentine and (d) interdigitated type [36].

2.3 CHALLENGES TO COMMERCIALISATION OF AUTOMOTIVE PEM FUEL CELLS

Research and development (R&D) activities on automotive PEM fuel cells, primarily driven by the promising potential of PEM fuel cells to enhance energy security and reduce greenhouse gas emissions in the transport sector, have been in the lime light for some decades. Extensive research efforts by governmental agencies in Europe, United States of America (US), Japan, etc. in collaboration with the academia and industry has resulted in remarkable progress evidenced by field demonstration of prototypes vehicles by major automotive companies such as Ford, Toyota, Daimler (Mercedes Benz), Hyundai, Honda etc. Nevertheless, the commercialisation of PEM fuel cell powered vehicles is faced with cost and technical challenges associated with both the PEM fuel cell stack and other balance of plant components, as well as hydrogen production and distribution [17, 40, 41].

Hydrogen PEM fuel cells systems presently cost about twice that of internal combustion engine and suffer severe degradation during operation. According to the United States Department of Energy (US DOE), cost of PEM fuel cells system would have to be reduced to ~ US\$30/kW and achieve stable performance for at least 5000 hours for light duty vehicles and 20,000 hours for a bus with minimal power loss (~ 10%) at the end of life, as well operate over a wide temperature range (- 40 to +40 °C), in order for PEM fuel cells powered vehicles to compete with traditional ones built on internal combustion engines [41]. In Europe, a consortium of automakers original equipment manufacturers (OEM), automobile component and system suppliers and academic researchers named 'AUTOSTACK CORE' have recently set the cost target for a 95 kW automotive PEM fuel cell stack at 40 €/kW for 100000 units with similar operating hours and degradation targets as the US DOE as well as other performance targets [42,43].

Cost reduction of the key components of PEM fuel cells; the membrane assembly electrode and bipolar plates is widely recognised as a necessary route to commercialisation of PEM fuel cells. To this end, cost reduction and improving the lifespan of these components have attracted global research attention. A significant portion of the research on these key components has been centred on materials selection and development for these components. For bipolar plates, developments of low cost and durable bipolar plates which are amenable to rapid, high volume and cost effective manufacturing processes as well as meeting durability targets, are major research interest. Hence, the present research is focused on the bipolar plates and the remaining part of this chapter is devoted to the important aspect of bipolar plates related to the research.

2.2.1 Cost and Durability of Bipolar Plates

The bipolar plates described in the previous section are important components of the PEM fuel stack that perform critical roles that can affect the performance and durability of PEM fuel stacks. Bipolar plates also account for a significant portion of the cost, weight and volume of the PEM fuel cells stack being the most repeated component in a PEM fuel cell stack. Earlier reports indicated that bipolar plates constitute about 35-45% and 60-80% of the cost and weight of typical PEM fuel cell stacks respectively [44,45]. However, it has recently been reported that the cost contribution of the bipolar plates to the overall cost of an 80 kW net automotive PEM fuel cell stack composed of 369 single fuel cells and 740 bipolar plates can be reduced to about 15-20% through replacement of conventional graphite bipolar plates with plates made from carbon /polymers composite or metals coupled with increased production rate [46]. However, since cost and durability are interrelated issues, for any of these alternative materials to be suitable for an automotive PEM fuel cell bipolar plate, the material is expected to satisfy not only the cost

requirement of US \$3/kW and be amenable to high volume cost effective manufacturing processes, but also durability requirements as list below [22, 37, 38]:

- Light weight
- High mechanical strength: > 41 MPa
- High bulk electrical conductivity: >100 S/cm
- Good hydrogen permeability : < $2 \times 10^{-6} \text{ cm}^3/\text{cm}^2 \text{ s}$
- Electrochemical stability in simulated PEM fuel cell environment of pH 3 sulphuric acid (H_2SO_4) + 0.1 ppm hydrofluoric acid (HF)
 - High corrosion resistance with corrosion current density at -0.1 V (SCE) and Hydrogen gas purge < $1 \mu/\text{Acm}^2$
 - High corrosion resistance with corrosion current at 0.6 V (SCE) and Air purge < $1 \mu/\text{Acm}^2$
- Low Interfacial contact resistance (ICR) at 140 N/cm^2 : $10 \text{ m}\Omega /\text{cm}^2$
- Good thermal conductivity : > 10 W/m K

2.2.2 Materials for Bipolar plates

(A) Graphite

Bipolar plates are conventionally fabricated from non-porous graphite due to its good chemical stability and corrosion resistance in the warm, acidic, and humid environment within the PEM fuel cell. Graphite also possesses low density and good electrical and thermal conductivity as well as low contact resistance with the gas diffusion layer. Nonetheless, there are concerns about its low mechanical strength which is compensated for by increasing the thickness of the plates to about (4-6 mm), resulting in low gravimetric and volumetric power density. Also, graphite has to be

impregnated with resin or treated thermally to block its pores and improve gas impermeability while flow field designs are incorporated by computer numerical control (CNC) machining which is expensive and time consuming. These secondary processing routes induce additional cost thereby hindering large scale production. Hence, from a cost and weight perspective, graphite is considered unsuitable for mass production. Extensive R&D on bipolar plates has led to two classes of alternative materials: carbon- polymers composites and metals [21-24, 37-39]

(B) Carbon-polymer composites

Carbon-polymer composites are composites that have a thermosetting (e.g. vinyl ester) or thermoplastic (e.g. polypropylene) polymer matrix loaded with conductive carbon fillers such as graphite, carbon black, carbon nanotubes, graphene [21, 24, 47] The polymer matrix provides structural support while the carbon fillers enhance electrical conductivity. These lightweight and corrosion resistant materials are manufactured by low cost injection or compression moulding, which are amenable for large-scale production. The main disadvantage associated with the use of carbon-polymer composite as bipolar plates, is their low electrical conductivity which is dependent of the content and particle size of the filler. Increasing the filler content improves electrical conductivity but is detrimental to mechanical strength, a basic requirement for automotive applications. Therefore, achieving optimum balance between mechanical strength and electrical conductivity is prerequisite for carbon-polymers composites to emerge as alternative to graphite [21, 24, 39, 47].

(C) Metals

Metals such as stainless steels, aluminium and titanium have several advantages over graphite and carbon-polymer composite materials particularly in terms of cost and weight. Metallic bipolar

plates can be produced at relatively low cost using economic and well-established industrial processes such as hydroforming, stamping, casting which are also amenable to mass production. Other advantages of metals besides cost reduction include: thickness and weight reduction by using thin sheets, foils, screens and foams, higher volumetric and gravimetric power density comparable to that attainable with thick graphite plates can be achieved. Other advantages of metals include gas impermeability, higher mechanical strength and electrical conductivity compared to the graphite and carbon composites as shown in Table 2. Metals are, however, susceptible to corrosion in the working environment of PEM fuel cells and exhibit high interfacial contact resistance with the GDL [21-23, 37, 38]. The consequences of these phenomenon on the performance of PEM fuel cells are briefly described as follows;

I. Corrosion of metallic bipolar plates in PEM fuel cells environment.

The environment within a typical PEM fuel cell is warm (60-80 °C), humid and acidic (~ pH 3). The PEM fuel cell environment could also be oxidising or reducing depending on the gas input at the electrodes. These conditions coupled with operating potentials (-0.1 V at the anode and 0.6 V at the cathode) are favourable for corrosion to occur. Metallic ions released from the oxidation of metallic bipolar plates either migrate to the proton exchange membrane via the GDL or are leached into the water by-product. In the former case, metallic ions can reduce the proton conductivity and efficiency of the membrane by replacing the hydrogen proton on the sulphonate group of the membranes, which has a higher affinity for metallic ions than protons.

Studies [17, 49-50] on membrane contamination indicates that the presence of metallic ions such as Al^{3+} , Cr^{3+} , Fe^{3+} in trace quantities such as parts per million (ppm) can significantly degrade cell performance. Furthermore, multivalent cations arising from corrosion of metallic bipolar plates

Table 2 Representative physical values for different bipolar plate material (adapted from 21-23).

Properties	Graphite (untreated Poco graphite)	Composite (SGL carbon)	Stainless steel (316/316L)
Density (g/cm³)	1.78 (20% porous)	1.97	8.00
Bulk electrical conductivity (S/cm)	200	680.30	13, 513
Hydrogen permeation (cm³/(cm²s)	10 ⁻² -10 ⁻⁶	2.5 x 10 ⁻⁵	< 10 ⁻¹²
Modulus of elasticity	10	-	193
Flexural strength (kg/cm²)	407.80	878.80	
Tensile strength (MPa)	15.85		515

can react with hydrogen peroxide formed by oxygen crossover at the anode as diagrammatically represented in Figure 11 or oxygen reduction processes at the cathode (Table 3) to form hydroxyl (OH[•]) and hydroperoxyl (HO₂[•]) radicals (Equation 4 & 5) which poisons the catalyst layer and degrade the membrane durability. In order to minimise dissolution of metals during corrosion,

corrosion resistant and low cost metals such as stainless steel, aluminium and titanium alloys which typically exhibit passivity in PEM fuel cells environments and working potentials are recommended. The use of chemically inert metals such as gold, platinum is not feasible due to their high cost [21-24, 37, 38, 47].

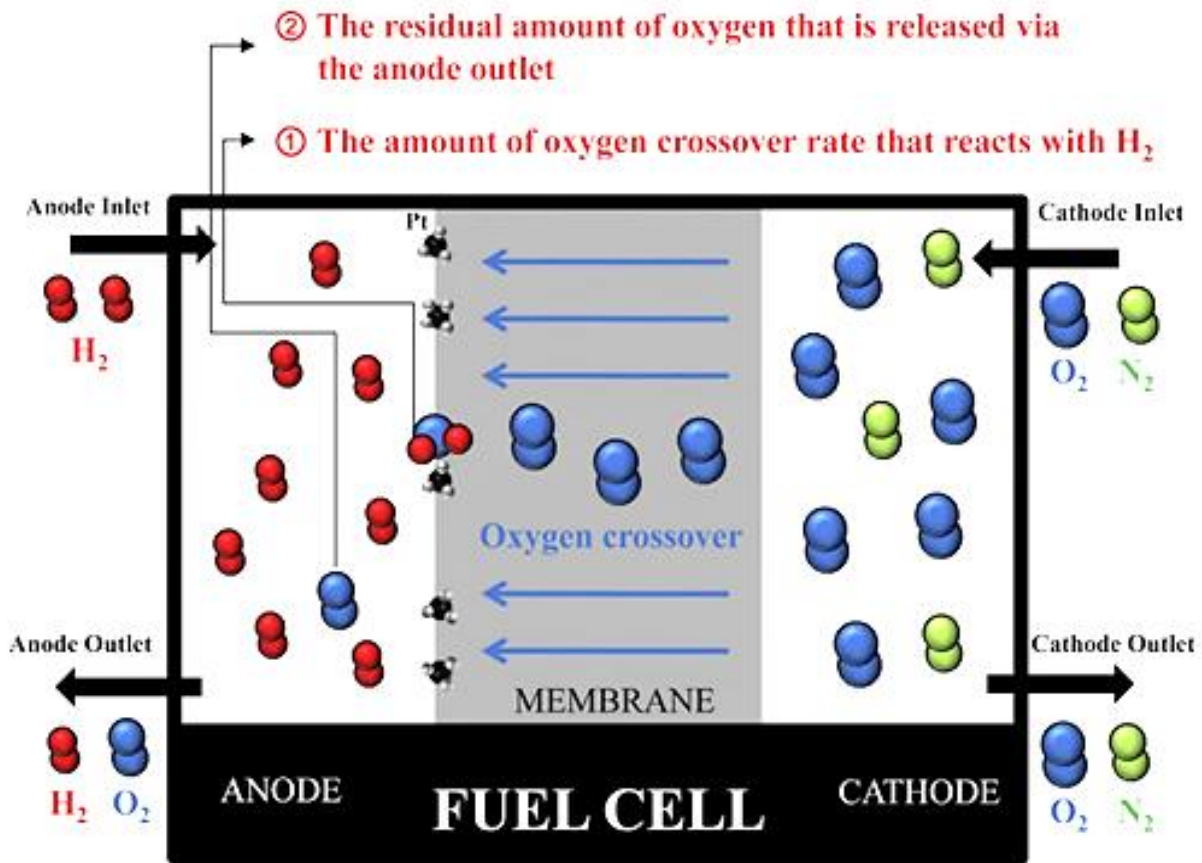
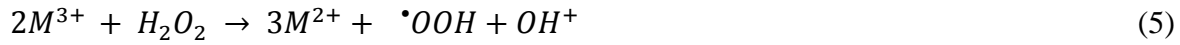


Figure 11 Schematic diagram of oxygen crossover through the membrane in a PEM fuel cell [51].

Table 3 Possible oxygen reduction reactions at the PEM fuel cell cathode and the thermodynamic electrode potentials of electrochemical O₂ reductions [34].

Oxygen reduction reactions	Thermodynamic electrode potential at standard conditions
$O_2 + 4H^+ + 4e^- \rightarrow H_2O$	1.229 V
$O_2 + 2H^+ + 2e^- \rightarrow H_2O_2$	0.70 V
$H_2O_2 + 2H^+ + 2e^- \rightarrow 2H_2O$	1.76 V



II. Interfacial contact resistance

Three main types of irreversible losses are encountered in PEM fuel cells: (1) Activation losses arising from the cathode catalyst and accounts for losses in the low current density region as shown in Figure 12. (2) Ohmic losses due to ionic resistance of the membrane and electron flow resistance (also known as interfacial contact resistance (ICR) between components in the PEM fuel cell stack. Concentration losses originate from mass transport limitations as oxygen is transported through the porous electrode. As shown in Figure 12, concentration losses are prominent in the high current density region. Among these operational losses, ohmic losses due to interfacial contact resistance between the bipolar plates and the GDL are of major concern for metallic bipolar plates. This is due to the fact that the native oxide layer in metals such as stainless steels,

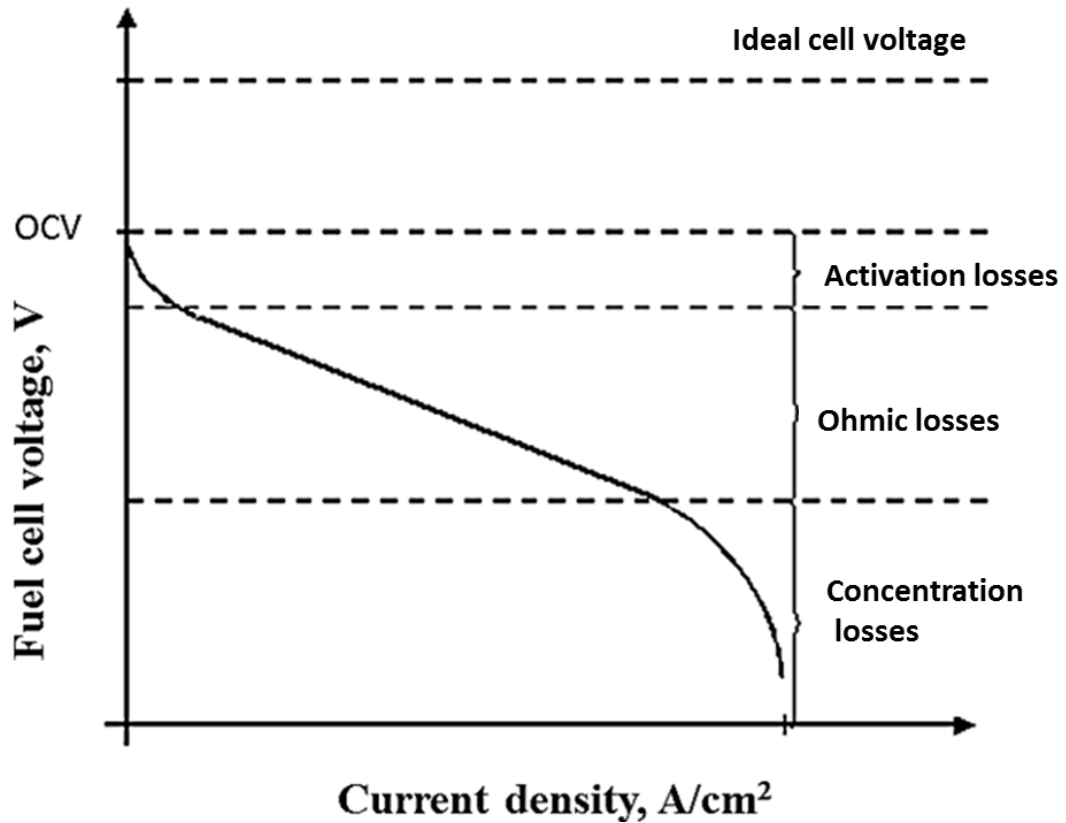


Figure 12 Energy losses in PEM fuel cells adapted from [52].

titanium and aluminium, which enhances the anti-corrosion properties of these metals, is semi conductive in nature. Hence, the native oxide layer reduces electronic conduction at the bipolar plate / GDL interface thereby favouring the conversion of chemical energy to heat rather than the desired electrical energy [53]. For instance, it was reported that about 59% of the power losses in a stack built with 316 stainless steel bipolar plates was due to the ICR between the stainless steel bipolar plates and the GDL [54]. Studies have also shown that the thickness of the passive oxide layer on these metals increases during operation thereby increasing contact resistance between the

bipolar plate and the GDL [21, 22, 37, 38]. Hence, surface modification of metallic bipolar plates via coatings and treatments is necessary for optimum cell performance.

Interfacial contact resistance between the bipolar plate and the GDL can be influenced by factors such as surface roughness, clamping pressure and the nature of the GDL material [21, 55-60]. Studies [55, 56] show that the higher the average surface roughness (Ra) of the bipolar plates, the lower the contact resistance. This trend is attributed to the fewer number of contact points and smaller area of contact between the GDL and the metallic bipolar plate with a higher surface roughness value.

The pressure at which the fuel cell stack is assembled plays a vital role in determining the contact resistance between the bipolar plates and the GDL. Generally, ICR decreases with increasing clamping pressure due to increasing contact area between the bipolar plate and the GDL. However, very high clamping pressure can damage the GDL and reduce its porosity while insufficient clamping pressure can lead to fuel leakage [51-53].

The nature of the GDL material i.e. the type of material and the type of enhancement process e.g. polytetrafluoroethylene (PTFE)-treatment has also been reported to adversely affect ICR between the GDL and the bipolar plate [58-60]. It is generally reported that increasing the PTFE loading of the GDL increases ICR between the bipolar plates. For instance, Ismail et al. demonstrated that increasing the PTFE loading contact of GDLs from SGL technologies, Germany from 0 to 30 wt. % lead to a corresponding increase in the contact resistance as compaction pressure increased (Figure 13).

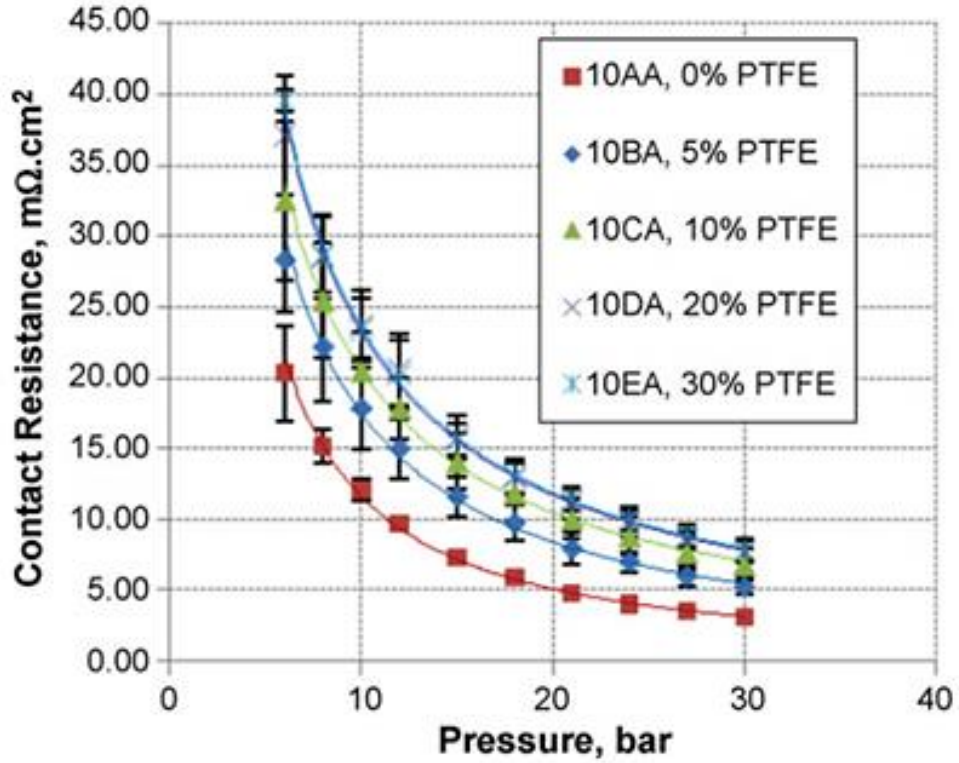


Figure 13 Effect of PTFE loading on contact resistance. [59]. (10AA, 10BA, 10CA, 10DA, 10EA are designated names for SGL carbon paper with 0%, 5%, 10%, 20%, 30% respectively).

2.4 A SURVEY OF THE LITERATURE ON METALLIC BIPOLAR PLATES

Metallic bipolar plates have recently attracted considerable research attention as alternative materials for PEM fuel cell bipolar plates due to their cost, volume and weight advantages of metal over non-porous graphite. Hence, most automotive PEM fuel cell stacks are built on metallic bipolar plates which can attain higher power densities than stacks built on graphite bipolar plates [26, 33, 34]. As indicated in the previous section, metals have low corrosion resistance and surface conductivities in PEM fuel cell environments which results in degradation of cell output. Therefore, research and development activities on metallic bipolar plates have focused on improving corrosion resistance and reducing ICR. The literature indicates that different types of metals which are sub-divided into bare metals, coated metals and porous metals (foams, screens and meshes) as shown in Figure 14 have been investigated. Therefore, a review of the performance of the different metals in in-situ and ex-situ testing is presented as follows;

2.3.1 Bare metals

(A) Stainless Steels

Stainless steels are iron based alloys containing at least 50% iron (Fe), minimum of about 11% chromium (Cr) and other elements such as nickel (Ni), molybdenum (Mo), titanium (Ti), nitrogen etc. [61, 62]. These ferrous based alloys are classified into different grades: austenitic, ferritic, martensitic, duplex stainless steels etc. based on chemical composition. Stainless steels derives its anticorrosion properties from the presence of a thin surface oxide layer (about 3-5 nm thick) which consist of an inner layer of a p-type chromium oxide (Cr_2O_3) and an outer layer of a n-type iron oxide and hydroxide [63].

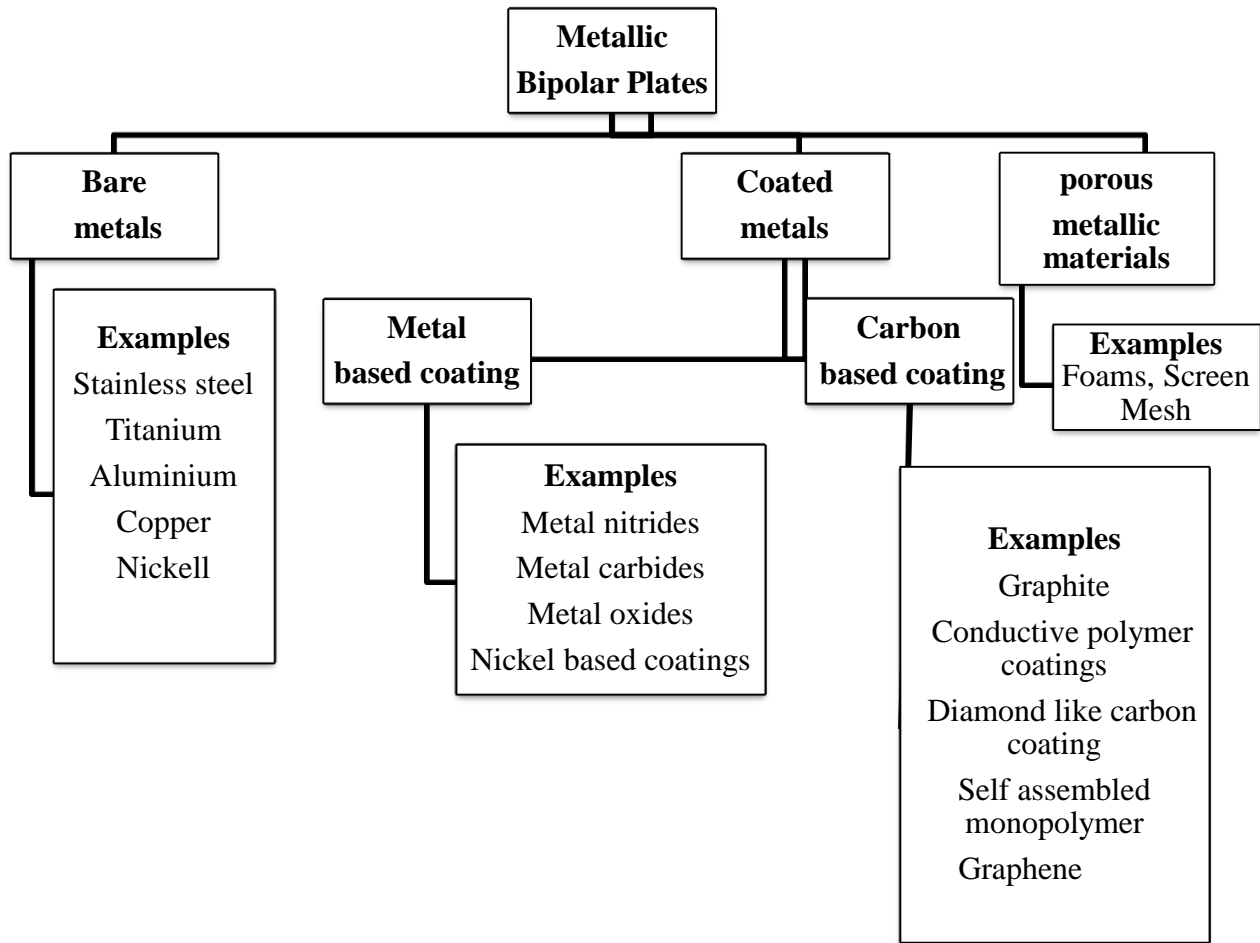


Figure 14 Classification of metallic materials for PEM fuel cells bipolar plate [21-23].

These alloys also possess outstanding physical, electrical and mechanical properties and are available at relatively low cost, thus, these ferrous based alloys have attracted much attention as potential replacement for graphite bipolar plates [21, 22, 37, 39, 47]. Investigations on the feasibility of using stainless steels as bipolar plate materials indicated that the performance of stainless steels in PEM fuel cell environment is dependent on its alloy content especially chromium content [64-67]. Wang et al. [65] reported that the higher the chromium content in

349TM (23 wt.% Cr), 904L (20.48 wt.% Cr), 317L (18.10 wt.% Cr) and 316L (16.20 wt.% Cr) austenitic stainless steels, the higher the corrosion resistance in simulated PEM fuel cell environment of 1 M H₂SO₄ + 2 ppm HF at 70 °C bubbled with air or hydrogen gas and the lower its contact resistance. A similar trend was also observed for ferritic stainless steels type AISI 434 (17.95 wt. % Cr), AISI436 (18.10 wt. % Cr), AISI441 (18.23 wt. % Cr), AISI444 (18.49 wt. % Cr) and AISI446 (28.4 wt. % Cr) [66]. For both grades of stainless steels, XPS analysis of the passive layer revealed that the passive layer was composed of Fe₂O₃ and Cr₂O₃, with the latter having a profound effect on corrosion resistance while ICR values of the different grades of stainless steel showed a dependency on the thickness and composition of the passive oxide layer. The findings of Wang et al. [65,66] was consistent with that of Davies et al. [67] wherein single fuel cell performance of 310L, 316L and 904L stainless steel bipolar plates were evaluated at 200 N/cm² for 3000 hours. Their results showed that the higher the chromium and nickel content of the stainless steels investigated, the lower the thickness of the oxide layer and the lower the ICR values. Hence, the single cell performance was given as 904L > 310L > 316L. Based on these results, they concluded that optimising the chemical composition of stainless steels was vital in selecting bare stainless steels for PEM fuel bipolar plate applications.

Generally, stainless steels with high Cr and Ni content such as 904L, 310L exhibit acceptable corrosion resistance and ICR values in PEM fuel cell environments but are considered too expensive for bipolar plate applications. Therefore extensive research work has focused on stainless steels alloys with lower Cr and Ni content such as 316 / 316L, 304 / 304L, low alloy ferritic stainless steels etc. Among the low cost austenitic stainless steel alloys 316 / 316L stainless steel, a Cr-Ni-Mo austenitic stainless steel alloy has been widely investigated due to its high resistance to corrosion. Ma et al. [68] investigated the corrosion resistance of eight types of

stainless steels (i.e. 410, 439, 301, 304, 316, 317L, 310 stainless steels and Incoloy alloy 825) in K_2SO_4 at 80 °C with oxygen and hydrogen gas purging to mimic the anodic and cathodic PEM fuel environment respectively. They concluded from the 72 hours corrosion test that 316/316L stainless steel was a good choice for PEM fuel cell bipolar plate having exhibited maximum corrosion resistance in the electrolyte, although its ICR increased from 10 $m\Omega.cm^2$ before polarisation to 11 $m\Omega.cm^2$ and 41 $m\Omega.cm^2$ after polarisation in simulated anode and cathode conditions respectively.

Davies et al. [67] reported that single fuel cell assembled with 316 stainless steel bipolar plates exhibited a stable performance with no evidence of corrosion after 3000 hours of operation. However their results showed the 316L stainless steel exhibited the lowest cell performance as well as the highest ICR among the investigated stainless steel alloys (904L, 310L) studied. The stable performance of 316L stainless steel could probably be attributed to the high compaction forces of 200 N/cm^2 utilised in the study as it is well established that ICR decreases with compaction forces [21, 58-60]. Secondly, the lack of evidence of corrosion could be explained using recent work by Papadias et al. [69]. They demonstrated via potentiostatic polarisation studies of 316L stainless steel in simulated PEMFC environment of pH 3 H_2SO_4 + 1 ppm HF at 80 °C that the degradation of 316L stainless steel at a given potential was dependent on the thickness of the passive film. Their work also showed that as soon as a steady-state passive thickness is reached, dissolution remains low and nearly constant. Hence, it is possible that during the 3000 hours of operation dissolution was very minimal such that visible damage could not be seen on the plates

Several other investigations argued that 316/316L stainless steels were not suitable as bipolar plate materials without surface modification [79-81]. Li et al. [79] reported that 316 stainless steel was in the active state under PEM fuel cell anode working conditions and environment when polarised

in 0.001 M hydrochloric acid solution with or without SO_4^{2-} ions at 80 °C. The finding of Makkus et al. [71] on the performance of single fuel cell assembled with 316L stainless steels bipolar plates further confirmed the results of Li et al. [70] as they found that the contaminants (Fe, Cr and Ni) on the anode side were higher than that at the cathode side. Also, the ICR and metallic ion generated from the cell with 316L bipolar plates was the highest among the seven grades of stainless steels (UNS 1.4439, UNS 1.4541(321), UNS 1.4529, UNS 1.3974, 1.4404 (316L)) studied. Hence, they concluded that bare 316 stainless steel was not an ideal choice for bipolar plate application but recommended surface modification of 316L stainless steel for optimum performance.

Wang and Northwood [72] studied the influence of PEM fuel cell operating environments on the corrosion resistance of 316L stainless steel exposed to 0.5 M H_2SO_4 at 70 °C. Inter-granular and pitting corrosion was observed at both electrodes with the alloy exhibiting a higher corrosion resistance in simulated cathode environment due to a higher tendency to passivate in oxygen rich environments. However, when polarised at typical anodic and cathodic PEM fuel cell potentials for 10 hours, lower transient current densities and metallic ions were recorded for 316L stainless steel in hydrogen containing environment indicating that under PEM fuel cell working conditions, corrosion of 316L stainless steel was minimal at the anode compared to the cathode. Based on the ICP-MS results, the author estimated that a total of 25 ppm and 42 ppm of metallic ions would have been leached from the anode and cathode respectively after 5000 operation hours has (as required for PEM fuel cell powered automobiles) thereby degrading performance. Hence, they recommended surface coatings for 316L stainless steel in agreement with previous investigations [70, 71].

(B) Titanium

Titanium and its alloys have high strength to weight ratio and excellent chemical stability in acidic environments. Although, titanium is about 40% lighter than stainless steels, its higher cost and lower formability than stainless steels prohibits its application in automotive PEM fuel cells [21, 23, 47, 64].

Titanium and its alloys form a thin layer of titanium oxide when exposed to air. This oxide layer is well known to be responsible for the resistance of titanium to corrosion in favourable conditions. However, it is reported that this naturally occurring oxide becomes unstable when exposed to PEM fuel cell anodic conditions due to the low applied potential (-0.1 V) resulting in high anodic currents at the inception of polarisation. After rapid dissolution of the naturally occurring oxide layer, a new oxide layer which cathodically protects the metal from further dissolution is formed. On the other hand, the surface oxide is stable at the cathode but cannot totally prevent dissolution leading to leaching of Ti^{2+} which could poison the membrane and degrade performance [73]. Similarly, Wang and Northwood [74] concluded from their 10 hours potentiostatic polarisation of Ti (II) alloy in 0.5 M H_2SO_4 at 70 °C that Ti^{2+} ions leached from the anode and cathode would lead to unacceptable deterioration of stack output.

Davies et al. [60] further demonstrated that bare titanium was not suitable for PEM fuel cell bipolar plate by comparing the performance of single cells assembled with titanium, 316 and 310 stainless steel and graphite bipolar plates. Their work revealed that at the end of 1300 hours of single cell polarisation, the ICR of titanium increased about eight fold from the initial $32 \text{ m}\Omega\cdot\text{cm}^2$ at 220 N/cm^2 compared to 7% and 16% increase in that of 310 and 316 stainless steels, which was given as $26 \text{ m}\Omega\cdot\text{cm}^2$ and $44 \text{ m}\Omega\cdot\text{cm}^2$ before polarisation respectively. Consequently, the cell

suffered significant power degradation compared to cells with bipolar plates fabricated from graphite, 316 and 310 stainless steel bipolar plates. In subsequent studies [75], they showed that surface modification of the titanium plates improved single fuel cell performance. Similar enhancement of single fuel cell performance has been recently reported by Jin et al. [76]. Their studies showed that 25 cm² active area single fuel cell assembled with TiN coated titanium bipolar plates exhibited approximately a double fold improvement in the current density of the cell with the uncoated plate (396 V) at 0.6 V. The improvement was attributed to ohmic losses due to growth of oxide arising from corrosion of the bare plates during operation.

(C) Aluminium

Aluminium and its alloys are lightweight, low cost metals which exhibit good corrosion resistance in atmospheric conditions due to the formation of a thin layer of aluminium oxide. The main advantages of aluminium as a bipolar plate material are its low density, cost effectiveness and ease of fabrication. Aluminium has a density of 2.7 g/cm³ which is comparatively lower than that of stainless steel and Titanium (Table 4).

Table 4 Densities of metals commonly used for bipolar plate

Material	Aluminium	Stainless steel	Titanium
Density (g/cm³)	2.7	7.48-8.00	4.51

The ease of fabrication combined with aluminium low cost denotes the possibility of achieving a much higher volumetric and gravimetric power density with aluminium bipolar plates than

stainless steels or titanium. However, aluminium has higher corrosion rates and shorter cell life than stainless steel and titanium under PEM fuel cell operating conditions. Studies have also shown that coatings for aluminium have to be absolutely defect-free to prevent the substrate from corrosion in PEM fuel cells environments [77-79].

(D) Copper

Pioneering studies on copper as PEM fuel cell bipolar plate material was conducted by Nikam et al. [80, 81]. They examined the corrosion behaviour of copper-beryllium alloy (C-17200) exposed to 0.5 M H₂SO₄ (pH 3–5) and a mixture of 5% HCl + 5% Na₂SO₄ respectively. The electrolytes were bubbled with oxygen and argon gases to simulate PEM fuel cell cathode and anode environments respectively. They concluded from the electrochemical polarisation results that copper-beryllium alloy was a potential candidate for bipolar plates given that copper alloys are conductive materials. Hence, they further examined the single cell fuel performance of the alloy and reported that the 16 cm² active area single fuel cell assembled with bipolar plates fabricated from copper-beryllium alloy exhibited good durability when tested for 100 hours under constant load of 1 A. The single fuel cell also exhibited maximum current density and power cell resistance comparable to single fuel cells with 316 stainless steel bipolar plates reported by Costamagna et al. [82] as shown in Table 5. Similar studies on bare copper alloys were also reported by Hsieh et al. [82]. However, Pan et al. [84] have recently demonstrated the need to enhance the performance of copper in PEM fuel cell environment via surface modification.

Table 5 Comparison of c-17200 Cu-Be alloy bipolar plate performance with 316L stainless steel bipolar plate [81].

Bipolar plate materials	Maximum current density at 0.2 V (mA/cm²)	Cell Resistance (Ω)
Cu-Be alloy (C-17200) (surface area – 16 cm ²)	500	0.084
SS316L stainless steel (surface area- 10.89 cm ²)	380	0.349
Carbon coated SS316L stainless steel (surface area 10.89 cm ²)	800	0.134

2.3.2 Coated Metals

Surface modification of metallic bipolar plates has been widely employed as means for enhancing the corrosion resistance and surface conductivities of metals in PEM fuel cell working conditions and environments. Surface coatings and/or treatments for PEM fuel cell bipolar plates are required to be electrically conductive, chemically stable and corrosion resistant under typical working conditions of the PEM fuel cells. Other requirements include strong adherence to the substrate and cost effectiveness. The integrity of the coating, which is dependent on the coating material and deposition process, is often the most important aspect for bipolar plate applications as it dictates performance and durability. However, the presence of coating defects such as pinholes, cracks, and pores in the coating as well as thermal mismatch between coating materials and the substrate are commonly reported to accelerate corrosion of coated metals in PEM fuel cell environments and thus promote loss of surface conductivity [33, 34, 63]. A wide range of coatings basically divided

into metal-based coatings and carbon based coatings as shown in Figure 14 have been investigated, the performance of the various types of coatings in simulated and real PEM fuel cells environments is reviewed below:

2.3.2.1 Metal-based coatings

(A) Noble metal coatings.

Thin micron layers of noble metal coatings such as gold and platinum exhibit excellent stability and corrosion resistance in PEM fuel cells. In some cases, comparable or better performance than graphite bipolar plates [77, 78, 85, 86] has been reported. Hentall et al. [77] compared the single cell performance of gold coated 316L stainless steel and aluminium bipolar plates to Poco™ graphite and reported that gold coated stainless steel showed superior performance to Poco™ graphite. The gold coated aluminium also showed equivalent current density to the graphite bipolar plates at the onset of experiments after which performance rapidly deteriorated from 1.2 A/cm² to 60 mA/cm² at 0.5 V. Examination of the plates after the experiments indicated that the coatings were weakly adhered to the base metal. Consequently some of the coatings were leached into the membrane thereby contaminating it and deteriorating power output. Woodman et al. [78] added that the difference in the coefficient of thermal expansion between aluminium (Al) and gold (Au) was also a factor that could contribute to low durability of gold coated aluminium bipolar plates. They stated that a differential of about 18 $\mu\text{m}/\text{m}/^{\circ}\text{C}$ existed between the coefficient of thermal expansion (CTE) of Au and Al and that during thermal cycling as encountered in automobiles, failure of gold coated Al plates is inevitable. To mitigate the poor adhesion between Au and Al, the authors demonstrated that the use of interfacial layers of copper and nickel between Au and Al reduced the corrosion rate of gold plated Al specimen by 30% and 37.5% before and

after thermal cycling respectively. In-situ testing of the coated plates revealed that the coated bipolar plates had higher open circuit voltage than graphite bipolar plates and maintained performance akin to graphite throughout the test. Their results also emphasised the importance of proper deposition process parameter selection. The use of pulse current during electroplating promoted better adhesion which resulted in better performance than the plates deposited by direct current electrodeposition which exhibited poorer output than the graphite plates.

Wind et al. [85] compared the performance of gold coated 316 stainless steel and graphite bipolar plates tested in a 49cm² active area single cells operated at 75 °C for 1000 hours. The results indicated the cell with the gold coated plates exhibited equivalent cell voltage with graphite bipolar plates showing negligible power degradation throughout the duration of the test. Wang et al. [86] also reported that 25 cm² active area single fuel cell assembled with Au coated titanium plates showed superior performance to cells with graphite plates at high membrane humidifier temperatures between 80 °C and 90 °C. On the other hand, at lower membrane humidifier temperatures (40-60 °C) an opposite trend was observed. However in both conditions, the Au coated titanium plates showed better output than the uncoated plates due to an increase in the surface conductivity of the plates induced by the precious metal coatings. In another study, the authors also reported that platinum coated titanium bipolar plates outperformed the uncoated plates showing comparable performance to the single fuel cell with graphite bipolar plates [87].

Generally, noble metal coatings are considered too expensive for automotive PEM fuel cell despite their comparable performance to graphite [21-23]. For instance, it is reported that gold coated aluminium bipolar plates cost about four times graphite bipolar plates [22]. However, recent work by Kumar et al. [88] showed that reducing the thickness of gold coatings to nano-meter scale could

be a viable option for cost reduction of gold coatings. In their study, they examined the electrochemical behaviour of 10 nm gold coated 316L stainless steel developed by Daido steel, Japan in 0.5 mM H₂SO₄ (pH 3) at 80 °C exhibited excellent corrosion resistance with current density less than 1 μA/ cm² at 0.8 V vs. NHE in 24 hours potentiostatic experiments and attained ICR values of 6.30 mΩ.cm² at 60 N/cm².

(B) Metal-Nitride coatings.

Hard ceramic nitrides coatings such as titanium nitride (TiN) and chromium nitride (CrN) are one of the most widely studied coatings for bipolar plate applications. These coatings, which are often deposited by vacuum based processes such as physical vapour deposition (PVD), chemical vapour deposition (CVD) or surface treatment processes such as thermal nitridation and plasma nitridation and more recently electrochemical nitridation and ion implantation, have been proven to be corrosion resistant and electrically conductive. However, the beneficial effect of these nitrides coatings is usually undermined by the presence of pinholes, cracks and other coating imperfections mostly related to the deposition processes.

(I) Titanium nitride coatings

The performance of TiN coatings deposited on titanium and stainless steel by various techniques in PEM fuel cell environments is widely reported. Zhang et al. [89] evaluated the in-situ and ex-situ performance of TiN coatings deposited by a PVD based process on titanium bipolar plates. The ex-situ test revealed that the coatings retarded the corrosion rate of the substrate while reducing its ICR. On the other hand, the 1000 hours in-situ testing of the coated plates in a 25 cm² active area single fuel cell indicated that the cell had a maximum power density of 0.68 W/cm² with a corresponding current density of 1600 mA/cm² at 0.65 V with minimal degradation. Based on these results, the authors further investigated the performance of TiN coated Ti plates in a

stack. The results showed that the stack had a high gravimetric power density of 1353 W/kg even though its volumetric power density was about 57% lower than that obtained in the single cell experiments [90]. This lower performance of the stack was attributed to the variation in flow field designs and flow channel parameters of the bipolar plates utilised in the stack. A similar investigation on the single cell and stack performance of TiN coated 316L stainless steel was reported by Cho et al. [91]. In the single cell test, TiN coatings improved the performance and lifetime of 316L stainless steel bipolar plates, which operated for 120 hours attaining a current density of 796 mA.cm² compared to the 700 hours and current density of 896 mAcm² at 0.6 V of the TiN-coated plates. Nonetheless, performance of the coated Ti plates was inferior to that of the graphite bipolar plates which operated for 1000 hours without performance degradation exhibiting about 11.2% improvement in the current density of the TiN coated plates at the same voltage. Analysis of the water droplets produced from the cell with the graphite and TiN coated bipolar plates revealed that the inferior performance of the TiN coated plates was due to contaminations of the MEA by metallic ion which originated from the dissolution of the coating. The authors further evaluated the performance of a 1 kW stack consisting of 12 single cells and operated at a constant load of 48 V for 1028 hours. The stack showed an average degradation rate of 11% per 100 hours while the individual cells showed a much lower degradation rate. The study emphasised the importance of a defect free coating in achieving better performance and lifetime with TiN coated bipolar plates.

The need for defect free TiN coatings was reiterated by other studies on the corrosion resistance of TiN coated 316L stainless steel in simulated PEM fuel cell working conditions [92, 93] and confirmed by Nam et al. [94] and Jeon et al. [95]. They both reported significant improvement in the corrosion resistance and surface conductivity of TiN coated 316L bipolar plates by increasing

the bias voltage [94] and partial pressure of nitrogen gas [95] during deposition respectively. In both cases, modification of deposition parameters improved the quality of the coating leading to better performance.

Plasma immersion ion implantation (PII) of titanium at 370°C was reported by Feng et al. [96] to enhance surface conductivity and corrosion resistance of titanium in a simulated PEM fuel cell environment of 0.5 M H₂SO₄ + 2 ppm HF, while the same process conducted at temperatures lower than 100°C deteriorated both ICR and corrosion performance of the substrate. The difference in the inhibitive properties of both samples was attributed to the thickness of the titanium oxy-nitride surface layer formed during the implantation process. Omrani et al. [97] also reported improvement in the performance of 316L stainless steel in simulative PEM fuel cell environment using nano-crystalline TiN ions implanted on 316L stainless steel. TiN coatings were deposited using a plasma device focus equipped with a nitrogen ion source and a titanium anode. In order to achieve variation in the morphology and thickness of the coatings formed, multiple nitrogen ions were fired using 10, 20 and 30 focus shots at a frequency of one shot by minute. Their results showed that the higher the nitrogen ion shots, the better the transient corrosion currents, with the 20 and 30 nitrogen ions shots exhibiting comparable currents of 1 μA/cm² in 1 M H₂SO₄ at 70 °C with air purging. The interfacial conductivity of the samples showed that the coatings formed with 30 shots of nitrogen ions exhibited the lowest ICR of 5 mΩ.cm² at 200 N/cm² while the coatings formed with 10 and 20 shots of nitrogen ions exhibited ICR of 20 mΩ.cm² and 30 mΩ.cm² respectively at the same compaction force. On the other hand, Zhang et al. [98] reported that a 3μm thick TiN coatings deposited on titanium by plasma nitriding could not adequately protect the base metal from corrosion when exposed to 0.5 M H₂SO₄ + 5 ppm HF but reduced its ICR by 60% exhibiting ICR value of 38.58 mΩ.cm² at 220 N/cm².

(II) Chromium nitride coatings

Chromium nitride is one of the most widely studied metal nitride coatings for metallic bipolar plate. Studies on PVD deposited chromium nitride coatings abound in the literature much more than TiN coatings, as it is reported that chromium nitride coatings are more compatible with stainless steels than TiN coatings [89, 99].

PVD deposited chromium nitride (CrN) coatings generally exhibit good corrosion resistance in PEM fuel cell environment. However, studies [100,101] indicate that the performance of these coatings is dependent on composition which in turns depends on factors such as the nitrogen gas flow rate. Wu et al. [100] reported that varying the nitrogen gas flow rate during deposition from 20 - 80 sccm increased the nitrogen content of the CrN coatings and resulted in better corrosion resistance in a simulative PEM fuel cell environment of 0.5 M H₂SO₄ + 2 ppm HF and lower ICR values. Single fuel cell performance of the CrN film with the lowest ICR of 6.4 mΩ.cm² at 1.2 MPa and chemical formula of Cr_{0.5}N_{0.5} was subsequently evaluated and compared to that of silver-plated bipolar plates. The results revealed that the cell with CrN coated bipolar plates exhibited 10% and 9% lower open circuit voltage and power density respectively at current density of 500 mA/cm² than the cell with the silver plated bipolar plates.

Similarly, Lavigne et al. [101] investigated the performance of two chromium nitride coatings deposited on 316 stainless steel using nitrogen gas flow rate of 8 sccm and 100 sccm. The latter consisted of a mixture of Cr₂N (20%) and Cr (80%) while the latter was a single phase CrN coatings. The authors reported that the performance of the coatings depended on the nature of the passive film of the coatings. Using Mott-Schottky measurements, it was shown that the passive film in both coatings exhibited similar p-type semiconductor behaviours with the single phase CrN

coating containing more cation vacancies which acted as dopants thereby favouring conductivity. Hence, the single phase CrN coating exhibited lower ICR values than the Cr₂N + Cr coating. At typical compaction force of 140 N/cm², the single phase CrN coating exhibited ICR value of 10 mΩ.cm², which was ~67% lower than that of the Cr₂N + Cr coating. Based on the ex-situ result, the performance of a five-cell stack assembled with CrN coated bipolar plates was examined and compared to that of gold coated bipolar plates. The result revealed that both stack exhibited similar performance while the 200 hours durability test for the stack with CrN bipolar plates did not show any mean voltage degradation over 200 hours of dynamic cycling.

PVD deposited chromium nitride coatings are well known to possess pin-hole defects, which degrade their performance in PEM fuel cell environments. Hence, various attempts have been reported in the literature to enhance their corrosion resistance and ICR in typical PEM fuel cell environments. A primary route often employed to improve performance of CrN coatings is the use of multi-layered coatings [21, 102-105]. Feng et al. [102] reported that multi-layered coating of C/CrN containing 100-400 nm thick carbon layers reduced the ICR of CrN (10 mΩ.cm²) by ~75% at compaction pressure of 150 N/cm². Similarly, potentiostatic polarisation experiments results indicated that in a simulated PEM fuel cell environment of 0.5 M H₂SO₄ + 2ppm HF at 80 °C, the transient current density of CrN coating was remarkably reduced from 2.5 μA/cm² to the values in the range of 2-9 pA/cm² range under cathodic conditions. However, the influence of the carbon layer on current density under anodic conditions was negligible although the C/CrN coatings exhibited more stable behaviours than the CrN coating. The study further established that a minimum thickness of 400 nm of carbon coating would be required for C/CrN coatings to provide adequate corrosion protection in PEM fuel cell environment. This was due to the fact that

SEM images and ICP-MS analysis of the 100 and 200 nm carbon coatings revealed evidence of pitting corrosion and higher metal ion release after 10 hours of polarisation.

Jin et al. [103] reported a slight improvement in the ICR and single fuel cell performance of CrN coated bipolar plates using CrN/TiN multi-layered coating. Their work showed that CrN/TiN multi-layered coating reduced the ICR of CrN coatings from $26.4 \text{ m}\Omega\cdot\text{cm}^2$ to $23.5 \text{ m}\Omega\cdot\text{cm}^2$ while its influence on corrosion resistance in $1\text{M H}_2\text{SO}_4 + 2 \text{ ppm fluoride ions}$ was negligible. Hence, the open circuit voltage of the 25 cm^2 active area single fuel cell assembled with CrN/TiN coatings exhibited a 5% increase in that of the cell with CrN coating, which was given as 0.62 V.

Several other studies [104-106] have also investigated the performance multi-layered CrN coatings in simulated PEM fuel cell environments. However, the influence of the additional coating layer cannot be deduced as the results were not compared to the single layered CrN coatings.

The performance of PVD deposited CrN coatings in PEM fuel cell environments can also be improved by incorporating elements such as Al, C to form ternary coatings. Bi et al. [107] recently demonstrated that incorporating 1.86 at. % of Al into CrN coatings reduced the corrosion current density of CrN coatings in a simulated PEM fuel cell environment of $0.5 \text{ M H}_2\text{SO}_4 + 5 \text{ ppm HF}$ at $70 \text{ }^\circ\text{C}$ by one order of magnitude and contact resistance by $\sim 50\%$ at 140 N/cm^2 . The improvement was attributed to reduction of CrN lattice and grain size by Al.

Chromium nitride coatings deposited by thermal nitriding have been extensively investigated by a group of researchers at the Oak Ridge National laboratory (ORNL) and National Renewable Energy Laboratory (NREL), USA [108-113]. In thermal nitriding, chromium nitride coatings are formed by heat treating the stainless steel alloy or chromium rich metal in a nitrogen rich gas at

temperatures above 1000 °C. Thermal nitriding was first applied to Ni-50Cr alloy for bipolar plate application by Brady et al. [108]. The Ni alloy was thermal nitrided at 1100 °C for 1 hour. The nitrided layer consisted of a continuous and external layer of CrN and Cr₂N coatings (Figure 15a). Ex-situ testing of the coatings in pH 3 H₂SO₄ at 80 °C for 4,100 hours showed minimal voltage change of 2 mV per 1000 hours and 2.7 mV per 1000 hours in the anode and cathode environments respectively with low ICR values which didn't increase during the test. Single fuel cell testing of the nitrided Ni-50Cr also showed very promising results. However, the author reported that Ni alloys were too expensive for mass production. Hence, they investigated the possibility of applying the thermal nitriding process to stainless steels [109-113].

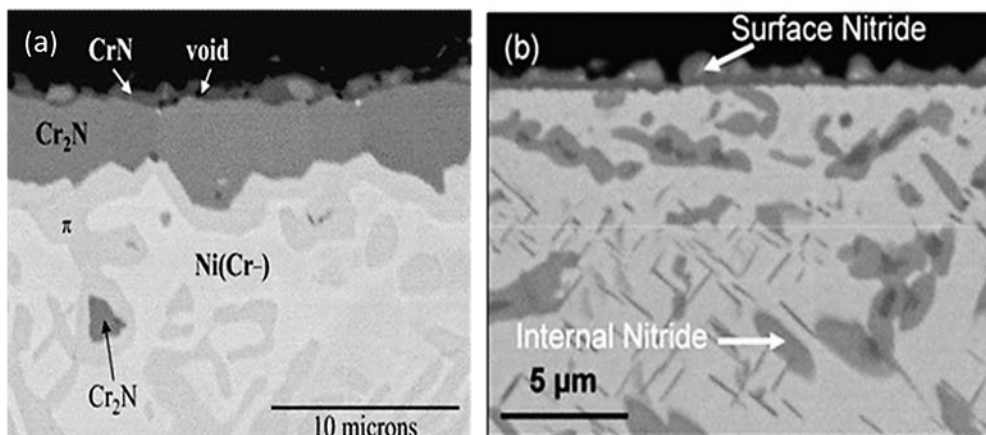


Figure 15 (a) SEM image of the cross-section of Ni-50Cr alloy nitrided at 1100 °C for 1 hour [108], (b) SEM image of the cross section of nitrided Fe-27Cr-6V stainless steel nitrided at 900 °C for 4 hours showing internal and external nitrides [109].

Their initial results showed that forming a continuous and external layer of chromium nitride on commercially available stainless steels was challenging because stainless steels have high permeability for nitrogen which favours the formation of discrete internal nitrides as shown in

Figure 15 (b). These discrete internal nitrides degrade the corrosion resistance of the nitrided steel due to the depletion of chromium at the grain boundaries.

Another group of researchers based in South Korea [114,115] attempted to solve this challenge by introducing a pre-oxidation step before nitridation of commercially available ferritic stainless steels (430 and 446) stainless steels. The authors proposed that the chromium oxide layer formed by oxidation prevented internal nitridation while their decomposition at the nitriding temperature facilitated the formation of chromium nitride. This approach yielded lower contact resistances before and after polarisation but the formation of discrete chromium nitride particles persisted (Figure 16).

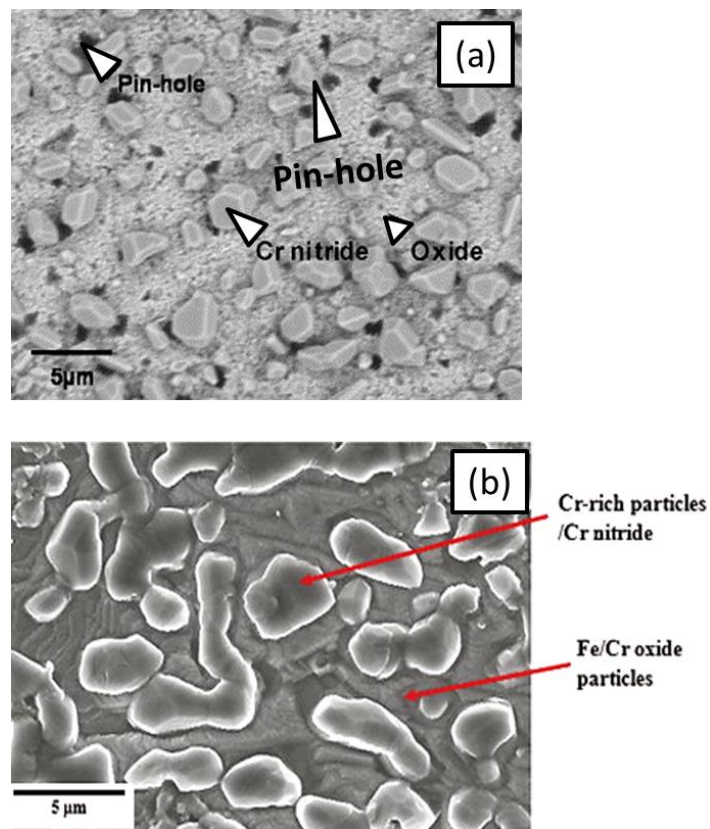


Figure 16 (a) pre-oxidised (900 °C for 10 hours) 446M stainless steel nitrided at 1100 °C for 2 hours [114] (b) pre-oxidised (900 °C for 5 hours) 430 stainless steel nitrided at 1040°C for 6 hours [115].

After a series of investigations, Brady et al. [113,114] demonstrated that adding vanadium to the composition of stainless steel coupled with pre-oxidation was a viable way to prevent internal nitridation and chromium particles precipitation. The pre-oxidation step process facilitated the formation of a continuous layer of vanadium doped chromium nitride overlaying an intermixed chromium oxide and nitride under layer as shown in Figure 17.

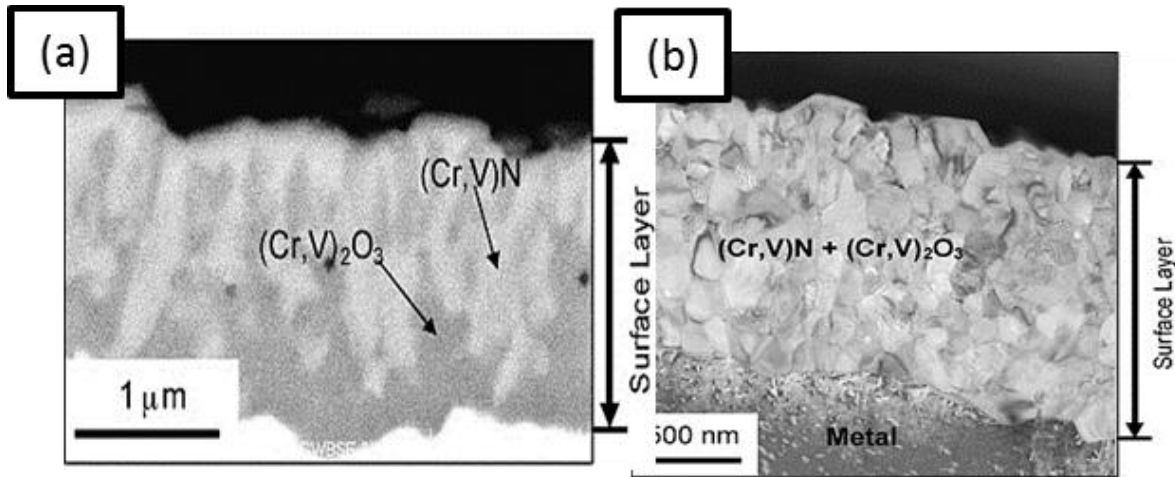


Figure 17 (a) SEM image of the cross-section of pre-oxidised nitrided Fe-27Cr-6V nitrided at 850 °C for 24 hours in N_2-4H_2 atmosphere. (b) Bright-field cross-section TEM of SEM image in (a) [162].

The feasibility of applying the process to Fe-(20-23%)-Cr-4%-V foils was subsequently demonstrated and ex-situ polarisation of the surface modified foils in 1M $H_2SO_4 + 2ppm\ HF$ at 70 °C revealed that the foils exhibited very low transient current densities in the range of $1\ \mu A/cm^2$ and a contact resistance of about $15\ m\Omega.cm^2$ at $150\ N/cm^2$ [111]. Based on the promising ex-situ result, a $15\ cm^2$ active area single cell with pre-oxidised and nitrided foils plates with a simple serpentine flow-field design was assembled. The initial performance of the single fuel cell showed that the cell attained an average power density of $222\ mW/cm^2$ at 0.55 V [112]. Durability testing of the foil plates for 1114 hours showed no significant degradation in cell power output X-ray fluorescence (XRF) analysis of the MEA after the test showed that negligible amounts of Fe, Ni,

Cr and V were leached into the MEA in the course of experimentation. In comparison to cells with untreated Fe–20Cr–4V, 2205, and 904L bipolar plates, the coated foil exhibited between 5% –20% improvements in peak power output.

In another study [113], the group further demonstrated the feasibility of scaling up the pre-oxidation and nitrided process to industrial scale by comparing the performance of bipolar plates made from short-cycle infrared quartz lamp furnace and conventional laboratory furnace. Hence, a 50cm² active area single cell with stamped, laser welded, and gas nitrided ferritic stainless steel foils produced from both furnaces were assembled and tested under aggressive humidification conditions (100% relative humidity and cycling relative humidity from 100%-40%) at 80 °C for 500 hours at 0.3 A/cm² so as to hasten degradation of the membrane and facilitate a more corrosive environment to assess durability of the foils. Details of single cell performance was not revealed but it was reported that after 500 hours of operation, the cell voltage output showed a 10% decline at a current of 1 A/cm² which was attributed to MEA degradation (as the post-MEA test revealed < 1 µg/cm³ ions of metallic ions) or other degradation process not related to bipolar plates as the cell resistance tested suggested there was no increase in ICR of the plates during the 500 hours of operation.

Wang and Turner [116, 117] employed electrochemical nitridation of 446M stainless steels in 0.1 M HNO₃ + 0.5 M KNO₃ solution at -0.7 V for 4 hours at room temperature to solve the issue of internal nitridation of stainless steel. The nitrided steel exhibited low transient current of 0.7 µA/cm² and -2.5 µA/cm² at the cathode and anode respectively. However, the nitrided alloy exhibited high ICR of 18 mΩ.cm². In another study, the authors reported that decreasing the

potential at which the stainless steel was nitrated to -0.9 V reduced the ICR of the nitrated 446 stainless steel alloy to $10 \text{ m}\Omega\cdot\text{cm}^2$ at 120 N/cm^2 without deterioration of corrosion resistance.

More recently, Jinlong et al. [118] demonstrated that grain refinement prior to electrochemical nitridation reduced the corrosion current of electrochemically nitrated 316L stainless steel by one order of magnitude while its transient current was in the range of $1 \mu\text{A/cm}^2$ when polarised in $0.5 \text{ M H}_2\text{SO}_4$ at $70 \text{ }^\circ\text{C}$ for 5 hours. The influence of grain refinement on ICR was, however, not reported. Moreover, none of the studies on electrochemical nitridation have evaluated the single fuel cell performance of electrochemically nitrated stainless steel despite the excellent results. This observation may not be unrelated to the fact that potentiostatic methods of electrochemical nitridation applied in these studies are limited to small surface areas.

Metal nitride coatings on Al bipolar plates are scarcely reported probably due to that fact that non-defective coatings are necessary to protect Al bipolar plates from corrosion in typical PEM fuel cells environments. However, defect-free coatings are difficult to achieve with vacuum based deposition processes. Barranco et al. [119] studied the performance of a three cell stack assembled with Al5058 coated with multi-layered chromium-zirconium nitride (ZrN/CrN) and mono layer chromium nitride (CrN) PVD deposited coatings. The plates exhibited current densities of 470 mA/cm^2 and 300 mA/cm^2 respectively in the 100 hours test. Visible damage was observed on the multi-layered coated plated while none was evident on the CrN coated plates. In subsequent studies [120], the authors attempted to improve on these results by varying the thickness of the CrN coatings. Their results showed that as thickness increased, the coated Al5038 samples exhibited better stability in $0.5 \text{ M H}_2\text{SO}_4 + 2 \text{ ppm HF}$ at $70 \text{ }^\circ\text{C}$, bubbled with oxygen to simulate the PEM fuel cell cathode environment. However, the samples were damaged after the 33 minutes

polarisation test due to pitting corrosion. They concluded based on their results that PVD deposited CrN coatings were not suitable for Al bipolar plates. Similar conclusions were made by Li et al. [121] on the performance of PVD deposited CrN and TiN coatings on 5052 Al in simulative PEM fuel cell environment. However, their work showed that multi-layered coating consisting of carbon and CrN (C/CrN) and TiN (C/TiN) showed better anticorrosion properties and lower ICR values than the single layered CrN and TiN coatings with transient currents in the range of 10 to 100 $\mu\text{A}/\text{cm}^2$ in the cathode and anode environment respectively.

(III) Other metal nitride coatings

Wang et al. [122] investigated the ex-situ performance of niobium nitride (Nb-N) and molybdenum nitride coatings deposited on 304 stainless steel by plasma surface diffusion alloying technique. The Nb-N coatings exhibited ICR values of 9.26 $\text{m}\Omega\cdot\text{cm}^2$ at 140 N/cm^2 and low and acceptable transient current densities in a simulated PEM fuel cell environment of 0.05 M H_2SO_4 + 2 ppm F^- bubbled with air and hydrogen gas at 70 $^\circ\text{C}$ to mimic PEM fuel cell cathodic and anodic environments respectively. After 4 hours of polarisation, the Nb-N coating exhibited approximately double fold increase with the highest value of 19.14 $\text{m}\Omega\cdot\text{cm}^2$. On the other hand, Mo-N coatings exhibited higher ICR values of 27.26 $\text{m}\Omega\cdot\text{cm}^2$ before polarisation and an increase of 36.98% and 25.64% at the cathode and anode after polarisation respectively. Its transient current at the cathode was similar to that of the substrate but an order of magnitude lower than that of the substrate at the anode. These results indicated that Nb-N coatings exhibited better performance than Mo-N in PEM fuel cell environments.

Studies on the suitability of Tantalum nitride (Ta-N) coated AISI 316L stainless steel as bipolar plates was conducted by Choe et al. [124]. The corrosion resistance of Ta-N coatings deposited by

varying the nitrogen flow from 0-3.6 sccm during deposition was evaluated in a simulated PEM fuel cell environment of 0.05 M H₂SO₄ + 0.2 ppm HF at 80 °C. The results indicated that the Ta-N coatings improved the corrosion properties of the substrate and exhibited corrosion current densities in the range of 0.1-1 μA/cm² in the cathodic environment and 0.01-0.01 μA/cm² in the anodic environment. The ICR of the samples at 150 N/cm² showed that the Ta-N coatings deposited at nitrogen gas flow rate of 3.6 sccm exhibited the lowest ICR value of 11 mΩcm². Evaluation of this coating under potentiostatic polarisation showed transient current density of ~0.2 μA/cm² and ~0.06 μA/cm² under cathodic and anodic conditions.

(1V) Plasma nitrided coatings

Plasma nitriding, a surface treatment technique involving the diffusion of nitrogen ions into a metallic surface in a plasma media, has also been reported for surface modification of stainless steels for bipolar plate application. In contrast to conventional gas nitriding of stainless steels, which yield discrete particles of CrN and Cr₂N at temperatures above 550 °C thereby deteriorating corrosion resistance, plasma nitriding is a low temperature process. Nitriding austenitic stainless steel at temperatures < 550 °C yields a supersaturated nitrogen layer, otherwise called expanded austenite (γN) or S phase. Tian et al. [125, 126] employed plasma nitriding at 370 °C for 2 hours to deposit a dense and supersaturated nitrogen layer on 316L and 304L stainless steels. Their result showed significant reduction in ICR of 316L stainless steel to 5-10 mΩ.cm² at compaction pressure of 100-200 N/cm². Corrosion resistance evaluated by potentiodynamic polarisation in 0.05 M H₂SO₄ + 2 ppm HF at 70 °C with air and hydrogen gas purging was, however, not improved. Although the potentiostatic polarisation results showed low transient currents, the result was not compared with that of the uncoated substrates; hence, the effect of the coatings in relation to the uncoated substrate could not be deduced. Moreover, ICR was increased by about six-fold at

the cathode and three-fold at the anode after 4 hours of potentiostatic polarisation. Similar results were reported for the nitrided 304L stainless steel.

Hong et al. [127] attempted to improve both ICR and corrosion resistance of 316L stainless steel by using inductively coupled plasma at 257 °C, 317 °C and 377 °C for 30 minutes at 6.6 Pa respectively. Their results indicated that all the stainless steels showed low transient current of $<0.25 \mu\text{A}/\text{cm}^2$ after 2.78 hours of potentiostatic polarisation in 0.1 N H_2SO_4 + 2 ppm HF solution at 80 °C with air bubbling to simulate PEM fuel cell cathodic environment. The ICR values of the samples, however, showed a dependency on nitriding temperature. ICR decreased with increasing temperatures attaining the highest value of $40 \text{ m}\Omega.\text{cm}^2$ at 257 °C and the lowest value of $11 \text{ m}\Omega.\text{cm}^2$ at 377°C. XPS of the samples showed the formation of Cr_2N and CrN at the outermost layer as it was undetectable by XRD due to its higher depth of penetration.

Studies on active screen plasma nitriding of 316 stainless steels were reported by Lin et al. [128 - 130]. In their study, 316L stainless steel was nitrided at 370 °C, 410 °C and 450 °C respectively. Their results was similar to Tian et al.'s work [125,126] showing no improvement in corrosion resistance but with higher ICR in the range $88\text{-}37 \text{ m}\Omega.\text{cm}^2$ as temperature increased. In further attempts to improve ICR and corrosion resistance of the active screen plasma nitrided 316L stainless steel in 0.5 M H_2SO_4 + 2 ppm HF at room temperature and ICR, niobium and silver was incorporated into the coated layer during deposition [129, 130]. ICR was significantly reduced to $8.9 \text{ m}\Omega.\text{cm}^2$ and $18.9 \text{ m}\Omega.\text{cm}^2$ with niobium co-alloying and silver incorporation respectively but corrosion resistance was not improved.

(C) Metal Carbides

Transition metal carbides coatings have excellent mechanical, anti-corrosion and electrical properties and have been investigated for bipolar plate application. These types of coatings can be deposited by a wide range of surface modification techniques.

Hung et al. [131] demonstrated that a patented chromium carbide based coating deposited on aluminium bipolar plates by thermal spraying outperformed graphite composite plates in a single-cell experiment that lasted for 1000 hours. At a current density of 200 mA/cm^2 , the cell with the coated bipolar plates exhibited an output voltage of 0.7 V achieving a maximum power density of 0.32 W/cm^2 and 58% efficiency. Conversely, the single fuel cell with the graphite composite bipolar plates recorded a lower cell voltage of 0.5 V, maximum power density of 0.14 W/cm^2 and efficiency of 45% at the same current density. The higher performance of the coated Al plates was credited to the lower bulk and interfacial contact resistances of the plates. Visual examination of the plates after the test showed no evidence of corrosion, but the surface morphology of the inactive part of the plates at the cathode revealed a microscale-crack in the coating. The authors, however, argued that the crack did not penetrate the coating because EDX analysis of both the aluminium and graphite composite bipolar plates indicated the presence of aluminium suggesting its presence could be due to Al impurities in the inlet gases. According to the authors, the Al impurities originated from the oxidation of the aluminium manifold in the end plates of the single cells. They further added that the cell with the coated Al bipolar plates consumed lesser amount of H_2 than the graphite plates achieving a 22% savings in hydrogen consumption thereby reducing cost.

Wang et al. [132] investigated the corrosion behaviour and ICR of niobium carbide diffusion layer deposited on 304 stainless steel by plasma surface diffusion alloying technique. The corrosion resistance of the niobium carbide (NbC) coating in simulated PEM fuel cell environment of 0.5 M H₂SO₄ + 2 ppm HF solution at 80 °C was evaluated using potentiodynamic polarisation, potentiostatic polarisation and electrochemical impedance spectroscopy measurements. The results indicated that the coatings enhanced the corrosion resistance of the substrate. In particular, the potentiostatic results indicated that the coating exhibited stable performance in the simulated PEM fuel cell cathodic and anodic environment exhibiting two order of magnitude lower transient current density than the substrate which stood at 7-8 μA/cm² after 10 hours of polarisation. At the anode, the NbC coating exhibited low transient current density of -0.05 μA/cm² while the substrate exhibited higher current density of 8 μA/cm². The ICP-MS analysis of the electrolyte also indicated that very low metallic ions were leached in the 10 hours of experimentation. ICR measurements at room temperature showed that the coating exhibited ICR of 8.47 mΩ.cm² at 140 N/cm² and exhibited negligible increase of 3.54% and 6.73% after potentiostatic polarisation under typical PEM fuel anodic and cathodic conditions respectively. In contrast, the substrate exhibited higher ICR values before polarisation (100.98 mΩ.cm²) and considerable increase after polarisation (81.68% increase at the anode and 182.54% increase at the cathode).

Chromium diffusion coatings deposited on low carbon steels and stainless steels by pack cementation at low and high temperatures have also been reported to exhibit good corrosion resistance and low ICR in simulated PEM fuel cell environments [25-29, 133,134]. This type of coatings typically contains a mixture of chromium iron carbide and chromium iron nitrides at the outermost layer while the bulk of the coatings consist of chromium iron carbide. The carbides are

formed by the reaction between chromium and carbon in the stainless steel while the nitrides are from the reaction between chromium and nitrogen decomposed from the ammonium chloride (NH_4Cl) activator.

Pioneering investigations on the application of chromised coatings for PEM fuel cells bipolar plates were reported by Cho et al. [25, 26]. Their studies demonstrated that transient current density of chromised 316L stainless steel deposited at $1050\text{ }^\circ\text{C}$ for 2.5 hours in PEM fuel cell environments of $0.5\text{ M H}_2\text{SO}_4$ bubbled with air at $70\text{ }^\circ\text{C}$ was in the $10\text{ }\mu\text{A}/\text{cm}^2$ range. Their studies further showed the effect of deposition time on the integrity of the coating. Chromised coatings deposited at $1050\text{ }^\circ\text{C}$ for 2.5 hours exhibited lower ICR ($19\text{--}17\text{ m}\Omega\cdot\text{cm}^2$ at $100\text{--}150\text{ N}/\text{cm}^2$) than the substrate ($52.5\text{--}35.3\text{ m}\Omega\cdot\text{cm}^2$ at $100\text{--}150\text{ N}/\text{cm}^2$) while the coatings deposited at longer hours (23 hours) exhibited much higher ICR values the range of $320.7\text{--}233.5\text{ m}\Omega\cdot\text{cm}^2$ at $100\text{--}150\text{ N}/\text{cm}^2$. The difference in ICR was attributed to the formation of a thin layer of chromium iron carbide formed during lower chromising time compared to the chromium rich layer formed at extended chromising times. In another study [27], the authors showed that shot peening pre-treatment prior to chromising at $900\text{ }^\circ\text{C}$ for 3 hours was beneficial in reducing transient current density of the chromised coatings in $0.5\text{ M H}_2\text{SO}_4 + 2\text{ ppm HF}$ at $70\text{ }^\circ\text{C}$ by one order of magnitude. The improvement in corrosion behaviour was attributed to the 100% increase in thickness of the chromised layer formed on pre-treated 316L stainless steel compared to the $1\text{ }\mu\text{m}$ thick coated layer formed at $1100\text{ }^\circ\text{C}$ for 3 hours without pre-treatment. ICR values of the shot peened and chromised sample was slightly lower than the untreated chromised sample which exhibited ICR values of $125\text{ m}\Omega/\text{cm}^2$ at $100\text{--}200\text{ N}/\text{cm}^2$.

Bai et al. [28, 29, 131, 132] investigated the effect of pre-rolling and EDM machining coupled with low temperature chromising at 700 °C on low carbon steel (AISI 1020) and stainless steels (420, 430, 316 type) in a simulated PEM fuel cell environment of 0.5 M H₂SO₄. The results showed that increased grain boundaries induced by the pre-treatments increased diffusion of chromium into the substrate thereby increasing the thickness of the coatings compared to their counterparts without pre-treatment. Similarly, the anti-corrosion properties of the pre-treated coatings in 0.5 M H₂SO₄ at 25 °C were superior to the untreated ones. Also, the ICR of the pre-treated samples were lower than that of the untreated one due to increase in surface roughness induced by the pre-treatments. ICR values as low as 5.9 mΩ.cm², 12 mΩ.cm² and 11.8 mΩ.cm² at 140 N/cm² were reported for pre-rolled and chromised 1045, EDM pre-treated and chromised AISI 1045 and AISI 1020 respectively.

The potential of chromium carbon (Cr-C) coatings deposited by PVD and electrodeposition techniques to enhance the corrosion resistance and surface conductivity of stainless steel alloys in simulated and real PEM fuel cell have also been explored [135-137]. It is, however, not clear whether the coatings deposited by electrodeposition contain chromium carbide as none of the investigations on electroplated Cr-C coatings conducted XRD phase analysis. Nonetheless, these coatings have been shown to possess good corrosion resistance in simulated and real PEM fuel cell environments.

Wang et al. [136] reported that electroplated Cr-C trivalent deposited on 304 stainless steel at current density (10 A/cm²) for 10 minutes exhibited ICR of 19 mΩ.cm² at ~140 N/cm², The coated steel, however, exhibited excellent corrosion resistance and stability in a simulated PEM fuel cell cathodic environment attaining low transient current density of 1.51 x 10⁻¹⁰ A/cm². Performance

evaluation of 25 cm² active area single fuel cells assembled with Cr-C coated and uncoated plates at 70 °C indicated that both cells exhibited similar OCV. However, as current density increased, the cell with the uncoated plates showed rapid decrease in voltage attaining 0.45 V at current density of 400 mA/cm² while the single fuel cell with the coated plates attained 0.57 V. The study further investigated the influence of gas flow rate and cell operation on the performance of the single cell with coated plates. Their results indicated that increasing the gas flow rate at 70°C from 200 sccm to 300 sccm as well as increasing the operating temperature from 70 °C to 80 °C at constant gas flow rate increased the cell performance. On the other hand, gas flow rate of 400 sccm at 70 °C and operating temperature of 90 °C at constant gas flow rate decreased performance of the single fuel cells.

The performance of PVD deposited chromium carbon coatings on 316L stainless steel in a simulated environment of 0.5 M H₂SO₄ + 5 ppm F⁻ at 70 °C was studied by Wu et al. [137]. XPS analysis of the coatings indicated the presence of chromium carbide on the outermost layer but its concentration was too low to be detected by XRD. Nonetheless, the coatings exhibited ICR in the range of 2.8-8.7 mΩ.cm² as carbon content increased from 0.77 at.% to 0.95 at.%. Potentiostatic polarisation of the coating with the lowest ICR (Cr_{0.23}C_{0.77}) for 7 hours indicated low transient current of in the range of 10^{-7.5} and 10⁻⁷ range in PEM fuel cathodic and anodic conditions respectively. However, surface morphology of the sample polarised under anodic conditions revealed evidence of pitting corrosion. The samples also showed increase in ICR from the initial value of 2.8 mΩ.cm² to 7.1 mΩ.cm² to 6.2 mΩ.cm² after potentiostatic polarisation.

(D) Metal oxide coatings

Wang et al. [138-140] investigated the performance of fluorine doped tin oxide (FTO), SnO₂: F coatings deposited by low-pressure chemical vapour deposition (CVD) on various grades of austenitic (grades 316L, 317L, 349™) and ferritic stainless steels (AISI 441, AISI 444, AISI416) in simulated PEM fuel cell of 1 M H₂SO₄ + 2 ppm HF at 70 °C. Their studies indicated that the substrate played significant role on the stability and corrosion behaviour of the coated steels in PEM fuel cell environments.

Among the SnO₂: F coated austenitic steels [138], SnO₂:F coated 317L stainless steel exhibited the lowest ICR and transient currents in PEM fuel cell cathode and anode environments. The SnO₂: F coated 346™ stainless steel exhibited the highest transient current in the cathode environment while SnO₂: F coated 316L stainless steel was unstable in in the anode environment, hence, it exhibited the highest transient current. However, SnO₂: F coated 316L stainless steel exhibited lower ICR than the SnO₂: F coated 346™ stainless steel.

For the ferritic SnO₂: F coated stainless steel coated steels [139], corrosion behaviour in the cathodic and anodic environment was ranked as AISI 446 > AISI 444 > AISI416. However, all the coated stainless steel exhibited higher ICR than their respective substrates. Hence, the authors attempted to reduce the ICR of the ferritic stainless steels (AISI 446 and AISI 444) by etching the surface oxide prior to deposition. The results showed that corrosion resistance was degraded although ICR was significantly reduced [140].

Recently, Park et al. [141] reported the single fuel cell performance of fluorine doped tin oxide coatings deposited on 316 stainless steel by cyclotron resonance-metal organic chemical vapour

deposition. Contrary to Wang's findings, they reported that both ICR and corrosion resistance was enhanced by mild plasma pre-treatment of the substrate before deposition. Hence, they further investigated the effect of pre-treating the substrate at varying microwave power (800-1100 W). The coating treated at a micro power of 1000W exhibited the lowest corrosion current density of $6.64 \mu\text{A}/\text{cm}^2$ in 1 M H_2SO_4 + 2 ppm HF under nitrogen gas at 80°C and ICR of $74 \text{ m}\Omega\cdot\text{cm}^2$ at $150 \text{ N}/\text{cm}^2$. The single fuel cell performance evaluation of this coating at 0.6 V indicated that coating exhibited maximum power density of $\sim 225 \text{ mW}/\text{cm}^2$.

Comparing Park et al. [141] work to that of Wang et al. [138-140], it can be seen that in both case ICR was significantly higher than the targeted $10 \text{ m}\Omega\cdot\text{cm}^2$. Hence, it may be possible to improve the performance of the coating by reducing its ICR. Also, corrosion performance evaluation under nitrogen gas conditions may be a true predication of the PEM fuel cell environment as it is well known that the cathodic environment is oxidising while the anodic environment is reducing in nature. Therefore, further studies on the corrosion performance of SnO_2 : F coatings in real PEM fuel cell environment are needed.

(E) Nickel-Phosphorous coatings

Nickel-phosphorous coatings deposited by wet deposition processes such as electro-less deposition or electroplating are a class of coatings well reported for enhancing the performance of Al alloys in real and simulated PEM fuel environments [140-145]. These coatings often exhibit very high transient current density and ICR values. Hence, elements such as molybdenum, copper, and cobalt are incorporated into the coatings to improve corrosion performance and decrease ICR. Nonetheless, the ICR values of the modified coatings are often significantly higher than the targeted value of $10 \text{ m}\Omega\cdot\text{cm}^2$. For instance, Fetohi et al. [142] demonstrated that incorporating

cobalt into Ni-P coating deposited by electro-less deposition reduced the ICR from 150.75 $\text{m}\Omega\cdot\text{cm}^2$ to 114.45 $\text{m}\Omega\cdot\text{cm}^2$ while the Ni-Co-P coating deposited by electroplating exhibited 33% decrease in the ICR of Ni-P coating (88.85 $\text{m}\Omega\cdot\text{cm}^2$). Lee et al. [145], however, recently reported that adding nano-graphite particles to Ni-Cu-P coatings can significantly reduce the in-plane electrical resistivity and in-plane electrical resistivity of modified Ni-P coatings to acceptable values.

2.3.2.2 Carbon-based coatings

(A) Carbon coatings

Carbon exists in many allotropic forms including amorphous carbon, graphite, and diamond. These forms of carbon when deposited on metallic substrates generally exhibit chemical inertness in many environments and low electrical contact resistance (except diamond). Hence they find application for surface modification of PEM fuel cell bipolar plates. In recent times, the possibility of employing graphene for surface protection of stainless steel bipolar plate has also been explored.

I. Amorphous carbon coating

Amorphous carbon coatings deposited by high vacuum based processes such as chemical and physical vapour deposition which are prone to pin holes defects are well reported for surface modification of bipolar plates [146-149]. Although, most of the studies on amorphous carbon coatings show that ICR is significantly reduced, only a few studies have demonstrated polarisation studies at typical PEM fuel cell environments & working potentials. Fukutsuka et al. [146] reported that plasma-assisted CVD deposited carbon-coating on 304 stainless steel decreased the contact resistance of the substrate at typical compaction pressure before and after polarisation in 0.5 M H_2SO_4 + 2 ppm HF solution bubbled with H_2 and O_2 at 80 °C to simulate the anode and

cathode environments respectively. At 140 N/cm^2 , the sample polarised under PEM fuel cell cathodic conditions exhibited 15% increase in ICR while the sample polarised under anodic conditions exhibited 10% decrease in ICR. However, these results, which were conducted after potentiodynamic test may not be representative of ICR changes under potentiostatic polarisation at 0.6 V (cathode) and -0.1 V (anode).

Feng et al. [147] studied the performance of a $3 \mu\text{m}$ thick amorphous carbon coating deposited on 316L stainless steel by close field unbalanced magnetron sputter ion plating (CFUMSI) in simulated PEM fuel cell electrolyte of $0.5 \text{ M H}_2\text{SO}_4 + 2 \text{ ppm HF}$ at $80 \text{ }^\circ\text{C}$. Their results showed that ICR of the substrate was reduced from $664.3\text{-}255.4 \text{ m}\Omega\cdot\text{cm}^2$ to $10.2\text{-}5.2 \text{ m}\Omega\cdot\text{cm}^2$ under $90\text{-}210 \text{ N/cm}^2$. However, the coated and uncoated samples exhibited comparable low transient currents in both simulated anode and cathode environments after ~ 9 hours polarisation test although the ICP-MS post-analysis of the electrolyte showed that the coated sample had a lower concentration of metallic ions.

Single fuel cell and durability evaluation of amorphous carbon coatings are seldom reported in the literature. Show et al. [148] reported the single fuel cell performance of amorphous carbon (a-C) coatings deposited on titanium bipolar plates by radio frequency enhanced chemical vapour deposition (RF-PECVD). At room temperature, the carbon coated plates exhibited very low contact resistance of $2.5 \text{ m}\Omega\text{cm}^2$, which represented a 50% reduction in that of the substrate. The difference in ICR translated to a two-fold increase in the power output of that of the cell with the uncoated bipolar plates.

Yi et al. [149] investigated the single fuel cell and stack performance of 304 stainless steel bipolar plates coated with a-C coatings deposited by CFUMSI. The 40 cm^2 active area single fuel cell

assembled with a-C coated bipolar plates attained a maximum power density of 1150.6 mW/cm² while the single fuel cell with uncoated bipolar plates exhibited a lower peak power output of 562.6 mW cm⁻². Durability testing of the single fuel cell at constant cell voltage of 0.6 V for 200 hours at 60 °C showed that the single fuel cell with the coated bipolar plates outperformed the cell with uncoated bipolar plates and experienced a lower performance degradation of 3.9% while the performance of the single fuel with the uncoated plates deteriorated by 28.7%. Based on these promising results, they further evaluated the performance of a three-cell stack at a constant voltage of 1.8 V for 48 hours. The results showed that the stack exhibited an output power density is 873.3 mW/ cm² at 1.8 V and maximum power density of 1040.1 mW/cm² at a current density of 2085.9 mA/cm² with good short-term lifetime performance.

II. Graphite coatings

Graphite coatings are rarely reported for bipolar plate application compared to the other forms of carbon coating. Wang et al. [150] developed a low cost method of depositing graphite coatings on 316L stainless steel by compressing a 10 cm x 10 cm layer of expanded graphite at 100 MPa on 316L stainless steel at 100 °C using carbon fillers and a polymer binder as schematically represented in Figure 18. The graphite coatings which were polarised in 0.5 M H₂SO₄ at room

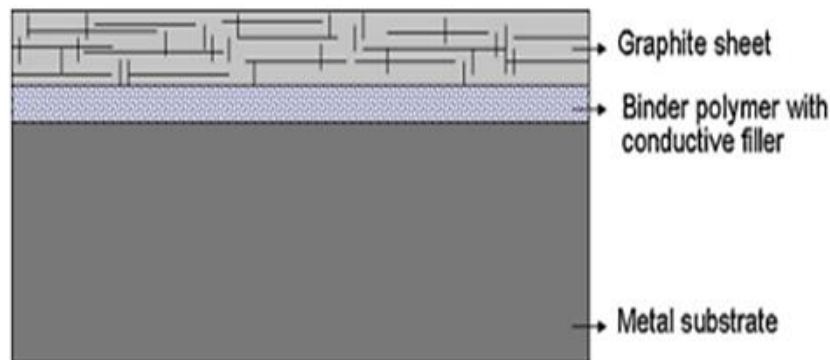


Figure 18 Schematic illustration of the design concept of the graphite-coated plates [153].

temperature significantly improved the corrosion resistance of the bare metal. However, the contact resistance of the graphite coatings was impaired by the non-conductive nature of the binder. The lowest contact resistance obtained at a filler content of 2.5 g was about 50% higher than that of the bare metal implying that such coatings are not suitable for PEM fuel cell bipolar plates. Husby et al. [151], however, demonstrated that by using a spraying technique followed by hot pressing, it was possible to decrease the ICR of graphite coatings to values below that of the substrate. The reduction in ICR was attributed to the reduction in porosity of the original coating by ~50% as shown in Figure 19. The study revealed that carbon-based coatings made up of 45% of graphite, 5% carbon black and 50% epoxy binder on 316L stainless steel had a contact resistance of $9.8 \text{ m}\Omega/\text{cm}^2$ at $125 \text{ N}/\text{cm}^2$ but its corrosion resistance was similar to that of the substrate due to the porosity of the coating.

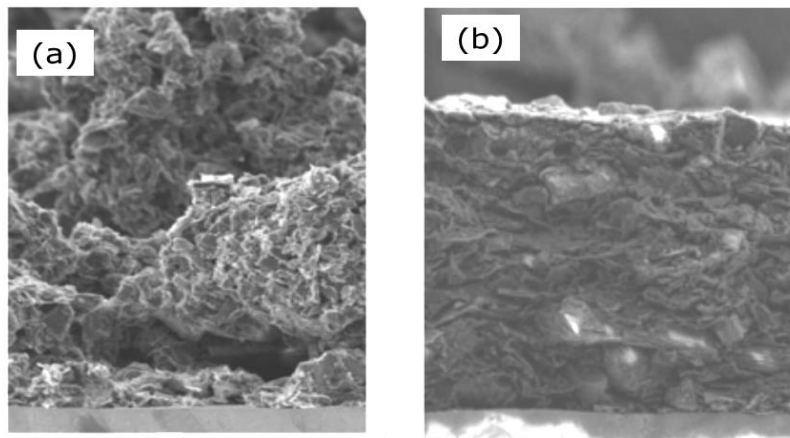


Figure 19 (a) non- hot pressed (b) hot-pressed graphite composite coating [151].

Chung et al. [152] deposited graphite like-carbon coatings on 304 stainless steel substrate coated with a layer of Ni by an unnamed CVD process using a gas mixture of acetylene/hydrogen at 680°C . The coating exhibited a disarranged graphite structure at the surface but maintained a

highly ordered graphite structure at the carbon/Ni interface. Electrochemical polarisation of the substrate coated 304 stainless steel and graphite in 0.5 M H₂SO₄ indicated that the anti-corrosion properties of the coating were similar to that of graphite but better than that of the substrate. Similarly, 100 hours of single cell testing of the coated bipolar plates at constant voltage of 0.6 V revealed comparable performance to graphite bipolar plates operated at the same temperature of 40 °C while the uncoated plate showed a 16% loss in current density output.

III. Graphene

Graphene grown on electroplated Ni coated 304 stainless steel was recently proposed for metallic bipolar plate application by Pu et al. [153]. Their work showed that graphene exhibited ICR values of 36 mΩ.cm² at 140 N/cm² before polarisation in 3.5% sodium chloride (NaCl) solution at ambient temperature. After 20 potentiodynamic polarisation scans, ICR of the graphene Ni/304 stainless steel increased by 18% while maintaining good corrosion resistance at ambient temperature. Hence, the authors concluded that graphene was promising for surface modification of stainless steel in PEM fuel cell environments. In another study, Stoot et al. [154] further demonstrated the beneficial effect of long term exposure (540 hours) of graphene to very harsh environments of boiling 3.5% NaCl in an Atlas glass cell (Figure 20). Their results showed that the excellent corrosion resistance of graphene grown on electroplated Ni stainless steel reported by Pu et al. [153] may not necessarily be attributed to graphene as the corrosion parameters of electroplated Ni stainless steel both with/without graphene coatings were very similar. However, these studies did not consider that bipolar plates do not corrode at free potential but at 0.6 V at the cathode and -0.1 V at the anode with the environment at each electrode either oxidising or reducing. In addition, PEM fuel cell typically operates in an acidic environment at 60-80 °C, hence, room temperature or boiling NaCl solution simulations may not be an adequate prediction.

Moreover, the ICR values reported by Pu et al. [153] were considerably too high for PEM fuel cell operations. Therefore, more studies on the application of graphene for PE fuel cell bipolar plate application are needed



Figure 20 Atlas cell containing 3.5 wt.% sodium chloride solution [154].

IV. Diamond like carbon coatings

Diamonds like carbon (DLC) coatings are a form of amorphous carbon coatings having a mixture of sp^3 of diamond and sp^2 bonds of graphite. These coatings exist in different forms and may or may not contain hydrogen. Conventionally, DLC coatings are non-conductive but corrosion resistant. However, Lee et al. [155] and Suzuki et al. [156] have reported the performance of electrically conductive and corrosion resistant DLC coatings.

Lee et al. [155] compared the single cell performance of PVD-YZU001 DLC coated Al 5052 with that of graphite and bare 316L stainless steel plate. Their results showed that YZU001 DLC coated Al 5052 was promising for bipolar plate application at low operating voltage and power density.

The PVD coated plates exhibited lower corrosion current densities in simulated PEM fuel cell environment of 0.5 M H₂SO₄ than the bare metal but was more corroded than 316L stainless steel and graphite polarised in the same environment. The ICR of the materials revealed an opposite trend and ranked as graphite < coated Al < bare 316L stainless steel. Hence, the coated Al plates outperformed the 316L plates with high contact resistance were attributed to the presence of passive oxides. At 0.6 V, the cell with the coated Al plates had a higher current density of 228 mA/cm² while the 316L stainless steel had 158 mA/cm². In comparison to the single fuel cell with the graphite plates, both metallic bipolar plates had lower performance and shorter lifetime even though their open circuit voltage was higher.

Suzuki et al. [156] deposited a double layer of DLC coatings consisting of conventional DLC formed at 200 °C and conductive DLC deposited at 350 °C by implanting nitrogen or boron ion via Plasma based ion implantation and deposition techniques on 316L stainless steel. They reported that the nitrogen/boron implanted DLC coatings exhibited very low ICR values (< 5 mΩ.cm² at 150 N/cm²) and transient current of 1 μA/cm² when polarised in pH 2 H₂SO₄ acid at 80°C at 1 V vs SHE for 2 hours. Hence, they further evaluated the performance of 25 cm² active area single fuel cell and 167 cm² active area stack containing 5 single fuel cells assembled with bipolar plates coated with Ni/B implanted DLC coatings at 80 °C for 1000 hours. Their result showed that both the single fuel cell and the stack exhibited very stable performance throughout the 1000 hours of testing.

(B) Conductive polymer coatings

Conductive polymers are a class of coating that combine the electrical conductivity of metals and the anti-corrosion properties of plastics. Examples include poly (o-phenylenediamine), polyaniline, and polypyrrole. These coatings are often formed by electro polymerization techniques which

basically involves cathodic polarisation of the metal in a solution of the desired coating material [157-159]. Recently, a group of researchers in Mexico have demonstrated that conductive polymer coatings for bipolar plate application can be deposited by Electrophoretic deposition (EPD) [160]. In EPD, coatings are deposited via the transport of charged particles dispersed in a suitable solvent towards an electrode, under an applied electric field [160].

Conductive polymer coatings often exhibit good corrosion resistance in PEM fuel cell environments but unacceptable ICR. Joseph et al. [157, 158] studied the performance of polypyrrole (PPy) and polyaniline (PANI) coatings on Al6061 and 304 stainless steel. They reported that PPy and PANI coated Al 6061 exhibited higher ICR than the substrate while the former was severely corroded when exposed to simulated PEM fuel cell environment of 0.1 M H₂SO₄ [157]. However, when deposited on 304 stainless steels the coatings exhibited better corrosion resistance and electrical conductivity [158]. In both studies, only potentiodynamic polarisation was conducted with no gas purging. It is well known that the oxidising and reducing nature of the PEM fuel cell electrodes cannot be correctly simulated in one environment. Moreover the temperature at which the polarisation was conducted was not stated.

The findings of Wang and Northwood [159] on polypyrrole electro-polymerised on 316L stainless steel by galvanostatic and cyclic voltammetry clarified the behaviour of PPy coatings under PEM fuel cell working conditions of -0.1 V and 0.6 V at the anode and cathode respectively. Their results showed that the morphology of the coatings produced by the two routes differed but their corrosion performance in 0.5 M H₂SO₄ purged with oxygen and hydrogen gas to simulate PEM fuel cathode and anode conditions was similar. The coatings exhibited with transient current density of about 10 $\mu\text{A}/\text{cm}^2$ and in the range -10 to -20 $\mu\text{A}/\text{cm}^2$ at the cathode and anode respectively. In further attempts to improve the corrosion properties of the PPy coatings, the

authors employed Taguchi design of experiment technique to determine the effect of process parameters (time of polymerisation and applied current as well as concentration of polypyrrole and H₂SO₄ used for deposition) on the corrosion properties of the PPY coatings [161]. Their results indicated that the coating produced at 2 A for 30 minutes with 0.05 mol/L and 0.2 mol/L polypyrrole and H₂SO₄ respectively exhibited the best corrosion properties. Evaluation of the performance of this coating in 0.5 M H₂SO₄ at 70 °C purged with hydrogen and oxygen gas for 10 hours indicated that the coatings exhibited transient current density of $-20 \mu\text{A}/\text{cm}^2$ and $\sim 10 \mu\text{A}/\text{cm}^2$ at the anode and cathode respectively. From the ICP-MS analysis of the dissolved metal ions leached during the testing, they estimated that about 10 ppm and 20 ppm of metallic ions such as Fe, Ni and Cr would have been leached into the electrolyte at the anode and cathode respectively after 5000 hours of operation. However, the coatings exhibited comparable ICR values to that of the substrate at typical PEM fuel cell compaction pressure with values significantly higher than the targeted $10 \text{ m}\Omega.\text{cm}^2$

Some other authors have demonstrated that incorporating carboneous fillers such as graphite and carbon nanotubes tubes into conductive polymer coatings can reduce the contact resistance of these coatings. Yang et al. [162] reported that incorporating graphite into polypropylene coatings during electro polymerisation enhanced the corrosion resistance and surface conductivity of PPY coated 316 stainless steel. The modified polypropylene coating exhibited low transient current densities of $0.003 \mu\text{A}/\text{cm}^2$ and $90 \mu\text{A}/\text{cm}^2$ in the cathodic and anodic simulated PEM fuel environment of 0.5 M H₂SO₄ + 2×10^{-6} fluoride ions at 70°C with air and hydrogen bubbling respectively. At 2.8 MPa, ICR of the graphite/PPY coating was $\sim 18 \text{ m}\Omega/\text{cm}^2$. It is however noted that 2.8 MPa is considerably higher than the compaction pressure (1-2 MPa) recommended for bipolar plates.

Lee et al. [163] also showed that the contact resistance of polypropylene coating can be further reduced by growing carbon nanotubes on 304 stainless before polymerisation rather than incorporating CNT fillers. The ICR of CNT filler /PPY composite coating was found to be 33.8 $\text{m}\Omega/\text{cm}^2$ while that of the CNT grown /PPY coating was 9.7 $\text{m}\Omega/\text{cm}^2$ at 200 N/cm^2 . Transient currents of the latter in a simulated PEM fuel cell environment of 1 M H_2SO_4 + 2 ppm HF at 70 °C for 2.78 hours were less than 1 $\mu\text{A}/\text{cm}^2$.

The contact resistance and corrosion performance of polypyrrole–Vulcan XC-72 carbon composite coatings deposited on 316 stainless steel substrates by EPD in 0.1 M H_2SO_4 at room temperature was investigated by Pech-Rodríguez et al. [162]. The authors employed Taugchi design of experiment technique was employed to study the influence of applied voltage, deposition time, concentration of the solvent used for polymerisation and pyrrole monomer concentration. Their results showed that corrosion resistance of 316 stainless was enhanced by the EPD deposited coatings. In particular, the coatings deposited at 50 V for 2 minutes using acetone only as the polymerisation media at pyrrole concentration of 0.1 mol/L exhibited lower corrosion current density of 2.3 $\mu\text{A}/\text{cm}^2$, representing a two order of magnitude difference in that of the substrate (171 $\mu\text{A}/\text{cm}^2$). However, its contact resistance at 1 N/m was ~60% higher than that of the substrate (0.3264 $\Omega\cdot\text{m}$) and ~97% higher than 0.2117 $\Omega\cdot\text{m}$ reported for the substrate at 1.6 N/m. These results imply that these coatings may not be suitable for the desired application.

(C) Composite coatings

Composites coatings with conductive fillers deposited by different coating techniques have also attracted attention as potential coatings for metallic bipolar plates.

Mawdsley et al. [164] developed composite coatings with an ethylenetetrafluoroethylene (ETFE) matrix and graphite and/or titanium carbide fillers. The corrosion resistance of the coatings which were deposited on 300 series Al by a combination of wet spraying and heat-treatment processes showed a dependency on the amount of fillers. In particular, the coating with equal volume percentage of TiC and graphite (50%ETFE/25%TiC/25%graphite) retarded the corrosion rate of the base metal when exposed to a simulated PEM fuel cell environment of 0.001 M H₂SO₄ + 2 ppm HF at 70 °C. However, whitish corrosion products were evident in the sample evaluated under anodic conditions (i.e. hydrogen bubbled electrolyte) after the test. The developed coated samples were further tested in 60 cm² active single fuel cell at 50°C. The polarisation results showed that the cell assembled with bipolar plate coated with 50%ETFE/25%TiC/25%graphite coatings exhibited relatively lower OCV compared to the cell with 50%ETFE/25%TiC coatings bipolar plate with rapid decrease in voltage. However, the single fuel cell coated with 92% volume fraction of graphite (90%Gr/8%ETFE) exhibited the best performance with OCV slightly higher than 0.9 V.

Fu et al. [165] compared the performance of electroplated silver-PTFE coatings on 316L stainless steel with silver plated-316 stainless steel. The PTFE modified coating exhibited a contact angle of 114° while the Ag-coated sample exhibited a contact angle of 73° implying that addition of PTFE increased the hydrophobicity of the coating which is beneficial for water management in PEM fuel cell. However, addition of PTFE to the Ag coated sample had negligible influence on the performance of the coatings in 0.5 M H₂SO₄ + 5 ppm HF bubbled with air and hydrogen at 70 °C to simulate PEM fuel cell cathode and anode conditions. Under these conditions, the transient current densities of both coatings were similar and were in the range of 10 μA/cm² and 100 μA/cm² at the cathode and anode respectively. On the other hand, Show and Takahashi [163]

demonstrated that 316 stainless steel coated with CNT/PTFE composite film containing 75% from the dispersion fluids of CNT and PTFE reduced the contact resistance of the substrate ($46 \text{ m}\Omega/\text{cm}^2$) by about four-fold. Similarly, the corrosion resistance of the substrate in 1 M H_2SO_4 was improved. Hence, single fuel cell performance of the coated plates showed about 58% increase in the maximum output power of the single fuel cell with the uncoated plates which was given as 1.7 W.

2.3.3 POROUS METALLIC MATERIALS (PMM)

Porous metallic materials (PMM) such as metal foams, metal screens/meshes are lightweight cellular structured materials which possess excellent mechanical and thermal properties as well as increased surface area and high gas permeability [167 -172]. Hence, these materials have also been considered for bipolar plate application.

PMM are advantageous for cost reduction of PEM fuel cells in two ways: first, the inherent porous nature of PMM eliminates the need for flow field designs as seen in Figure 21. Secondly, PMMs can also serve as the gas diffusion layer and provide support for the catalyst layer [169-171]. Nevertheless, PMM are susceptible to corrosion in PEM fuel cell environments and need to be coated for better performance.

Murphy et al. [170] studied the performance of two PEM fuel cell stacks consisting of eight single cells with gold coated Ni foams and expanded Ti bipolar plates respectively. Their results indicated that the porous nature of PMMs enhanced the flow and distribution of reactant gases over the entire reaction area and showed comparable performance to conventional flow designs. They demonstrated that using PMM produced by low cost mass production technique as bipolar

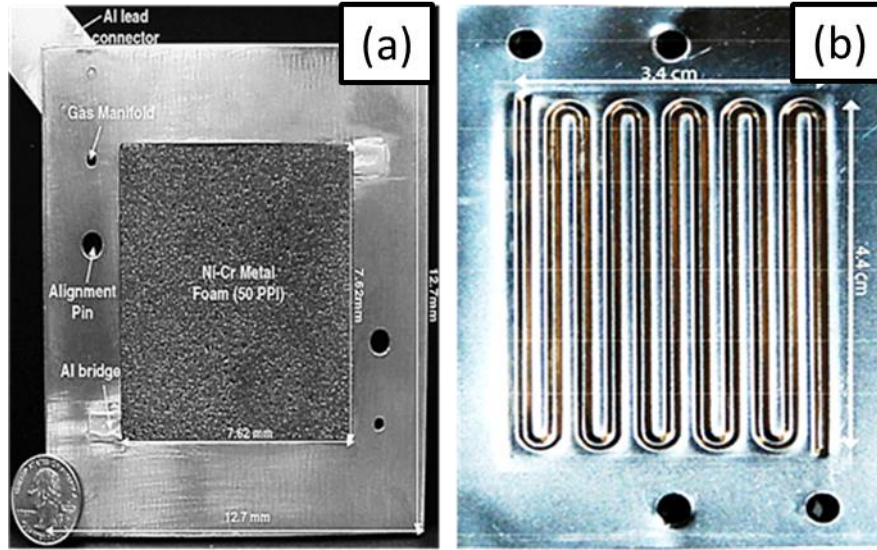


Figure 21 Comparison of bipolar plates made from (a) metal foam [168] (b) bulk stainless steel [111].

plate would lead to significant reduction in the weight and cost of PEM fuel cells. Hence, they recommended TiN coated Ti expanded plates for large scale production. Similar conclusions were made by Tseng et al. [171] who compared the single cell performance of PTFE coated Ni foam with that of graphite bipolar plate. The polarisation results revealed that in the low current density region, the cell with the metal foam and graphite had equivalent voltage output but in the high current density region, the voltage output of the metal foam-cell exceeded that of the graphite plate-cell. Likewise, Kumar and Reddy [168, 172] reported that bipolar plates fabricated from Ni-Cr and 316 stainless steel foams out-performed conventional 316 stainless steel bipolar plates with multi parallel flow field designs in single fuel cell experiments. The better performance of the PMM was attributed to the decrease in the permeability of the flow field design which had a positive impact on the pressure drop across the plate resulting in better mass transport between the plates and the membrane. In addition, they proposed that MEA contaminations can be minimised by optimising the fluid flow of PMM so that the ions are swept away with the by-product water.

2.5 SUMMARY AND INDICATION OF GAP WITHIN THE LITERATURE

Metals are promising for automotive PEM fuel cells bipolar plates due to their potential to significantly reduce cost, weight and volume. Metallic materials considered for bipolar plates applications are, however, prone to corrosion in the humid and acidic PEM fuel cells environments and exhibit high interfacial contact resistance with the gas diffusion layer due to the existence of a semi-conductive oxide layer. From the foregone review the following conclusions can be deduced:

- Different bare metals have been considered as potential alternative materials to replace graphite bipolar plates. Among the metals considered, stainless steel has emerged as the material of choice owing to its cost effectiveness, availability of variety of alloys and amenability to low cost/high volume and rapid manufacturing processes. Nevertheless, bare stainless steel alloys are not suitable for bipolar plates as these ferrous based alloys exhibit high ICR values at least an order of magnitude higher than the targeted $10 \text{ m}\Omega\cdot\text{cm}^2$ due to the presence of a thin non-conductive surface oxide layer. In addition, the thickness of the passive oxide layer has been shown to increase during operation leading to cell voltage output degradation. Hence, stainless steels require surface coatings and/or treatment for optimum performance in the PEM fuel cell environments.
- Extensive research work has been conducted on surface-modified stainless steels. Nonetheless, depositing defect-free coatings is challenging therefore the search for coatings and treatments which satisfy the corrosion resistance and ICR requirements have continued to attract considerable research attention. Some coatings such as the metal nitrides have been widely studied while some have been scarcely investigated despite their

promising potential. An example of such under-studied coatings is graphite coatings. Graphite coatings are often deposited by low temperature vacuum deposition processes and spraying/compression techniques using binding agents. However, the binding agents used in spraying/compression techniques are often non-conductive in nature, thereby deteriorating the conductivity of these carbon-based coatings. Therefore, this study, explored the potential of a room temperature process named CoBlast™ technology to deposit graphite coatings on metal for PEM fuel cell bipolar plate application.

- There is a general need for single fuel cells and durability evaluation of coatings that have exhibited the targeted ICR and corrosion current densities in simulated PEM fuel cell environments. Similarly, durability studies of foam materials which are reported to exhibit good single cell performance comparable to bulk materials or graphite bipolar plates are also needed to assess the suitability of these materials for real life applications.
- Although a wide range of coatings have been investigated, optimisation of the coating parameters and systematic investigation of the influence of process parameters on the performance of the coatings in PEM fuel cell environments are scarcely reported. In the few cases where optimisation of process parameters were conducted, classical experiment methods which depend on varying one factor while keeping the other constant was employed. However, optimisation by classical experimental methods does not give possible interactive effects between different coating parameter and is both time consuming and expensive. Hence, this study also considered the optimisation of corrosion resistance of chromised coatings in simulated PEM fuel cell environments.

CHAPTER THREE

Experimental Methodology

3.1 INTRODUCTION

In this chapter, details of the experimental methodology and related theory where applicable are presented. The experimental methodology consisted of the coating deposition, surface characterisation and corrosion resistance evaluation experiments. The methodology for interfacial contact resistance evaluation and single fuel cell experiments of selected coatings was also presented.

3.2 MATERIAL AND COATING PROCESSES

This section presents an overview of the surface modification processes employed in this study as well as the materials, equipment and methodology employed for each process.

3.2.1 PHASE 1: COBLAST™ DEPOSITED GRAPHITE COATINGS & MODIFICATION

(A) GRAPHITE COATINGS DEPOSITED BY COBLAST™ TECHNOLOGY

Graphite coatings are effective barriers against corrosion provided the substrate is cathodic relative to graphite in the galvanic series. In the first phase of this study, the potential of a novel micro blasting process called CoBlast™ to deposit graphite-based coatings on stainless steel and titanium for bipolar plate application was explored.

CoBlast™ is a low cost, modified micro blasting process owned by EnBio Materials Limited, Ireland. The ambient temperature and pressure process utilises a mixture of abrasive blast medium mixed with a stream of ‘dopant’ particles to modify the substrate surface. The abrasive roughens

the metal surface while simultaneously disrupting the oxide layer and exposing the reactive metal to bond chemically with the dopant [173-179]. The adhesion of the coatings to the substrate is due to a combination of tribo-chemical bond formation and mechanical interlock between the dopant and the substrate. Attractive features of the process includes its simplicity and low cost, as no wet intermediate stages, vacuum or inert environment are involved; rather coatings are deposited from the powder phase at room temperature. The deposition process is also reported to be energy and time efficient. The technical versatility of the CoBlast™ process has been demonstrated in the deposition of bio ceramic coatings such as hydroxyapatite (HA) [174-176] and industrial coatings such as polytetrafluoroethylene (PTFE) [177] and optical/emissive black coatings for space applications [178].

150mm x 150mm x 1mm coupons of titanium (V) alloy (Ti6Al4V) and stainless steel alloy (AISI316) purchased from Lisnabrin Engineering Limited, Cork, Ireland was selected as substrates for the study. Aluminum was not considered because it is anodic to graphite in the galvanic series; hence, it corrodes in preference to graphite [179,180]. The nominal composition of the alloys is as presented in Table 6. Prior to coating, the coupons were ultrasonically cleansed in deionised water for 10 minutes, air dried and wiped with isopropanol.

Deposition of the coatings was conducted in a single nozzle CoBlast™ process as schematically represented in Figure 22 (a). A picture of the equipment used for deposition is also displayed in Figure 22 (b). The coating powder consisted of a mixture of amorphous graphite powder (particle size: 44 µm, microfyne grade) and alumina powder (particles size: 50 µm) in a 1:1 ratio. The surface morphologies of the different coating powders are shown in Figure 23 with graphite powder having a flaky morphology and alumina particles, an irregular morphology. The powders

were blended in a laboratory tubular for 5 minutes and thereafter blasted onto the metal surfaces at a standoff distance of 30 mm, pressure of 620 kPa and speed of 20 mm/s.

Table 6 Nominal composition of metallic substrates used for CoBlast™ process

Metal	Nominal composition
316 stainless steel alloy	0.08% C, 16 -18% Cr, 10-14% Ni, 2-3% Mo, balance Fe
Ti6Al4V alloy	5.5-6.76% Al, 3.5 -4.5% V, Balance Ti

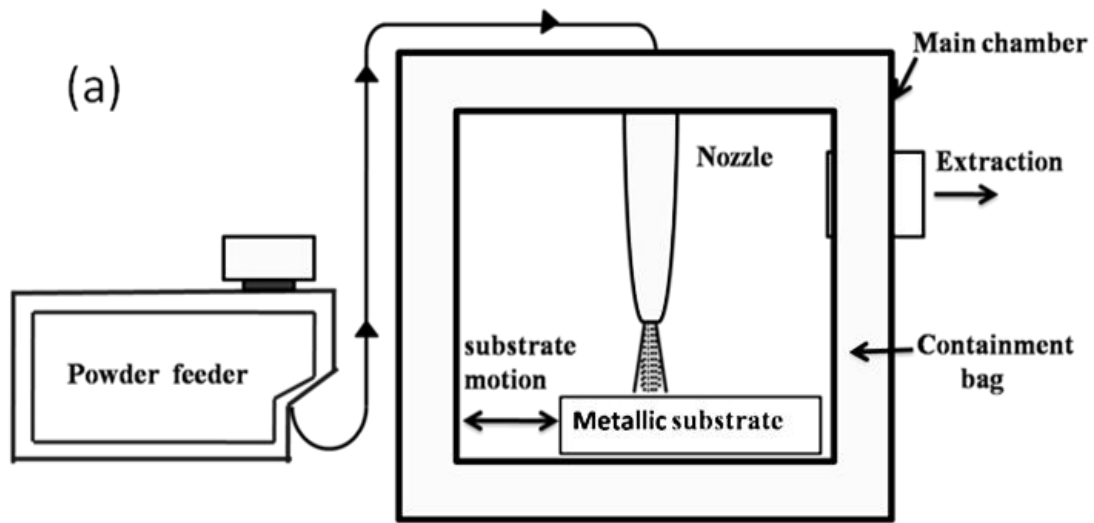


Figure 22 (a) Schematic representation of the CoBlast™ process adapted from [176], (b) picture of the CoBlast™ equipment.

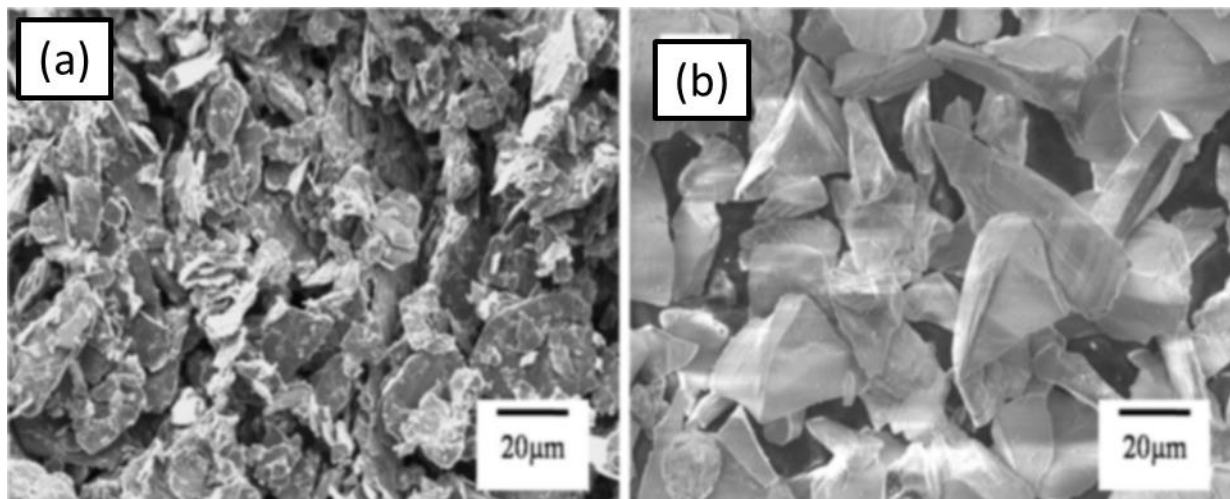


Figure 23 SEM images of (a) microfyne graphite (b) alumina powders

After coating, the surfaces were blasted with dry air and ultrasonically washed in water for two minutes to remove any loosely adhered powder particles. The process parameters employed in the deposition of graphite based coatings have been optimised for CoBlast™ deposited bio-ceramic and black coatings [175, 176, 177].

(B) MODIFICATION OF COBLAST™ COATINGS.

CoBlast™ treated 316 stainless steels were modified by pack chromising (an overview of the process will be given in the next section) in order to enhance its performance in PEM fuel cell environments. The CoBlast™ treated stainless steel samples were buried in a powder pack of 50% chromium (particle size: 44 μm), 43% alumina (particle size: 50 μm) and 7% NH₄Cl (particle size 100 μm) which has been previously ball milled for 12 hours. Chromium and ammonium powders were purchased from Sigma Aldrich, Ireland. Figure 24 shows the morphologies of the powders. The Cr powder had a flaky and irregular morphology while the

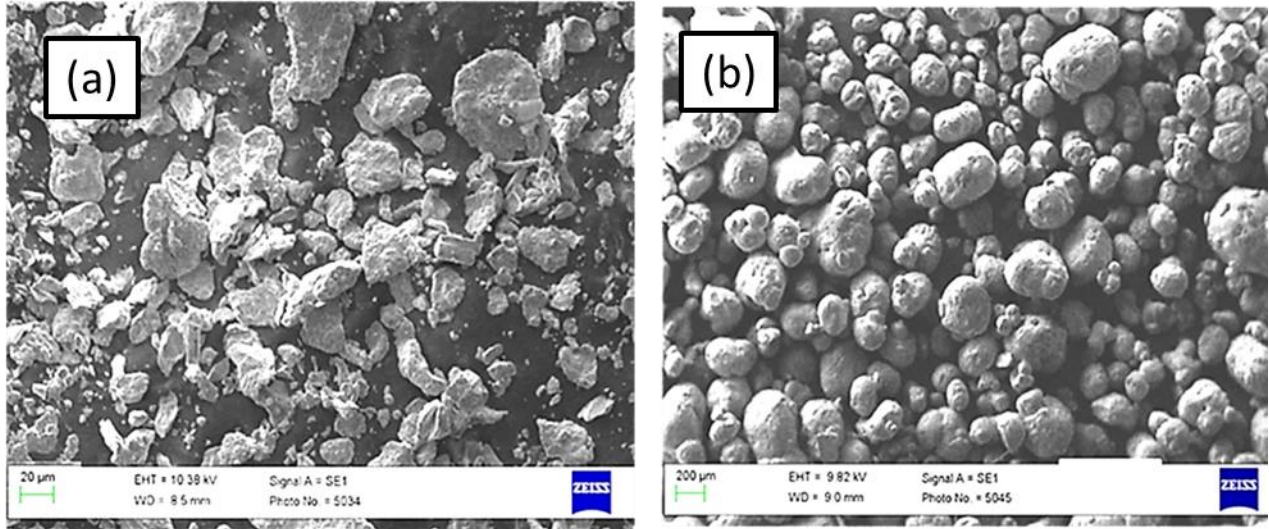


Figure 24 SEM images of (a) chromium powder (b) ammonium chloride powder.

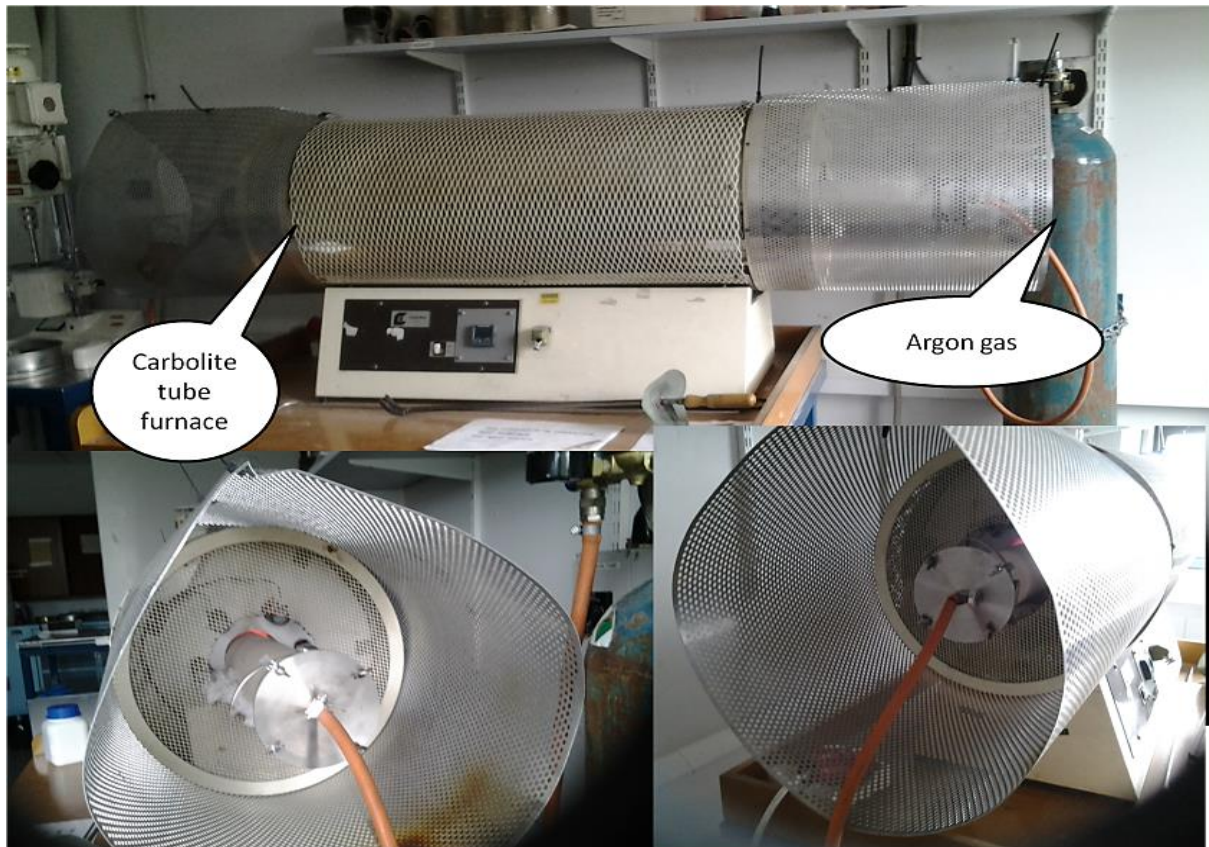


Figure 25 Carbolite tube furnace used in the study.

NH₄Cl powder had a spherical morphology. The crucibles were covered with lids and placed in a Carbolite tube furnace in an argon gas protective environment as shown in Figure 25. The crucibles were thereafter heated to 900 °C and held for 3 hours at a heating rate of 10 °C per minute in a tube furnace. The furnace was thereafter cooled to room temperature at the same heating rate while the gas supply was turned off at about 200 °C. After the heating cycle, the chromised surfaces were ultrasonically cleansed in acetone for 15 minutes, dried with nitrogen gas and weighed.

3.2.2 PHASE 2: CHROMIUM DIFFUSION COATINGS & MODIFICATION

In the second phase of this study, chromium diffusion coatings otherwise called chromised coatings were deposited on AISI 304 stainless steels by pack cementation. Response surface methodology (RSM), a design of experiment (DoE) technique, was employed to optimise selected pack chromising process parameters. The objective of this aspect of the study was to investigate the influence of the selected process parameters on the corrosion current density of chromised coating in a simulated PEM fuel cell environment of 0.5 M H₂SO₄ + 2 ppm HF at 70°C as well as optimisation of the selected process parameters.

The chromised coatings produced at the optimal process parameters were thereafter modified. The modification process entailed depositing a carbon rich layer via pack cementation prior to chromising at optimal process parameters. An overview of pack cementation process is first presented, thereafter, RSM technique is discussed and the details of the materials and equipment employed for pack cementation is given.

(A) Overview of pack cementation process

Pack cementation is an in-situ chemical vapour deposition (CVD) batch process used for producing corrosion and wear resistant coatings on metallic materials such as steel, aluminium, nickel etc. The thermochemical process essentially entails four components: the substrate and three powders consisting of a master alloy (the element to be deposited), halide salt activator (usually NH_4Cl) and inert filler. The nature and characteristics of pack cementation coatings are influenced by the composition of the substrate, temperature, time and powder pack composition [181-184].

In pack cementation processes, the substrate is either embedded in the powder mixture or placed on top of the mixture and subsequently heated to high temperatures (800-1200 °C) in a reducing or inert environment. The major steps in pack cementation are summarised in Figure 26. The activator decomposes and reacts with the master alloy to form volatile metal halides vapours, which diffuses through the powder pack to the substrate's surface to deposit the desired coatings via solid state diffusion. The mechanism of formation and growth kinetics as well as the phase and microstructure of the coatings depend on the chemical composition and activity of the metallic halides produced at the deposition temperature, which in turn depends on the amount of the activator and master alloy in the powder mixture [181-185].

Pack cementation was first reported in the 20th century and since then have been widely employed to deposit different types of coatings. However, in this work, chromium and carbon diffusion coatings were formed via pack cementation. These processes are otherwise referred to as pack-chromising and pack-carburisation respectively.

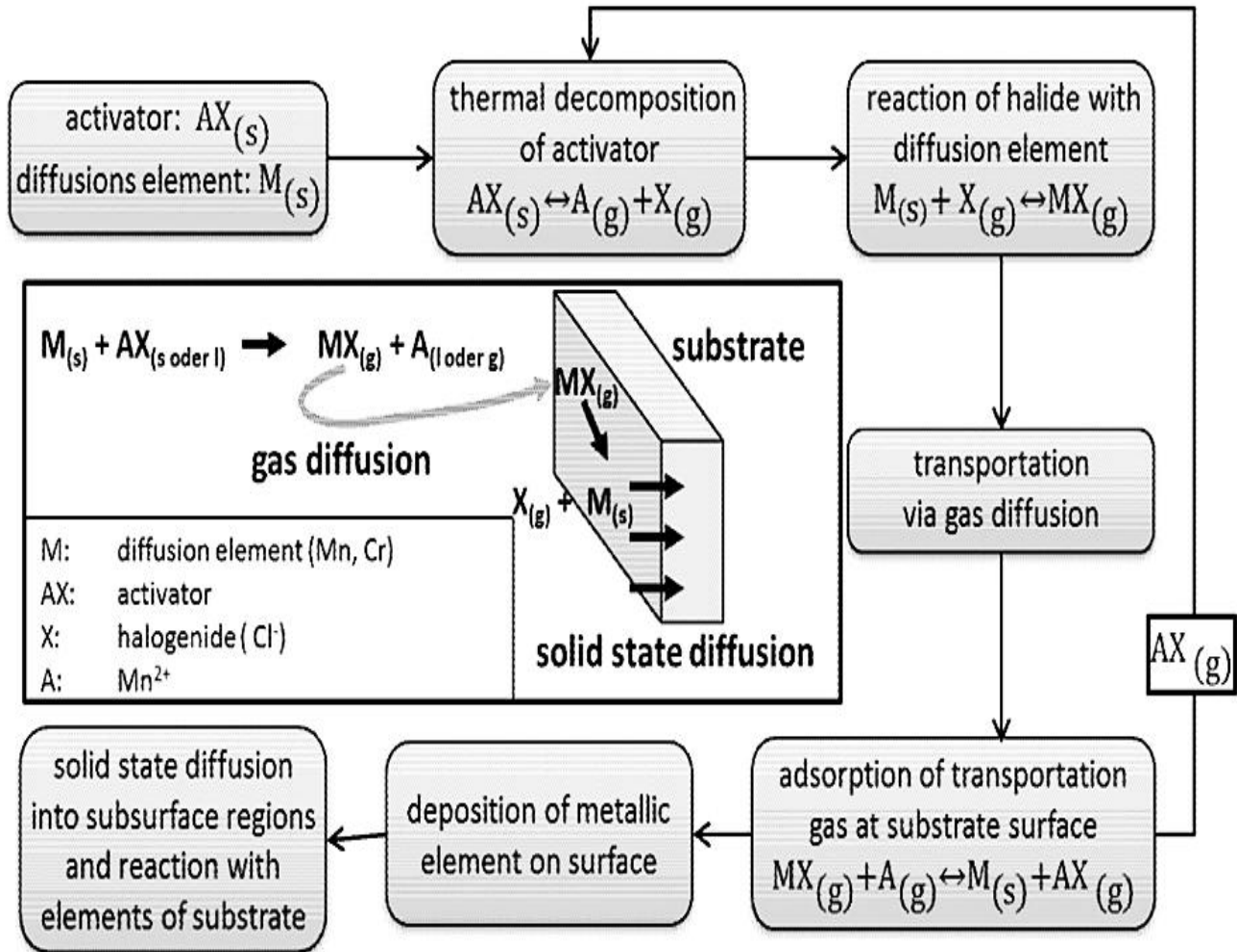


Figure 26 Major steps involved in pack cementation [181].

I. Chromising

Chromising is a surface treatment involving the formation of chromium (Cr) rich surfaces on ferrous based and nickel alloys via diffusion of Cr atoms at high temperatures (≥ 900 °C). The process is widely used for improving the corrosion, wear and oxidation resistance of ferrous based and nickel alloys [183, 184, 186]. Fundamentally, chromising of ferrous based alloys containing less than 0.2 wt. % carbon e.g. stainless steels enhances corrosion and oxidation resistance and is termed called soft-chromising. On the other hand, chromising of alloys with carbon content higher

than 0.2 wt. % enhances wear resistance and is referred to as hard chromising. The resulting chromised layers differ from each other. In soft chromising, the chromised coatings are typically a solid solution of chromium in ferrite (α -iron) while hard chromium carbides are formed in hard chromising processes.

Chromising can be achieved by a number of techniques such as molten salt bath, pack cementation, gas chromising, fluidised beds CVD, vacuum chromising and physical vapour deposition (PVD) process [183, 184, 186]. Among these techniques, chromising by pack cementation otherwise called pack chromising is a simple and inexpensive in-situ CVD process that requires no specialised equipment. In pack chromising, the substrate is embedded in a pack of powders containing pure chromium or ferro-chromium powders as the master alloy, ammonium chloride as the activator and alumina as the inert filler contained in an alumina crucible or heat resistant material and sealed. The sealed crucibles are heated in an inert environment (e.g. argon gas protective environment) or under vacuum in a furnace to the chromising temperature (typically between 900 °C and 1200 °C) [182-184, 186].

The chemical reactions involved in chromising treatment based on the steps shown in Figure 26 are :

1. Thermal decomposition of the activator



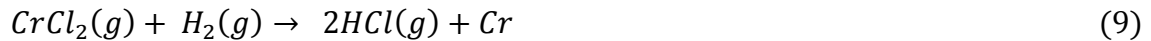
2. Reaction between the halide gas and chromium powder to form volatile halides



3. Dissociation of ammonia



4. Adsorption of transportation gas at the substrate surface



Chromium atoms deposited on the surface of the metal (Equation 9) diffuses inwards into the ferrous based metal. Depending on the carbon content, carbon diffuses outwards from the ferrous metal to react with inwardly diffused chromium to form chromium carbide in iron solution. Also, nitrogen decomposed from ammonia according to Equation 6 reacts with chromium to form chromium nitrides. This chemical reaction is, however, peculiar to pack chromising only.

II. Chromising of stainless steels

As earlier discussed in chapter 2, stainless steel are low cost, corrosion resistant iron based alloys. The structure of stainless steels is determined by its alloying elements which are basically classified into austenite stabilisers (e.g. Nickel, Nitrogen, Carbon) and ferrite stabilisers (Chromium, Molybdenum, etc.). Austenite stabilisers have face centred cubic (FCC) structure while ferrite stabilisers have body centred cubic (BCC) structure as shown in Figure 27. Stainless steels with high amount of austenite stabilisers are called austenitic stainless steel e.g. 300 series stainless steel (AISI 316, AISI 304, AISI 310, AISI 317 etc.) while alloys with high amount of ferritic stabilisers are called ferritic stainless steels e.g. the 400 series stainless steel (AISI 430, AISI 444, AISI 446 etc.).

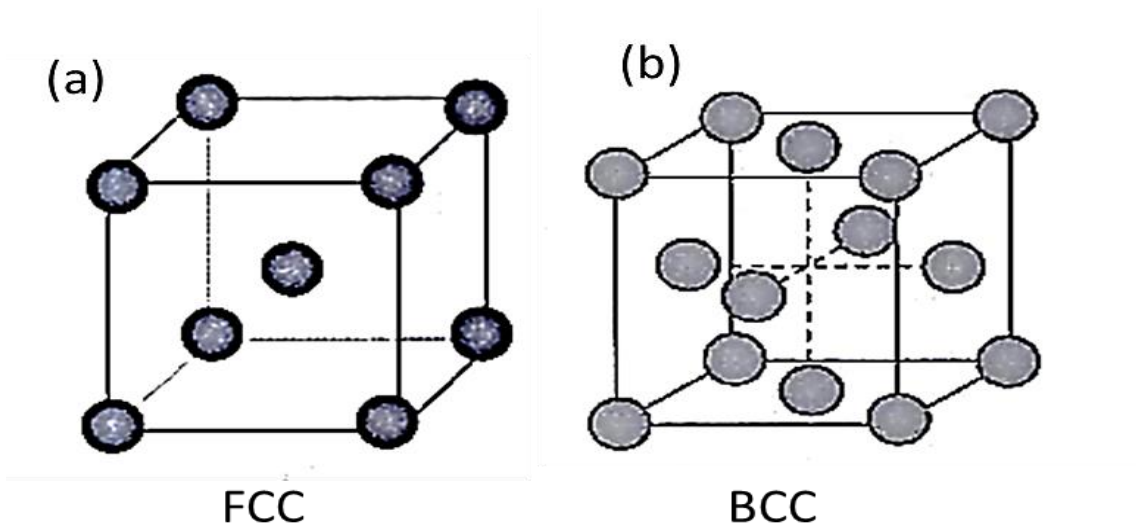


Figure 27 Structure of alloying elements in stainless steel alloys (a) face centered cubic structure (FCC) (b) Body centred structure (BCC) (adapted from [187])

Chromium is a ferritic stabiliser; hence, chromising of austenitic stainless steels involves phase transformation from the FCC structure of austenite to BCC structure of Cr during deposition [183-186,188]. According to Bangaru and Krutenat [188], FCC to BCC transformation in austenitic stainless steels is dependent on the austenite stability of the steels. High austenite stability, which is associated with high nickel content, opposes FCC to BCC transformation resulting in lower coating thickness while low austenite stability engenders higher coating thickness. This fact was evidently demonstrated in the work of Ralston et al. [186] on chromised coatings produced by fluidised Bed CVD wherein AISI316 stainless steel with the highest Ni content among the stainless steel studied exhibited the lowest thickness. Austenite stability of commercial stainless steels can be calculated using empirical equations such as Hammar and Svensson's chromium and nickel equivalents [188,189]. Using this equation, Lopez et al. [189] classified the austenite stability of common austenitic stainless steels in terms of increasing austenite stability as 310 > 309 > 316 > 303 > 304 . Hence, AISI 304 stainless steel was adopted in this study in order to

achieve thicker coated layers which could possibility enhance resistance to corrosion. Also, the performances of chromised 304 stainless steels in simulated and real PEM fuel environments have not reported in the literature before now.

III. Carburisation

Carburisation is the absorption of carbon onto the surface of low carbon steels when heated in a carbon-rich medium. Traditionally, carburisation is conducted at temperatures within the austenitic region in the iron-cementite phase diagram as shown in Figure 28. The essence of carburisation is to harden the surface of the steel against wear and tear. However, the depth of diffused carbon in the treated material otherwise referred to as ‘the case depth’ is dependent on factors such as temperature, time, and composition of the carbon medium etc. [191-193].

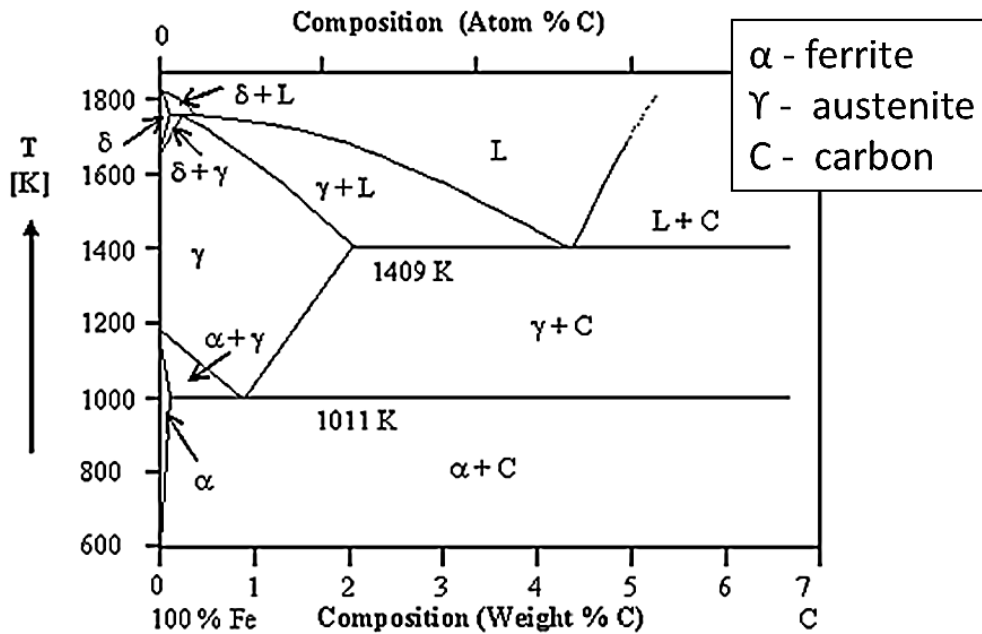


Figure 28 Iron –Carbon phase diagram [190].

Carburisation processes are classified based on the medium of carburising which could be gaseous, plasma, pack, ion beam and salt bath [191-193]. Pack carburisation involves heating the metallic substrate in a pack mixture of a carbon rich material e.g. charcoal, ash etc. and an activator usually a carbonate salt e.g. barium carbonate ($BaCO_3$), sodium carbonate (Na_2CO_3), calcium carbonate ($CaCO_3$). At the carburising temperature, typically above 900 °C, the activator decomposes releasing carbon monoxide needed for the carburisation reaction (Equation 10)



The liberated carbon dioxide gas reacts with carbon in the carboneous material to form carbon monoxide which decomposes at the steel surface (Equation 11-13) to form atomic carbon.



The carburising process depends on the CO/CO₂ ratio; the higher the ratio the higher the carbon potential achieved within the pack and the higher the carbon at the surface of the metal to be carburised. The carburising potential is, however, uncontrollable in pack cementation.

IV. Carburisation of austenitic stainless steels

Austenitic stainless steels are iron based alloys with 10-18% chromium and 8-14 % nickel. This type of stainless steels is widely used for variety of applications due to their good mechanical properties and high corrosion resistance derived from the high chromium content [191, 192]. Carburisation of austenitic stainless steels at high temperatures (> 450 °C) facilitate the formation of chromium carbide precipitates along the grain boundaries and depletes chromium from the steel

matrix thereby degrading the corrosion resistance of the steel. As shown in Figure 29, the formation of carbides at the grain boundaries otherwise called sensitisation is a time-temperature dependent phenomenon, which engenders inter granular corrosion.

In austenitic stainless steel, the $M_{23}C_6$ type carbides, which contain about two to four times chromium than the base metals, are formed [191]. These carbides not only form during at high temperature but also during cooling in high temperatures carburisation. Hence, modern carburisation of austenitic stainless steel is conducted at temperatures below 500 °C and is termed Low temperature carburisation. The low temperature process yields a colossal supersaturated carbon layer [192]. However, pack carburisation at such low temperatures is difficult because the carbon potentials at such low temperature would be too low for carbon deposition [192,193].

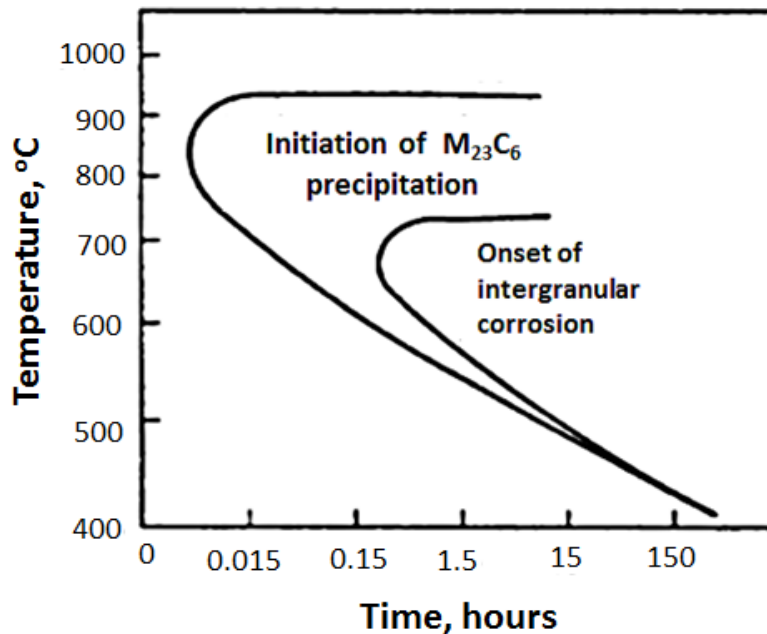


Figure 29 Relationship between $M_{23}C_6$ precipitation and intergranular corrosion in 304 stainless steel (adapted from [191])

(B) Response surface methodology

Response surface methodology (RSM) is a design of experiment (DoE) technique which consists of a collection of mathematical and statistical tools used for designing experiments, developing empirical models and optimising process output(s) influenced by many factors [194-198]. In contrast to classical experimental method, RSM can establish optimal process parameters with fewer experiments and can also deduce interactive effects between process parameters if any. RSM consists of five basic model designs: Box–Behnken design, Central Composite design, Plackett-Burman design, Doehlert matrix and full and fractional factorial design. Among these model designs, Box–Behnken and Doehlert designs are reported to be more efficient than the others. However, Box–Behnken design was adopted in this study because it required fewer experiments and avoids combinations involving extreme conditions of higher or lower levels of factors which could yield unsatisfactory results [194-196].

Box–Behnken designs are a family of rotatable or nearly rotatable three-level second-order designs based on incomplete factorial designs. In Box-Behnken design, the values of the factors are equally spaced and represented as high (+1), centre (0), low (-1). These values can be pictorially represented on a cube as the edge, middle and edge points with a central point as shown in Figure 30 (a) or as three interlocking 2^2 factorial designs with a central point (Figure 30 (b)). The number of experiments required in Box-Behnken designs is given by

$$N = 2k(k + 1) + C_o \quad (14)$$

Where k is the number of factors and C_o is the replicate number of the central point [194-196].

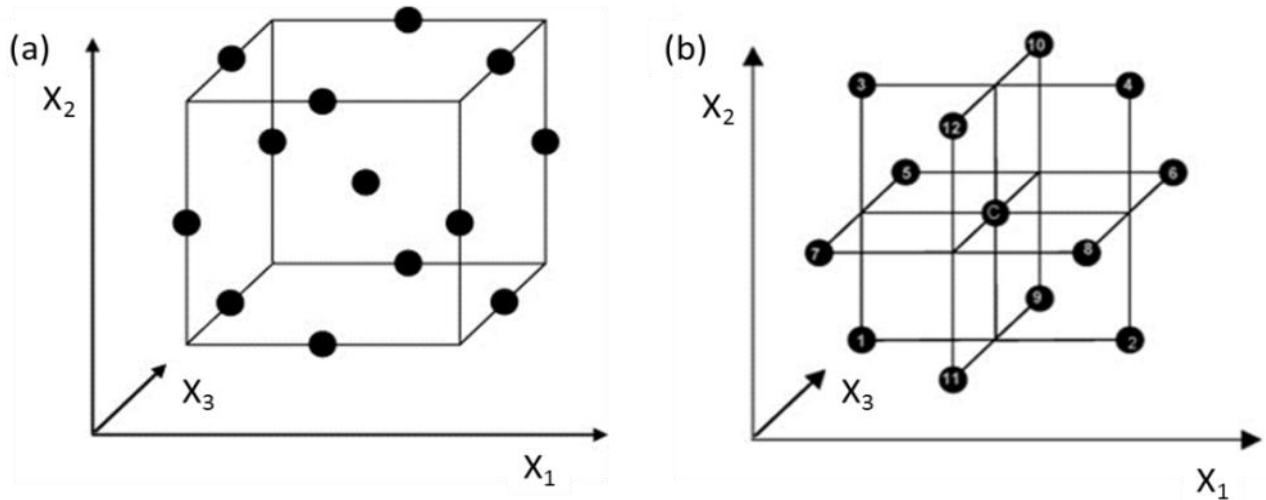


Figure 30 Pictorial representation of Box-Behnken design [194]

Optimisation of anti-corrosion properties of coatings via Box-Behnken designs are increasingly being reported in the literature [199-201]. In the present study, experimental design and statistical modelling as well as optimisation of selected process parameters were conducted with Design Expert statistical software package version 9.0.2.0 (State-Ease Inc., USA). The design matrix was based on three-level, three-factor Box-Behnken design. The selected process variables or factors are presented in Table 7. The variables were coded using Equation 15 and inputted in the design software yielding a design matrix of a total of 17 experiments with 5 centre point replicates as shown in Table 8.

$$x_1 = \frac{X_i - X_0}{\Delta X_i} \quad (15)$$

where x_i is the coded value of the i th process variable; X_i , actual value of the i th process variable; X_0 , actual value of the i th process variable at the central point; ΔX is the step rate change value.

Table 7 Process factors and design levels

Factors	Levels		
	Low (-1)	Centre (0)	High (+1)
Time (hours)	3	6	9
Activator content (wt. %)	3	5	7
Temperature (°C)	1000	1050	1100

The experimental data obtained was thereafter analysed were fitted into in quadratic model defined by Equation 16.

$$Y = \beta_o + \sum_{i=1}^3 \beta_o x_i + \sum_{i=1}^3 \beta_{ii} x_i^2 + \sum_{i=1}^3 \sum_{i<j}^3 \beta_{ij} x_i x_j + \varepsilon \quad (16)$$

where Y is the predicted response, β_o is the coefficient of intercept, β_i is the coefficient of linear effect, β_{ii} is the coefficient of quadratic effect, β_{ij} , is the coefficient of interaction effect, i and j are index numbers for the independent variables and ε is the random error [194-200].

Table 8 Design matrix based on three- level, three –factor Box–Behnken design

Run	Actual values			Coded values		
	Time (Hours)	Activator content (wt%)	Temperature (°C)	Time (Hours)	Activator content (Wt%)	Temperature (°C)
1	6	3	1100	0	-1	+1
2	6	5	1050	0	0	0
3	6	7	1000	0	+1	-1
4	9	5	1000	+1	0	-1
5	3	5	1000	-1	0	-1
6	6	3	1000	0	-1	-1
7	9	5	1100	+1	0	+1
9	6	7	1100	0	+1	+1
10	6	5	1050	0	0	0
11	6	5	1050	0	0	0
12	3	3	1050	-1	-1	0
13	3	7	1050	-1	+1	0
14	6	5	1050	0	0	0
15	6	5	1050	0	0	0
16	9	7	1050	+1	+1	0
17	9	3	1050	+1	-1	0

(C) Materials and Equipment for chromised coating and modification

I. Chromised coatings

25mm x 25mm x 2 mm coupons cut from commercially available AISI 304 stainless steel sheets purchased from Impact Metals Ireland, Dublin, Ireland with nominal composition of 0.08 C, 18-20Cr, 8-10.5Ni, Mn < 2, Si < 1, balance Fe (wt %) were cut into 25 mm x 25 mm coupons. The coupons were ground with silicon carbide abrasive papers and ultrasonically cleansed in acetone after which the samples were dried in air. The coupons were thereafter embedded in a previously ball-milled powder pack of 50 wt. % Cr powder, x wt. % of NH₄Cl and (50 - x) wt. % of alumina where the value of x is as shown in Table 7. The crucibles were sealed with fire clay as shown in Figure 31, cured in a laboratory oven at 60-100 °C for about an average of about 30 minutes in order to solidify the clay. The sealed crucibles were thereafter loaded into a tube furnace (Lenton LTF 1200° C, USA) with an argon gas protective environment (Figure 32). The chromising temperature ranged from coating prepared at 1000- 100 °C for different duration and powder composition as shown in the design matrix (Table 8). After the heat treatment cycle, the chromised samples were cleansed in acetone and dried in open air. The selected parameter was chosen based on preliminary experiments and the literature on chromising of stainless steel [37-39,184]. Further details on selection of process parameters and values can be found in Appendix I.



Figure 31 Picture of crucible containing pack powder mixture of chromium, ammonium chloride and alumina and sealed with fire clay

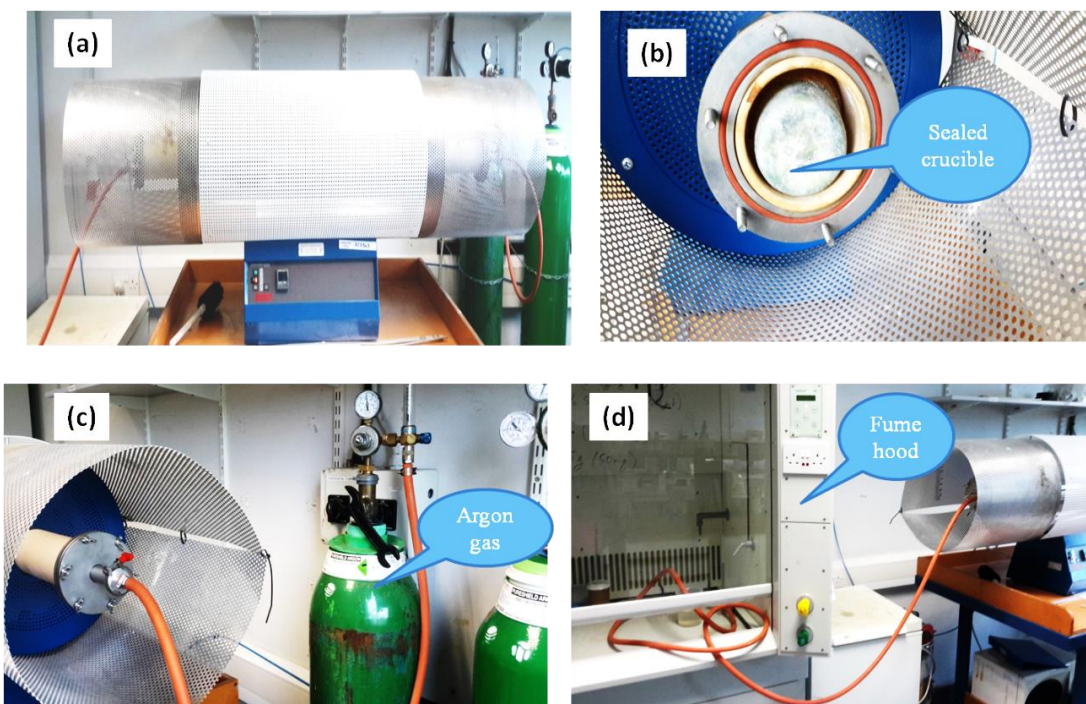


Figure 32 Picture of the pack chromising procedure (a) Lenton tube furnace (b) sealed crucible in tube furnace (c) tube furnace sealed and argon gas is passed through the tube (d) end of the tube connected to the fume hood.

II. Pre-carburised and chromised coatings.

The coupons for pack carburisation were 20 mm x 20 mm x 2 mm in dimension. The surface of the coupons was activated in 4 M hydrochloric acid at 60 °C for 10 minutes and thereafter embedded in a carburising mixture of charcoal and sodium carbonate and sealed with fire clay to prevent air infiltration. The carburising mixture was prepared by dissolving Na₂CO₃ in hot water and gradually adding crushed charcoal powder in 1:2 proportions. The mixture was stirred and exposed to sunlight for 2-3 days to remove any moisture. On drying, the mixture was crushed into powder. Figure 33 shows the picture of the charcoal, sodium carbonate and the resulting mixtures.

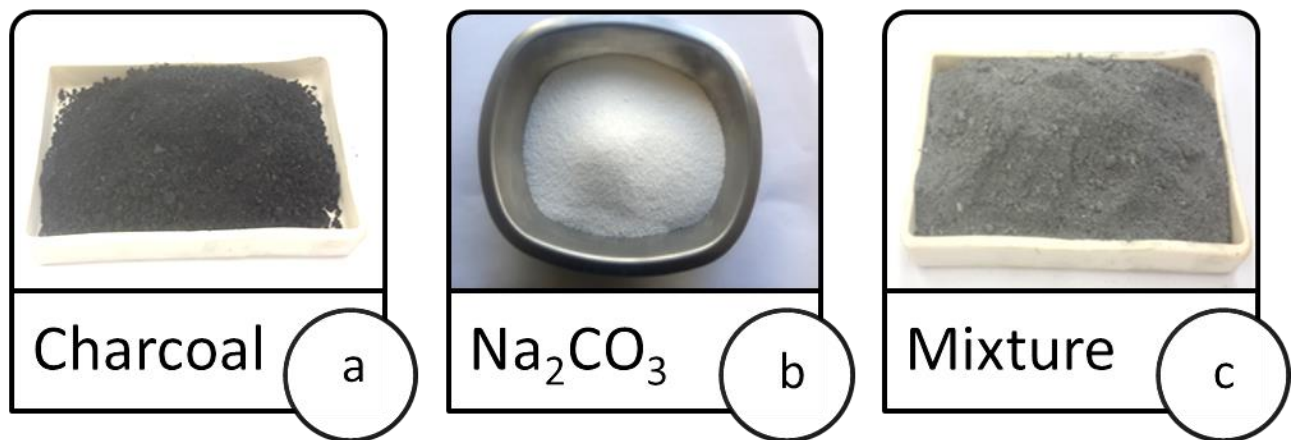


Figure 33 Materials for pack carburising.

The sealed alumina crucibles were heated for 1-3 hours in a muffle furnace (Carbolite, England) preheated to the carburising temperature (925 °C). At the end of each test, the crucibles were taken out of the furnace, forced open by breaking the clay and the samples were quenched in water. All samples were cleansed in acetone, weighed and afterwards chromised at the optimised chromised coating process parameters (i.e. 1040 °C for ~3 hours in powder composition of 50 wt. % chromium powder, 6.84 wt.% ammonium chloride and 42.8 wt. % alumina). After the heat

treatment cycle, the pre-carburised-chromised samples were cleansed in acetone, dried in open air and weighed.

3.3 SURFACE CHARACTERISATION

(A) Scanning electron Microscope

The scanning electron microscope (SEM) is a versatile surface characterisation tool widely employed for surface morphology analysis of crystalline or amorphous samples. When equipped with Energy dispersive X-ray (EDX) spectrometer information on elemental composition, mapping etc. can also be obtained. The working principle in SEM involves the generation of a beam of electrons in the electron gun and accelerating the beam towards a sample via a series of condensers lens or magnetic lens as shown in Figure 34 (a) at a voltage difference (typically between 1-30 V). When the electron beam strikes the sample a couple of signals (electrons, x-rays and photons) are emitted from the sample depending on the depth of penetration of the beam (Figure 34 (b)) and with appropriate detectors the signals can provide the needed information.

The signals relevant to this study were:

- The secondary electrons which are emitted from the surface and provide information on the surface topography
- The backscattered electrons which are reflected from the atoms in the sample and give information on the surface topography based on the atomic number of the elements present on the sample. A typical backscattered electron image will provide information on the distribution of chemical phases in the sample - elements with low atomic numbers would give a darker contrast compared to elements with higher atomic numbers.

- The characteristic X-rays are used in the Energy-Dispersive X-ray Spectrometer (EDX) to provide qualitative and quantitative information on chemical composition and distribution of elements in a sample.

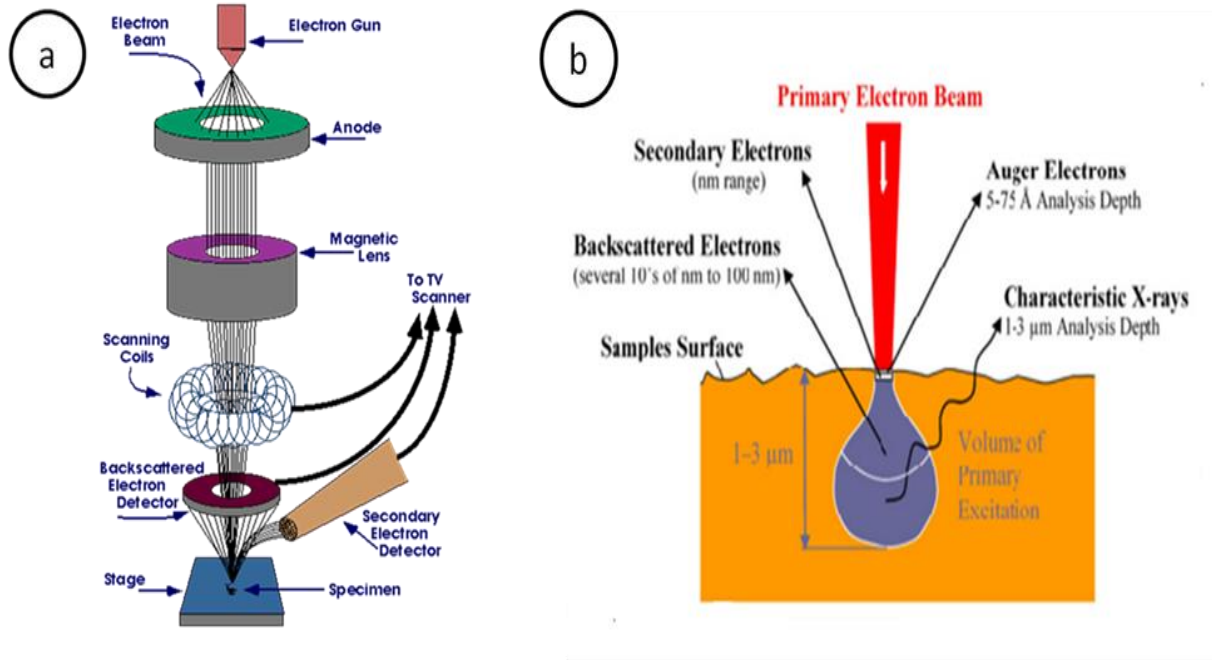


Figure 34 Schematic representations of (a) the operating principles of the SEM [202] (b) Signals produced within the SEM at different depth of penetration [203].

The SEM used in this study was a ZEISS EVOLS 15 SEM equipped with INCA Energy dispersive X-ray (EDX) spectrometer (Oxford instruments). Surface morphologies, cross sectional images, EDX composition, line scans and mapping were obtained at an accelerating voltage of 15 kV. All samples for cross-section imaging except the CoBlast™ treated samples were embedded in Bakelite and metallographically prepared to 0.05 μm finish.

(B) X-ray diffraction

X-ray diffraction (XRD) is a non-destructive surface characterisation tool that works on the principle of constructive interference between a monochromatic x-ray beam and a crystalline material. In this work, XRD was primarily used for phase identification of the coatings produced at the different stages. The X-ray diffractometer used in this study was a D8 Advance Buker XRD with a Cu K α radiation ($\lambda = 1.5405$ nm). When in operation, collimated X-ray beam produced in the cathode tube at 40 KV and 40 mA is accelerated towards the metal sample. The X-ray beam hits the metal sample at an incidence angle of Θ as shown in Figure 35.

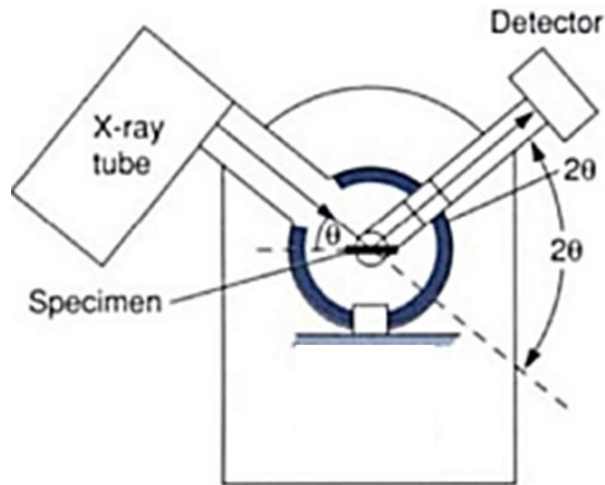


Figure 35 Schematic representation of XRD [204]

When Bragg's law given as:

$$n(\lambda) = 2d \sin\theta \quad (17)$$

Where n is the order of diffraction, λ is the wavelength of the x-ray beam, d is the spacing between atomic planes of the crystalline phase, and Θ is the angle of incidence of the x-ray.

is satisfied, interactions between the incident X-ray beam and the sample produce diffracted X-rays by constructive interference.

The diffracted X-ray is recorded by the detector in form of peaks with different intensities as a function of the diffraction angle 2θ to give a diffraction pattern otherwise called XRD diffractogram, which can thereafter be analysed using standard Joint Committee on Powder Diffraction Standards (JCPDS) database via the Eva software.

In this work, conventional XRD and glancing incidence angle XRD (GXRD) techniques were employed for phase analysis. Conventional XRD as described above is not surface sensitive as it gives bulk phase analysis to a depth of about $10\mu\text{m}$. However, by rotating the detector at angle of incidence ranging from 0.1° to 3° , the depth of penetration of the X-rays can be reduced and surface information about the coatings without significant interference from the substrate can be obtained. This technique is called glancing incidence angle XRD. All scans were conducted in the continuous scanning mode at a speed of $1^\circ/\text{second}$ and scan step of 0.02 from $20^\circ \geq 2\theta \leq 80^\circ$.

(C) X-Ray Photoelectron Spectroscopy

X-Ray Photoelectron Spectroscopy (XPS) also known as Electron Spectroscopy for Chemical Analysis (ESCA) is a surface-sensitive analytical tool used for obtaining elemental and chemical information about the outermost layers of specimen to depth of 0 to 10 nm. In typical XPS experiments as shown in Figure 36, the sample is irradiated with a high energy radiation (typically monochromatic aluminium K_α or magnesium, K_α X-ray) under ultra-high vacuum causing photoelectrons emission from the outermost layer of the specimen. The kinetic energy of the ejected photoelectrons is a function of its binding energy as shown in Equation 18.

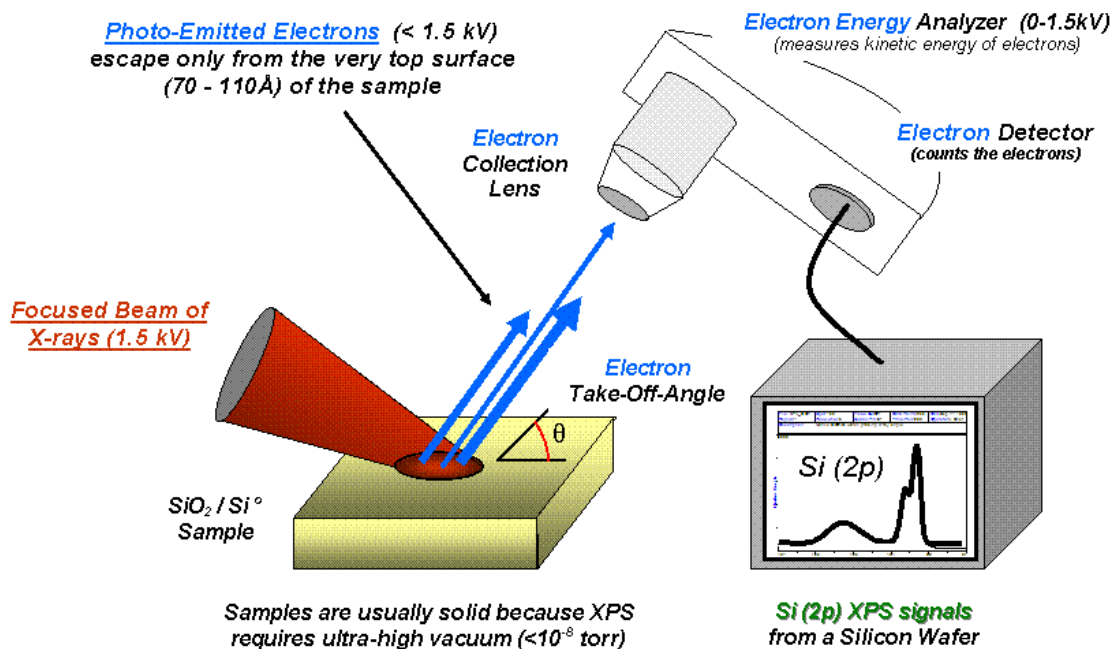


Figure 36 Operating principles in XPS [205]

$$E_K = hv - E_B - W \quad (18)$$

Where E_k is the kinetic energy of the emitted electron, hv is the incident x-ray photon energy, E_B is the binding energy of the electron from a particular energy level, and W is the work function of the spectrometer. The binding energy of the photoelectron, however, depends on the oxidation state and environment of the element which it was ejected from and is a characteristic feature of that element. The intensity of the photoelectron is proportional to its concentration and can be used to determine the concentration of the element associated with that photoelectron in the specimen.

In this study, XPS analyses were accomplished commercially at the Nano Imaging and Material Analysis Centre (NIMAC), University College Dublin (UCD), Ireland and Materials and Surface Science Institute (MSSI), University of Limerick (UL), Limerick. XPS analysis of the CoBlast™

metals were conducted at the NIMAC, UCD with a Thermo ESCALAB 250X while that of the modified CoBlast™ 316 stainless steel was done at MSSI, UL with a Kratos Axis 165 Ultra XPS model. All XPS analysis in phase 2 was done at NIMAC, UCD. All XPS had monochromatic Aluminium X-ray source (Al K_α 1486.6 eV). XPS Spectra were obtained at constant pass energy of 20 eV and 0.05 stepwise unless otherwise stated. Surface composition and survey spectrum as well as narrow region scans of the elements on the coating surface were obtained before and after argon ion sputtering. All spectra were referenced to adventitious C1s set at 284.5 eV unless otherwise stated.

(D) Surface Roughness

Surface roughness of samples in the first stage was conducted with a TR200 portable surface roughness tester. The portable device measures roughness of a flat sample via a sensor with an built-in probe as shown in Figure 37, which uniformly slides across the sample during measurements and roughness values are obtained after digital processing by an in built chip system.

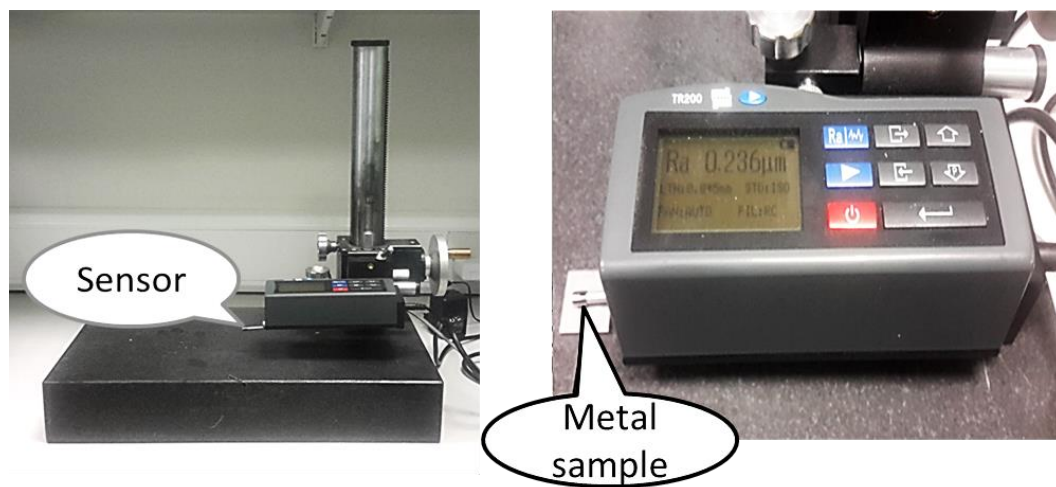


Figure 37 (a) TR200 surface roughness tester (b) close-up view

(E) Contact angle measurement

Water contact angle measurements were conducted with a First Ten Angstroms (FTA° 200) dynamic contact angle goniometer. Contact angles were obtained based on sessile drop principle wherein a defined droplet of water is deposited on a surface via a computer controlled syringe as shown in Figure 38. Only CoBlast™ coated metals were tested.

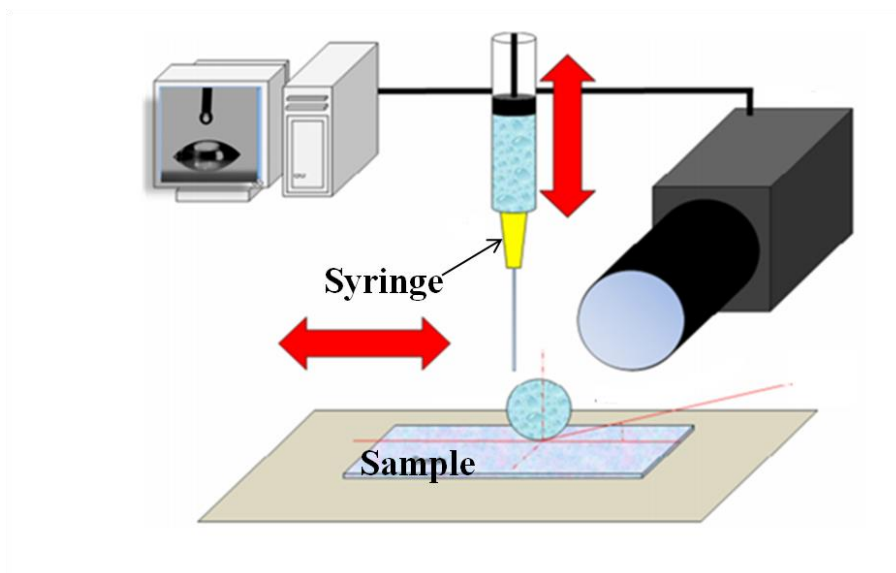


Figure 38 Schematics of water contact angle set up adapted from [206]

3.4 EVALUATION OF CORROSION PERFORMANCE OF COATED METALS IN SIMULATED PEM FUEL CELL ENVIRONMENT.

Corrosion can generally be described as the degradation of materials due to its electrochemical reaction with the environment. The electrochemical nature of corrosion implies that the process involves the transfer of electrons. However, for corrosion to occur, four basic components are required: an anode, a cathode, an electrolyte and an electrically conductive path. These components form an electrochemical cell as shown in Figure 39 [207-210].

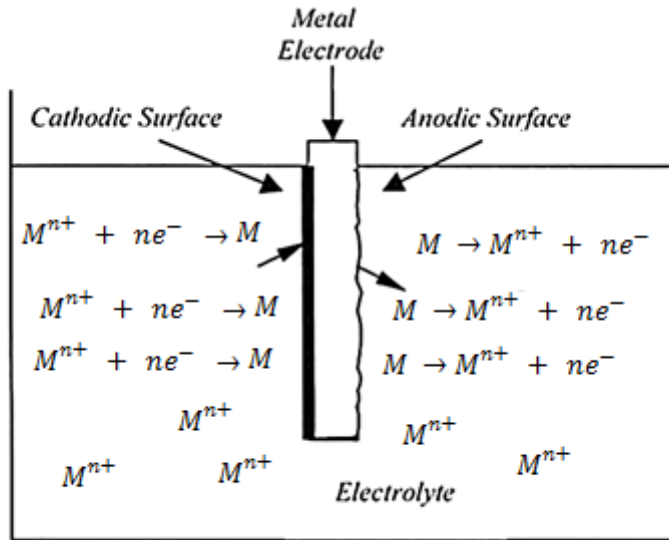
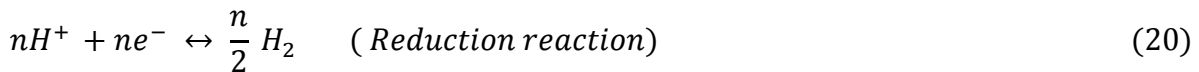


Figure 39 Corrosion cell in action (adapted from [207])

As shown in Figure 39, the metal is oxidized by losing its electrons (Equation 19) while the electrolyte is reduced by accepting the electrons from the metal (Equation 20), the transfer of electrons between the metal and the electrolyte provides a conductive path for the reaction to continue. It can also be seen in Figure 39 that the metal surface acts as both the anode and the cathode at the same time, hence, the metal surface is referred to as a mixed electrode.



The electrochemical nature of corrosion facilitates the application of electrochemical techniques to the study of corrosion rates otherwise called corrosion kinetics, which is fundamentally governed by the Butler–Volmer equation. For an electrode process involving a slow reaction step at the electrode surface (activation polarisation), the relationship between the current density and the electrode potential is given by Butler–Volmer equation (Equation 21) [208- 212].

$$i = i_0 \left[\text{Exp} \left(\frac{\alpha n F}{RT} (E - E_0) \right) - \text{Exp} \left(\frac{-(1-\alpha)n F}{RT} (E - E_{corr}) \right) \right] \quad (21)$$

Where i_0 is the exchange current density at the equilibrium potential E_0 , α is the transfer coefficient (usually 0.5) and n is the number of electrons transferred.

(A) MIXED POTENTIAL THEORY AND ITS APPLICATION TO CORROSION RATE MEASUREMENT

The mixed potential theory was postulated by Wagner and Traud in 1938 and it states that:

(1) Any electrochemical reaction can be divided into two or more partial oxidation and reduction reactions.

(2) The sum of anodic current in an electrochemical reaction must be equal to the sum of cathodic current; hence, there is no accumulation of electric charges.

Based on this theory, the corrosion process represented in Figure 39 the total rate of oxidation is equal to the total rate of reduction. Also, the oxidation and reduction processes can be described by half-cell reactions equations given in Equation 19 and 20 respectively and represented as shown in Figure 40 (a).

For there to be no accumulation of charges, the independent half-cell potentials has to polarise to a single potential called the mixed electrode potential or corrosion potential, E_{corr} as shown in Figure 40 (b).

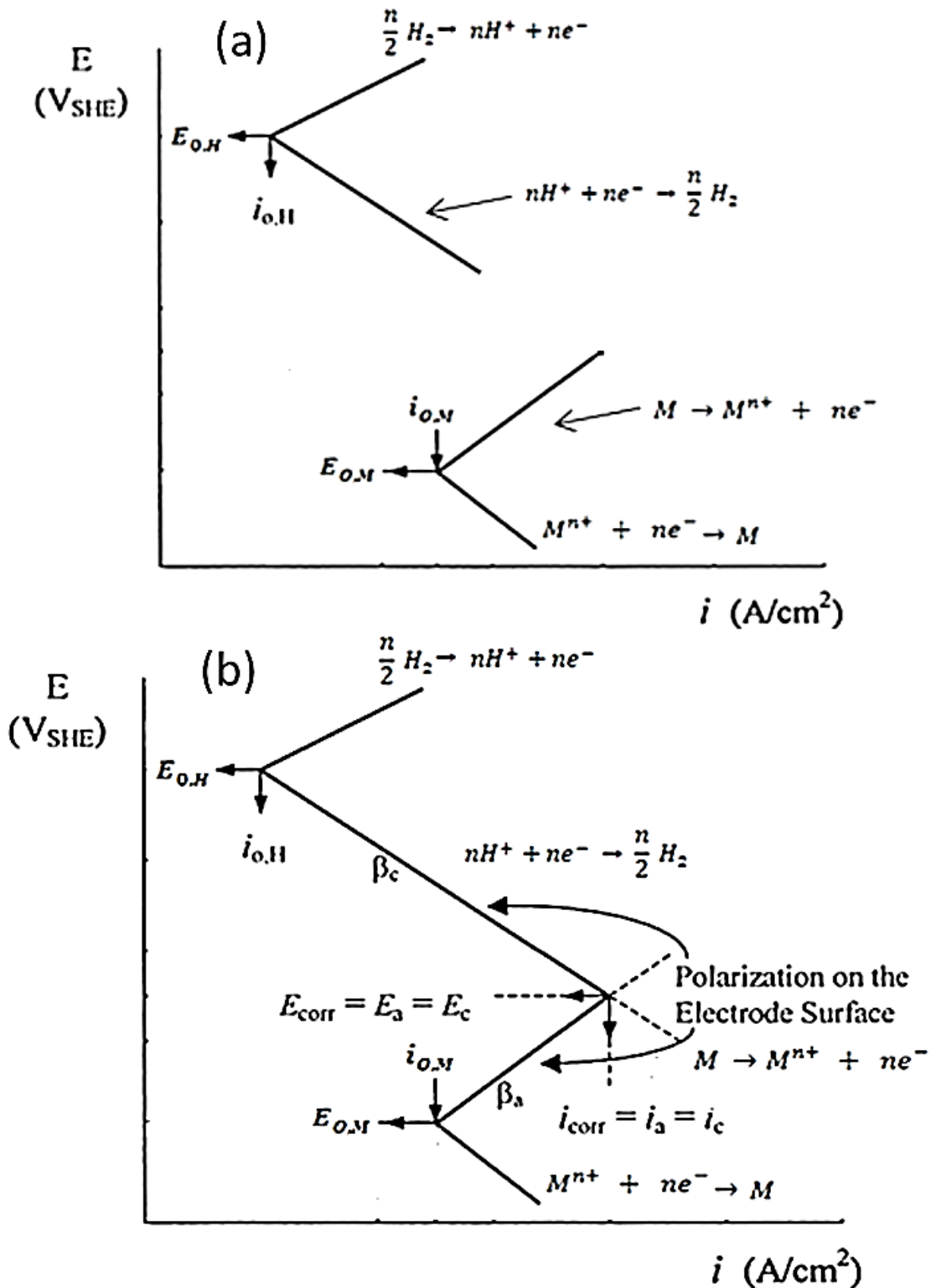


Figure 40 (a) Anodic and cathodic half-cell reactions (b) Evans diagram for a mixed electrode state of a metal, M corroding in an acidic electrolyte [adapted from [207]].

At the corrosion potential, the measurable current ($i_{measure}$) is zero since no current was applied externally. This condition combined with the second premise of the mixed potential theory gives:

$$i_{measured} = i_{oxidation} - i_{reduction} = 0 \quad (22)$$

However,

$$i_{oxidation} = i_{reduction} = i_{corr} \quad (23)$$

Also, when the second premise of the mixed potential theory is fulfilled, the Butler–Volmer equation given in Equation 21 becomes:

$$i = i_{corr} \left[\text{Exp} \left(\frac{\alpha n F}{RT} (E - E_{corr}) \right) - \text{Exp} \left(\frac{-\beta n F}{RT} (E - E_{corr}) \right) \right] \quad (24)$$

Where $\beta = (1 - \alpha)$

When the rate of the back reaction in Equation 19 and 20 is negligible, Equation 23 becomes the Tafel Equation:

$$E = a + b \log i \quad (25)$$

Where a and b are constants

For anodic polarisation

$$a = \frac{(2.3 RT)}{\alpha F} \log i_{corr} \quad (26)$$

$$b = \frac{-(2.3 RT)}{\alpha F} \quad (27)$$

For cathodic polarisation

$$a = \frac{(2.3 RT)}{\beta F} \log i_{\text{corr}} \quad (28)$$

$$b = \frac{-(2.3 RT)}{\beta F} \quad (29)$$

When $E - E_{\text{corr}} = 0$ in Equation 24

Then $i = i_{\text{corr}} = \text{corrosion current density}$. This theoretical frame work is the basis for determination of corrosion current density by Tafel exploration method, illustrated in Figure 41.

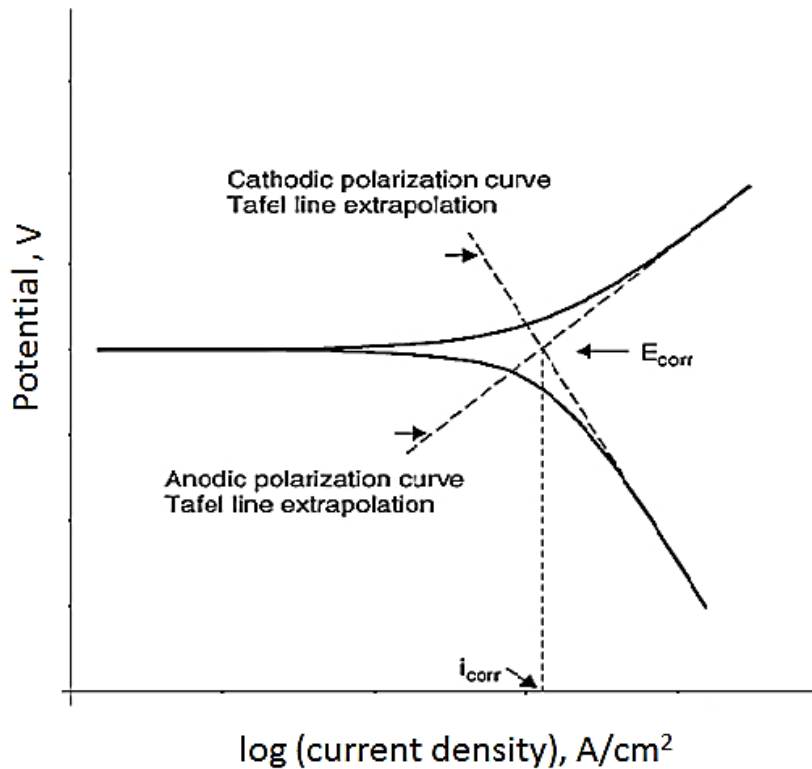


Figure 41 Tafel line extrapolation method (adapted from [209])

Corrosion current density can be determined experimentally by polarizing the electrode about ± 300 mV away from the corrosion potential as shown in Figure 41, otherwise called Tafel plot. The value of corrosion current density can be obtained by extrapolating the linear portion of the curve as shown in Figure. The linear portion of the curve otherwise called the Tafel region is often within 100 mV away from the corrosion potential, E_{corr} , after which Tafel region can be extended due to concentration polarisation and IR drops. Hence, determination of corrosion current by extrapolation may be difficult [210- 212]. Another limitation of the Tafel plot is that the metal surface can be destroyed during polarisation due to high voltage employment for polarisation.

Stern and Geary developed a new approach to corrosion rate measurement which overcomes the limitation of the Tafel plot method. The technique, which is called polarisation resistance, is based on the principle that within ± 10 mV from the corrosion potential, the applied current is a linear function of the electrode potential. Hence, the plot of over-potential against current density is approximately linear and the slope of the plot gives the polarisation resistance [210-212].

Polarisation resistance is related to corrosion current density by the Stern and Geary-equation, which is given as:

$$R_p = \frac{b_a b_c}{2.3 i_{corr} (b_a + b_c)} \quad (30)$$

Where b_a and b_c are anodic and cathodic Tafel slopes, and R_p is the polarisation resistance.

3.4.1 MATERIALS AND METHODS USED IN THE STUDY FOR CORROSION

ASSESSMENT

(A) Electrolyte used in the study.

The selected simulated PEM fuel cell environment in this study was 0.5 M H₂SO₄ + 2 ppm HF solution. H₂SO₄ acid was chosen based on the fact that the membranes are pre-treated in H₂SO₄ acid. Hydrofluoric acid was selected as a source of fluoride ion as it is reported that water by-product of PEM fuel cell contains trace amount of fluoride ions, leached from the membrane [65,213]. Fluoride salts such as NaF, KF were not chosen as a source of fluoride ion to avoid possible contamination and solubility problems as well as simulate the Nafion membranes, which will be used for the single fuel cell tests. It is however, noted that 0.5 M H₂SO₄ + 2 ppm HF is quite aggressive as it had been recently shown that the actual PEM fuel cell environment is slightly acidic with pH range of 3-4 [214].

The electrolyte was prepared in a fume hood by adding 56 ml of 95 wt.% concentrated sulphuric acid (H₂SO₄) to 2 litres of deionised (DI) water after 8 µl of 98 wt. % concentrated Hydrofluoric acid (HF) was added to the sulfuric acid. All acids were purchased from Sigma Aldrich, Ireland. Precautionary measures taken during acid preparation can be found in Appendix II.

(B) Potentiodynamic and Potentiostatic Polarisation

Corrosion behaviour and long term performance of coated metals for bipolar plate application are well reported to be evaluated by potentiodynamic and potentiostatic polarisation techniques respectively [21-23, 37-40]. Hence these techniques were adopted in this study.

All polarisation experiments were conducted in a flat corrosion cell (model K0235, Princeton Applied Research, USA) using a conventional three electrode system comprising of the coated or uncoated samples as the working electrode, Ag/AgCl (saturated KCl) as the reference electrode, platinum mesh as the counter electrode. As shown in Figure 42, the working electrode was pressed against a Teflon ‘O’ ring exposing 1cm^2 of the working electrode to the electrolyte, $0.5\text{ M H}_2\text{SO}_4 + 2\text{ ppm HF}$. The counter electrode was located 80 mm away from the working electrode. On the other hand, the reference electrode was positioned in the Luggin capillary with its tip very close to working electrode to minimise solution resistance between the reference electrode and the working electrode. Solution resistance could lead to ohmic drop leading to error in the potential difference measured between the two electrodes.

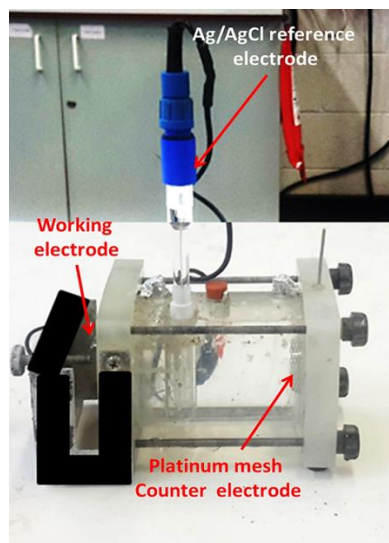


Figure 42 Flat corrosion cell and the electrodes used in the study.

(I) Phase 1: CoBlast™ samples

Polarisation experiments in the first phase were conducted at the FOCAS Institute, Dublin Institute of Technology (DIT), Ireland using a Solartron SI 1287/1255B system comprising of a frequency

analyser and potentiostat. The samples were stabilised at open circuit potential (OCP) for 15 minutes, after which potentiodynamic polarisation was conducted at a scanning rate of 1 mV/s from a potential range of -1 V vs. OCP vs +1 V (Ag/AgCl) at room temperature. Potentiostatic polarisation was conducted at -0.1 V (Ag/AgCl) and 0.6 V (Ag/AgCl) to simulate the anode and cathode operating conditions respectively for four hours. For both polarisation experiments, the electrolyte was bubbled thoroughly either with hydrogen gas or with air prior to and during the experiments. For potentiostatic polarisation, the corrosion cell was immersed in a water bath to raise the temperature of the electrolyte to 70 °C (Figure 42) in order to simulate the working temperatures of PEM fuel cells. The experimental set up was thereafter enclosed in a faraday cage to minimise noise.

Polarisation of the modified CoBlast samples was conducted with a CHI 630C potentiostat (CH Instruments, USA) in Dublin City University (DCU), Ireland. Potentiodynamic and potentiostatic polarisation were conducted at 70 °C using similar procedure as described for CoBlast™ samples. However, only the cathode PEM fuel cell environment was investigated. Potentiodynamic polarisation was conducted at -0.3 V vs. OCP vs 1.2 V (Ag/AgCl).

(II) Phase 2: Chromised coatings

Chromised 304 stainless steels samples were exposed to the electrolyte for 3 hours at 70 °C prior to polarisation measurements. OCP was measured for 15-30 minutes and Tafel polarisation was conducted at ± 0.3 V (Ag/AgCl) vs. OCP at 1 mV/s using CHI 630C potentiostat (CH Instruments, USA). Corrosion potential (E_{corr}) and corrosion current density (i_{corr}) were evaluated by the Tafel analysis software in the CHI software. Tafel polarisation of the optimised sample was carried out using the same experimental procedure.

Potentiodynamic and potentiostatic polarisation of the optimised coating was conducted with Gamry Interface 1000™ potentiostat/galvanostat. Potentiodynamic polarisation was conducted at 1mV/s from -0.1 V (vs. Ag/AgCl) to 1.2 V (vs. Ag/AgCl) from Open circuit potential (OCP). Potentiostatic polarisation was conducted at -0.1 V (vs. Ag/AgCl) with hydrogen gas bubbling and 0.6 V with air bubbling for 180 minutes to simulate PEM fuel cell anodic and cathodic working potentials respectively. The scanning rate for the potentiostatic experiments was 1 mV/s.

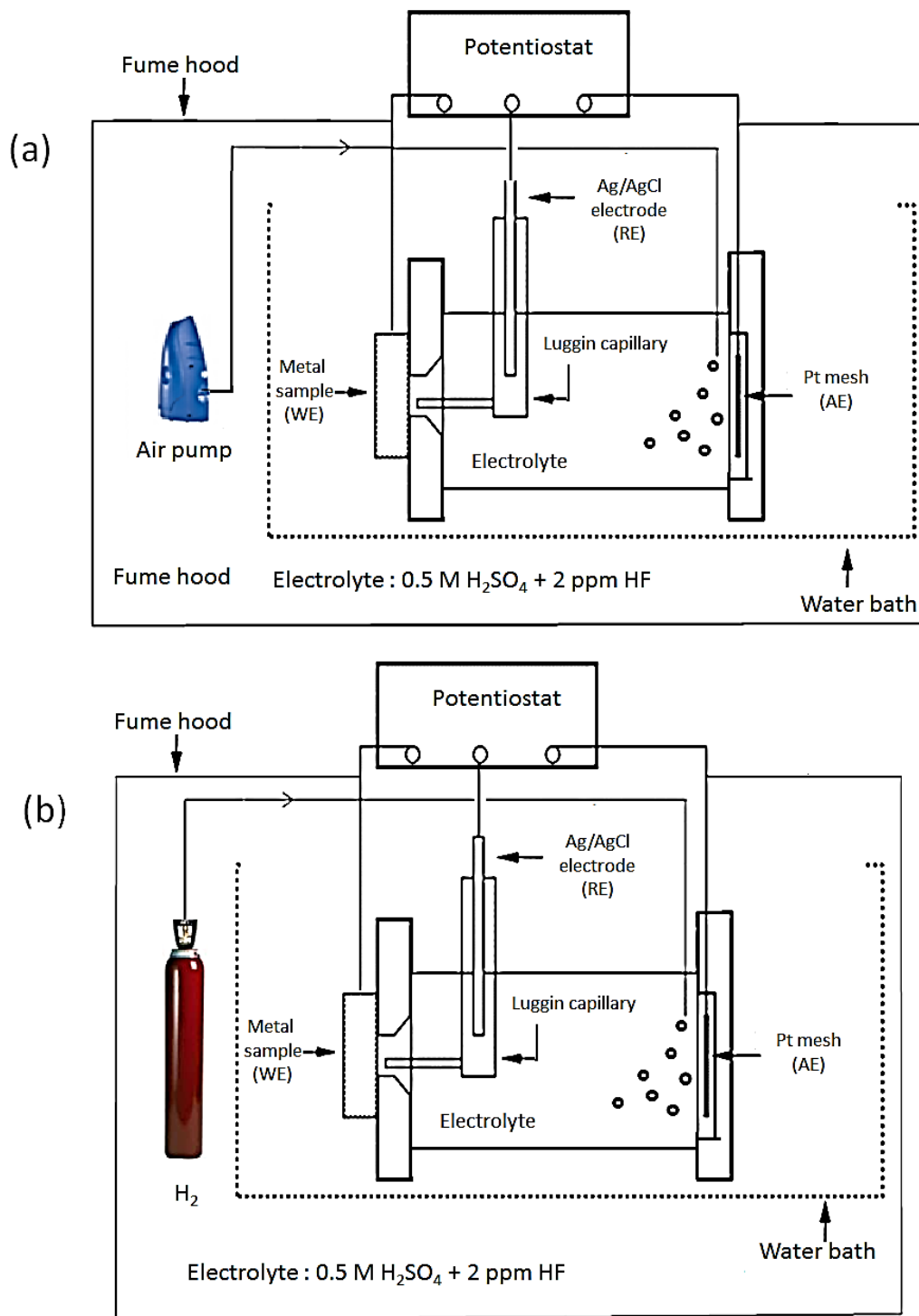


Figure 43 Schematic representation of experimental set up for electrochemical polarisation experiments. (AE: Auxiliary electrode, WE – Working electrode, RE – Reference electrode)

(III.) Pre-carburised and chromised stainless steel samples

Potentiodynamic polarisation of pre-carburised stainless steel samples was conducted after 10 minutes OCP measurement at 1 mV/s from -0.1 V (vs. Ag/AgCl) vs. OCP to 1.2 V (vs. Ag/AgCl) vs. OCP at 70°C using a Gamry Interface 1000™ potentiostat/galvanostat. All polarisation experiments were repeated at least twice, in some cases (potentiostatic polarisation) they were repeated up to five times to ensure reproducibility of the results. Experiments were set up as shown in Figure 43 while Figure 44 and Figure 45 shows pictures taken at different stages of the experiment in DIT and DCU respectively. Precautionary measure taken during all experiments involving HF acid can be found in Appendix II.

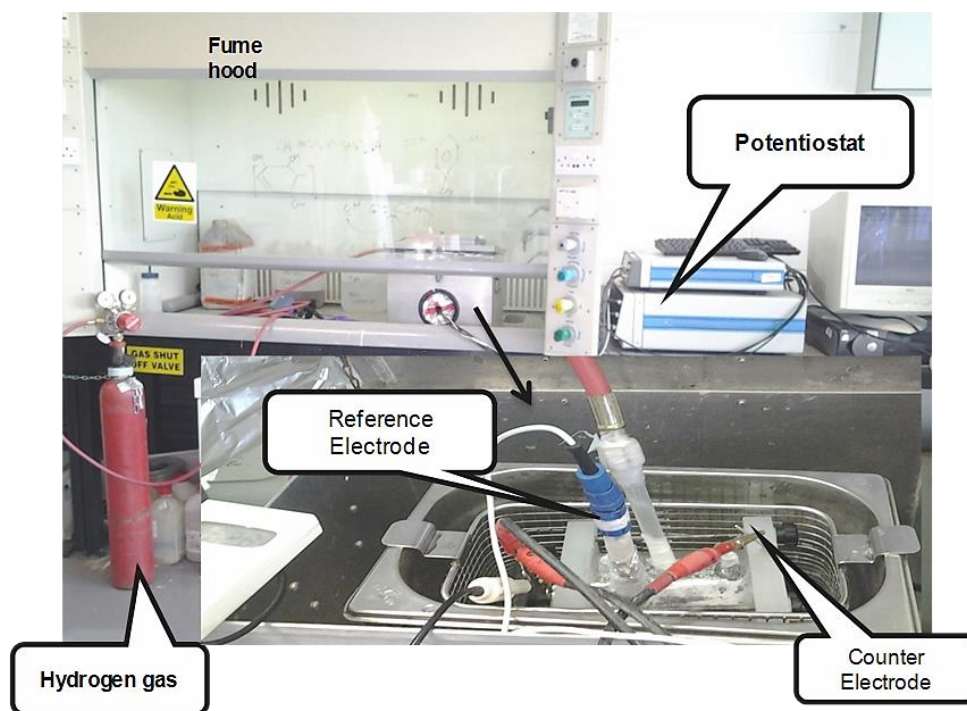


Figure 44 Experimental set up at FOCAS Institute, Dublin Institute of Technology, Ireland.

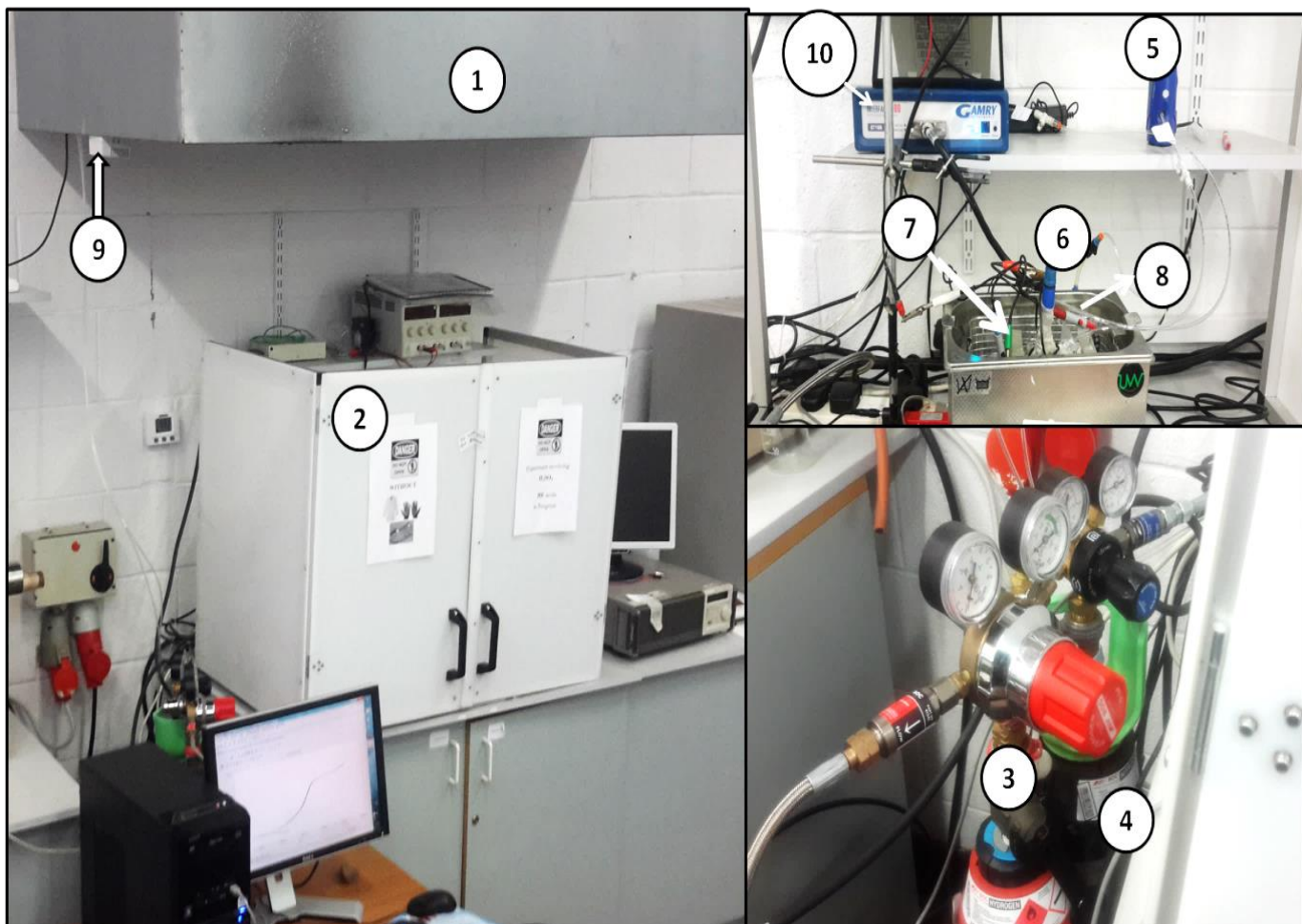


Figure 45 Experimental set up at Dublin City University, Ireland (1) extraction hood (2) polyethylene frame with danger signs (3) H₂ gas cylinder (4) N₂ gas (5) air pump (6) Reference electrode (7) working electrode (8) counter electrode (9) H₂ leak sensor (10) Gamry potentiostat.

(IV) Inductively Coupled Plasma Mass Spectrometry

The concentration of metallic ions leached in the electrolyte after 4 hours of potentiostatic polarisation for CoBlast™ samples was analysed commercially using an Agilent 7700C Inductively Coupled Plasma Mass Spectrometry (ICP-MS) at the Centre for Microscopy Analysis (CMA), Trinity College, Dublin. The test was conducted for CoBlast™ samples only.

3.5 INTERFACIAL CONTACT RESISTANCE MEASUREMENT

Interfacial conductivity of all samples was evaluated by a well-documented method developed by Davies et al. [60] and modified by Wang et al. [58]. The experimental set up for the measurement is schematically represented in Figure 46. The set up consisted of two of pieces of Toray Teflon treated carbon paper (Fuel cell store, USA, or Fuel cell Earth, USA) sandwiched between the bipolar plate material and two copper electrodes. A direct current of 0.5 A (CoBlast™ samples) or 1.0 A (chromised samples and pre-carburised and chromised samples) was supplied to the copper electrodes via a XHR 300-3.5 DC power source. The voltage drop across the setup shown in Figure 46 was measured with a Tektronix DMM912 digital multimeter while the compression forces was gradually applied by a ZwickRoell Universal tensile testing (UTS) machine controlled by a computer. The experimental set up used for ICR measurements is shown in Figure 47.

The total resistance (R_1) across the set up in Figure 46 (a) was calculated using ohm's law multiplied by the surface area of the samples (Equation 31)

$$R = \frac{VA_s}{I} \quad (31)$$

Where R is the electrical contact resistance in ohms (Ω), V is the voltage drop in volts (V), I is the current applied in Amperes (A), A_s is the surface area in cm^2 . The surface area of the samples for ICR measurements in this study was dependent on capacity of the load cell of the UTS machine employed. As-received CoBlast had a surface area of 2.25 cm^2 and the load cell of the

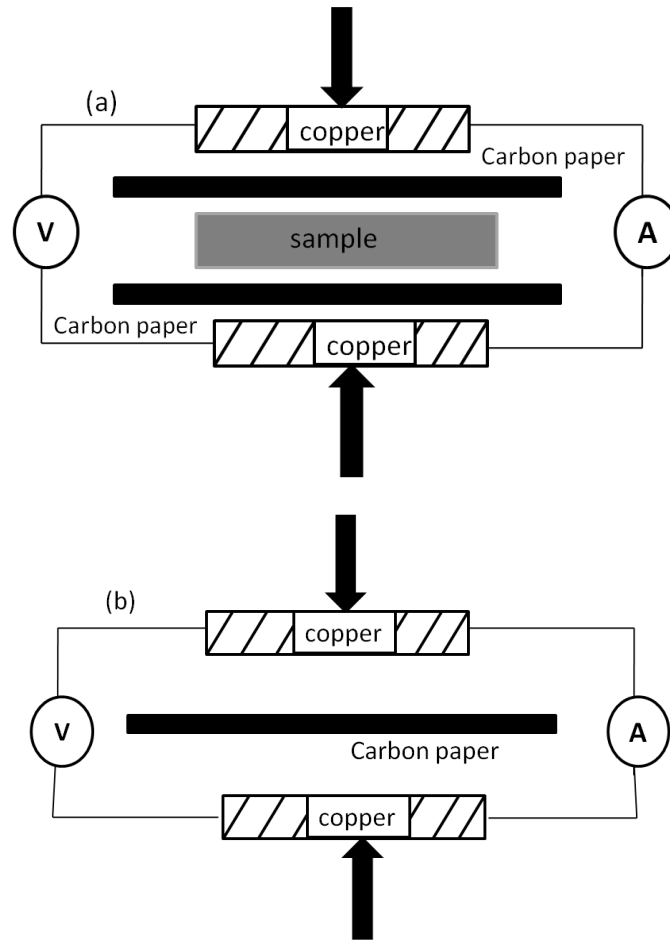


Figure 46 Schematic of the test assembly for interfacial contact resistance.

UTS machine was 500 N. However, the load cell of the UTS machine was later replaced with a 5 kN load cell and the sample size of the chromised and pre-carburised then chromised samples were changed to 4 cm² to accommodate 25 N/cm² step change in the compaction pressure as against the 16 N/cm² change with the CoBlast™ metal samples.

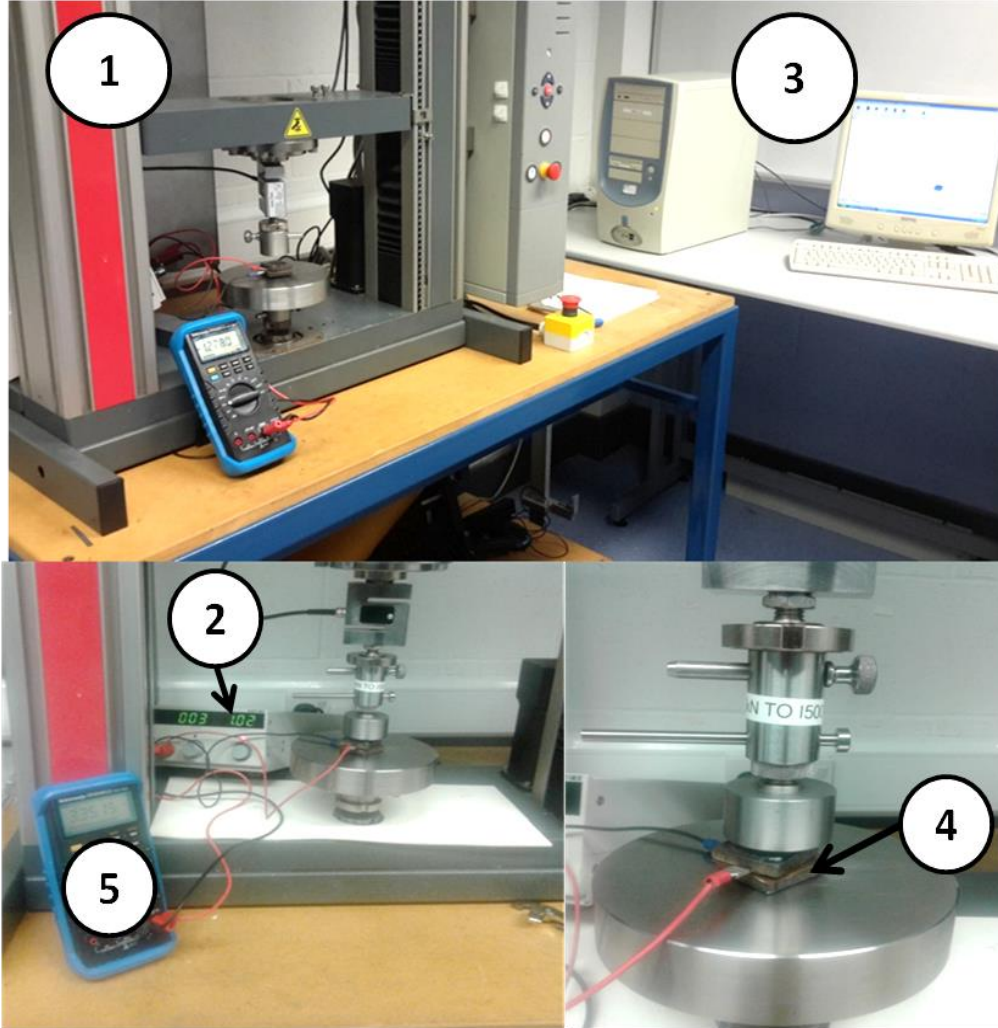


Figure 47 Picture of experimental set up for ICR (1) ZwickRoell UTM (2) power source (3) computer (4) copper electrodes (5) multi-meter.

Based on Equation 31, the total resistance (R_1) across the setup is given as:

$$R_1 = 2R_{Cu} + 2R_{Cu/c} + 2R_{C/m} + R_m + 2R_c \quad (32)$$

Where $R_{C/Cu}$ is the contact resistance between carbon paper/copper plate interfaces, $R_{C/M}$ is the contact resistance between carbon paper and the metal sample, R_M , R_C and R_{Cu} represent the bulk resistance of the metal sample, carbon paper and copper electrodes respectively. In order to find

$2R_{C/M}$, The total resistance(R_2) across another set up shown in Figure 46 (b) and made up of a piece of carbon paper sandwiched between two copper plates was used. R_2 is given by:

$$R_2 = 2R_{C/cu} + R_c + 2R_{Cu} \quad (33)$$

Therefore,

$$2R_{C/m} = R_1 - R_2 - R_m - R_c \quad (34)$$

Assuming the bulk resistance of the metal (R_m) and carbon paper (R_c) are negligible then

$$2R_{C/m} = R_1 - R_2 \quad (35)$$

Therefore, ICR between the sample and carbon paper is given by Equation 36

$$R_{C/m} = \frac{1}{2}(R_1 - R_2) \quad (36)$$

3.6 SINGLE FUEL CELL PERFORMANCE EVALUATION

Three pairs of bipolar plates 35mm x 35mm x 2mm with serpentine flow field designs as shown in Figure 48 were fabricated in-house at the School of Mechanical & Manufacturing Engineering workshop, Dublin City University (DCU).The plates were prepared as shown in Table 9 and

assembled into three single cells with a commercially available MEA (Fuel cell store, USA) with an active area of 5 cm² (Figure 48). The single fuel cells were secured using six bolts at a compaction pressure of 125 N/cm² using the procedure described for ex-situ ICR measurement in section 3.4.

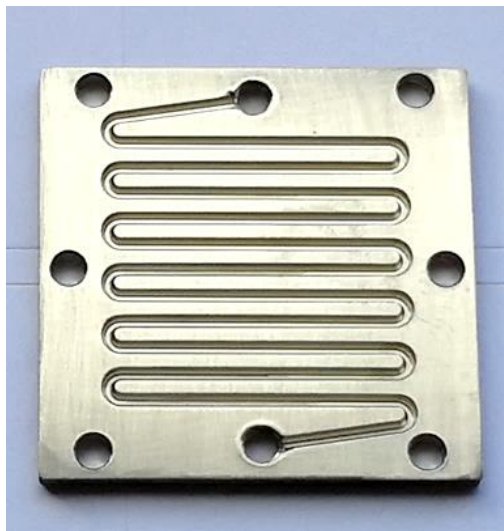


Figure 48 304 stainless steel bipolar plate with serpentine flow field design.

Table 9 Preparation methods for Materials used for the bipolar plates

Sample	Designation	Treatments
Bare 304 stainless steel	SS304	Slightly polished with SiC paper (grade 600)
Chromised 304 stainless steel	Cr-304	Chromised at 1040 °C for 3 hours (slightly polished to remove residue alumina particles)
Pre-carburised and chromised stainless steel	CPC-304-3	Pre-carburised for 3 hours and chromised at 1040 °C for 3 hours (slightly polished to remove residue alumina particles)



Figure 49 The three single cells investigated in this study.

Each single fuel cell was connected to hydrogen and compressed air gas lines and purged with nitrogen gas before cell operation. Humidified hydrogen gas and compressed air were thereafter supplied to the cell at gas flow rates of 50ml/min. Single cell experiments were performed at room temperature and the cell temperature was monitored. Cell voltage as a function of current density was evaluated and power density of the cells were calculated using Equation 37.

$$\text{Power density} = \text{Cell current density} \times \text{Cell voltage} \quad (37)$$

The single fuels cells were thereafter tested for durability for ten hours using chronoamperometry via a Gamry Interface 1000™ potentiostat/galvanostat. After the durability test, the cells were dismantled and the GDLs were characterised with SEM/EDX. Figure 50 gives a picture of the single cell testing station at the School of Mechanical & Manufacturing Engineering, Dublin City University, Ireland.

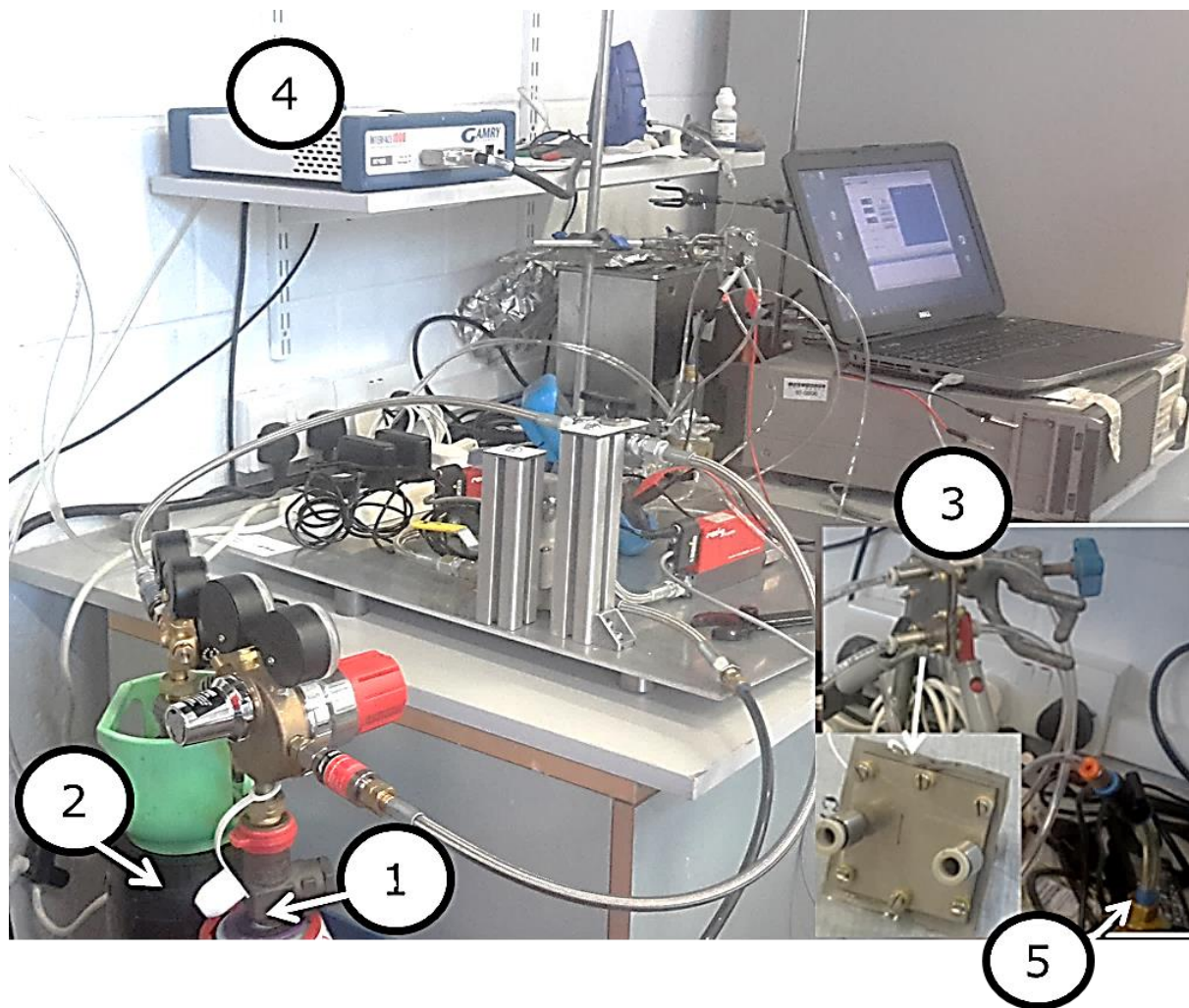


Figure 50 Experimental set up for single cell fuel testing. Hydrogen gas cylinder (1), Nitrogen gas cylinder (2), single fuel cell (3), potentiostat (4), humidifier (5).

3.7 SUMMARY

In this chapter, a description of the material, methods and equipment utilised in the study has been presented. Four types of coatings were produced as shown in Figure 51. These coatings were surface characterised and tested in simulated PEM fuel cell environment of 0.5 M H_2SO_4 + 2 ppm HF. Interfacial contact resistance of the coatings was also evaluated. The flow chart presented in Figure 51 gives a summary of the experimental methodology.

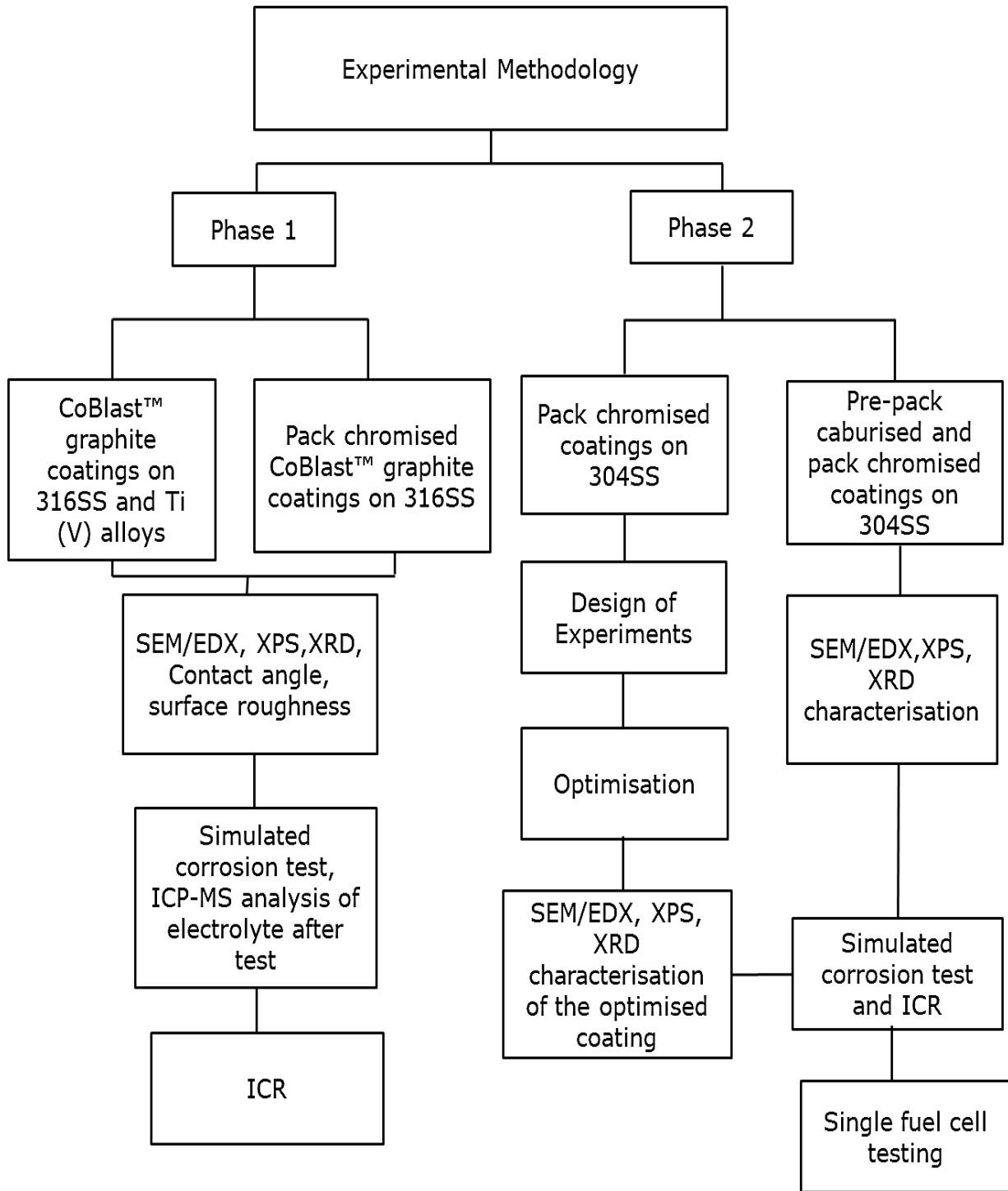


Figure 51 Summary of the experimental methodology employed in the study.

CHAPTER 4

Graphite Coatings deposited by CoBlast™ Technology

4.1 INTRODUCTION

In this chapter, the characterisation and performance evaluation for the suitability of CoBlast™ coated metals for PEM fuel cells bipolar plates are presented and discussed

4.2 SURFACE CHARACTERISATION

(A) Surface morphology and cross section.

Figure 52 presents the surface morphologies of CoBlast™ graphite/alumina coated 316 stainless steel and titanium grade (V) alloys, hereafter designated as Gr-SS and Gr-TiV respectively.

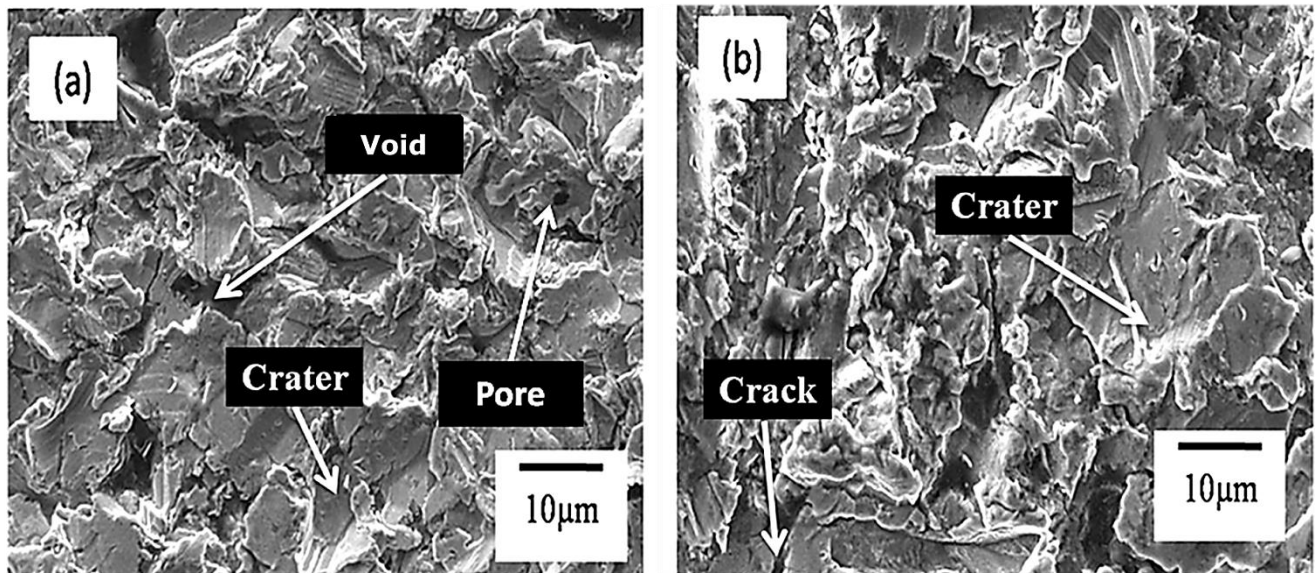


Figure 52 Surface morphologies of Gr-SS and Gr-TiV.

Rough morphologies characterised by craters, cracks and other surface defects can be observed for both Gr-SS and Gr-Ti due to the blasting nature of the deposition process. In the CoBlast™ process, similar to conventional micro blasting or grit blasting process, the kinetic energy of the abrasive powder particles during blasting at high pressures (620 kPa) induces localised substrate surface oxide layer deformation resulting in the formation of craters, dimples and other surface defects. However, in contrast to conventional blasting processes, the underlying reactive metals bonds with the coating material (the dopant) in the powder mixture to form a thin coated layer as shown in Figure 53.

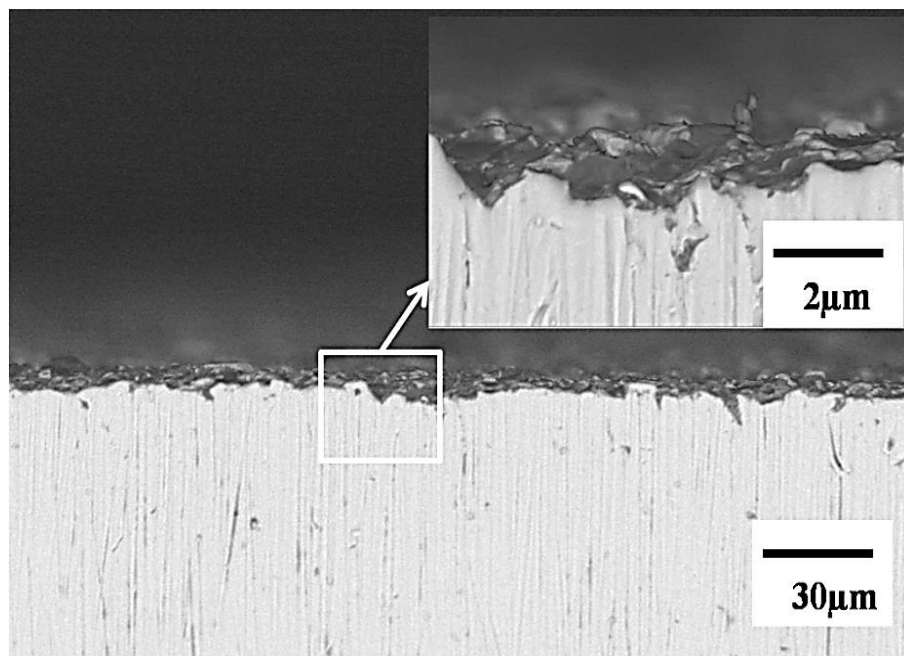


Figure 53 Cross section of CoBlast graphite coated stainless steel. Similar thin and discontinuous coated layer was obtained for graphite coated titanium grade (V) alloy.

Figure 54 and 55 presents the backscattered SEM image of the surface of Gr-SS and Gr-TiV respectively. Combining these morphologies with the inset of Figure 53, it can be deduced that the graphite/alumina coatings were discontinuous. EDX analysis of the morphologies shown in Figure 54 and 55 indicated that the surfaces consisted of isolated pockets of carbon rich phase (interpreted as graphite based on EDX analysis which showed over 90% carbon) and Al-O rich phases (interpreted as a mixture of alumina) heterogeneously dispersed in an iron-chromium (Fe-Cr) rich matrix for 316 stainless steel and titanium- oxygen (Ti-O) rich matrix for titanium grade (V) alloy.

The discontinuous nature of the graphite coatings could be related to the low density of graphite relative to that of alumina. The likely relationship between the densities of the powders and the nature of the coatings could be justified by comparing the cross-sections of CoBlast™ graphite coatings (Figure 53) and CoBlast™ deposited hydroxyapatite (HA) coatings (Figure 56) [175] on Ti grade (V) alloy.

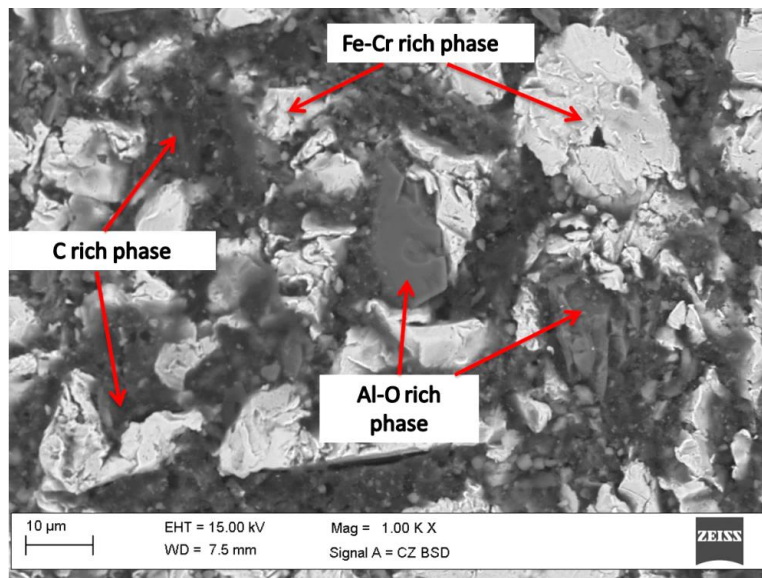


Figure 54 SEM/ BSD of graphite coated AISI 316 stainless steel.

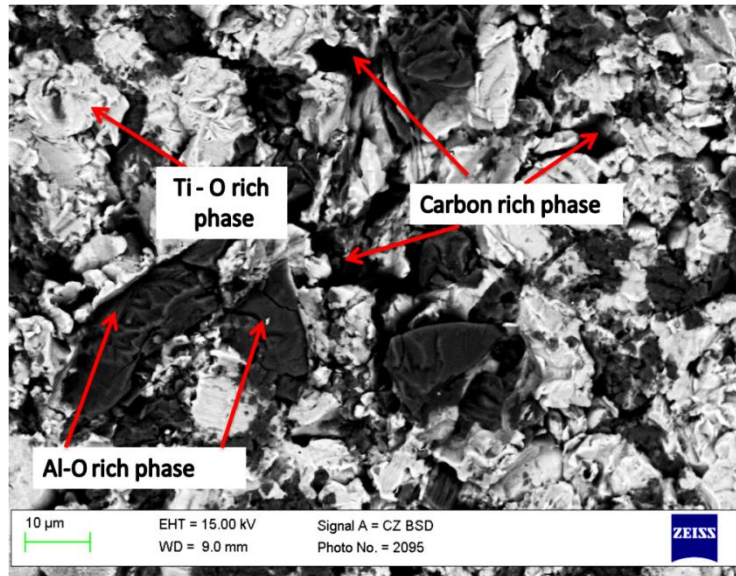


Figure 55 SEM/BSD view of the surface morphology of graphite coated titanium grade (V) alloy.

In contrast to the thin and discontinuous layer formed in Gr-TiV, a dense and continuous coated layer of HA with an average thickness of 8 μm was formed on the same metallic alloy as seen in Figure 56. Hence, it can be concluded from these results that the capability of the CoBlast™ process to deposit coatings from powder phase may be limited to certain powders.

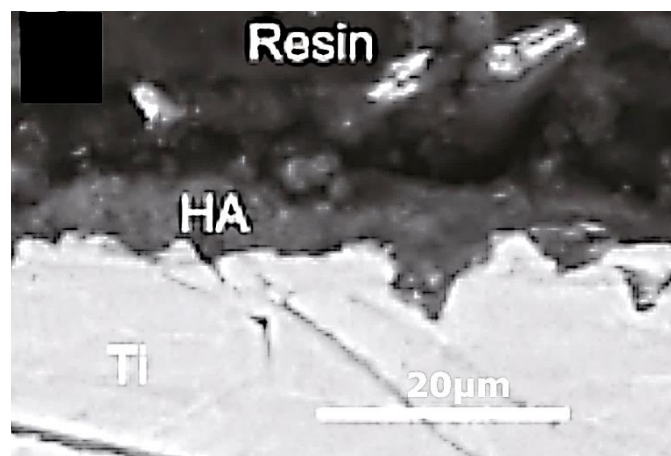


Figure 56 Cross section of CoBlast HA coating on Ti (V) alloy [175].

(B) Surface roughness and contact angle

Table 10 compares the surface roughness and contact angles of the CoBlast™ coated metals and uncoated substrates. It can be seen in Table 10 that CoBlast™ coated metals exhibit significant increase in surface roughness (R_a) and contact angles. The increase in R_a is attributed to the plastic deformation induced by blasting of particles under high pressure. Increasing the surface roughness is also well known to reduce the wettability of a surface, hence the increase in contact angle of the treated samples [215-217]. A similar increase in contact angle was reported for CoBlast™ deposited Teflon coatings on titanium (V) alloy [177] while a decrease in contact angle was reported for HA coated titanium (V) alloy [175,176]. This trend suggests that the nature of the dopant material may have significant effect on the wettability of CoBlast™ modified surfaces. Also, this observation is consistent with the fact that chemical composition of a surface can influence its wettability [215].

Table 10 Surface roughness and contact angle of coated and uncoated surfaces.

Material	Gr-SS	Bare Stainless steel	Gr-TiV	Bare TiV
Surface roughness, R_a (μm)	1.34	0.20	1.59	0.34
Contact angle ($^\circ$)	100.00	65.00	99.63	66.32

(C) XPS analysis.

XPS survey spectra of the outermost layer of Gr-SS and Gr-TiV as well as that of the uncoated substrates is presented in Figure 57 and Figure 58 respectively. Figure 57 reveals the presence of Fe2p, Cr2p, C1s, O1s and Ni2p for both Gr-SS and the uncoated substrate. The presence of Al2p peak in the spectrum of Gr-SS is attributed to alumina. Similarly, Gr-TiV and the bare substrate showed similar Ti2p, O2p, V2p, C1s, Al2p, N1s, and Si2p peaks (Figure 58). However, the spectrum of Gr-SS shows additional peak of Si2p which was also present in the spectrum of Gr-TiV with a higher intensity suggesting that Si could be considered as an impurity probably from the graphite powder. The spectrum of TiV also shows the presence of Fe2p peak which could still be regarded as impurities from the graphite powder. The presence of C1s and O1s peaks with higher intensity in the coated samples than that of the substrate in Figure 57 and Figure 58 is attributed to the presence of graphite and substrate oxide and/or alumina respectively. This observation is consistent with the compositional analysis given in Table 11 which indicates that Gr-SS and Gr-TiV consisted mainly of carbon, aluminium and oxygen evidenced by an increase in the concentration of these elements, compared to that of the substrate after treatment. The presence of carbon on the substrate is related to the presence of a thin layer of adventitious carbon common to XPS analysis.

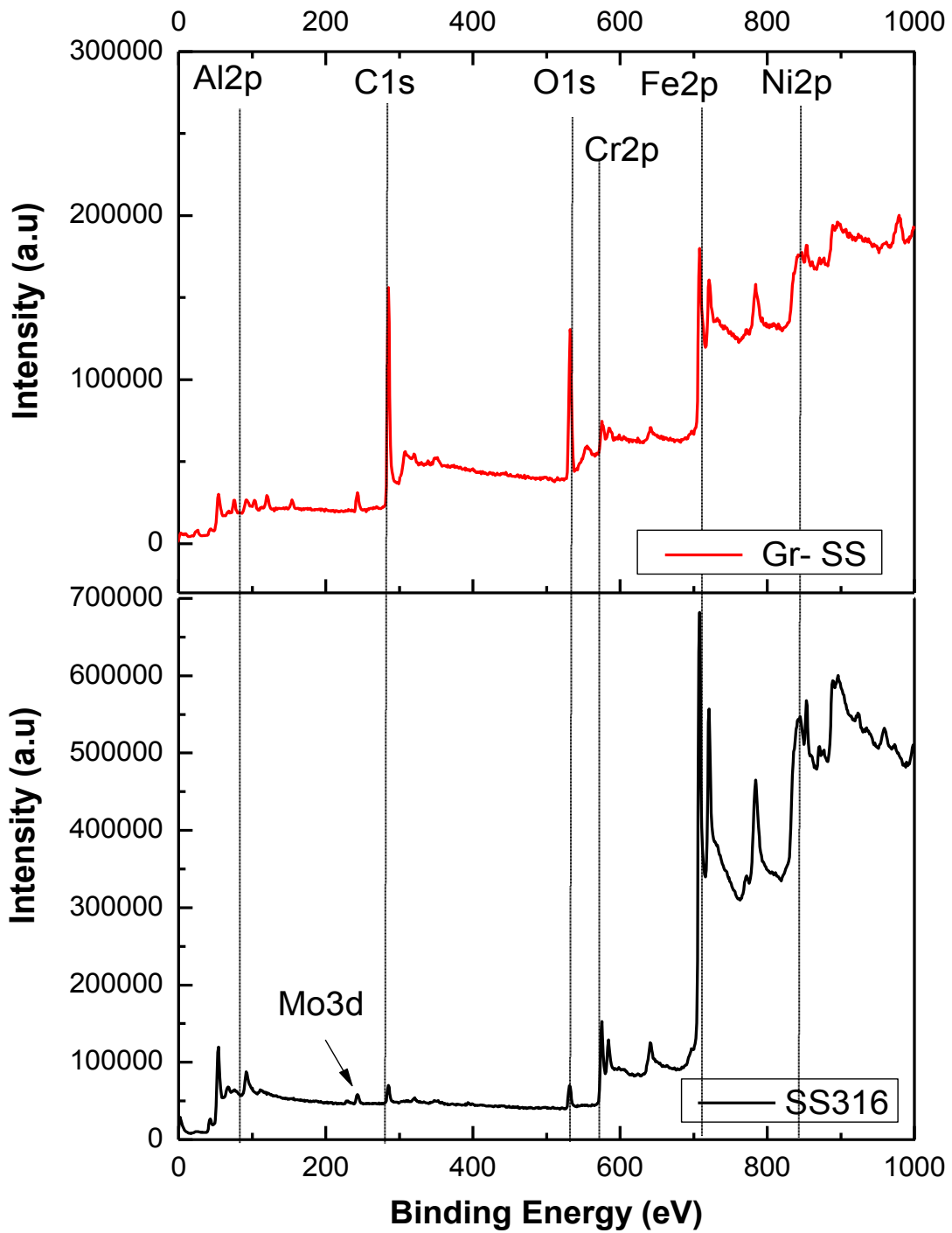


Figure 57 Survey spectra of coated (Gr-SS) and uncoated 316 stainless steel.

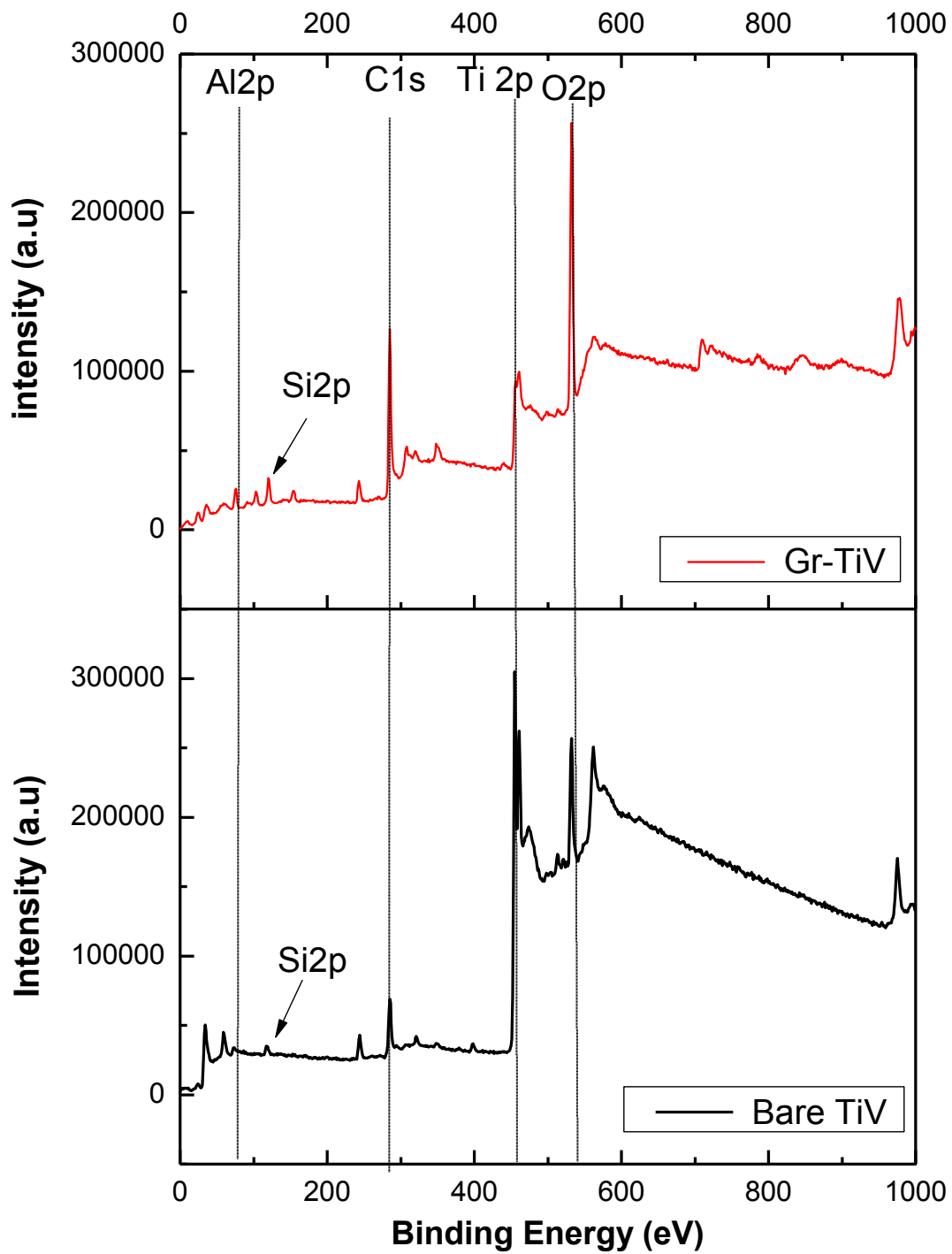


Figure 58 Survey spectra of coated (Gr-TiV) and uncoated titanium (V) alloys.

Table 11 XPS Chemical composition (atomic %) of the outer layer for the coated and uncoated metals.

(a)

Material	C	Al	O	Fe	Cr	Ni	Mo	Si
Gr-SS	58.7	5.5	18.7	11.2	2.0	0.7	-	2.4
Bare stainless steel	15.0	-	7.6	63.4	9.3	3.7	0.3	-

(b)

Material	C	Al	O	Ti	V	Si	N	Fe
Gr-Ti	43.8	8.6	32.1	6.5	1.3	4.1	1.4	2.3
Bare titanium	29.5	4.1	26.5	34.4	1.7	0.5	3.3	-

Figure 59 shows the XPS narrow region scan of the main elements in Table 11. The presence of graphite on the outermost layer of both Gr-SS and Gr-TiV is confirmed by a symmetric peak at 284.48 eV (Figure 59 (a)) corresponding to carbon sp^2 electrons in graphite [218]. Al2p peak at a

binding energy of 75.28 eV corresponds to the aluminium in alumina (Figure 59 (b)) while O1s peak at 532 eV and 531.8 eV for Gr-SS and Gr-TiV respectively corresponds to the presence of metal oxides (Figure 59 (c)).

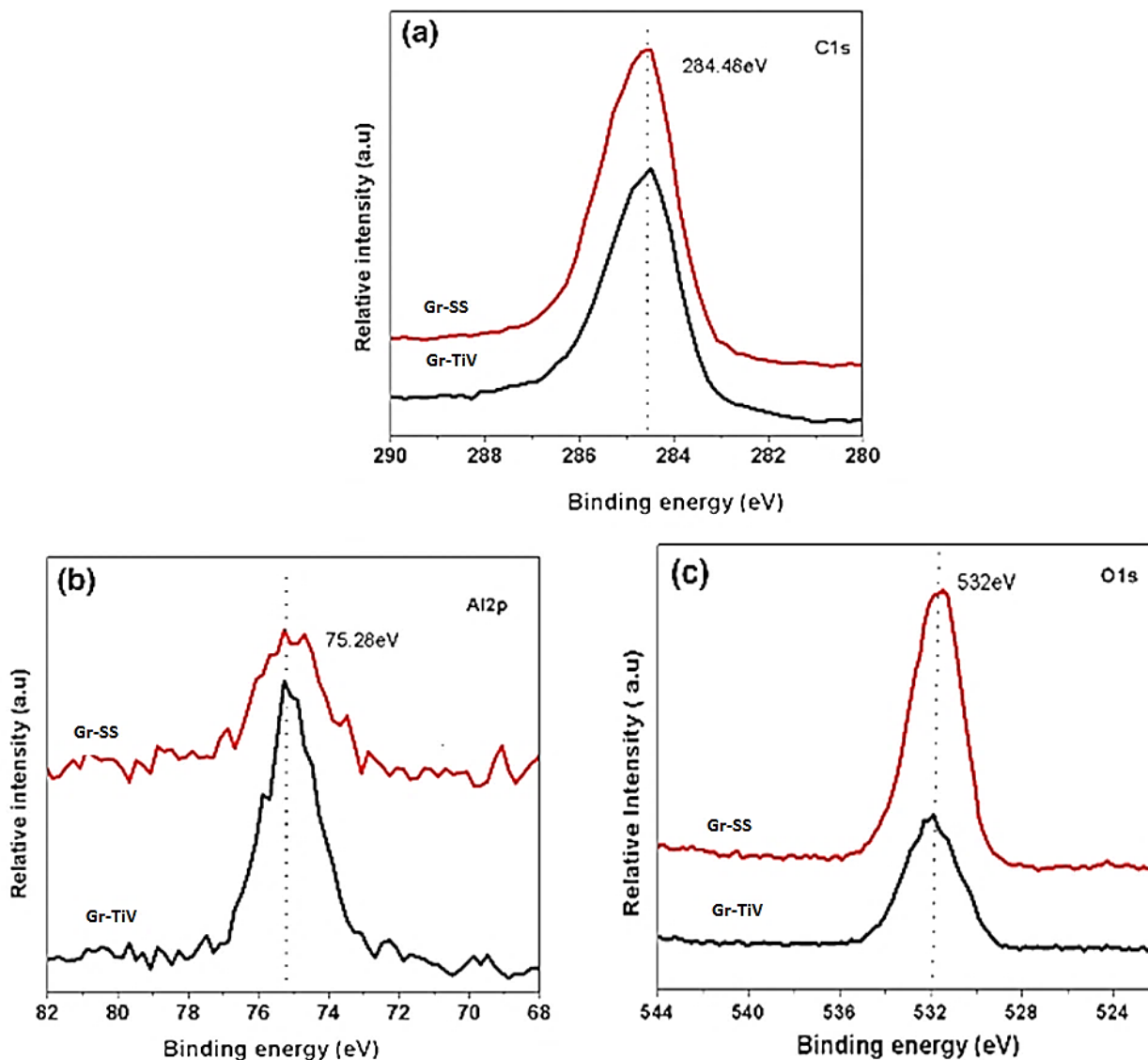


Figure 59 XPS narrow scan region for (a) C1s (b) Al 2p and (c) O1s for Gr-SS and Gr-TiV.

Figure 60 displays the narrow scan region of Cr2p, Fe2p for Gr-SS and Ti2p for Gr-Ti. In Figure 60 (a), the Cr2p spectrum for Gr-SS indicates the presence of Cr₂O₃ at ~577 eV and 586.65 eV as well as metallic chromium at 574.55 eV and 583.85 eV [218-220]. Similarly, the Fe2p spectrum

also shows the presence of metallic Fe (707.08 eV and 720.28 eV) and Fe₂O₃ (710.6 eV, 723.8 eV) [218, 219, 221]. Combining these spectra with that given in Figure 59 for Gr-SS, it can be deduced that the Gr-SS surface consisted of graphite/ alumina coatings on an exposed substrate layer, which is consistent with the SEM analysis. A similar conclusion can also be made for Gr-TiV based on the combination of and Figure 59 and 60 (c), which shows the presence of metallic Ti and Ti oxides [218, 222].

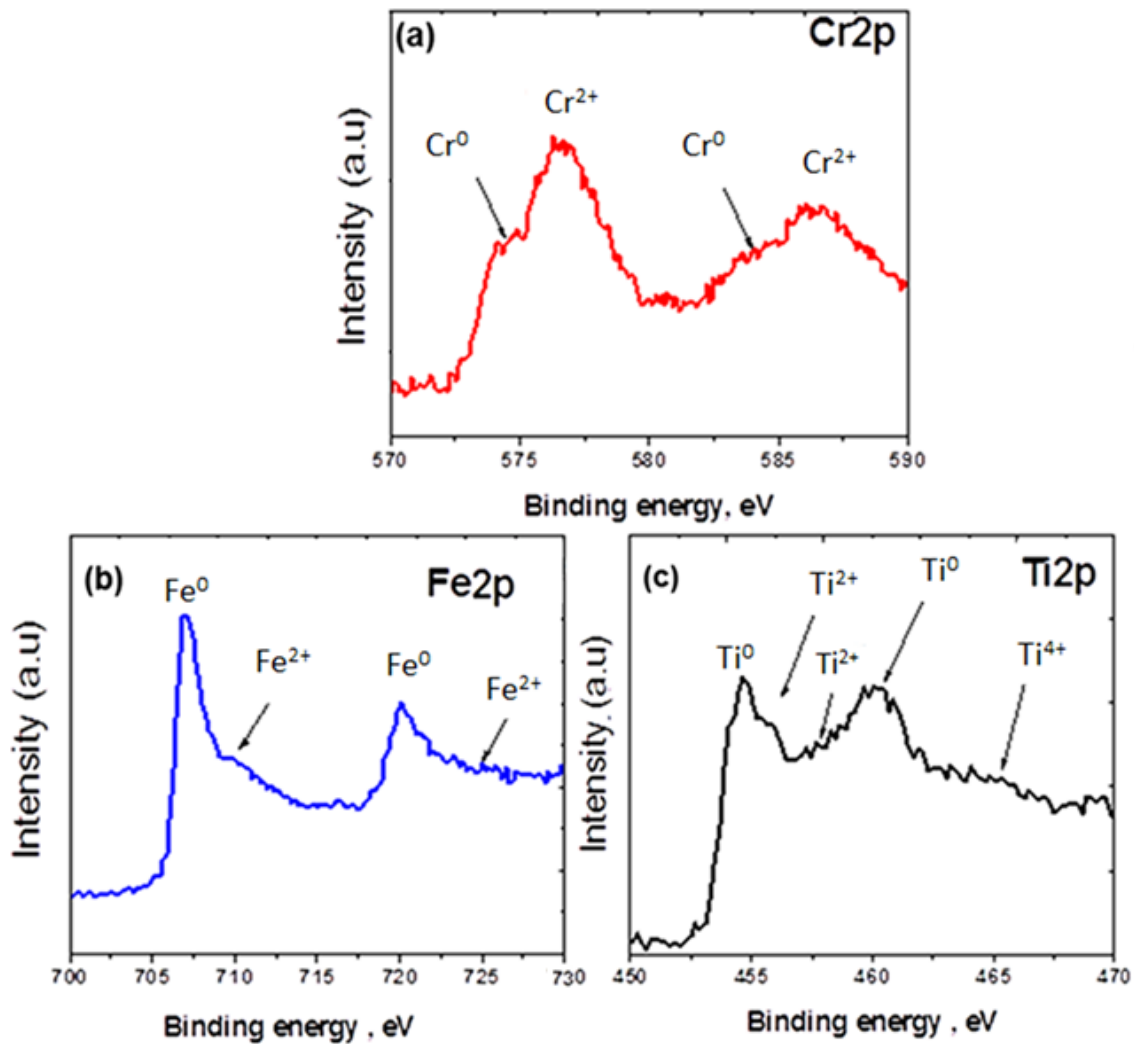


Figure 60 XPS narrow scan region for (a) Cr2p (b) Fe2p for Gr-SS (c) Ti2p for Gr-TiV.

(D) XRD

The XRD pattern of CoBlast™ coated metals and the respective substrates are given in Figure 61. Comparison of the diffraction patterns of Gr-SS and Gr-TiV (Figure 61 (a) & (c)) indicates that graphite and alumina phases are common to both coated metals thereby implying that graphite and alumina was successfully impregnated into these surfaces. This observation is in agreement with the SEM and XPS results. Also present in the CoBlast™ treated metals are the substrate phases: austenite (γ -Fe) for Gr-SS and titanium (TiV) for Gr-TiV. The weak intensity of graphite and alumina peaks coupled with strongly intense peaks of the substrate phases in Figure 61 (a) & (c) is consistent with the fact that the coated layer was very thin as earlier discussed.

A closer look at the patterns for Gr-SS and the substrate reveals an additional phase not present in the substrate. The formation of this additional phase named, strain induced martensite (α' -Fe), is attributed to strain hardening effect of the sub-layer as the powder particles impinge the surface during blasting leading to partial transformation of austenite to martensite. The presence of martensite in Gr-SS is consistent with previous reports on blasting of austenitic stainless steel by different surface severe plastic deformation processes such as grit blasting [223], shot peening [224], surface mechanical attrition treatment (SMAT) [225, 226]. Furthermore, a comparison of the peaks for austenite (γ -Fe) for Gr-SS and titanium (TiV) for Gr-TiV and that of the substrate reveals a broadening of the peak, which is suggestive of grain refinement, lattice deformation and/or increase in micro-strain at the sub-layer of the substrate as commonly reported for blasted surfaces [223-227]. However, further investigations to characterise these features in the CoBlast™ treated metals were not conducted.

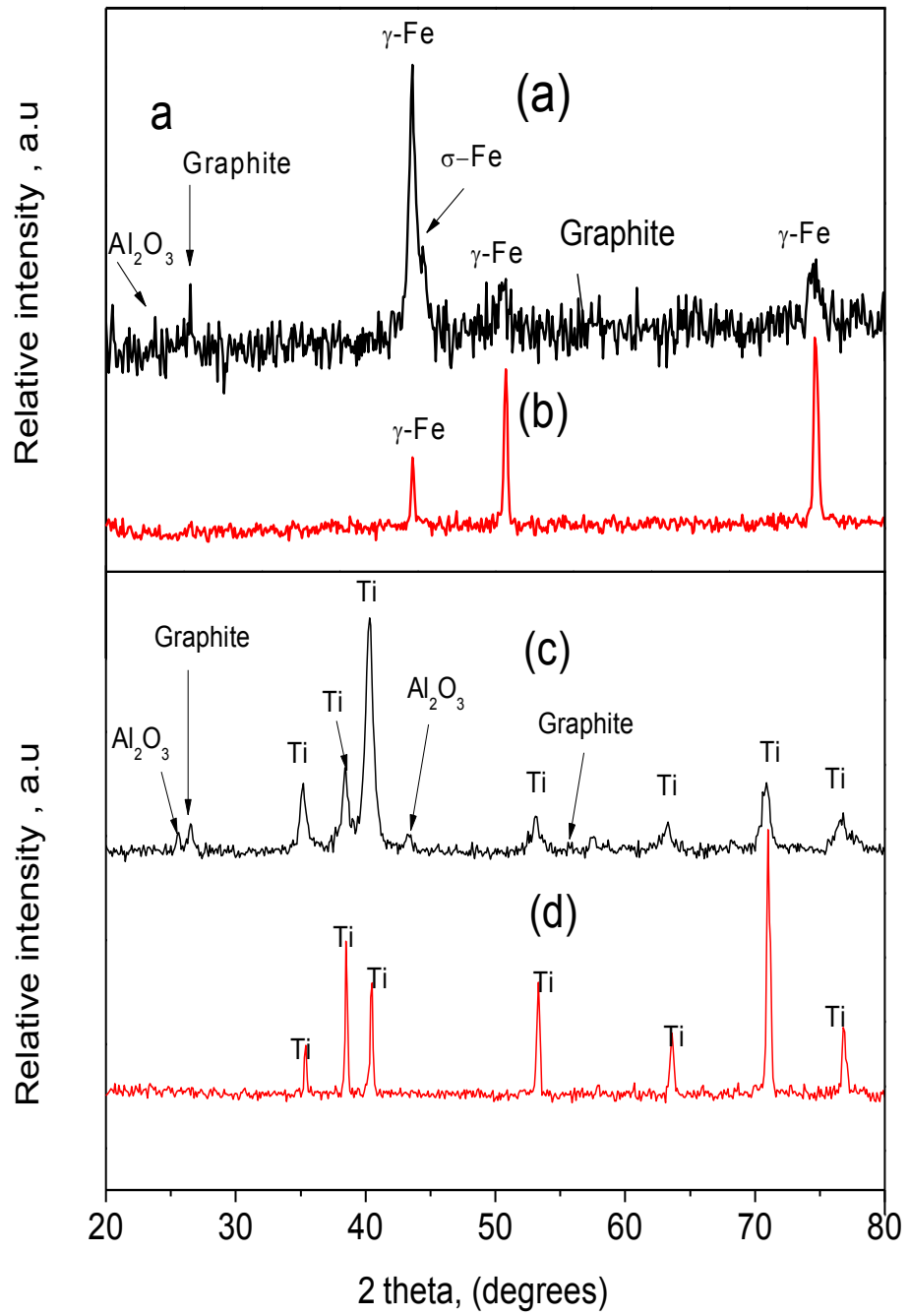


Figure 61 XRD patterns for (a) Gr-SS (b) SS316 (c) Gr-TiV (d) Bare-TiV.

In summary, it could be concluded from the surface characterisation results that CoBlast™ deposited graphite coatings on 316 stainless steel and titanium grade (V) alloy consisted of a thin and rough modified layer, which was composed of isolated pockets of graphite, alumina and/or a mixture of both overlaying an exposed substrate.

4.2 EVALUATION OF GRAPHITE COATED TITANIUM (V) ALLOY AS PEM FUEL CELL BIPOLAR PLATES

(A) Interfacial contact resistance (ICR)

Figure 62 presents the plot of 2 x ICR data as a function of compaction pressure for CoBlast treated titanium (Gr-TiV) and bare substrate (Bare-TiV). The ICR data for graphite, the industry bench mark, is also shown for reference. It can be seen in Figure 62 that ICR decreased with

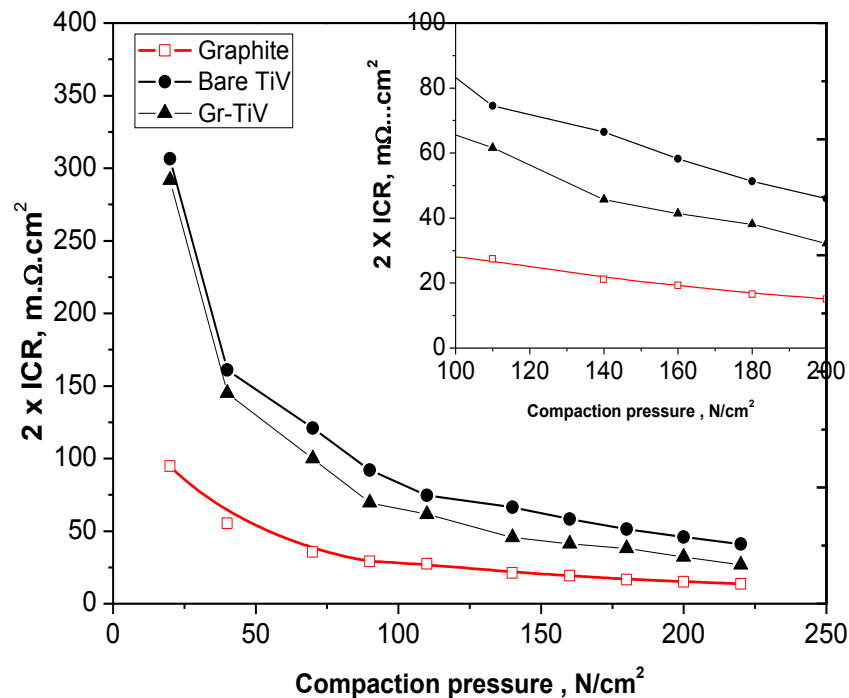


Figure 62 Plot of Interfacial contact resistance vs. compaction pressure for Gr-TiV, Bare TiV and graphite.

increasing compaction pressure for all materials due to increasing contact area between the carbon paper and the specimens [74-76]. At compaction pressure of interest for PEM fuel cell application (100-200 N/cm²) shown in the inset in Figure 62, Gr-TiV exhibited reduced ICR compared to that of bare-TiV. The decrease in ICR is attributed both to the outermost layer composition and surface roughness. As revealed in the XPS analysis, the passive layer of Gr-TiV consisted of a mixture of conductive graphite, alumina and titanium oxides, which is more conductive than the naturally occurring titanium oxide from the substrate. Also, the higher surface roughness of Gr-TiV compared to that of bare-TiV would contribute to the reduction in ICR as the rougher the sample, the lower the ICR [21, 30, 55, 56]. At typical compaction pressure of 140 N/cm² as shown in the Table 12, Gr-Ti exhibited ~ 32% lower ICR value compared to that of bare-TiV and about 100% higher ICR value compared to that of graphite. Compared to the targeted ICR of 10 mΩ.cm², it can be seen that the ICR of Gr-TiV is significantly higher than the targeted value implying that Gr-TiV is not suitable for PEM fuel cell bipolar plate application.

Table 12 2 x ICR of Gr-TiV and Bare-TiV at 140 N/cm².

Material	Graphite	Gr- TiV	Bare-TiV
ICR (mΩ.cm²)	21.19	45.70	66.50

(B) Potentiodynamic and potentiostatic Polarisation

I. Potentiodynamic Polarisation

Figure 63 displays the potentiodynamic polarisation curve for Gr-TiV and bare TiV alloy in simulated PEM fuel cell cathode (0.6 V, air purged) and anode (-0.1 V, bubbled with H₂)

environments and working potential at room temperature respectively. It can be deduced from Figure 63 that both Gr-TiV and bare TiV behaved identically in the simulated PEM fuel cell cathodic and anodic environments indicating that the graphite /alumina coating had negligible influence on the corrosion resistance of the bare metal and this is attributed to the discontinuous nature of the coatings. In the simulated cathode environment, the corrosion potential of the bare alloy is shifted towards more noble potential and the corrosion current density is about one order of magnitude less than that of the substrate as shown in Table 13. A reverse trend is, however, observed at the simulated anodic environment. At typical PEM fuel cell cathodic working potential of 0.6 V, both Gr-TiV and the bare TiV are within the passive region. However, in Figure 63 (b), the PEM fuel cell anodic working potential of -0.1 V is close to the free corrosion potential of TiV.

Table 13 Corrosion parameters of Gr-TiV and TiV in 0.5 M H₂SO₄ + 2 ppm at room temperature.

Material	Cathode		Anode	
	E_{corr} (V vs. Ag/AgCl)	i_{corr} ($\mu\text{A}/\text{cm}^2$)	E_{corr} (V vs. Ag/AgCl)	i_{corr} ($\mu\text{A}/\text{cm}^2$)
Gr-TiV	0.0	50	-0.25	2
TiV	-0.3	10	-0.15	0.7

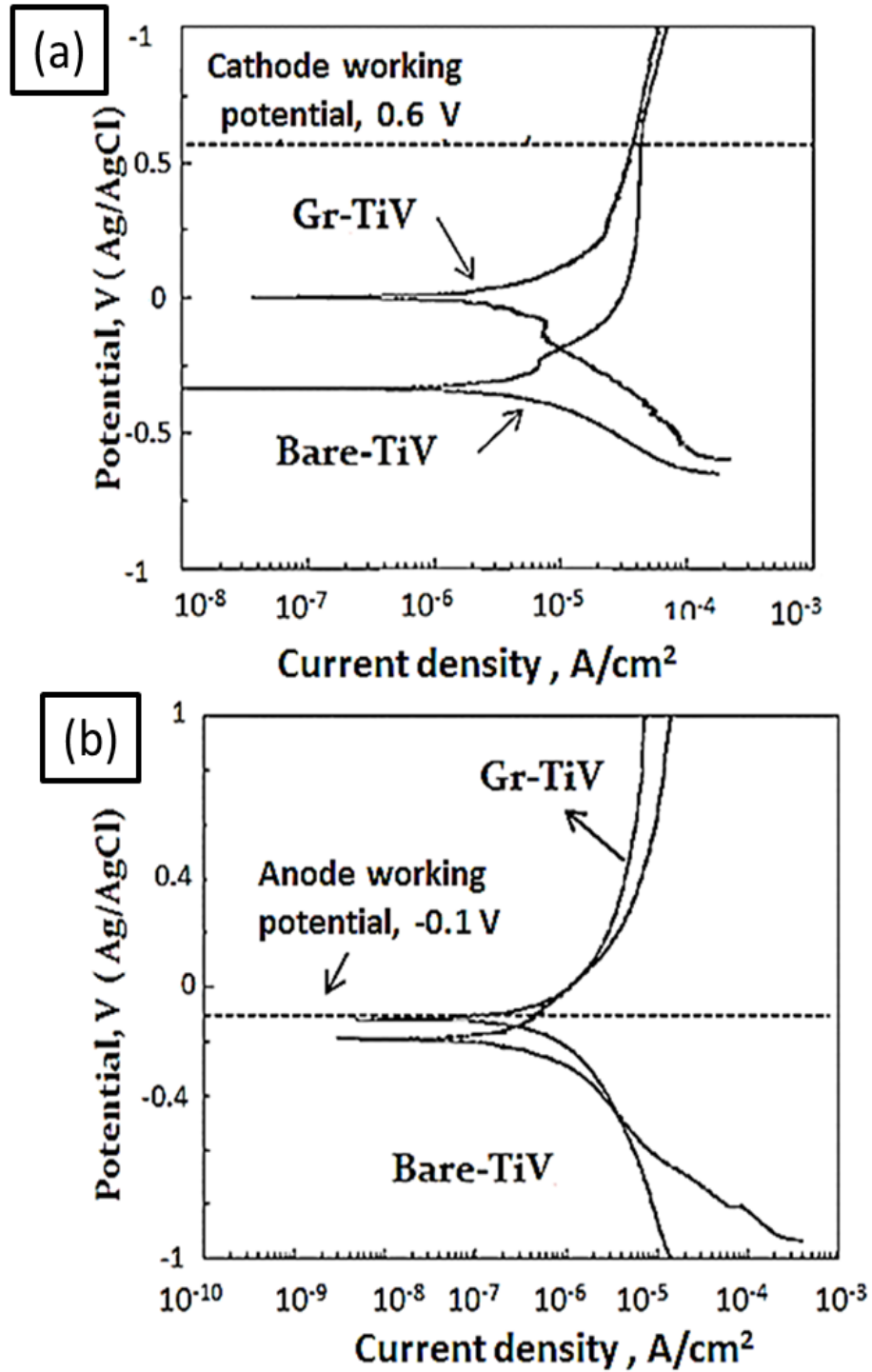


Figure 63 Potentiodynamic polarisation curves for Gr- TiV and Bare- TiV in 0.5 M H₂SO₄ + 2 ppm HF at room temperature with (a) air bubbled (b) H₂ gas bubbled into the electrolyte. Scan rate 1 mV/s.

II Potentiostatic Polarisation

Figure 64 shows the potentiostatic curves for Gr-TiV and bare TiV in simulated cathode and anode PEM fuel cell working conditions of 0.6 V and -0.1 V with air and hydrogen gas bubbling. In the simulated cathodic environment as shown in Figure 64 (a), Gr-TiV and bare -TiV samples exhibited an initial decay at the inception of polarisation due to the formation of passive films in agreement with the potentiodynamic curves [21, 58, 59]. Gr-TiV, however, exhibited a more stable performance than the bare TiV, reaching a current density of $\sim 42 \mu\text{A}/\text{cm}^2$ in the first 400 seconds and gradually stabilised at $17 \mu\text{A}/\text{cm}^2$ while the bare alloy stabilised at $\sim 46 \mu\text{A}/\text{cm}^2$.

In Figure 64 (b), both Gr-TiV and TiV exhibited negative transient current density. The potentiostatic behaviour of both Gr-TiV and bare-TiV in the simulated anodic environment is consistent with previous studies on other Ti alloys [73, 74, 96]. This behaviour is attributed to the low applied potential of -0.1 V at the anode which facilitates the formation of a stable oxide after the initial dissolution of the air-formed film. From the results presented in Figure 64, it can be seen that the CoBlast™ deposited graphite coatings did not enhance the corrosion properties of titanium (V) alloy

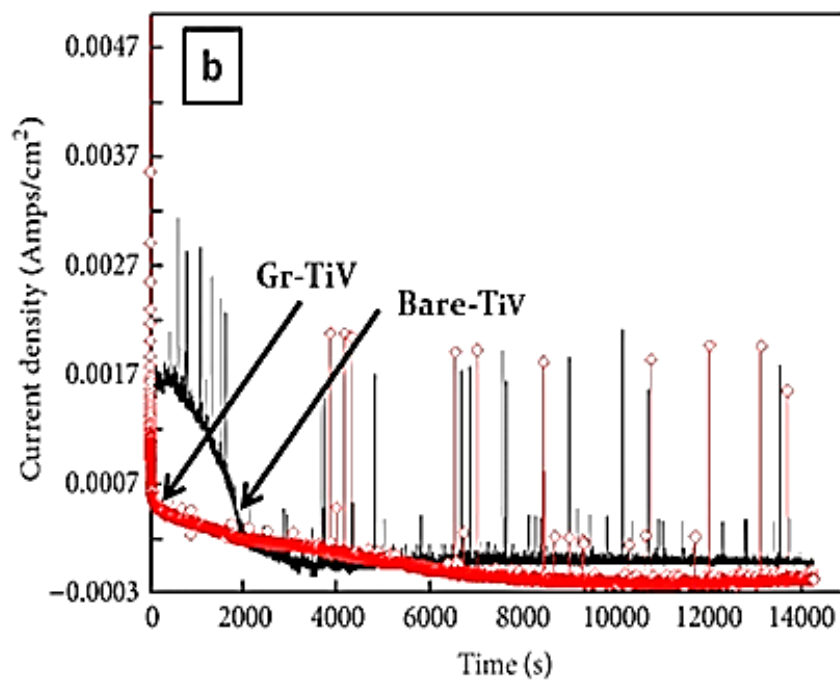
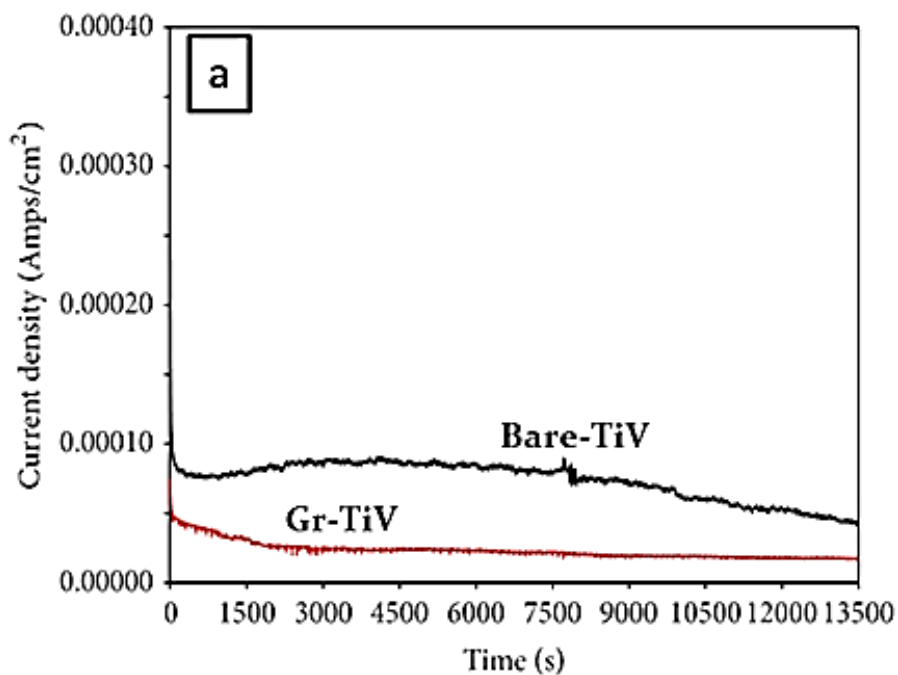


Figure 64 Potentiostatic polarisation of Gr-TiV and Bare –TiV in 0.5 M H₂SO₄ + 2 ppm HF at 70 °C (a) air bubbled (E = 0.6 V (Ag/AgCl) and (b) H₂ gas bubbled (E = -0.1 V (Ag/AgCl) into the solution.

III. ICP-MS analysis

Metallic ions arising from corrosion of metals have a detrimental effect on the proton exchange membrane and the catalyst layer as earlier discussed in Chapter 2. Therefore, the amount of Ti ions leached in to the bulk solution after 14,400 seconds of potentiostatic polarisation was investigated and is presented in Table 14. In general, the amount of titanium ion leached into the electrolyte under simulated anodic condition (-0.1 V) exceeded that in the simulated cathodic conditions for Gr-TiV and TiV thereby suggesting that dissolution is higher under PEM fuel cell anodic conditions than under the cathodic conditions. This observation is consistent with that reported by Feng et al. [89] for pure Ti and could be related to the reducing nature of the anodic environment which prevents spontaneous passivation.

It can also be seen from Table 14 that the amount of titanium ion leached in the electrolyte during static polarisation of Gr-TiV is more than that of the substrate. Although not in comparable electrolyte solution, a similar observation was reported by Brown et al. [227] for grit blasted surfaces compared with polished surfaces and their findings were attributed to the increased surface area of the grit blasted sample which led to increased sites for corrosion reactions. Hence, the increased amount of leached metallic ions in Gr-TiV compared to TiV can be attributed to higher surface roughness of Gr-TiV.

Table 14 Total metal ion concentration after 14400 seconds of potentiostatic polarisation of Gr-TiV and TiV in simulated PEM fuel cell environment of 0.5 M H₂SO₄ +2 ppm HF at 70 °C

Metal ion	Gr-TiV		TiV	
	Cathode	Anode	Cathode	Anode
Titanium (ppm)	3.240	6.960	0.422	1.056

4.3 EVALUATION OF GRAPHITE COATED STAINLESS STEEL AS PEM FUEL CELLS BIPOLAR PLATES

In this section, only the potentiodynamic, potentiostatic polarisation and ICP-MS results for Gr-SS are presented. The ICR of Gr-SS will be presented in the next chapter in comparison with the ICR of the modified graphite coated stainless steel.

(A) Potentiodynamic polarisation

Figure 65 displays the potentiodynamic curves for Gr-SS and the substrate (SS316) in 0.5 M H₂SO₄ + 2 ppm HF solution at room temperature in simulated anode (hydrogen bubbling) and cathode (air bubbling) PEM fuel cell conditions. In the simulated cathode environment (Figure 65(a)), both Gr-SS and SS316 exhibited active-passive- transpassive behaviour typical of stainless steels. The corrosion current density of both materials is within the 10⁻⁵A/cm² range at free corrosion potential (Table 15) implying that corrosion properties of SS316 were not improved by Gr-TiV.

It can also be seen in Figure 65 that PEM fuel cell cathode potential of 0.6 V, SS316 is within the passive region signifying retardation of corrosion [64, 65]. On the other hand, Gr-SS is within the transpassive region denoting that corrosion will be accelerated within the cathodic environment.

The potentiodynamic curve of SS316 and Gr-SS in the simulated PEM fuel cell anode environment is presented in Figure 65 (b). Both SS316 and Gr-SS exhibited extended active region due to the inability to form passive film in hydrogen containing environment [21, 65, 66]. This behaviour is typical of stainless steels in a reducing environment and is generally attributed to the oxidation of Cr_2O_3 , a primary constituent of the passive layer to higher valences (e.g. Cr^{6+}) [33, 73].

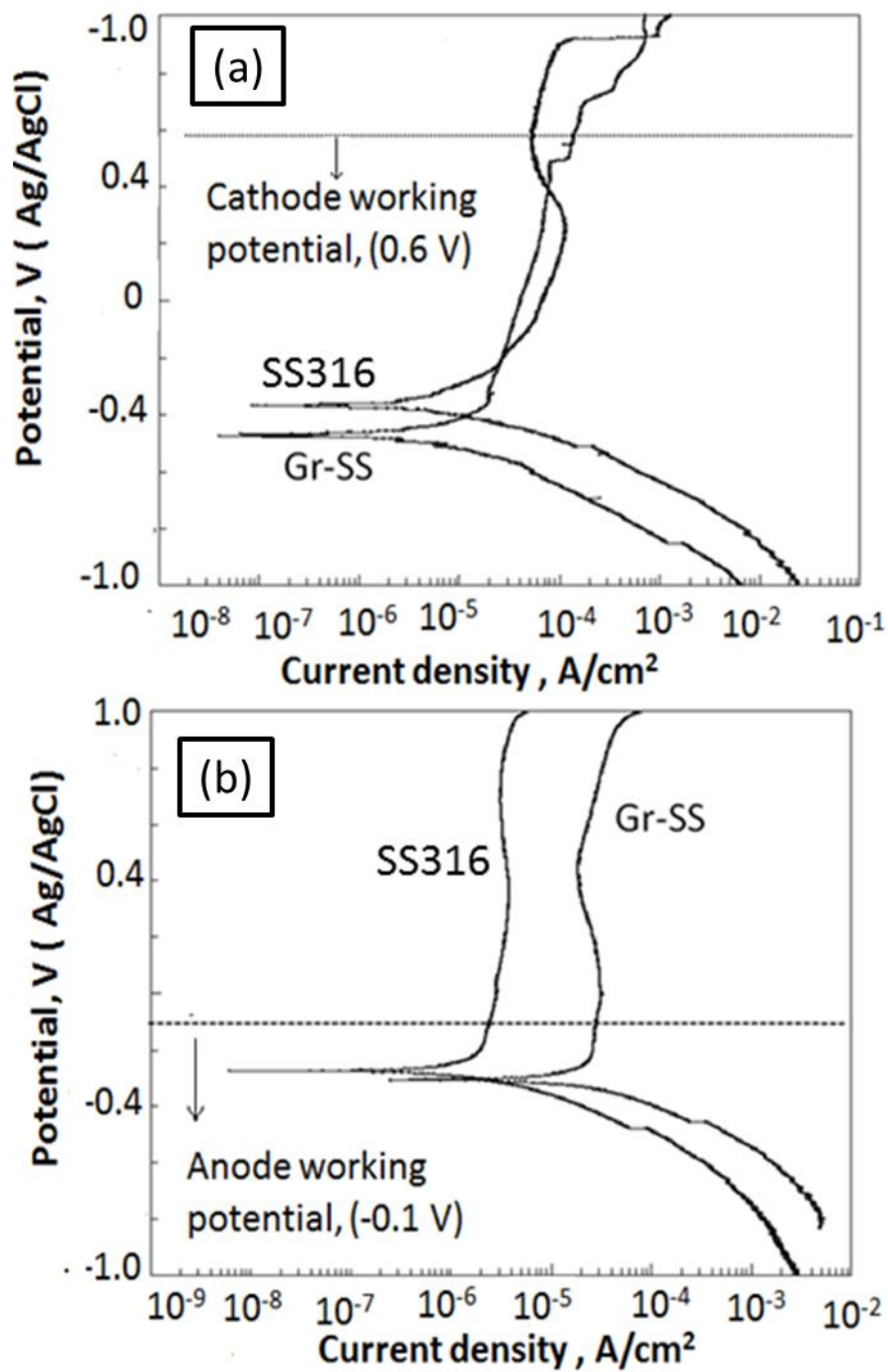


Figure 65 Potentiodynamic curves for Gr-SS and SS316 in 0.5 M H₂SO₄ + 2 ppm HF at room temperature in simulated (a) cathode (air bubbled into the solution) and (b) anode environments (hydrogen gas bubbled into the solution). Scan rate = 1 mV/s.

Table 15 Corrosion potential and corrosion current density of Gr-SS and SS316 in simulated PEM fuel cell environment of 0.5 M + 2 ppm H₂SO₄ at room temperature with air bubbling (cathode) and hydrogen gas bubbling (anode).

Material	Cathode		Anode	
	E_{corr} (V vs. Ag/AgCl)	i_{corr} ($\mu\text{A}/\text{cm}^2$)	E_{corr} (V vs. Ag/AgCl)	i_{corr} ($\mu\text{A}/\text{cm}^2$)
Gr-SS	-0.48	20	-0.25	30
SS316	-0.34	10	-0.15	20

The polarisation curve for Gr-SS in simulated PEM fuel cell anodic environment indicated that the coating had unsatisfactory anti-corrosion properties. The corrosion potential of the SS316 is shifted in the negative direction from -0.29 V to -0.31 V while its corrosion current density increased by one order of magnitude from 5 μA to 20 μA when coated with graphite. These results signify that the coated sample has a lower corrosion resistance and corrodes faster than the uncoated sample in the simulated PEM fuel cell environment. At the PEM fuel cell anode working potential of -0.1 V, both samples are within the active dissolution area and would corrode when used under PEM fuel cell anodic conditions.

(B) Potentiostatic Polarisation

Figure 66 shows the potentiostatic polarisation for Gr-SS in 0.5 M H₂SO₄ + 2 ppm HF with air bubbling to mimic the PEM fuel cell cathode environment. It can be seen that SS316 exhibited passivity indicated by a current decay, as soon as the whole surface is covered with the passive

film the current begins to decrease and thereafter stabilises [21, 65, 66]. This behaviour can be further supported with the potentiodynamic curve wherein SS316 is within the passive region at the applied potential of 0.6 V. SS316 begins to stabilise after about 800 seconds reaching a stable current density of $55.2 \mu\text{A}/\text{cm}^2$ at the end of 14400 seconds. Gr-SS also showed passivation characteristics but could not stabilise until about 5000 seconds.

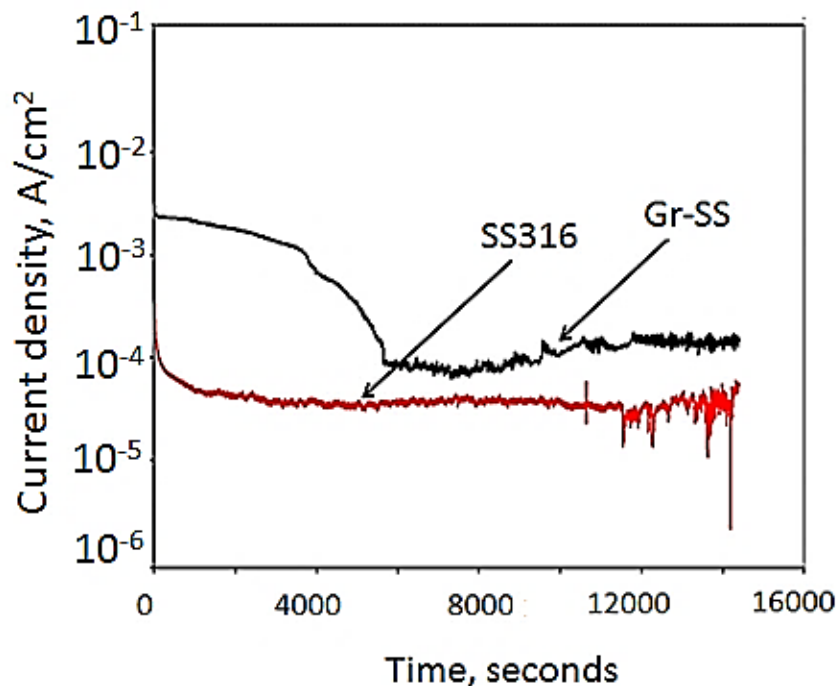


Figure 66 Potentiostatic polarisation of Gr-SS and SS316 in 0.5 M H_2SO_4 +2 ppm HF at 70 °C, air bubbled, $E = 0.6 \text{ V}$. Scan rate 1 mV/s.

The instability of Gr-SS can be explained by the fact that the applied potential (0.6 V) is at the threshold of the trans-passive region i.e. the region where the passive film break down and corrosion is accelerated in the potentiodynamic curve. At the end of the 14400 seconds, Gr-SS stabilised at $151 \mu\text{A}/\text{cm}^2$, which is an order of magnitude higher than that of SS316 and four orders of magnitude higher than the targeted $1 \mu\text{A}/\text{cm}^2$ for bipolar plates. Potentiostatic polarisation in

simulated PEM fuel cell anodic environment was not investigated because the potentiodynamic results revealed that the substrate (SS316) exhibited better corrosion resistance than Gr-SS in simulated PEM fuel cell anodic environment.

(C) ICP-MS analysis

The ICP-MS analysis of the concentration of metallic ions leached into the solution after potentiostatic polarisation is shown in Table 16. Iron (Fe) has the highest concentration in both samples due to preferential dissolution which is consistent with previous studies on stainless steels [138-140]. It can be seen that the total metallic ions from the coated sample is more than that from the bare metal signifying that Gr-SS could not protect the substrate from dissolution during polarisation which is consistent with the potentiostatic polarisation result.

Table 16 Metallic ion concentration (in ppm) after potentiostatic polarisation in PEM fuel cell cathode environment and working potential.

Material	Fe	Cr	Mn	Ni	Total
Gr-SS	2.253	0.592	0.059	0.277	3.181
SS316	2.140	0.290	0.036	0.196	2.662

(D) Factors that influenced the corrosion resistance of CoBlast™ coatings in simulated PEM fuel cell environments.

It can be deduced from the potentiodynamic and potentiostatic curves of Gr-SS and Gr-TiV that both coated materials exhibited poor corrosion behaviour in the simulated PEM fuel cell environments. This behaviour can be attributed to a number of factors which are discussed below:

(1) **Nature of the coatings:** The SEM, XPS and XRD characterisation of Gr-SS and Gr-TiV revealed a thin and discontinuous coated layer. Discontinuities in coatings are well known to promote dissolution of the substrate, in preference to the coatings. The defects provide pathway for interaction between the substrate and the corrosive media thereby facilitating the formation of micro-galvanic couples on the coated surface, which leads to dissolution of the substrate [228-230]. In the case of Gr-SS and Gr-Ti, the discontinuous coatings acted as the cathode and the exposed substrate the anode, resulting in preferential dissolution of the substrate.

(2) **Blasting nature of the coating process:** It is well established that plastic deformation via blasting generally induces an increase in surface roughness and increase in lattice defects such as dislocations and grain boundaries of metallic materials [223-226]. An increase in surface roughness and lattice defects engenders the formation of active sites which promote corrosion. This phenomenon can be related to the electron work function of the metal in question. The electron work function (EWF) is the minimum energy required to dislodge electrons from the interior of a metal to its surface [225, 226,233].

The EWF of a metallic surface is closely related to the electron transfer phenomenon in corrosion and can give an indication of the susceptibility of a surface to dissolution [218, 225]. An increase in surface roughness corresponds to a decrease in EWF implying that a rough surface would more readily give up its electrons than a smooth surface, hence resulting in an increase in the corrosion rate. Similarly, dislocations generated during blasting increase the activity of electrons on the surface and decrease the energy required to transfer such electron from the interior to the surface thereby promoting corrosion [233].

- (3) **Phase transformation in austenitic stainless steel:** Austenitic stainless steels such as 316, 304 stainless steels are metastable in nature, hence austenite can undergo partial phase transformation during blasting leading to the formation of strain induced martensite. It is well reported that the presence of small amounts of strain-induced martensite deteriorates corrosion resistance of austenitic stainless steels in both acid and alkaline media due to galvanic effect between the austenite and martensite phases [225, 233].

4.4 SUMMARY

The surface characterisation, ICR and electrochemical polarisation of graphite/alumina coatings deposited by CoBlast™ process on 316 stainless steel and titanium grade (V) alloys was reported in this chapter. SEM/EDX, XRD and XPS results revealed that graphite and alumina (the grit material) were impregnated on the substrates after the CoBlast™ treatment. The modified layer had rougher morphologies and higher contact angles when compared with that of the bare substrates, but the depth of modification was low and discontinuous with patches of graphite, alumina, or a mixture of both overlaying an exposed substrate. Hence, the graphite coatings could not adequately protect the base metal from corrosion. The presence of substrate surface oxides also impaired the electrical conductivity of the coating, although it was lower than the substrate, yet it was higher than graphite, the industrial benchmark. These results indicated that improvement in the continuity and thickness of the coating is needed for the CoBlast™ process to be feasible for surface modification of metallic PEM fuel cell bipolar plate.

Chapter 5

Post Modification Of Graphite Coated Stainless Steel.

5.1 INTRODUCTION

In the last chapter, it was established that CoBlast™ deposited graphite coatings did not offer the desired corrosion protection in PEM fuel cell environments, due to its discontinuous nature amongst other factors. Attempts to improve the continuity of the graphite coatings via process optimisation were not successful; hence, it was not included in this thesis. However, it may be possible to enhance the corrosion resistance of the coatings by post-deposition treatments. Whilst there are many surface modification techniques that can be employed, the presence of increased grain boundaries and high dislocation density defects arising from severe plastic deformation induced by grit-blasting suggest that a thermochemical post-treatment could be appropriate for enhancing the thickness and corrosion behaviour of CoBlast™ coatings. However, only graphite coated 316 stainless steel (Gr-SS) was considered for post-modification treatments. Graphite coated titanium (V) alloy was not considered due to its high cost compared to stainless steel [47].

Among the available thermochemical process, chromising has been widely employed for improving the corrosion and oxidation resistance of nickel and ferrous based alloys [183,184]. Chromising as earlier described in Chapter 3, involves surface modification of a ferrous-based or Ni alloy via diffusion of chromium atoms at high temperatures into a ferrous-based or Ni alloy surface. The process is of interest for PEM fuel cell bipolar plate applications because corrosion resistance and surface conductivities of stainless steels increases with its chromium content [21, 64-66].

Chromising is typically a slow process; hence, it is conducted at temperature $\geq 1000^{\circ}\text{C}$. However, It is well reported that the chemical kinetics and diffusivity of chromium during chromising process can be enhanced by the presence of lattice defects such as increased grain boundaries and high dislocation density induced by surface severe plastic deformation processes (S^2PD) such as shot peening, surface mechanical attrition (SMAT) [223-225]. These lattice defects are reported to enhance chemical kinetics by acting as channels for faster atomic diffusion thereby resulting in thicker chromised coatings than the untreated substrate [223, 224]. It is also reported that the chromised layers formed after such surface treatments exhibit better corrosion resistance than their untreated counterpart processed at the same temperature [27-29, 232].

Yang et al. [27] reported that shot peening prior to pack chromising generated a thicker coating which exhibited one order magnitude reduction in the current density of untreated 316 chromised polarised in simulated PEM fuel cell environment of 0.5 M H_2SO_4 + 2 ppm HF at 70°C . Wen et al. [284] investigated the effect of rolling pre-treatments and EDM machining coupled with low temperature chromising at 700°C on 420 stainless steel and reported that rolling pre-treatments was more effective in enhancing the performance of chromised 420 stainless steel than EDM machining. A similar improvement in single fuel cell performance with bipolar plates which were rolled prior to chromising was also reported by Bai et al. [29].

In this chapter, results obtained for post chromising treatment of graphite coated stainless steel (Gr-SS) at 900°C for three hours are presented and discussed in comparison with that obtained for Gr-SS and the untreated substrate (SS316).

5.2 SURFACE CHARACTERISATION

I. Surface morphology

Figure 67 (a) and (b) displays the surface morphology of Gr-SS after chromising treatments at 900 °C for 3 hours in the secondary electron (SE) and backscattered (BSD) modes respectively. The secondary electron image of chromised Gr-SS (Figure 67(a)) revealed a granular morphology with defects such as craters, pores. On the other hand, the BSD image of chromised Gr-SS showed a heterogeneous distribution of the former graphite/alumina coatings in a chromium rich matrix (Figure 67 (b)).

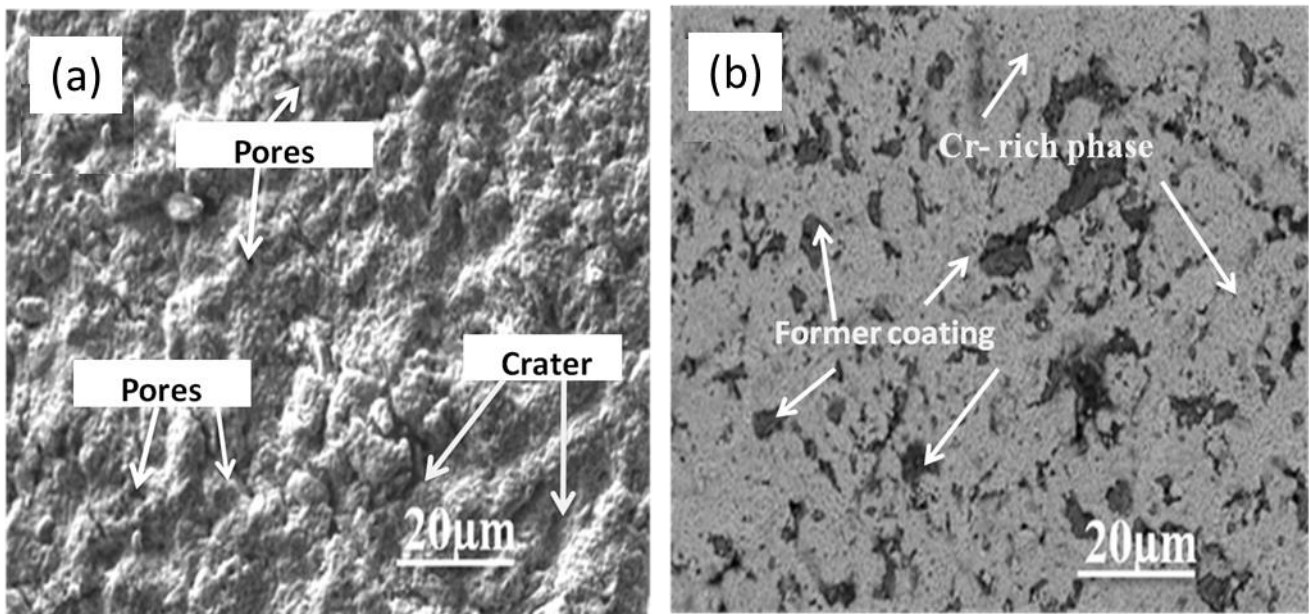


Figure 67 SEM images of chromised Gr-SS (a) secondary electron view (b) backscattered (BSD) view (dark patches – graphite /alumina coatings, light area –chromium rich region)

The surface morphology of the untreated 316 stainless steel (chromised SS316) presented in Figure 68 shows a similar granular morphology with relatively smoother surface without any inclusions. However, faint polishing lines conducted before chromising treatment, are visible in

the chromised SS316, indicating that the amount of chromium uptake was small; hence, a thin coated layer was formed. The thickness of the coated layer was estimated to be $\sim 1.8 \mu\text{m}$. In contrast, the thickness of chromised Gr-SS was estimated to be $\sim 4.0 \mu\text{m}$ based on measurements across different points on the coated layer. The two fold increase in the thickness of the coated layer in chromised-Gr-SS is attributed to the higher diffusivity of chromium during deposition, engendered by lattice defects in agreement with previous studies on pre-treated chromised coatings [39-41, 223, 224].

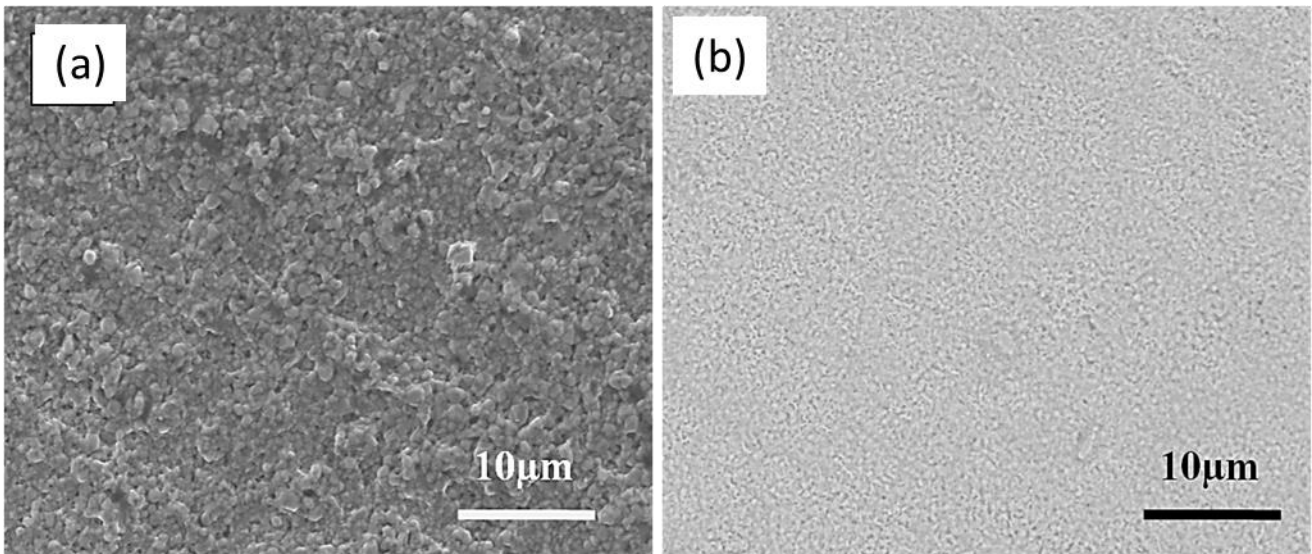


Figure 68 SEM images of chromised SS316 (a) secondary electron view (b) backscattered view. Surface morphologies provided at higher magnifications than in Figure 67 in order to reveal the granular morphology.

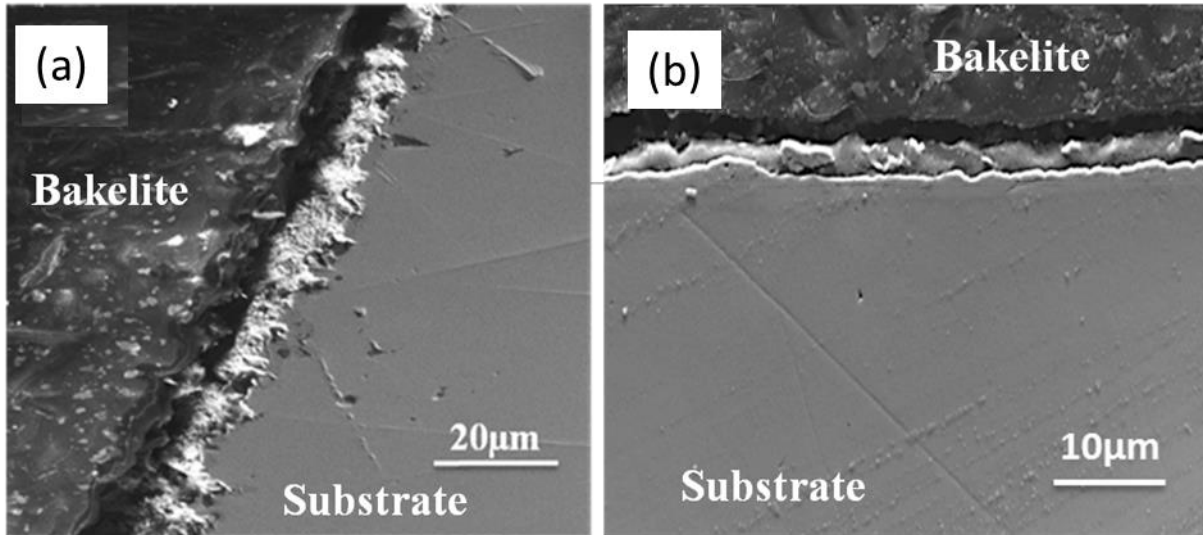


Figure 69 Cross-section of (a) chromised Gr-SS and (b) chromised SS316 both samples were pack chromised at 900 °C for 3 hours.

III. XRD analysis

Figure 70 presents the diffraction patterns for chromised Gr-SS and chromised SS316. Both XRD patterns showed similar phases of austenite, chromium iron nitride ($(\text{Cr, Fe})_2\text{N}_{1-x}$ where $x = 0-0.5$) and chromium iron carbide ($(\text{Cr, Fe})_3\text{C}_7$, $(\text{Cr, Fe})_{23}\text{C}_{26}$, $(\text{Cr, Fe})_3\text{C}_2$), however, the intensities of these phases differ. In particular, the intensity of the austenite peak in chromised Gr-SS (Figure 70(a)) was significantly reduced compared to that of chromised SS316 (Figure 70(b)). The difference in the intensities of the austenite peaks is consistent with the two fold increase observed in the thickness of chromised Gr-SS compared to that of chromised SS316.

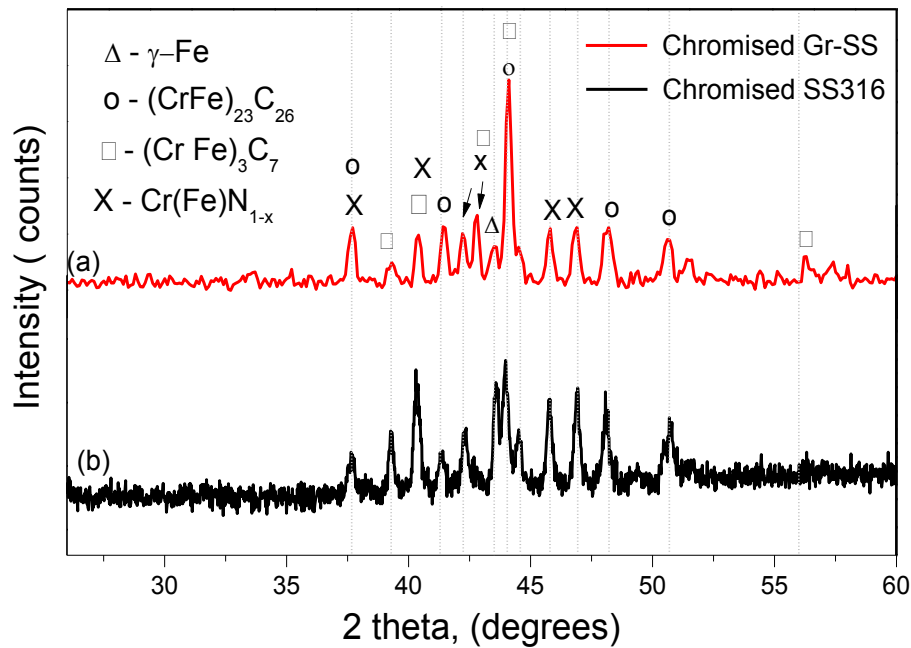


Figure 70 XRD patterns of (a) chromised Gr-SS and (b) chromised SS316.

It can also be seen in Figure 70 (a) that graphite or alumina phases were not detected, is in contrast to the surface morphology of chromised Gr-SS shown in Figure 68. The absence of these phases could be related to the high depth of X-ray penetration in conventional locked couple XRD. Hence, glancing angle XRD was conducted at relatively low depth of x-ray penetration of 0.1 to 1°.

Figure 71 shows the glancing angle XRD patterns for chromised Gr-SS. At a glancing angle of 1°, which is about 198nm into the coated layer [223], no austenite peak was observed implying that only chromium compounds were present at this depth which agrees with the ~4µm thick coated layer shown in Figure 69 (cross-sectional view). At all glancing angles, graphite and alumina

peaks were not detected suggesting that the concentration of graphite and alumina was very low compared to the chromium based compounds.

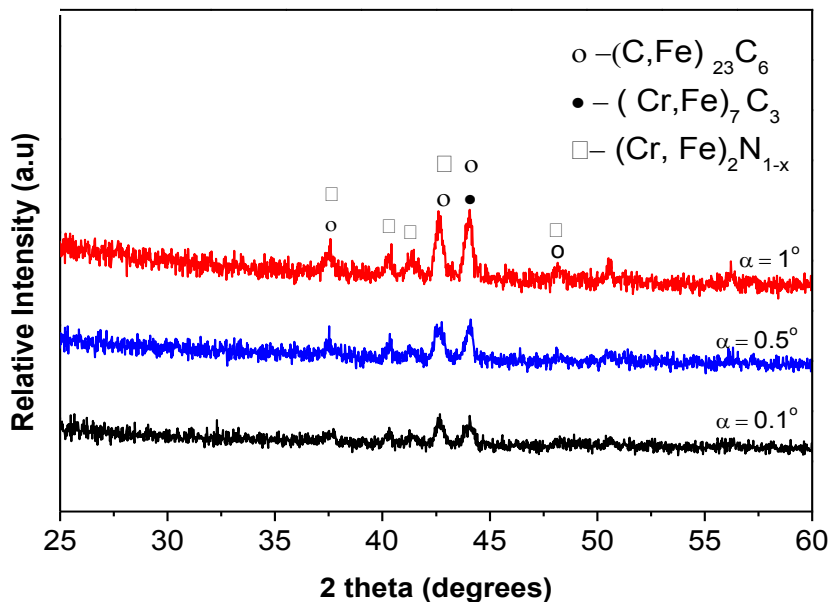


Figure 71 Glancing XRD patterns for chromised Gr-SS.

1V. XPS Analysis

XPS analysis was conducted in order to confirm the presence of graphite and alumina on the surface of chromised Gr-SS. After 10 minutes of sputtering, which is representative of the depth revealed at glancing incidence of 0.1° , the XPS survey spectra for chromised Gr-SS (Figure 72) revealed the presence of Cr2p, O1s, N1s, C1s and Al2p peaks. Figure 72 also indicate the absence of Fe2p peaks in agreement with the glancing XRD result (Figure 71).

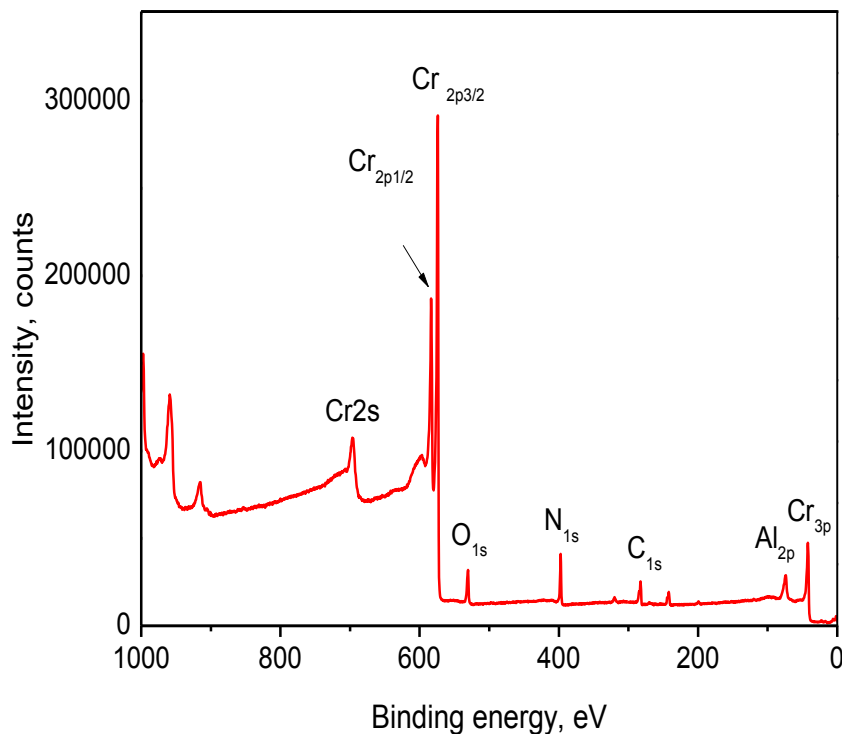


Figure 72 XPS survey spectra for chromised Gr-SS after 10 minutes of Argon sputtering.

The high resolution scan for C1s at this depth (Figure 73) revealed the presence of C-Cr at binding energy of 282.75 eV and C-C bond at binding energy of 284.60 eV [205, 235, 236]. The C-Cr bond is attributed to chromium carbide, while the C-C bond at 284.60 eV is attributed to graphite [205] thereby confirming the presence of graphite on the outermost layer. Graphite was not detected by GXRD due to its very low concentration compared to that of chromium based compounds. The Cr2p_{1/2} peak at 574.2 eV in Figure 74 further establishes the presence of chromium carbide on the outermost layer of chromised GR-SS.

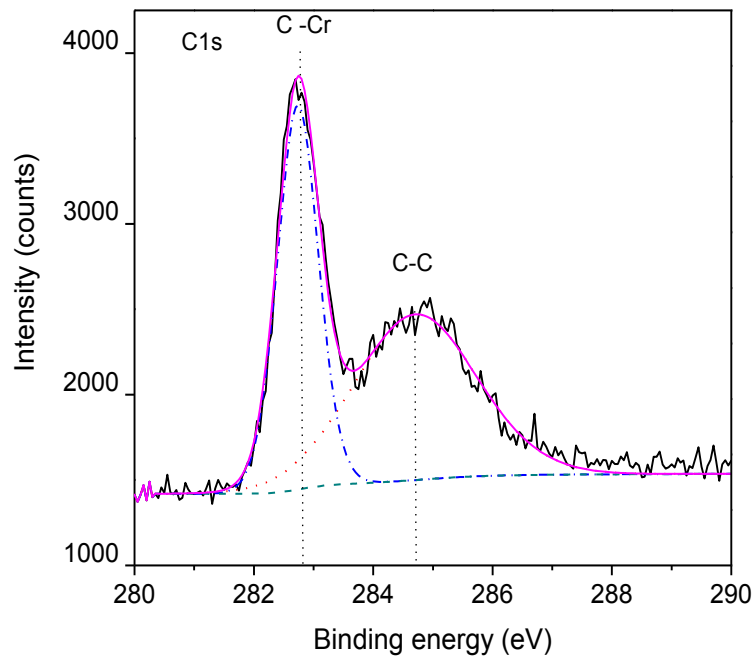


Figure 73 High resolution scan for C1s in Chromised Gr-SS.

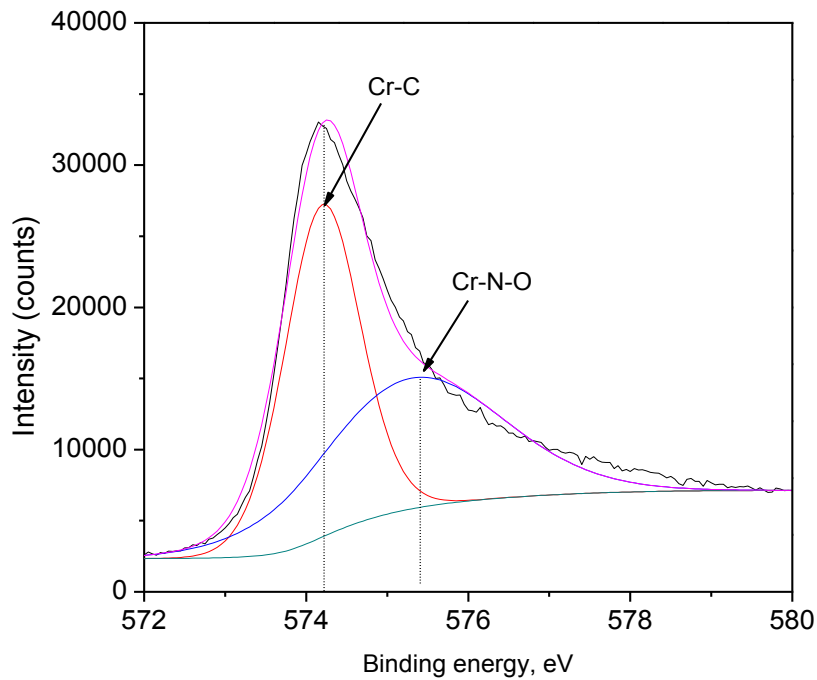


Figure 74 High resolution scan for Cr2p in Chromised Gr-SS.

It is noted that the binding energies of the Cr-C bonds in Figure 74 are consistent with the reported binding energies for chromium carbides or metallic Cr [205, 235, 236]. However, it is well reported, that if the band gap of the XPS is greater than the difference in binding energies of Cr-Cr and Cr-C bonds (which is about 0.2 eV), the difference between the two bonds cannot be resolved [235, 236]. The band gap of the XPS used in this study was 0.6 eV; hence, the peak at 574.2 eV can be attributed to Cr-C bonds given that a C-Cr bond can be seen in the C1s spectrum shown in Figure 73.

Figure 74 also indicates the presence of Cr-N-O bonds at binding energy of ~575.5 eV. The Cr-N-O bonds are due to the presence of chromium nitride in oxygen environment [219, 220]. Hence from the XPS and the GXRD result, it can be concluded the outermost layer of chromised Gr-SS consist of graphite, alumina and chromium based compounds.

5.3 INTERFACIAL CONTACT RESISTANCE

Figure 75 gives the plot of $2 \times \text{ICR}$ as a function of compaction pressure for chromised Gr-SS and chromised SS316, Gr-SS and SS316. The ICR data for graphite is also shown for reference. ICR decreased with increasing compaction pressure for all materials due to increasing contact area between the carbon paper and the specimens as compaction pressure increased. At the compaction pressures of interest for PEM fuel cell applications ($100\text{-}200 \text{ N/cm}^2$) as shown in the inset, chromised Gr-SS exhibited ICR values of $49.06\text{-}15.93 \text{ m}\Omega\cdot\text{cm}^2$ which were comparable to that of graphite ($27.47 - 15.07 \text{ m}\Omega\cdot\text{cm}^2$) at higher compaction pressures of $\sim 160\text{-}200 \text{ N/cm}^2$. On the hand, the ICR values of chromised SS316 ($122.52 - 70.82 \text{ m}\Omega\cdot\text{cm}^2$) and SS316 ($319.5 - 146.92 \text{ m}\Omega\cdot\text{cm}^2$) were significantly higher than that of chromised Gr-SS under the same range of compaction pressure. At typical compaction pressure of 140 N/cm^2 , the $2 \times \text{ICR}$ of these materials

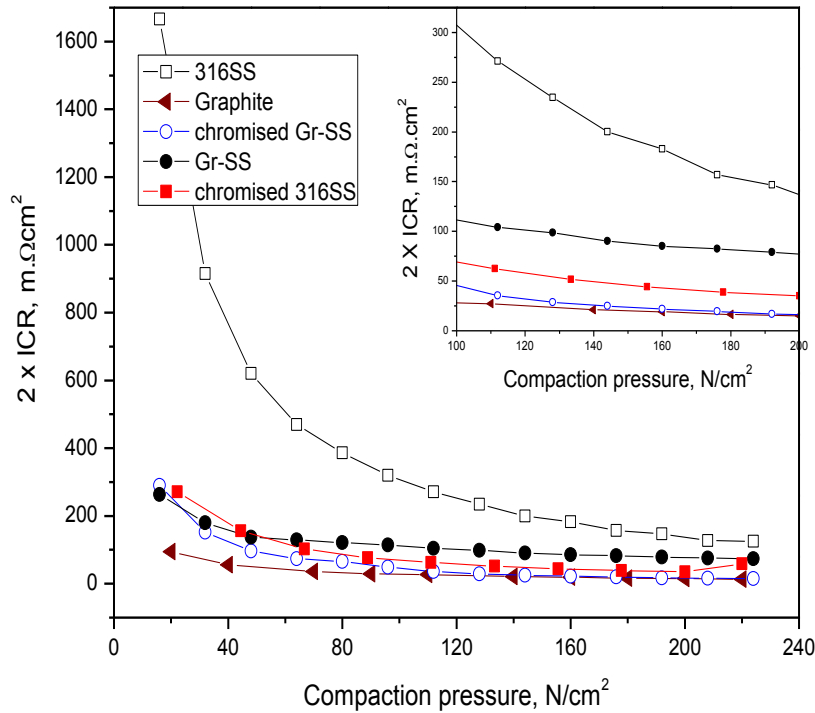


Figure 75 ICR of chromised Gr-SS and chromised Gr-SS compared with that of graphite and Gr-SS.

was found to be: chromised Gr-SS – 25.00 mΩ.cm², graphite - 21.19 mΩ.cm², chromised 316 – 49.37 mΩ.cm², Gr-SS - 90.31 and SS316 – 200.03 mΩ.cm². The difference in ICR of these materials can be explained thus:

The ICR of metallic bipolar plates is fundamentally influenced by outermost composition and surface roughness. The high contact resistance of SS316 at the compaction pressure of interest to PEM fuel cells is consistent with previous studies on 316 stainless steel and is attributed to its outermost composition which consists of Fe-rich and Cr-rich surface oxide layers which are well known to be semi-conductive [73-75]. Conversely, the reduction in ICR of Gr-SS compared to that of SS316 can be attributed to both to the doping effect of

graphite on the oxide layer and higher surface roughness than the substrate. Similarly, the decrease in ICR of Gr-SS after chromising can be attributed to its chemical composition of the outermost layer and surface roughness.

Previous studies on chromised studies have shown that increasing surface roughness of the chromised coating through the use of pre-treatments such as shot peening, rolling etc. decreases ICR of chromised coating albeit marginally. For instance, Yang et al. [27] reported a 16% reduction in ICR at 200 N/cm² while Bai et al. [29] reported a 14.3% decrease in ICR at 140 N/cm² for pre-rolled and chromised coatings on 420 stainless steel. Hence, the ~72% reduction in ICR of Gr-SS at 140 N/cm² after post chromising can be attributed to the chemical composition at the outermost layer. As shown in the XPS analysis in Figure 72-75, the outermost layer of chromised Gr-SS contained graphite in addition to the chromium based compounds on the passive layer, graphite is known to be conductive, hence, the ~50% reduction in ICR of chromised Gr-SS compared to chromised SS316 at 140 N/cm². This observation suggests that increasing carbon content (since graphite is an allotrope of carbon) on the outermost layer of chromised coatings can decrease ICR.

5.4 CORROSION BEHAVIOUR IN SIMULATED PEM FUEL CELL ENVIRONMENT AT 70 °C

(A) Potentiodynamic polarisation

Figure 76 presents the potentiodynamic polarisation curves of chromised Gr-SS and chromised SS316 as well as that of Gr-SS and SS316 exposed to 0.5 M H₂SO₄ + 2 ppm HF at 70 °C without

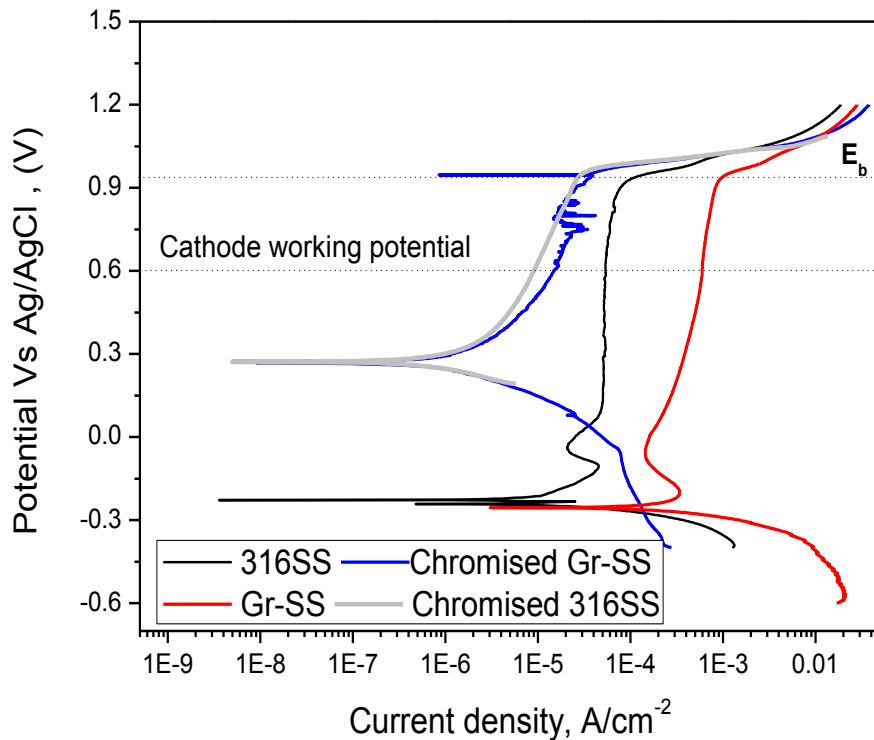


Figure 76 Potentiodynamic polarisation of chromised Gr-SS, chromised SS316, SS316 and Gr-SS in 0.5 M H₂SO₄ + 2 ppm HF at 70 °C, scan rate =1 mV/s.

air or hydrogen bubbling. It can be seen from Figure 76 that SS316 exhibited an active-passive-trans-passive behaviour typical of stainless steels in simulated PEM fuel cell environment.

Table 17 gives the corrosion parameters derived from Figure 76 for the materials investigated. Comparing the corrosion parameters of SS316 and Gr-SS, it can be seen that blasting SS316 with graphite and alumina particles via CoBlast™ process degraded the corrosion resistance of SS316, evidenced by a one of magnitude reduction corrosion current density (i_{corr}).

Table 17 Corrosion parameters for chromised Gr-SS, chromised SS316, SS316 and Gr-SS.

Materials	Corrosion potential (E_{corr}) (V vs. Ag/AgCl)	Corrosion current density (i_{corr}, $\mu\text{A}/\text{cm}^2$)	Breakdown potential (E_b) (V vs. Ag/AgCl)	Critical passive current (i_c $\mu\text{A}/\text{cm}^2$)
Chromised Gr-SS	0.27	2.21	0.94	-
Chromised SS316	0.27	3.20	0.94	-
SS316	-0.28	276	0.89	32.40
Gr-SS	-0.43	5920	0.90	300

It is reported that grit blasting degrades the corrosion resistance of austenitic stainless steels [229 - 231]. Otubo et al. [229] reported that grit-blasted 304 stainless steel exhibited lower corrosion resistance than the substrate in 1 N H₂SO₄ at room temperature [229]. The loss of corrosion resistance was attributed to the surface roughness rather than the presence of martensite on the grit blasted surface, as stress relieved grit-blasted samples, which had no martensite exhibited similar corrosion properties with the untreated grit blasted sample. This fact was reiterated by Galvan et al. [230] on the corrosion of medical 316LVM stainless steel in simulated human fluids. On the other hand, Celik et al. [239] demonstrated that grit-blasting prior to coating deposition increased the susceptibility of the thermal sprayed coatings to corrosion. Hence, from these studies, the poor performance of Gr-SS compared to the SS316 can be attributed to its higher surface roughness.

The loss of corrosion resistance due to increase in surface roughness is related to the electron work function (EWF) of the surface, as discussed earlier. An increase in surface roughness of a surface corresponds to a decrease in its EWF and corrosion resistance.

Post chromising treatment of Gr-SS yielded a modified chromised surface, which exhibited more noble corrosion potential (E_{corr}) and lower corrosion current density (i_{corr}) than Gr-SS and SS316 respectively (Table 17), implying that corrosion properties of Gr-SS was enhanced. Interestingly, both chromised Gr-SS and chromised SS316 exhibited similar corrosion potential and corrosion current density. However, at higher potentials, chromised Gr-SS becomes unstable while the latter maintained its pseudo-passive state i.e. increase in current density with an increasing potential after active dissolution.

The corrosion behaviour of the investigated material at typical PEM fuel cell cathode potential of 0.6 V can also be deduced from Figure 76. It can be seen that all materials investigated are within the passive region. However, chromised Gr-SS showed some degree of instability at potentials close to 0.6 V which suggest that in more aggressive environment with air bubbling chromised Gr-SS may be active; hence, it may not be suitable for PEM fuel cell bipolar plates.

(B) Potentiostatic polarisation

Figure 77 shows the potentiostatic polarisation curves for chromised Gr-SS and chromised SS316 at 0.6 V in 0.5 M H_2SO_4 + 2 ppm HF at 70 °C with air bubbled into the electrolyte during polarisation. As seen in Figure 77, chromised Gr-SS exhibited an anodic to cathodic oscillatory behaviour throughout the 4 hours test while chromised SS316 exhibited a more stable performance than chromised Gr-SS and stabilised within the 10 $\mu A/cm^2$ range.

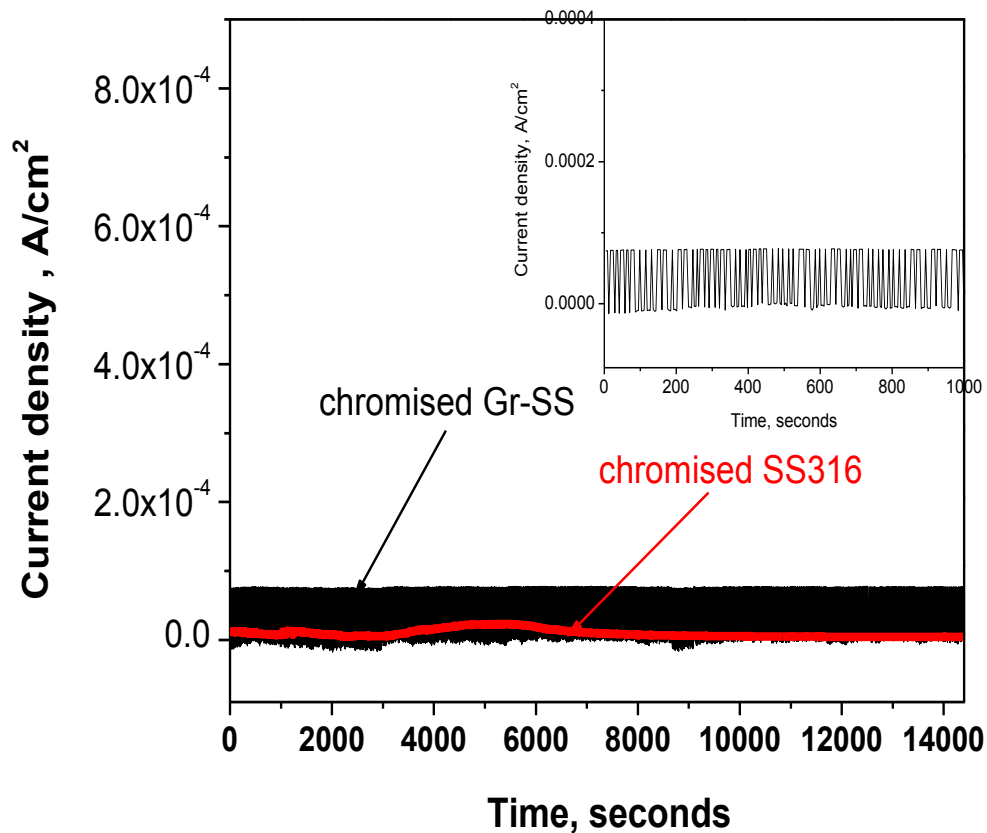


Figure 77 Potentiostatic polarisation of chromised Gr-SS and chromised SS316 at 0.6 V vs. Ag/AgCl in 0.5 M H₂SO₄ + 2 ppm HF purged with air at 70 °C, scan rate =1 mV/s. The inset shows the oscillatory behaviour exhibited by chromised Gr-SS.

Figure 78 (a) and (b) presents the surface morphologies of chromised Gr-SS and chromised SS316 after potentiostatic polarisation. Fig. 78 (a) indicates that chromised Gr-SS showed evidence of corrosion attack characterised by the formation of micro-pits. These micro-pits appear to be on the chromium based matrix while the graphite-alumina particles appear un-attacked (circled in red). This observation could be attributed to the potential difference between the chromium matrix and the graphite/alumina based coatings thereby resulting in the formation of galvanic couples between the graphite/alumina coatings and chromised matrix, wherein the latter acted as the cathode and

the former the anode, hence, its preferential dissolution. On the other hand, Figure 78 (b) indicate a relatively smooth morphology with negligible evidence of corrosion attack for chromised SS316. These results imply that chromised Gr-SS is not suitable for PEM fuel cell bipolar plate application. However, the stable performance of chromised SS316 despite its lower thickness compared to chromised Gr-SS suggests that it may be possible to improve the performance of chromised coatings through process parameter optimisation.

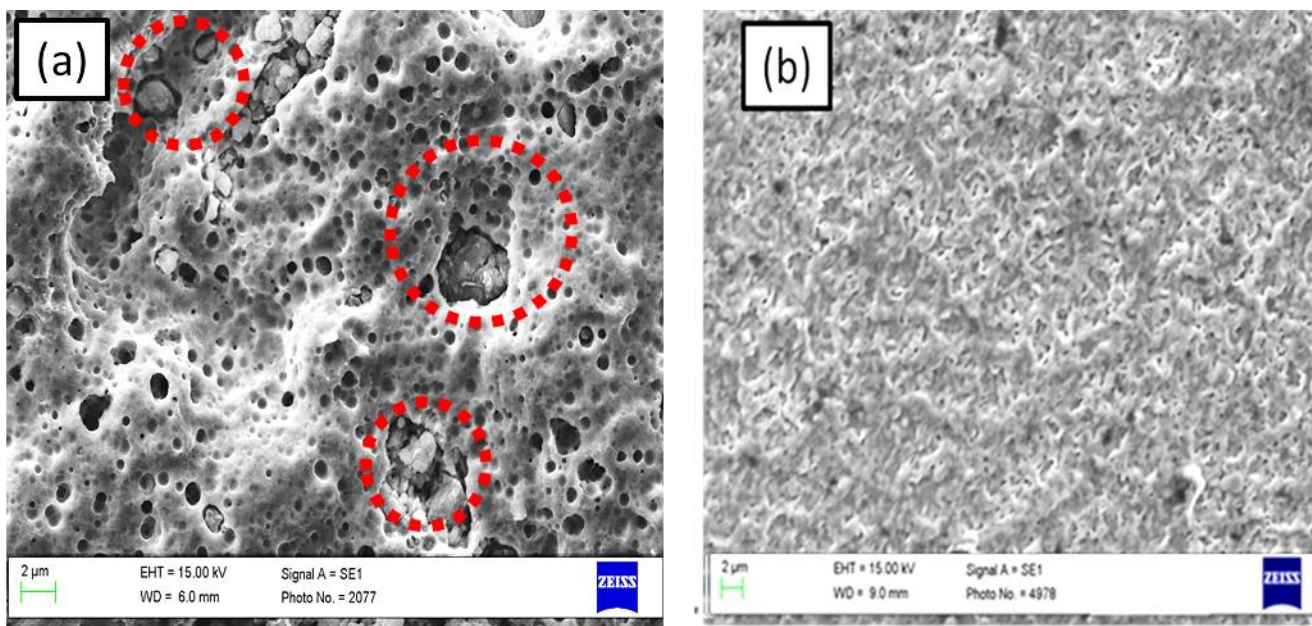


Figure 78 SEM micrographs of (a) Chromised Gr-SS (b) Chromised SS316 after 4 hours of potentiostatic polarisation in 0.5 M H₂SO₄ + 2 ppm HF at 70 °C.

5.5 SUMMARY

Post chromising of CoBlast™ coated 316 stainless steel (Gr-SS) and its performance in simulated PEM fuel cell environment was investigated in this chapter. Post chromising was conducted at 900 °C for 3 hours and the modified surface was characterised. The SEM/EDX, XPS and XRD results indicated that post chromising of Gr-SS yielded a multiphase coating composed of a chromium

rich matrix with graphite and alumina inclusions. Hence, the modified CoBlast™ coated stainless steel (chromised Gr-SS) exhibited ICR values significantly lower than Gr-SS. At typical PEM fuel cell compaction pressure of 140 N/cm², chromised Gr-SS exhibited ~72% reduction in the ICR of Gr-SS. Chromised Gr-SS also exhibited about three order of magnitude decrease in the corrosion current density of Gr-SS in 0.5 M H₂SO₄ + 2 ppm HF at 70 °C. However, examination of the surface morphologies of chromised Gr-SS after potentiostatic polarisation for 4 hours at 0.6 V vs. Ag/AgCl showed evidence of pitting corrosion. This observation was attributed to the potential difference between the chromium matrix and the graphite/alumina coatings which facilitated the preferential dissolution of the matrix relative to the graphite/alumina coatings.

In order to ascertain the influence of the graphite/alumina coatings on the performance of chromised coatings, the performance of chromised Gr-SS in simulated PEM fuel cell environments was compared with that of chromised 316 stainless steel (chromised SS316). It was found that both materials exhibited similar corrosion resistance in 0.5 M H₂SO₄ + 2 ppm HF at 70 °C. Potentiostatic polarisation of both materials at 0.6 V vs. Ag/AgCl for 4 hours indicated that chromised SS316 was more stable in the simulated PEM fuel cell environment with transient current density in the 10⁻⁵ A/cm² range. However, chromised Gr-SS exhibited 50% reduction in the ICR of chromised stainless steel at 140 N/cm². The reduction in ICR of chromised Gr-SS compared to that of chromised SS316 was attributed to the graphite coatings inclusions. This result suggest that it might be possible to reduce the ICR of chromised coatings by increasing its carbon content, given that graphite predominately consists of carbon.

Chapter 6

Chromium Diffusion Coatings

6.1 INTRODUCTION

This chapter presents and discusses the results of the systematic investigation of the influence of selected process parameters namely: time, activator content and temperature on corrosion current density (i_{corr}) of pack chromised 304 stainless steel in aerated 0.5 M H₂SO₄ + 2 ppm HF at 70 °C. The main objective was to optimise these process parameters using a design of experiments approach. The optimised coating was thereafter characterised and its performance in simulated and real PEM fuel cell environments was evaluated.

6.2 EXPERIMENTAL RESULTS AND MATHEMATICAL MODELLING

Table 18 gives the experimental results obtained for Tafel polarisation of pack chromised 304 stainless steels in aerated 0.5 M H₂SO₄ + 2 ppm HF acid solution at 70 °C. The polarisation experiments were conducted randomly according to design matrix given in Table 8. The thicknesses of the chromised coatings and polarisation resistance data for each run in the design matrix calculated using Equation 30 is also presented. Representative Tafel plots and cross-sectional SEM images of the chromised coatings for each run in Table 18 can be found in Appendix III. These experimental results were fitted into a quadratic model, as suggested by the sequential model sum of squares shown in Table 19 to obtain the regression model relating corrosion current density to time, activator content and temperature. The best fit model was obtained after using a square root transformation and step-wise regression.

Table 18 Design matrix based on three level-three factor Box–Behnken design.

Run	Factors			Responses		
	Time	Activator	Temperature	Thickness	Corrosion current	Polarisation
	(Hours)	Content (wt. %)	(°C)	(µm)	density (µA/cm ²)	Resistance (kΩ)
R1	6	3	1100	78.19	2.053	107.79
R2	6	5	1050	47.30	1.850	473.70
R3	6	7	1000	31.23	1.990	311.95
R4	9	5	1000	48.01	9.127	762.85
R5	3	5	1000	19.04	3.306	136.50
R6	6	3	1000	22.96	10.00	262.23
R7	9	5	1100	92.09	4.536	191.35
R8	3	5	1100	50.90	2.743	248.55
R9	6	7	1100	80.73	4.400	145.70
R10	6	5	1050	43.25	1.016	2533.75
R11	6	5	1050	46.31	1.020	548.00
R12	3	3	1050	34.89	0.415	4988.00
R13	3	7	1050	34.17	0.757	2111.50
R14	6	5	1050	45.21	1.056	438.95
R15	6	5	1050	47.75	1.260	547.40
R16	9	7	1050	55.02	1.879	257.75
R17	9	3	1050	55.13	2.345	433.56

Table 19 Sequential model sum of squares

Source	Sum of Squares	Degree of freedom	Mean Square	F Value	Prob> F	Comments
Mean vs Total	4.181 x 10 ⁻⁵	1	4.181 x 10 ⁻⁵			
Linear vs Mean	1.856 x 10 ⁻⁶	3	6.186 x 10 ⁻⁷	1.33	0.3082	
2FI vs Linear	1.630 x 10 ⁻⁶	3	5.433 x 10 ⁻⁷	1.23	0.3507	
Quadratic vs 2FI	4.163x 10 ⁻⁶	3	1.388 x 10 ⁻⁶	36.18	0.0001	Suggested
Cubic vs Quadratic	1.777X 10 ⁻⁷	3	5.922 x 10 ⁻⁸	2.61	0.1886	Aliased

The empirical equation for the model in terms of coded factors is given in Equation 38.

$$(i_{corr})^{0.5} = +0.473 + 1.280E - 04 * A - 6.402E - 03 * B - 8.648E - 04 * C + 6.0373E - 06 * (BC) + 3.950E - 0.07 * C^2 \quad (38)$$

Where A is time in seconds, B is the activator content in weight percentage and C is temperature in degree Celsius

(A) Analysis of variance (ANOVA)

The model was statistically analysed using analysis of variance (ANOVA) and the result is presented in Table 20. The Fisher variance ratio (the F-value) with the probability value (the p-value) was used to estimate the statistical significance of the model. The F-value is the ratio of the

Table 20 ANOVA for response surface quadratic model.

Source	Sum of Squares	Degree of freedom	Mean Square	F Value	p-value Prob> F	
Model	7.443×10^{-6}	5	1.489×10^{-6}	34.50	< 0.0001	Significant
A-Time	1.180×10^{-6}	1	1.180×10^{-6}	27.34	0.0003	
B-Activator content	1.280×10^{-7}	1	1.280×10^{-7}	2.97	0.1130	
C-Temperature	5.481×10^{-7}	1	5.481×10^{-7}	12.70	0.0044	
BC	1.458×10^{-6}	1	1.458×10^{-6}	33.79	0.0001	
C ²	4.129×10^{-6}	1	4.129×10^{-6}	95.70	< 0.0001	
Residual	4.746×10^{-7}	11	4.315×10^{-8}			
Lack of Fit	3.838×10^{-7}	7	5.482×10^{-8}	2.41	0.2061	not significant
Pure Error	9.085×10^{-8}	4	2.271×10^{-8}			
Cor Total	7.917E-006	16				
R-Squared	Adjusted R ²		Predicted R ²		Adequate precision	
0.9401	0.9128		0.8051		20.1760	

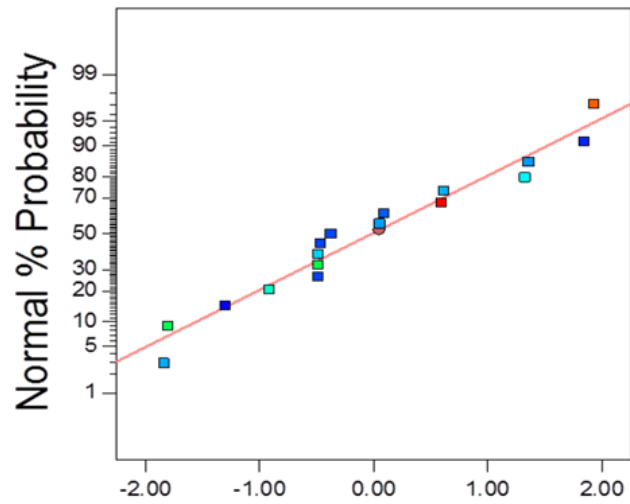
mean square of the model and the mean square error [195–197]. An F-value greater than the tabulated value of F-distribution for the degree of freedom in the model at a given level of significance is required for the model to be adequate and be a good predictor of the experimental values [197]. For the corrosion current density model represented by Equation 38, the tabulated F-value for the degree of freedom at a 95% level of significance (i.e. {F (5, 17)}) was given as 2.81).

This F-value is less than the calculated F value of 34.50 thereby signifying that the model is adequate. The large F value and p-value less than 0.0001 as shown in the Table 20 indicate that the model is significant. On the other hand, the significant factors with p-values less than 0.05 were temperature (C^2), two level interaction between activator content and temperature (B x C), time (t), Temperature (T).

The adequacy of the model was further evaluated using the coefficient of regression (R^2), adjusted R^2 , and predicted R^2 values. R^2 is a measure of the degree of fit of the model and a value close to 1 is desirable [195 – 197]. Table 20 indicates that corrosion current density model showed a good degree of fit with R^2 value of 0.9401 thereby implying that the model can account for 94.01% of the variation in the data. The predicted R^2 and the adjusted R^2 values for the model also showed good correlation with values close to 1.

The lack of fit test, adequate of precision and distribution of the residuals (i.e. the difference between the predicted and experimental values) were also employed in checking the adequacy of the model. The lack of fit for the model was 2.41, implying that the lack of fit is not significant relative to pure error. On the other hand, the signal to noise ratio of 20.176 implies that the model has an adequate signal to noise ratio and can be used to navigate the design space. Figure 79 shows the normal plot of residuals for the developed model. The closeness of the data points to the straight line signifies that the models showed no serious abnormalities and that the errors are normally distributed. Hence, the model can make accurate prediction as shown in the plot of the experimental values versus the predicted values (Figure 80).

Normal Plot of Residuals



Externally Studentized Residuals

Figure 79 Normal probability plot of the studentised residual for corrosion current density.

Predicted vs. Actual

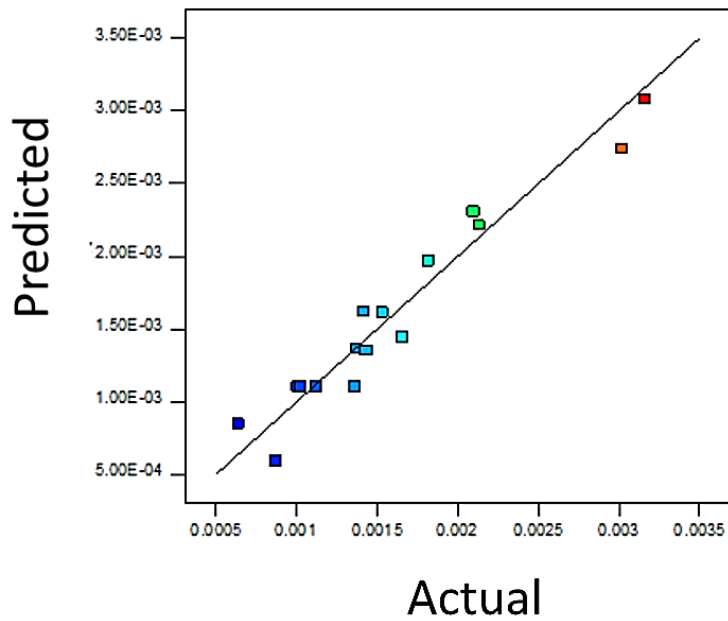


Figure 80 Predicted versus actual values plot for corrosion current density.

(B) Influence of process parameters on corrosion current density.

The main and interaction effects of time, activator content and temperature on corrosion current density of chromised 304 stainless steel in simulated PEM fuel cell environment can be deduced from Equation 38. The factors with positive coefficient i.e. time (A), two-level interaction of activator content and temperature (BC) and second order term for temperature (C^2) have a synergistic effect while the factors with negative coefficient i.e. activator content and temperature have an antagonistic effect on corrosion current density.

The main effect of the factors can also be represented in graphical forms using the perturbation plot, while the interaction effect can be represented on a two-dimensional contour plot and three dimensional response surface plots.

Figure 81 gives the perturbation plot for the corrosion current density model at the central point in the design space (i.e. time of 6 hours, activator content of 5 wt. % and temperature of 1050°C). The effect of each factor at the central point while keeping other factors constant is determined the shape on the perturbation plot. A curvature or steep slope denotes sensitivity of the factors to the response measured, while a straight line denotes insensitivity of the factor to the response measured.

I. Effect of temperature

The perturbation plot (Figure 81) indicates that temperature had a curvature effect on the corrosion current density of chromised 304 stainless steel in 0.5 M H_2SO_4 + 2 ppm HF at 70 °C. As temperature increased from 1000 °C to 1050 °C, corrosion current density decreased after which it gradually increased as temperature increased to 1100°C. For instance, at constant

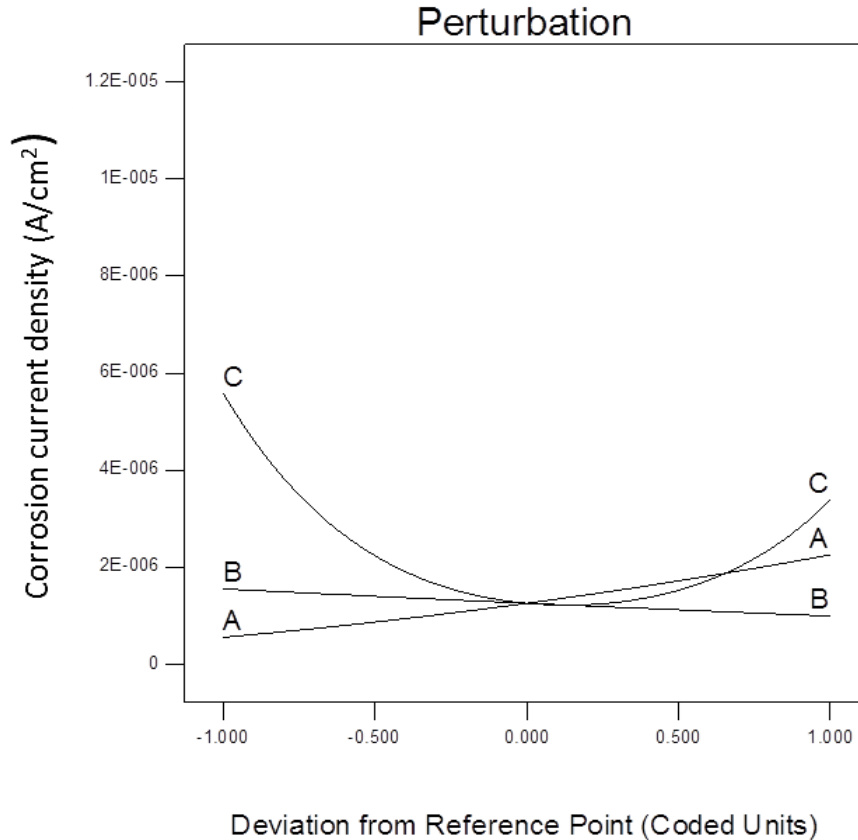


Figure 81 Perturbation plot for corrosion current density.

activator content of 3 wt.% and time of 6 hours, corrosion current density of chromised stainless steel produced at 1000 °C (R6 in Table 2) was $1.00 \times 10^{-5} \text{ A/cm}^2$, however, when temperature increased to 1100 °C, corrosion current density decreased to $2.05 \times 10^{-6} \text{ A/cm}^2$.

Examination of the surface morphologies of samples R6 and R1 shown in Figure 82 indicated significant changes in the morphologies of the coatings as temperature increased. At 1000 °C, a porous network-like structure matrix with small sized clusters is formed as shown in Figure 82(a), The inset of Figure 82(a) shows the porous matrix of R6 at a higher magnification.

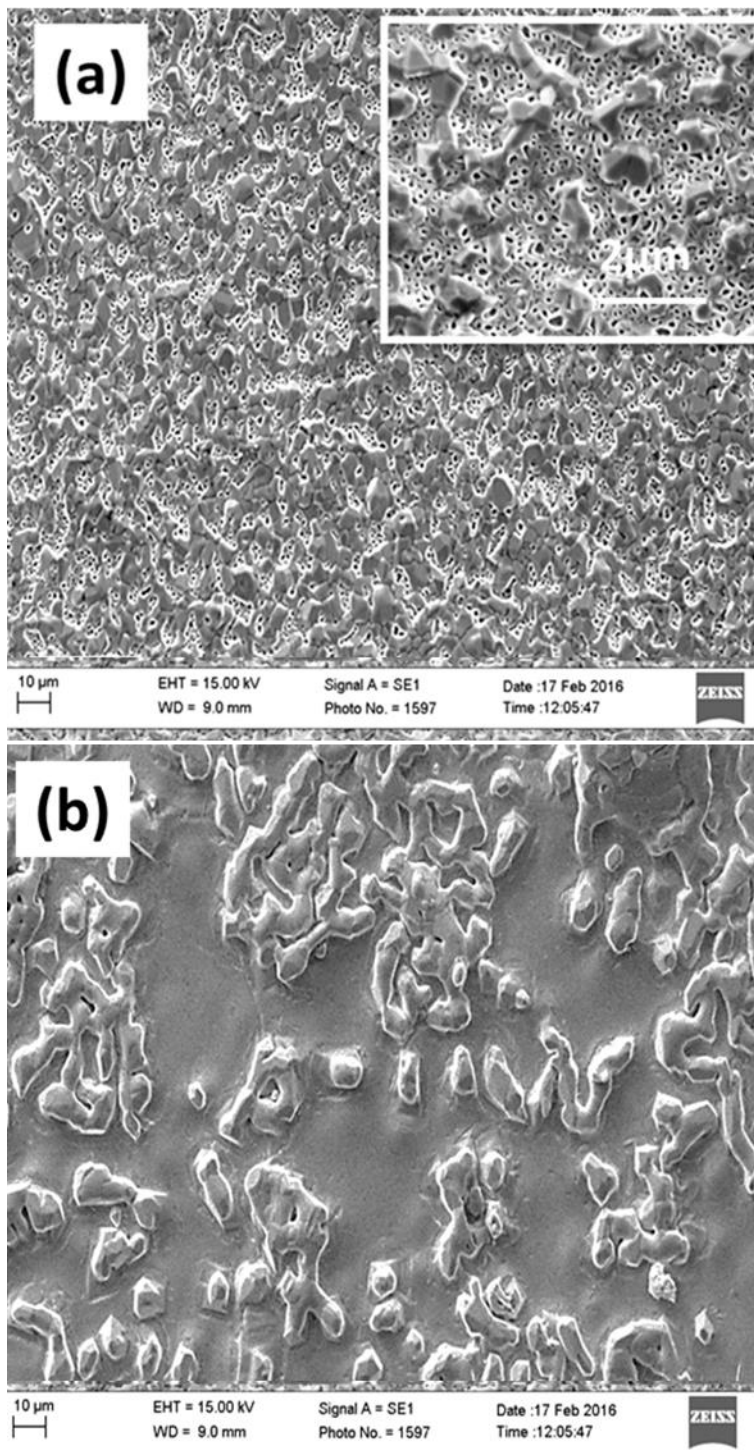


Figure 82 Surface morphologies of coatings produced at (a) 1000 °C (R6) and (b) 1100°C (R1) at 3 wt.% activator content and 6 hours. Inset shows R6 at magnification of 2 μ m.

The porous matrix will facilitate electrolyte-substrate interaction thereby deteriorating the corrosion resistance of R1. However, as temperature increased to 1100 °C, a compact surface with bigger- sized clusters and large grain size of network carbide which can provide better corrosion resistance than a porous coating was formed.

The enhancement of corrosion resistance as temperature increased from 1000 °C to 1100 °C can also be attributed to the phases formed at the different temperatures [241]. Figure 83 presents the XRD pattern of sample R6 and R1. The XRD patterns indicate that more nitrogen based compounds were formed at 1000 °C than 1100 °C. This observation can be related to the diffusion of chromium into the substrate at the chromising temperature. At 1000 °C, chromium diffusion into the substrate is slower than at 1100 °C; hence the nitrogen released by the activator can react with the un-diffused chromium at the surface to form chromium iron nitrides.

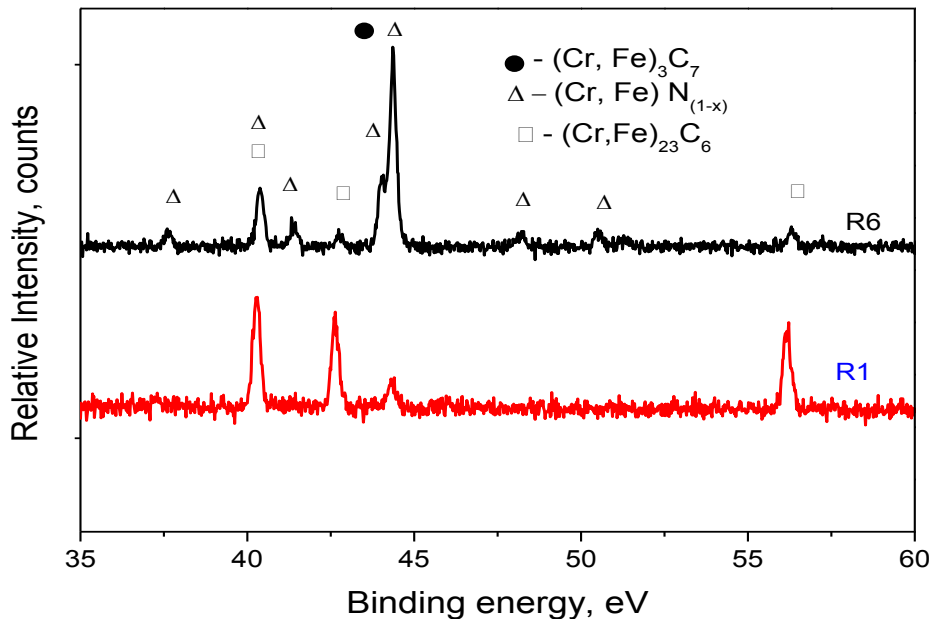


Figure 83 XRD of chromised coating formed with process parameters specified for R6 and R1.

II. Influence of time

It can be deduced from the perturbation plot in Figure 81 shows that time had a linear influence on corrosion current density of chromised 304 stainless steel in 0.5 M H₂SO₄ + 2 ppm HF at 70°C. This effect could be related to the surface morphologies of the coatings as time increased. Longer duration of chromising treatment can facilitate higher coating thickness at constant temperature and activator content as indicated by the thickness of the coatings in Table 18 and agrees with Naiming et. al.'s work on chromising of low carbon steel [201]. The chromised coating formed is more susceptible to defects such as voids pores and cracks as shown in Figure 84 for samples R12 and R17 pack-cemented for 3 hours and 9 hours respectively. These defects originate from the difference in the inward diffusion rate of chromium and outward diffusion rate of carbon (otherwise called Kirkendall effect). Coating defects are well known to compromise the anti-corrosion properties of coatings [242, 243]. Hence, the coatings pack cemented for 9 hours exhibited higher corrosion current density. Similar observation was reported by Cho et al. [25] for chromised 316 stainless steels polarised in 0.5 M H₂SO₄ at 80 °C.

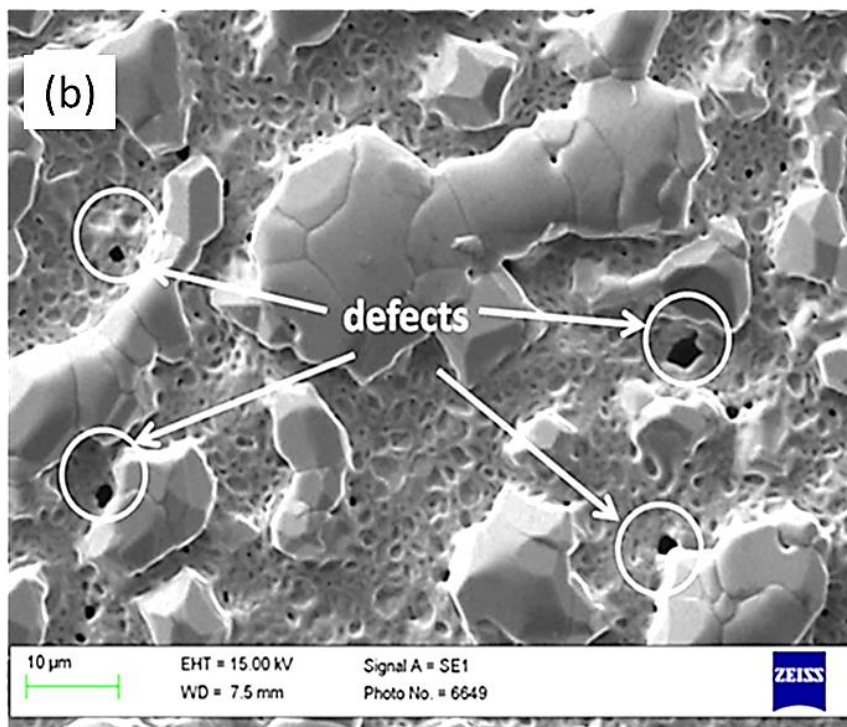
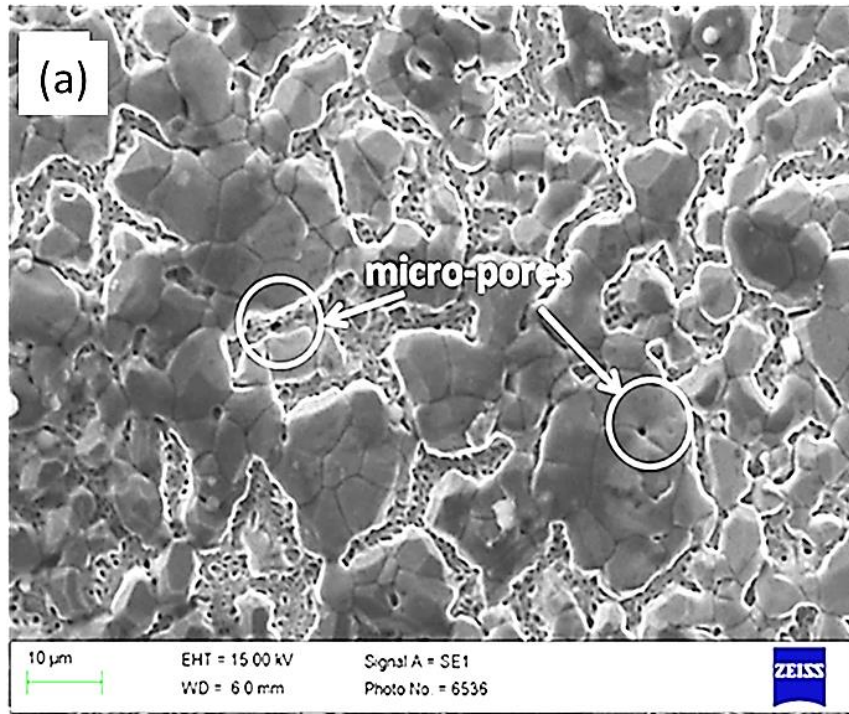


Figure 84 Surface morphologies of coatings formed at process parameters indicated by (a) R12 and (b) R17.

III. Influence of activator content.

The perturbation plot shown in Figure 81 indicates that the influence of activator content on corrosion current density of chromised 304 stainless steel in 0.5 M H₂SO₄ + 2 ppm HF at 70°C is considerably low. This observation can be supported by the surface morphologies of sample processed with process parameter specified by R12 and R13 (Figure 85). It can be seen that similar surface morphologies were produced at 3 wt. % and 7 wt. % activator content. This observation is consistent with previous studies on chromising of low carbon steel [19] and suggests that the range of the activator content used in the study is within acceptable range for pack cementation of stainless steels as it is reported that insufficient or excess amount of activator content can facilitate coatings with high volume of pores [198].

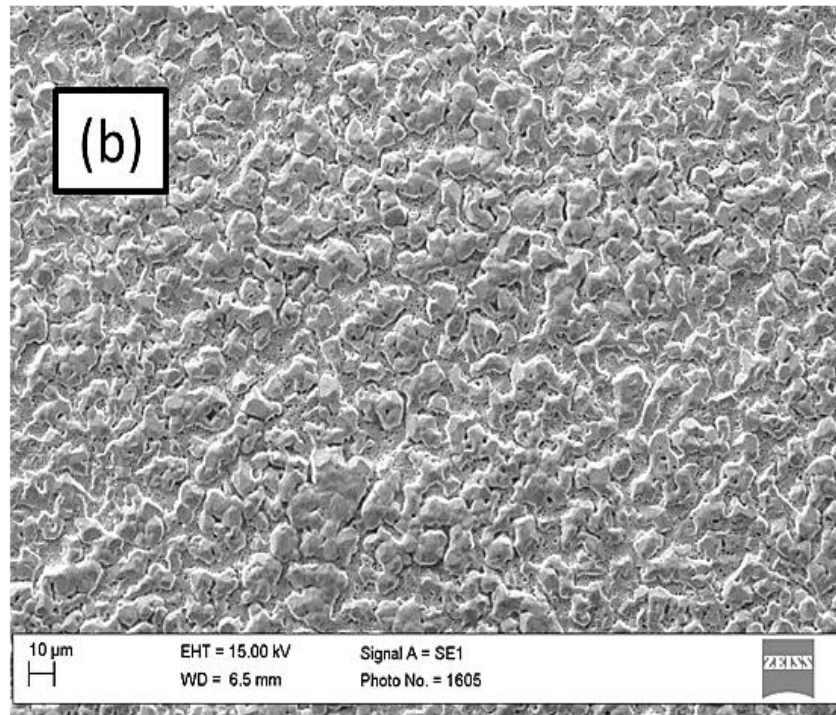
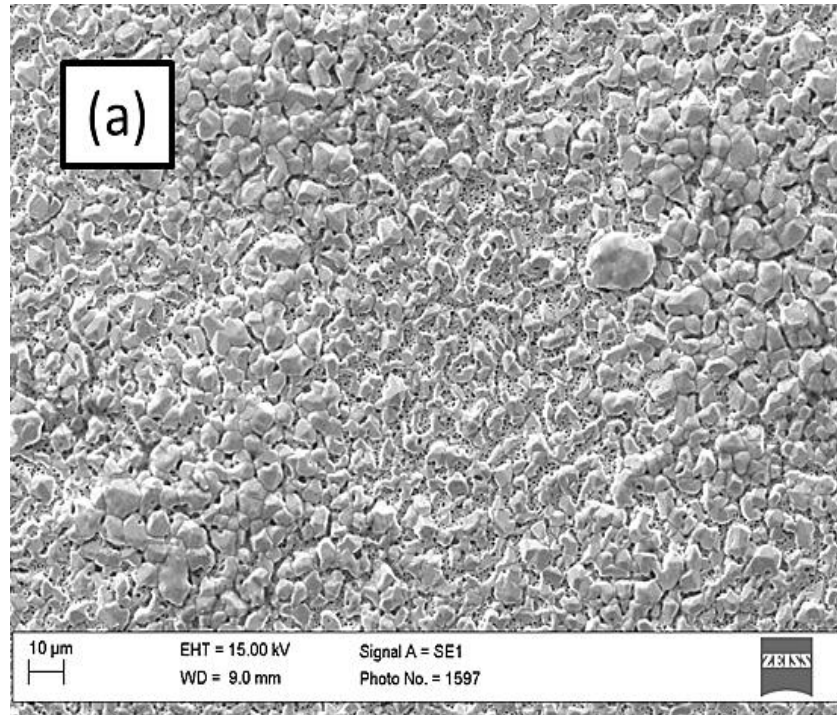


Figure 85 Surface morphologies of coatings produced at 1100°C for 3 hours with powder containing (a) 3 wt.% (R12) (b) 7wt% activator content (R13).

(IV) Interaction effect between temperature and activator content

The interaction effect between temperature and activator content as indicated by the corrosion current density model given in Equation 38 is depicted graphically by the contour plot (Figure 86) and the response surface plot (Figure 87).

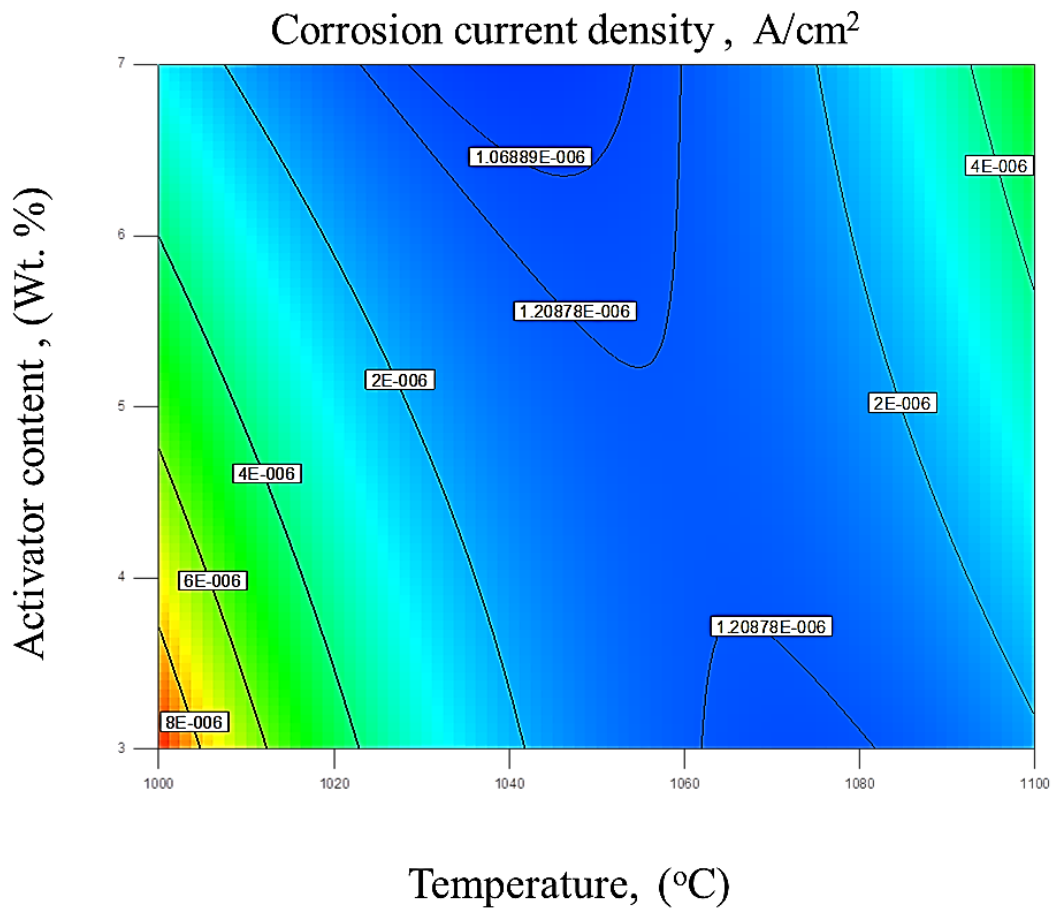


Figure 86 Contonur plot showing the interaction between temperature and activator content.

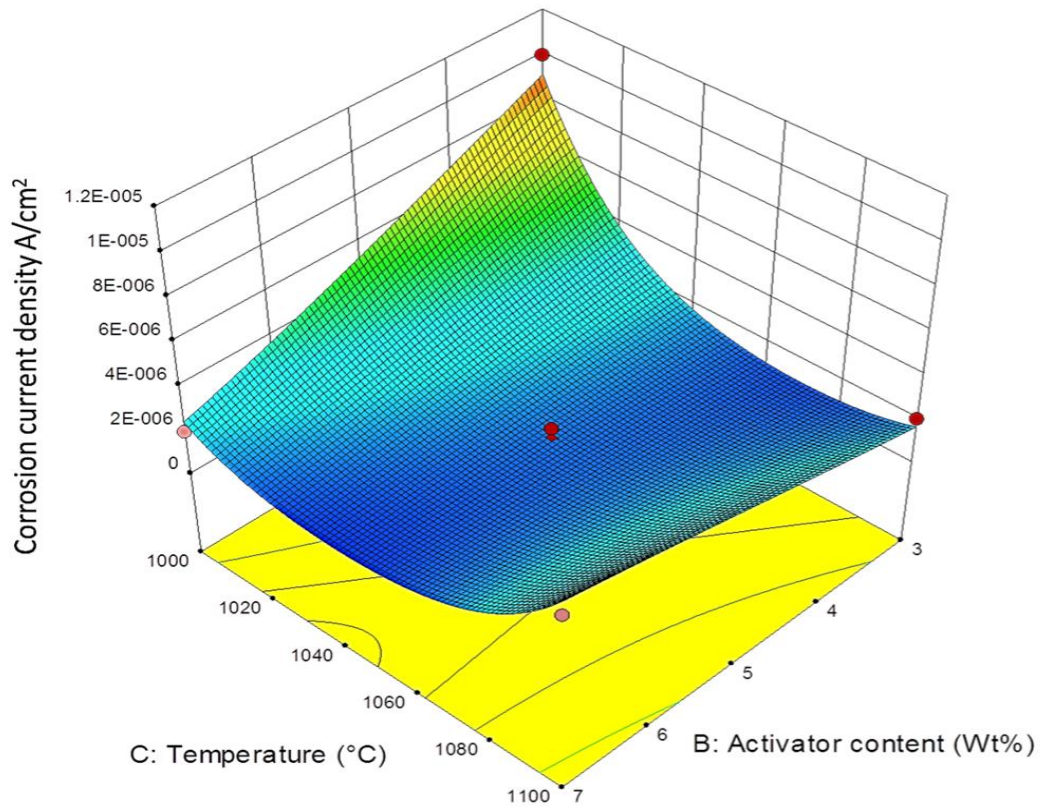


Figure 87 Response surface plots showing the interaction between temperature and time.

It can be seen in Figure 86 and 87 that at low temperature (1000°C), increasing the activator content from 3 wt. % to 7wt %, decreased corrosion current density. On the other hand, increasing the activator content at high temperature showed a reverse inverse effect albeit, marginally. An example of this interactive effect between temperature and activator content is given in Figure 88.

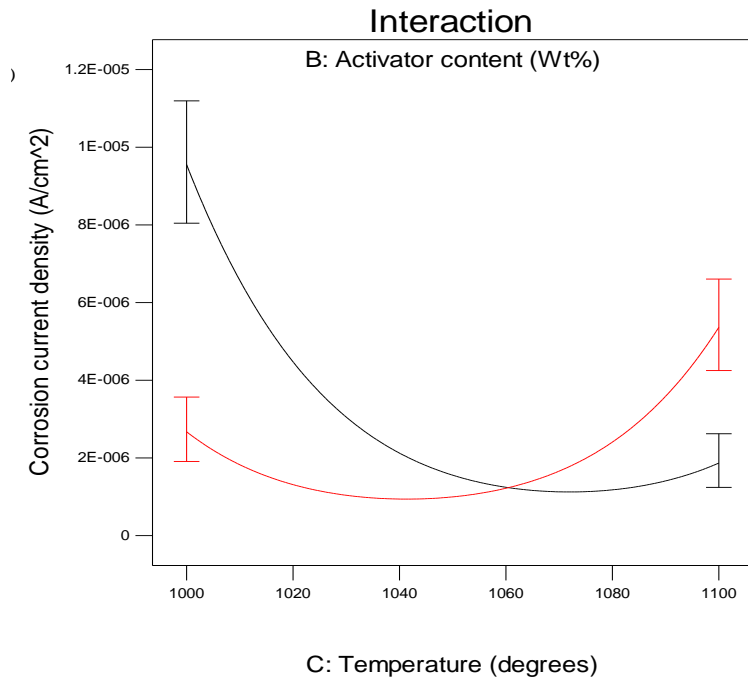


Figure 88 Interaction plot showing interaction between temperature and activator content.

In Figure 88, it can be seen that at low temperature of 1000°C and activator content of 3 wt. % , corrosion current density was 1×10^{-5} A/cm², however, as activator content increases to 7 wt. %, corrosion current density decreased by about one order of magnitude. On the other hand, as temperature increased to 1100°C, the effect of the activator content becomes less pronounced causing a marginal decrease in corrosion current density as seen in Figure 88. This interaction effect between temperature and activator content could be attributed synergy between the diffusion rate of chromium and carbon at the chromising temperature.

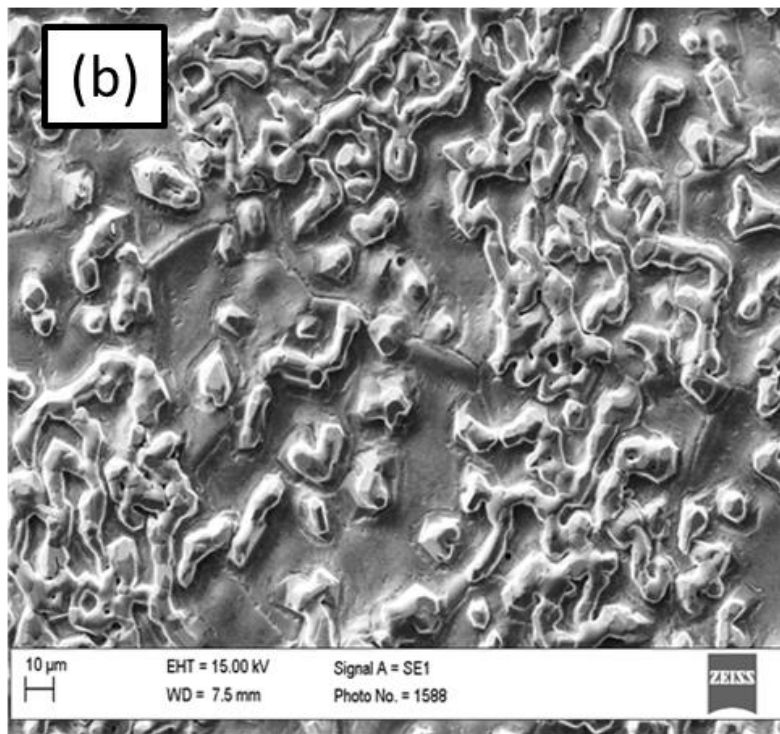
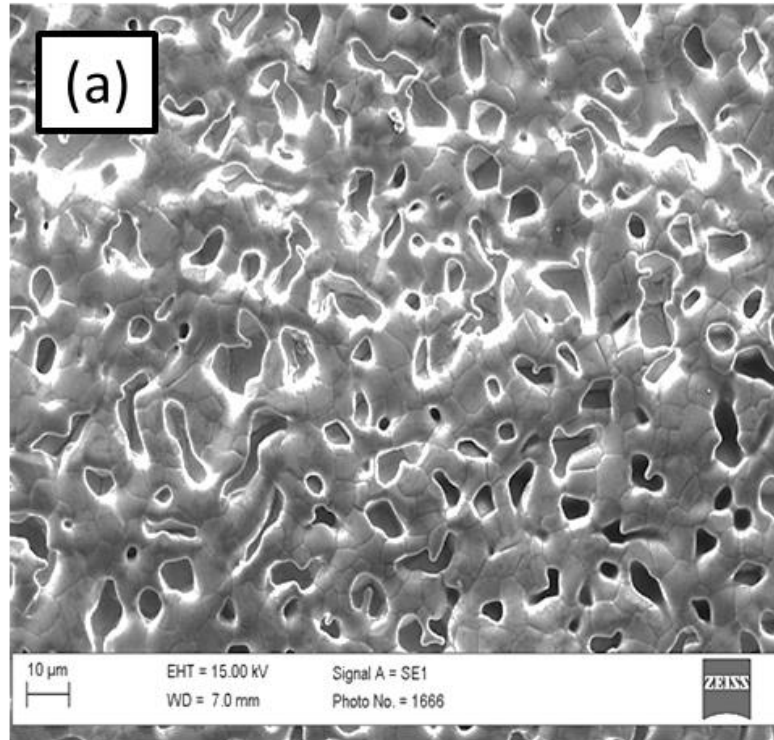


Figure 89 Surface morphology of (a) R1 and (b) R9.

Fast chemical kinetics and high diffusion rates engendered by a combination of high activator content (7wt. %) and temperature (1100 °C) respectively promote formation of voids and cavities. as seen in the surface morphology of R1 (Figure 89(a)). On the other hand, a combination of low activator content (3 wt. %) and high temperature (1100 °C) promote a compact structure with fewer pores and discrete particles of chromium nitrides (Figure 89 (b)). Similarly, slow chemical kinetics and low diffusion rates facilitated by low activator content (3 wt.%) and low temperature (1000 °C) engendered a porous network structure (Figure 90 (a)) which is susceptible to attack in the aggressive PEM fuel cell environment. On increasing the activator content to 7 wt.%, the porous nature of the morphology is still sustained but with a higher volume of chromium iron nitride particles as seen in Figure 90 (b)). These observations are consistent with the fact that insufficient or excess amount of activator content can facilitate coatings with high volume of pores [199]; however, the interactive effect between temperature and activator content has not been reported before now.

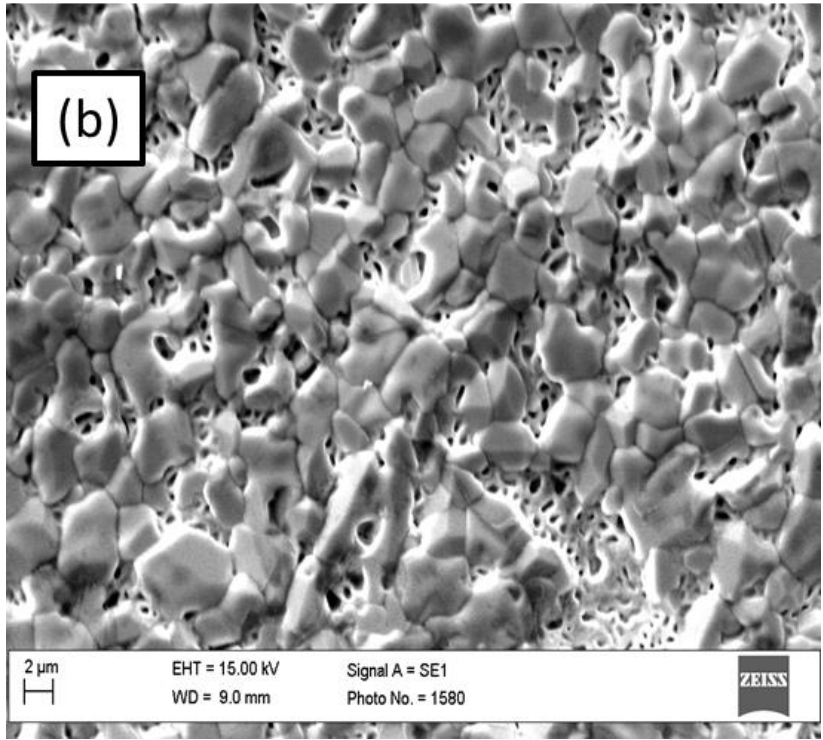
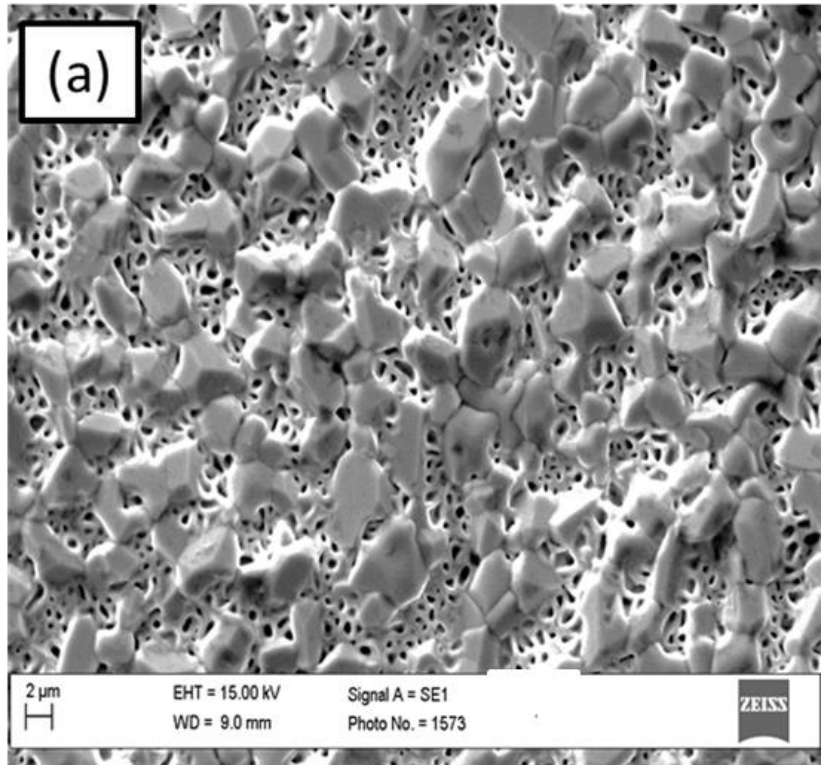


Figure 90 Surface morphology of R6 and (b) R3.

C. Process optimisation

Optimum condition for deposition of chromised coatings with minimum corrosion current density in simulated PEM fuel cell environment of 0.5 M H₂SO₄ + 2 ppm HF at 70 °C within the investigated experimental range was obtained by numerical simulation coupled with the desirability function. This method determines the optimum condition by first locating the level of each factor that can achieve the predicted response, after which the overall desirability is maximised based on the set goals [195, 196]. The constraints applied for optimisation are as shown in Table 21. Numerical simulation results predicted a set of solutions with desirability value of 1; however, the condition selected by the software indicated that optimal process parameters were: activator content of 6.84 wt.%, Time of 3.04 hours and Temperature of 1040°C, with a predicted corrosion density value of 3.895×10^{-7} A/cm² and thickness of 30.84 μm as shown in Figure 91. Experiments to validate the model produced a ~30 μm chromised layer which had an average corrosion current density value of 4.304×10^{-7} A/cm² when polarised in aerated 0.5 M H₂SO₄ + 2 ppm HF at 70 °C. In Figure 92, the Tafel plot of the optimised chromised stainless steel and the substrate in the simulated PEM fuel cell environment are compared.

Table 21 Constraints for optimisation

Factor	criteria	Lower limit	Upper limit	Importance
Time (hours)	In range	3	9	3
Activator content (wt.%)	In range	3	7	3
Temperature (°C)	In range	1000	1100	3
Thickness (µm)	In range	19.035	92.085	3
Corrosion current density (A/cm ²)	minimise	4.05x 10 ⁻⁷	1 x 10 ⁻⁵	5

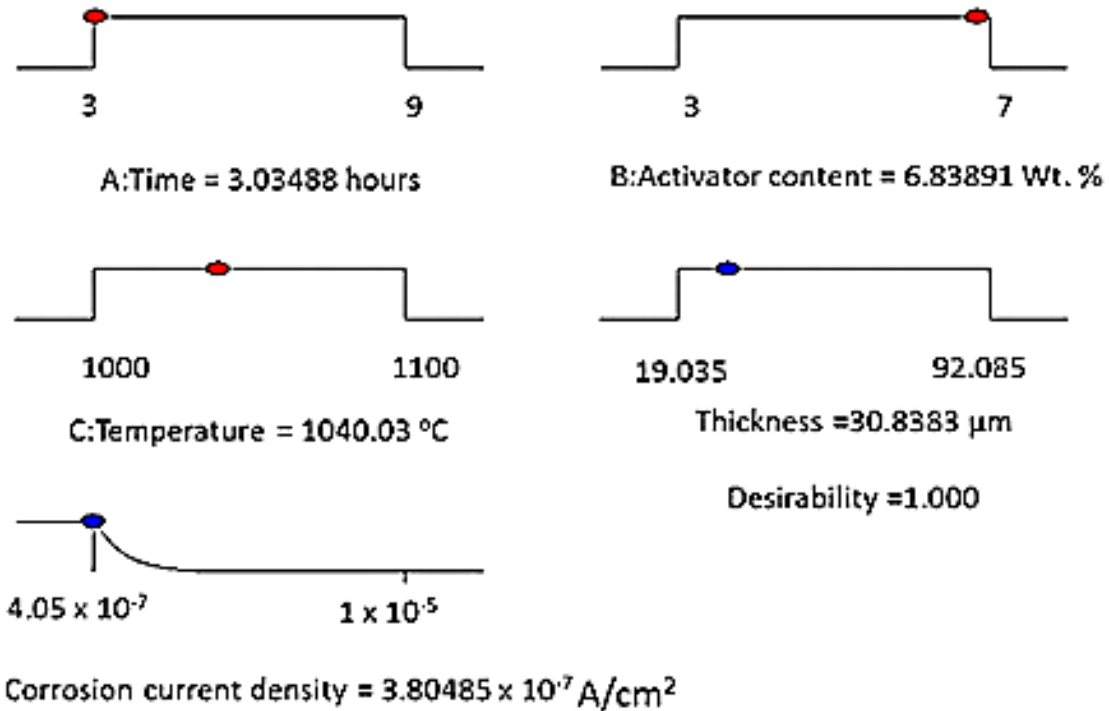


Figure 91 Optimum conditions for minimum corrosion current density of chromised 304 stainless steel in 0.5 M H₂SO₄ + 2 ppm HF at 70 °C.

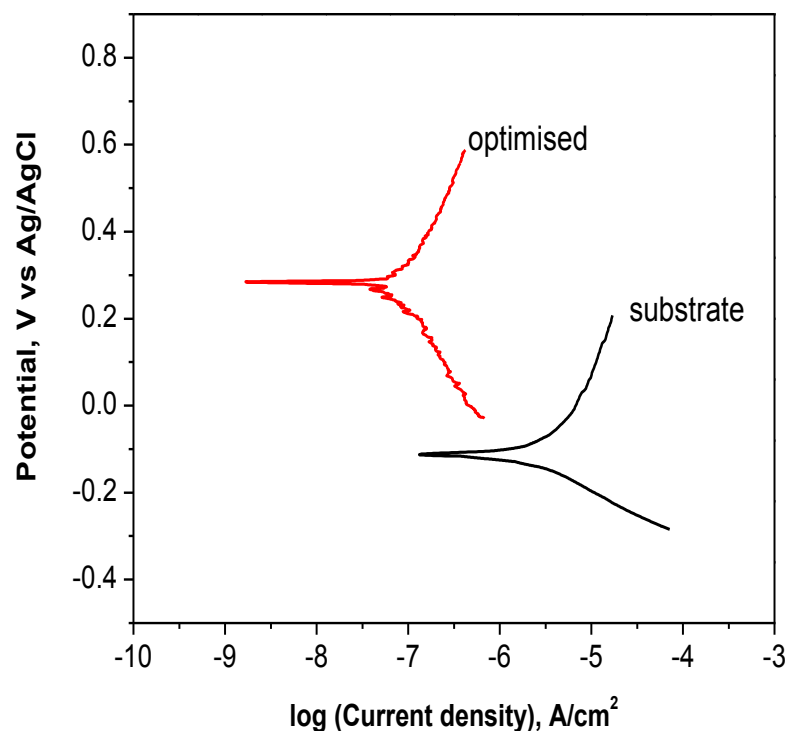


Figure 92 Tafel plot for coating produced with optimal process parameters and the substrate in 0.5 M H₂SO₄ + 2 ppm HF at 70 °C. Scanning rate = 1mV/s.

6.3 EVALUATION OF OPTIMISED CHROMISED COATING

(A) Surface characterisation

I. Surface Morphology and Composition

The surface morphology and chemical composition of the chromised 304 stainless steel produced at optimal process parameters (afterward named Cr-304) is presented in Figure 93. The SEM image (Figure 93(a)) revealed a granular surface morphology with surface micro-pores attributed to the Kirkendall effect during solid state diffusion of chromium into the substrate at the

chromising temperatures [25, 26, 182]. EDX composition analysis of the surface (Figure 93(b)) indicated that the chromised surface consisted primarily of chromium, carbon and nitrogen as well as small amount of oxygen and iron. Trace amount of nickel and aluminium were also present. The presence of Al is attributed to the alumina in the pack powder mixture while that of nitrogen is due to decomposition of the NH_4Cl activator. The presence of Fe in the EDX composition is due to the fact that the coating is formed in a solution of iron [183,184]. Figure 94(a) presents the cross sectional view of Cr-304. The coated layer was estimated to have a thickness of $\sim 30\mu\text{m}$ (Figure 94 (b)).

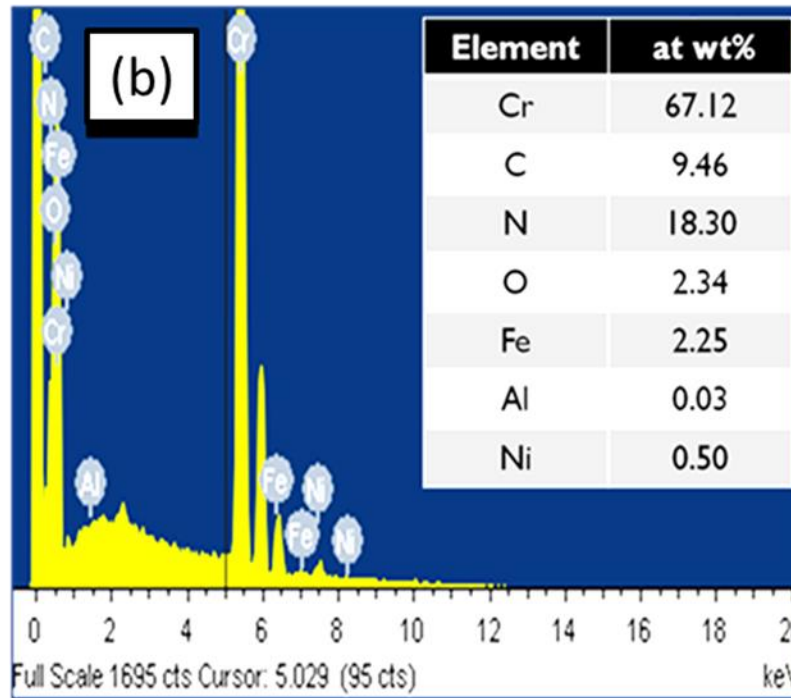
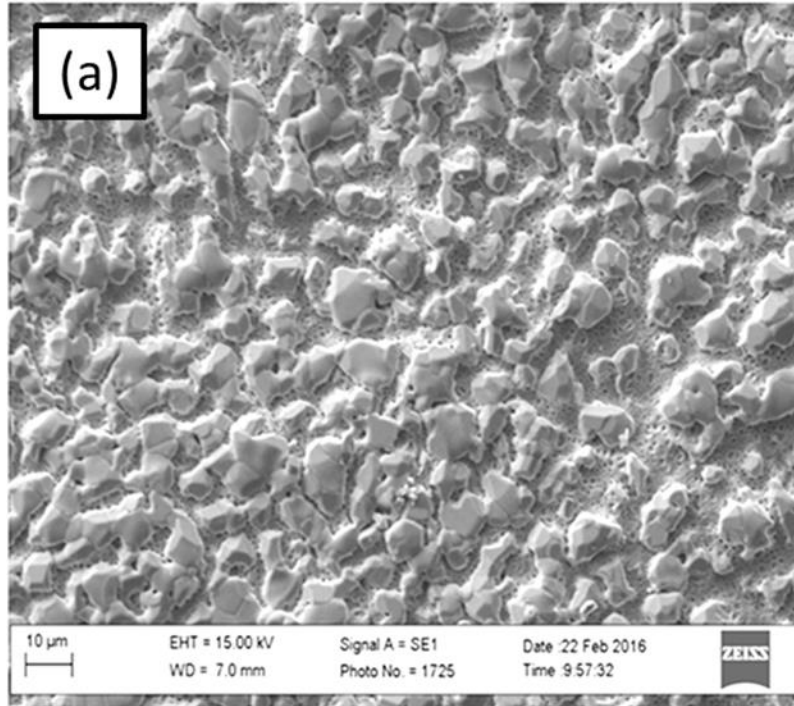


Figure 93 Chromised coatings produced at optimised process parameters (a) Surface morphology of the optimised coating (Cr-304) (b) EDX spectrum and average composition.

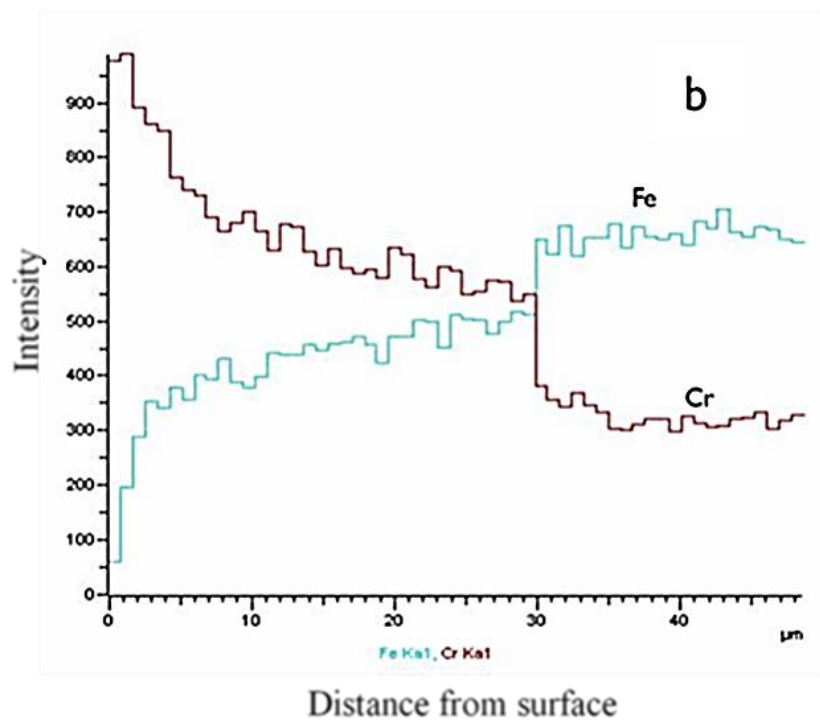
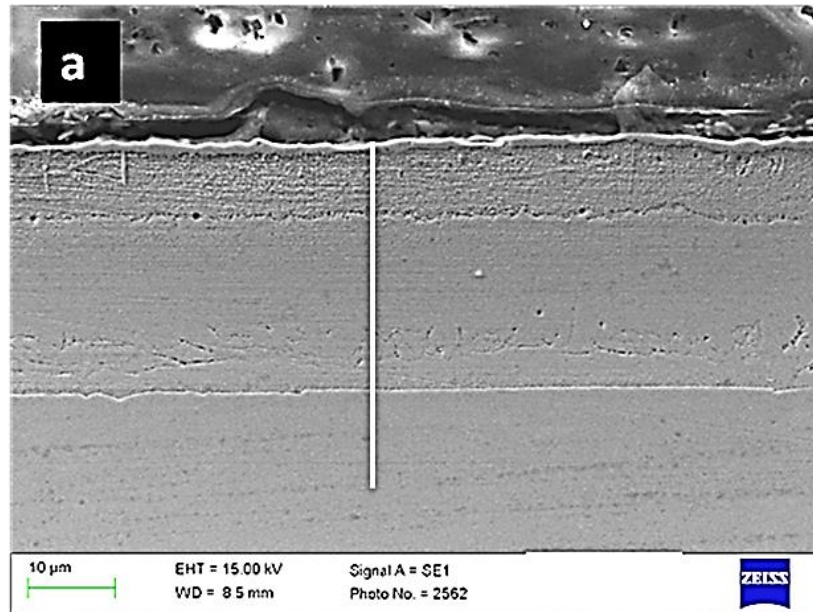


Figure 94 Chromised coatings produced at optimised process parameters (a) Cross-section SEM image (b) EDX line scan of Cr-304.

II. X-ray photoelectron spectroscopy

Figure 95 presents the XPS survey spectra of Cr-304 before and after sputtering. The XPS spectrum before sputtering revealed the presence of Cr, C, and O, however, on sputtering, additional elements: N and Al were observed. Photoelectron peaks of Fe2p were not detected on the outermost layer suggesting minimal concentration of Fe on the outermost layer in agreement with Ralston et.al. [186] investigation on chromised 304 stainless steel produced by fluidised bed CVD at 1000 °C for three hours. The presence of an Al2p peak at 74-75 eV confirms the presence of alumina [218], as suggested by the EDX compositional analysis. Considering alumina and adventitious carbon as contaminants, the estimated composition of the coatings given in Table 22 indicates that the Cr, N, C (carbide) content on the outermost layer increases as the sputtering time increases while the concentration of oxygen and carbon decreases as sputtering time increases.

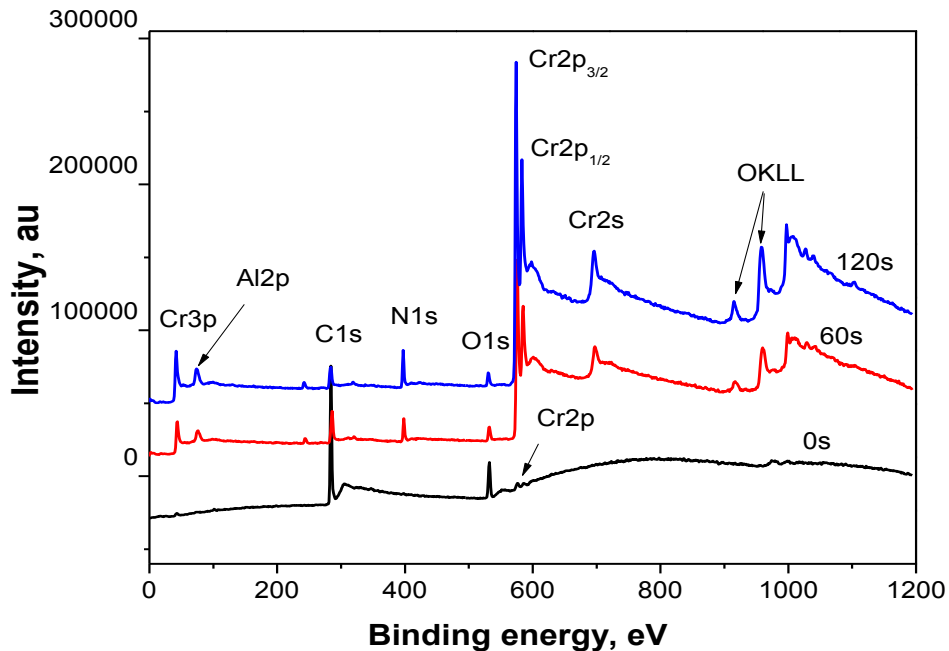


Figure 95 Survey spectrum of Cr-304 before and after argon ion sputtering.

Table 22 XPS parameters for composition and binding energy of Cr-304 with the sputtering profile.

Time of sputtering (Seconds)	Cr (*at. %)	C (Carbide) (*at. %)	C Adventitious (*at. %)	O (*at. %)	N (*at.%)	Fe (*at. %)
0	1.06	-	88.56	10.44	-	-
60	46.52	-	34.45	6.97	12.06	-
120	59.76	10.21	10.20	4.49	15.34	-

*at. %-atomic percentage

The chemical oxidation state of the major elements identified in Table 22 is presented in Figure 96. The C1s spectrum presented in Figure 96(a) indicates the presence of C-C and C=O bonds, attributed to surface contamination, at ~284.5 eV and ~289 eV respectively before sputtering. On sputtering for 1 minute, the C-C bonds was shifted to ~285 eV and its intensity was significantly reduced, while the C=O bond was eliminated. A small intense peak attributed to chromium carbide appeared at ~283 eV. However, on further sputtering, the C-Cr peak is shifted to 282.5 eV while that of C-C is shifted back to 284.5 eV. The C-Cr bond is attributed to chromium carbide formed by the reaction between the inwardly diffused chromium and the outwardly diffused carbon.

The O1s spectrum presented in Figure 96 (b) revealed the presence of Cr-OH bonds at ~532 eV, Cr-O bonds at 530.4 eV before sputtering [218]. The Cr-OH bond is attributed to surface contamination while the Cr-O bonds are due to surface oxidation.

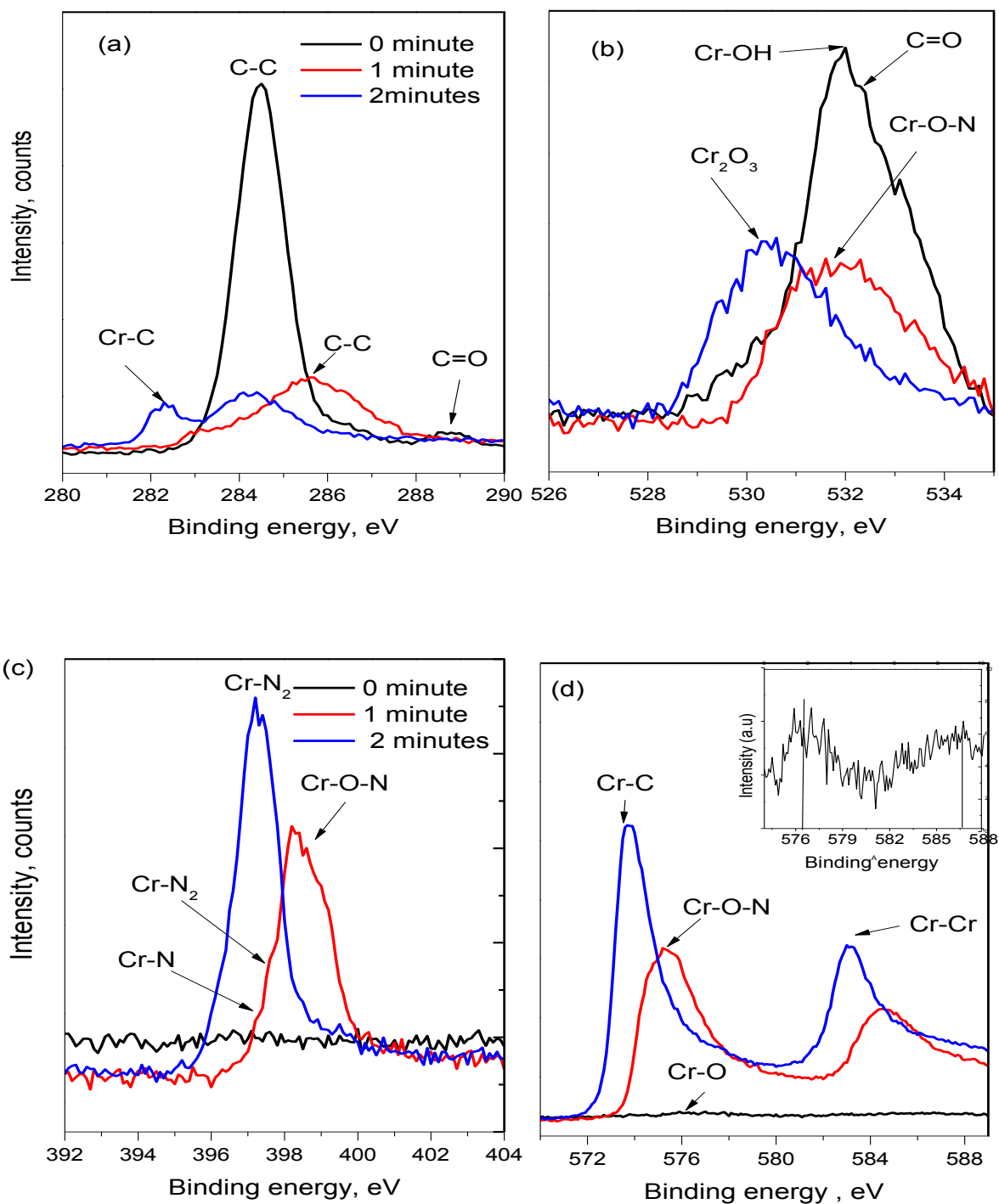


Figure 96 XPS spectrum of (a) Carbon (b) Oxygen (c) Nitrogen and (d) Chromium in Cr-304 after 0s, 60s and 120s of sputtering. Inset of (d) shows the Cr2p before sputtering.

After 60 seconds of argon ion sputtering, the wide nature of the O1s spectrum indicate the presence of Cr-O bonds, Cr-O-N and Cr-OH bonds sat 530.4 eV, 531.2 eV and 532 eV respectively [116, 117, 118-120]. The Cr-O-N bonds are attributed to chromium nitrides in oxygen environment otherwise called chromium oxynitride. These types of nitrides are formed due to the similarity in the crystallographic structure of CrN and Cr₂O₃. Hence, their electrical conductivity depends on the oxygen content and range between that of CrN (~5.5 x 10⁻¹ S/cm at room temperature) and Cr₂O₃ (~1.8 x 10⁻⁷ S/cm at room temperature) [244]

The N1s spectrum shown in Figure 96 (c) established the presence of three types of Cr-N bonds attributed to Cr (O)_x N_y, CrN and Cr₂N at 398.4 eV, 396 eV and 397.3 eV respectively in agreement with binding energies reported for chromium nitrides [116, 218-220, 244, 245]. Chromium nitrides are formed from the reaction between chromium and nitrogen decomposed from the activator.

Figure 96 (d) displays the Cr2p spectrum for the outermost layer of Cr-304. The presence of Cr2p peaks at ~577 eV and ~586 eV as shown in the inset of Figure 96 (d) establishes the presence of chromium oxide and hydroxide respectively before sputtering [218]. After sputtering, the presence of chromium-oxy-nitrides confirmed by Cr2p peaks at 573.9 eV and 583.3 eV [219, 220], while that of chromium carbide is established by Cr2p peaks at 573.9 eV and 583.3 eV [235, 236].

III. Glancing incidence angle XRD

Figure 97 displays the glancing incidence XRD (GXR) patterns of Cr-304 at 0.5-5°. The GXR patterns indicates the presence of (Cr, Fe)₂₃C₆, (Cr, Fe)₃C₇ and (Cr, Fe)₂N_{1-x} (where x = 0 - 0.5) phases at incidence angle of 5°. No austenite phase was detected at this depth as the thickness of the coating was higher than the depth of X-ray penetration (10µm). As incidence angle decreases

from 5° to 2° , intensity of $(\text{Cr, Fe})_3\text{C}_7$ peaks gradually diminished and finally disappeared at an incidence angle of 1° , suggesting that only $(\text{Cr, Fe})_{23}\text{C}_6$ and $(\text{Cr, Fe})_2\text{N}_{1-x}$ phases are present on the outermost layer. A similar observation was reported by Lee et al. [246] for chromised Fe–Mn–Al–Cr alloy.

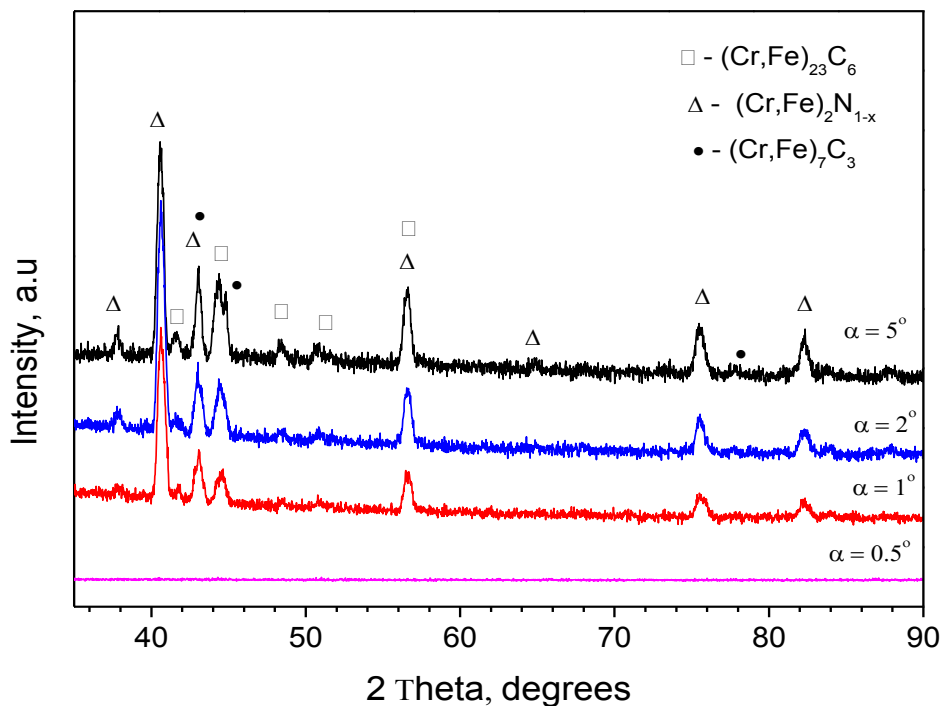


Figure 97 Glancing incidence angle XRD of Cr-304.

It can be further observed in Figure 97 that peaks due to alumina are absent in contrast to the XPS and EDX results. The absence of alumina peaks can be ascribed to very low concentration of alumina compared to that of the nitrides and carbides.

From the SEM/EDX, XPS and XRD results presented above, it can be concluded that the outermost layer of Cr-304 consist majorly of chromium iron nitrides, chromium iron carbide and chromium iron oxide. This analysis is in agreement with previous works on chromised stainless steels [25-28, 246].

(B) Electrochemical Polarisation

I. Potentiodynamic polarisation

Figure 98 (a) and (b) shows the potentiodynamic polarisation curves for Cr-304 and SS304 in 0.5 M $\text{H}_2\text{SO}_4 + 2 \text{ ppm HF}$ at 70°C with air and hydrogen gas bubbling to simulate PEM fuel cell cathode and anode environments respectively. The corrosion parameters obtained for both Cr-304 and the substrate (SS304) are presented in Table 23. From the corrosion potential (E_{corr}) and corrosion current density (i_{corr}) values in Table 23, it can be deduced that in both environments, Cr-304 exhibited higher E_{corr} and lower i_{corr} values compared to SS304, thus, implying that chromising treatments improved the corrosion resistance of the substrate in agreement with previous studies [25-29].

In the simulated cathode environment (Figure 98 (a)), both Cr-304 and SS304 exhibit similar passive –transpassive behaviours. It can also be seen from Figure 98 (a) that at typical PEM fuel cell cathode working potential of 0.6 V, both Cr-304 and SS304 are within the passive region. On the other hand, at the anode potential Cr-304 the open circuit potential of Cr-304 is close to the anode PEM fuel cell working potential while SS304 is still within the passive region in the simulated anode environment. Furthermore, in the anode environment, SS304 exhibited an active region of dissolution after which it experienced similar passivity behaviour with Cr-304 within a potential range of $\sim -0.1 \text{ V}$ to $+0.9 \text{ V}$. The improvement in corrosion behaviour of Cr-304 compared to SS304 in both oxidising and reducing environments is

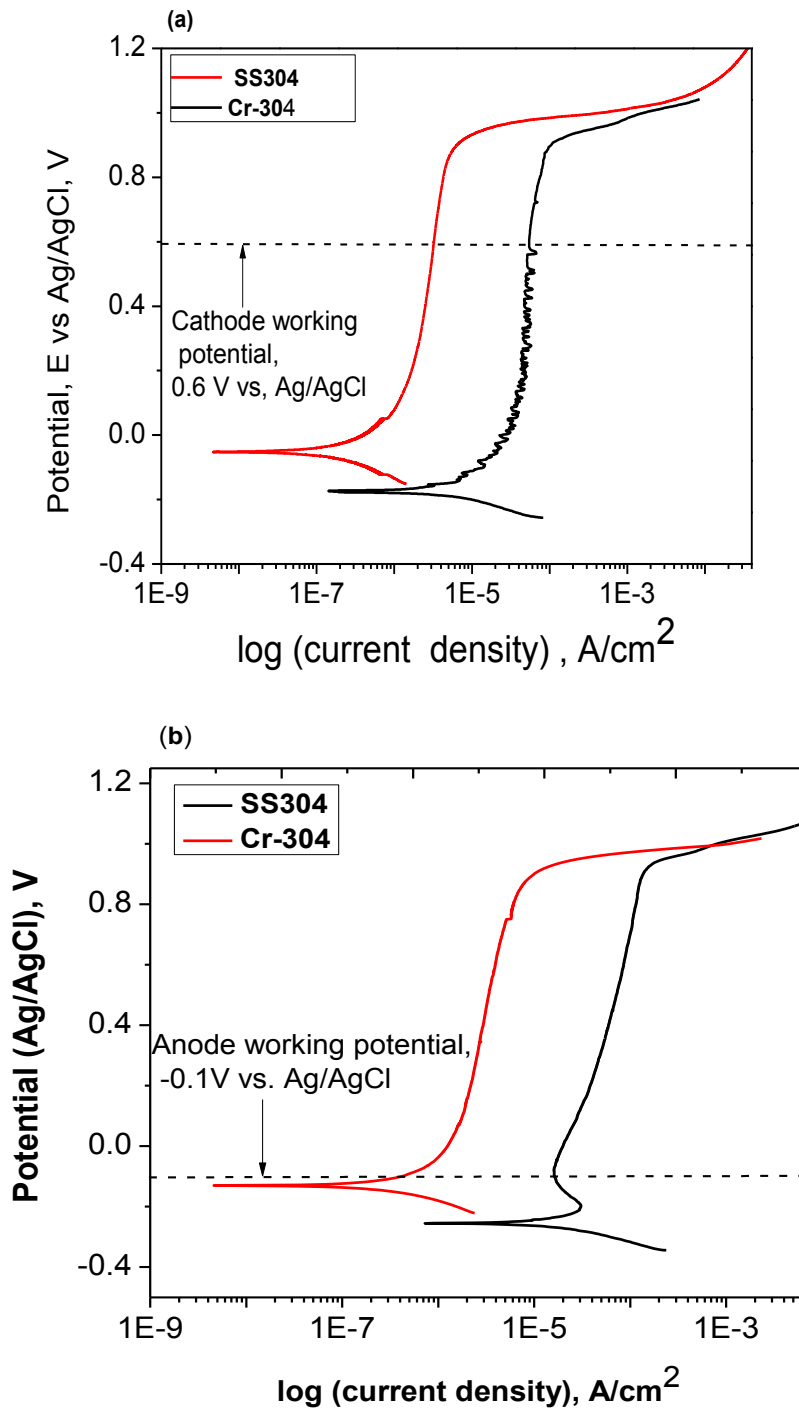


Figure 98 Potentiodynamic polarisation of Cr-304 and SS304 in 0.5 M H₂SO₄ + 2 ppm HF at 70 °C (a) air bubbled (b) hydrogen bubbled into the electrolyte, scan rate = 1 mV/s.

Table 23 Corrosion parameters of SS304 and Cr-304 in simulated PEM fuel cell environments.

Material	E_{corr} (V vs Ag/AgCl)		i_{corr} ($\mu\text{A}/\text{cm}^2$)	
	Cathode	Anode	Cathode	Anode
	Cr-304	-0.52	-0.13	0.47
SS304	-0.17	-0.25	5.38	60.10

attributed to the presence of chromium nitrides and carbides on the chromised layer as revealed by XPS and XRD results.

III. Potentiostatic Polarisation

Potentiostatic Polarisation curves for Cr-304 and SS304 under simulated PEM fuel cell cathodic and anodic conditions are presented in Figure 99. In simulated cathodic conditions of 0.6 V and air bubbling (Figure 99), both materials experienced an initial current decay as soon as the potential was applied. The current decay is related to the formation of passive oxide and is consistent with the potentiodynamic polarisation result, wherein both materials are within the passive region at 0.6 V. After the current decay, SS304 stabilised at $\sim 20 \mu\text{A}/\text{cm}^2$ and Cr-304 at $\sim 2 \mu\text{A}/\text{cm}^2$, representing an order of magnitude reduction in corrosion current density of SS304.

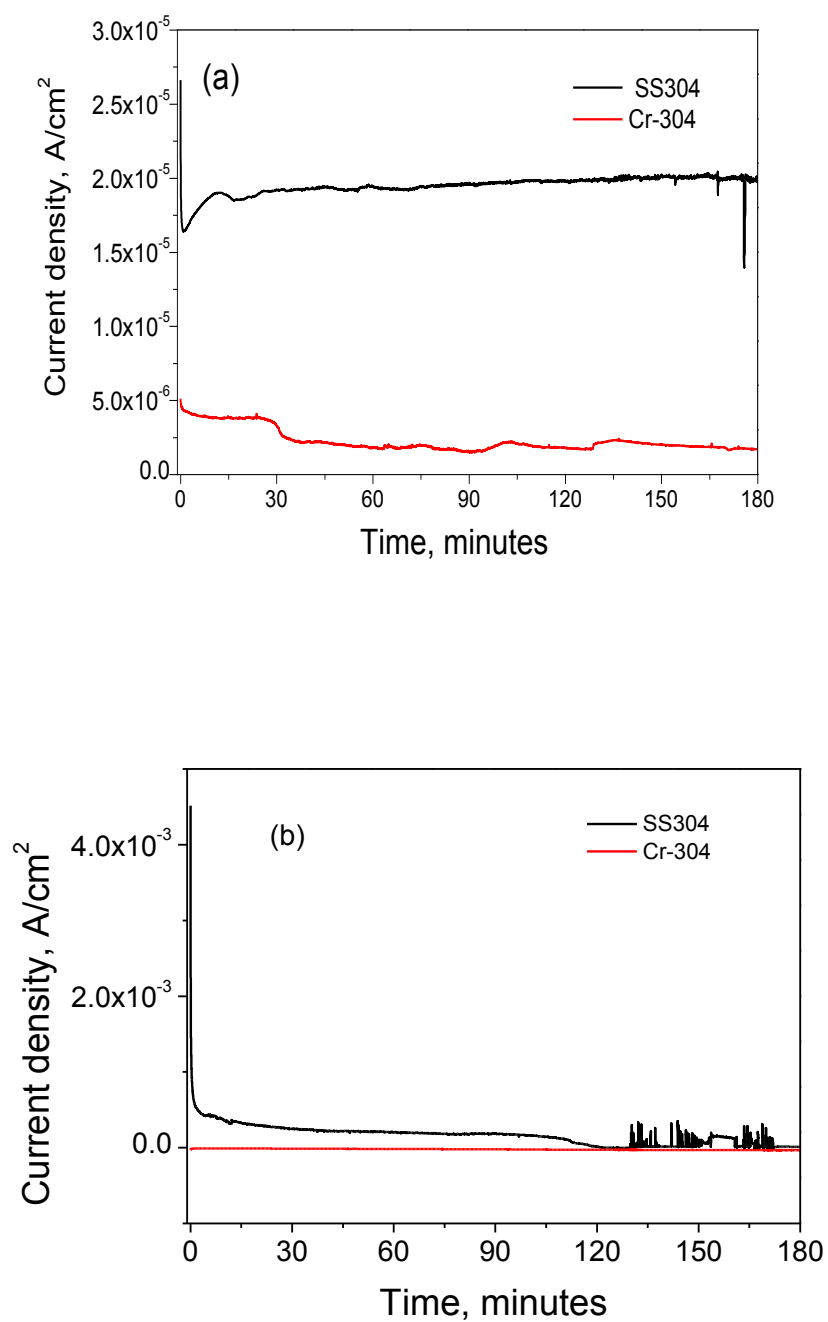


Figure 99 Potentiostatic polarisation of Cr-304 and SS304 in 0.5 M H₂SO₄ + 2 ppm HF at 70 °C in simulated PEM fuel cell (a) cathodic environment, E = 0.6 V vs. Ag/AgCl (b) anodic environment, E= -0.1 V vs. Ag/AgCl. Scan rate = 1 mV/s.

At the anode, Cr-304 exhibited low current density stabilising at $-6 \mu\text{A}/\text{cm}^2$ after 180 minutes of polarisation. On the other hand, SS304 stabilised at about $161 \mu\text{A}/\text{cm}^2$ within the 100 minutes of polarisation after which it finally stabilised at about $10.5 \mu\text{A}/\text{cm}^2$ (Figure 99 (b)).

Comparing the corrosion performance of Cr-304 in $0.5 \text{ M H}_2\text{SO}_4 + 2 \text{ ppm HF}$ described above with other published work on chromised stainless steel without pre-treatments [37-41] as shown in Table 24. It can be seen that Cr-304 exhibited remarkable reduction in corrosion current density compared to untreated chromised stainless steel (No. 2-4 in Table 24), while it showed comparable performance with pre-treated and chromised SS316L and 420 stainless steels (No. 5 & 6 in Table 24). The improved performance of Cr-304 is attributed to a thicker chromised layer and the beneficial effect of the optimisation via design of experiment approach.

Table 24 Comparison of the performance of Cr-304 with published works on chromised stainless steels for PEM fuel cell bipolar plate application.

S/N	Chromised stainless steel (processing conditions)	Potentiostatic polarisation current density		Ref.
		Cathode	Anode	
1.	SS304 (1040 °C, ~3 hours)	2-5 $\mu\text{A}/\text{cm}^2$ (3 hours @ 70 °C)	- 6 $\mu\text{A}/\text{cm}^2$ (3 hours @ 70 °C)	Present study
2.	SS316 (1050 °C, 2.5 hours)	-	10 $\mu\text{A}/\text{cm}$ range (4 hours @ 80 °C)	26
3.	SS316 (1100 °C, 2.5 hours)	10 $\mu\text{A}/\text{cm}^2$ (4hrs @ 80 °C)	-	25
4.	SS316 (1100 °C, 3 hours)	10 $\mu\text{A}/\text{cm}^2$ (3 hours @ 70 °C)	0.1 $\mu\text{A}/\text{cm}^2$ (3 hours @ 70 °C)	27
5.	SS316 (shot peened + 900 °C, 3 hours)	10 $\mu\text{A}/\text{cm}^2$ (3 hours @ 70 °C)	0.01 $\mu\text{A}/\text{cm}^2$ (3 hours)	27
6.	SS420 (Rolling + 700 °C, 2 hours)	5 $\mu\text{A}/\text{cm}^2$ (1 hours @ 80 °C)	-	28

(C) Interfacial contact resistance

Figure 100 displays the ICR of Cr-304 and SS304 as a function of compaction pressure. For both materials, ICR decreases as compaction pressure increases due to increasing contact area between the carbon paper and the metal samples. Cr-304 exhibited an order of magnitude decrease in ICR compared to SS-304 within the range of compacting pressure investigated signifying the beneficial effect of chromising on surface conductivity of SS304.

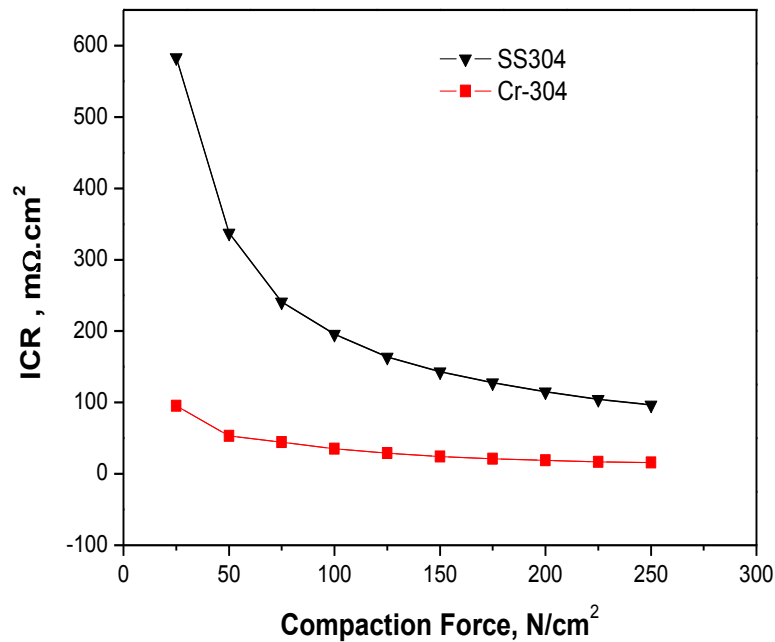


Figure 100 ICR of Cr-304 and SS304 as a function of compaction pressure.

At the compaction pressure range of interest for PEM fuel cell applications (i.e. 100-200 N/cm²) [115, 116], SS304 exhibited ICR values in the range of 195.7-114.9 mΩ/cm² while Cr-304 exhibited ICR values in the range of 35.1-19 mΩ/cm². Furthermore, at typical PEM fuel cell compaction pressure of 150 N/cm², Cr-304 exhibited ICR value of 24 mΩ.cm² while that of the

substrate was $143.29 \text{ m}\Omega/\text{cm}^2$. Reduction of ICR values after chromising treatments is ascribed to the conductivity of chromium nitrides and carbide on the outermost layer of Cr-304. As shown in the XPS analysis (Figure 96), the outermost layer of Cr-304 consisted of a mixture of chromium - carbide, nitrides, and oxides. Carbides and nitrides are well known to be more electrically conductive than naturally occurring surface oxides of the substrate, which consist primarily of iron oxide and chromium oxide [21, 64-66].

Tables 25 and 26 presents the ICR values for 304 and chromised stainless steels reported in the literature. Comparing these ICR values with that obtained for SS304 and Cr-304, it can be seen that the ICR values of SS304 and Cr-304 at typical PEM fuel cell compaction pressure were higher than ICR values reported in the literature. This increase can be attributed to the PTFE loading of the Toray carbon paper employed for the ICR measurement. It is well reported that increasing the PTFE loading on the GDL material increases the contact resistance measured between the bipolar plate and the GDL [57- 60]. In particular, Ismail et al. [59] reported about 50% increase in ICR of graphite plates when the PTFE loading of the carbon paper changed from 0% to 20-30 wt.%. It is, however, noted that previous work on chromised stainless steels did not specify the PTFE loading of the carbon paper employed for ICR measurements. Hence, it can be deduced from Figure 101, which compares the ICR of SS316 reported in Figure 75 with that of SS304 in Figure 100, that the increase in ICR values of SS304 and Cr-304 compared to that of the literature can be attributed to the nature of the carbon paper.

Table 25 ICR of 304 stainless steel in the literature

Material	ICR ($\text{m}\Omega\cdot\text{cm}^2$)	Ref.
304/304L stainless steel	~100 @ 150 N/cm ²	132, 149

Table 26 ICR of chromised stainless steel in the literature

S/ N	Chromised stainless steel (deposition temperature and time)	ICR ($\text{m}\Omega\cdot\text{cm}^2$)	Ref.
1.	SS316 (1050 °C, 2.5 hours)	17.0 @ 150 N/cm ²	[26]
2.	SS316 (1100 °C, 2.5 hours)	~17.0 @ 150 N/cm ²	[25]
3.	SS316 (1100 °C, 3 hours)	17.0 @ 200 N/cm ²	[27]
4.	SS316L (shot peened + 900 °C, 3 hours)	15.0 @ 200 N/cm ²	[27]
5.	SS420 (Rolling + 700 °C, 2 hours)	10.2 @140 N/cm ²	[28, 29]
6.	SS430 (Rolling + 700 °C, 2 hours)	11.6 @140 N/cm ²	[29]
7.	SS316 (Rolling + 700 °C, 2 hours)	11.1 @140 N/cm ²	[29]

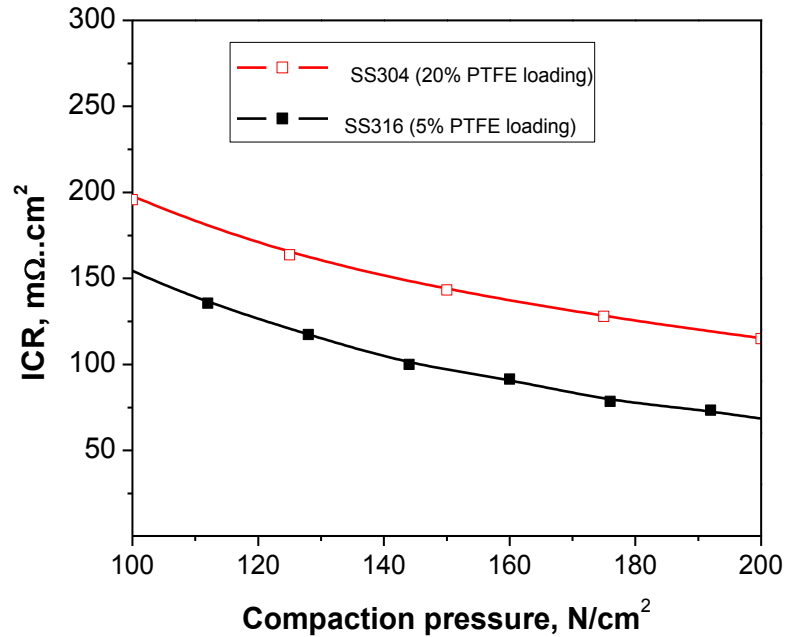


Figure 101 Comparison of ICR of SS316 in Figure 75 and SS304 in Figure 100 in order to show the influence of PTFE loading of the Toray carbon paper (T-GH-90) on ICR.

(D) Single Fuel Cell Performance Evaluation of the Optimised Chromised 304 Stainless Steel.

Figure 102 displays the polarisation and power density curves of the single fuel cells assembled with Cr-304 and the substrate (SS304) bipolar plates. The open circuit voltage (OCP) for Cr-304 and SS304 was 0.92 V and 0.85 V respectively. As current density increased, the beneficial influence of the chromised coatings becomes evident as the voltage of SS304 decreased rapidly compared to that of the coated plates. The single fuel cell with Cr-304 bipolar plates attained a maximum power density of 8.47 mW/cm² at a current density of 21.60 mA/cm² representing a two-fold increase in the maximum power density of the single fuel cell with SS304 bipolar plates as shown in Table 27.

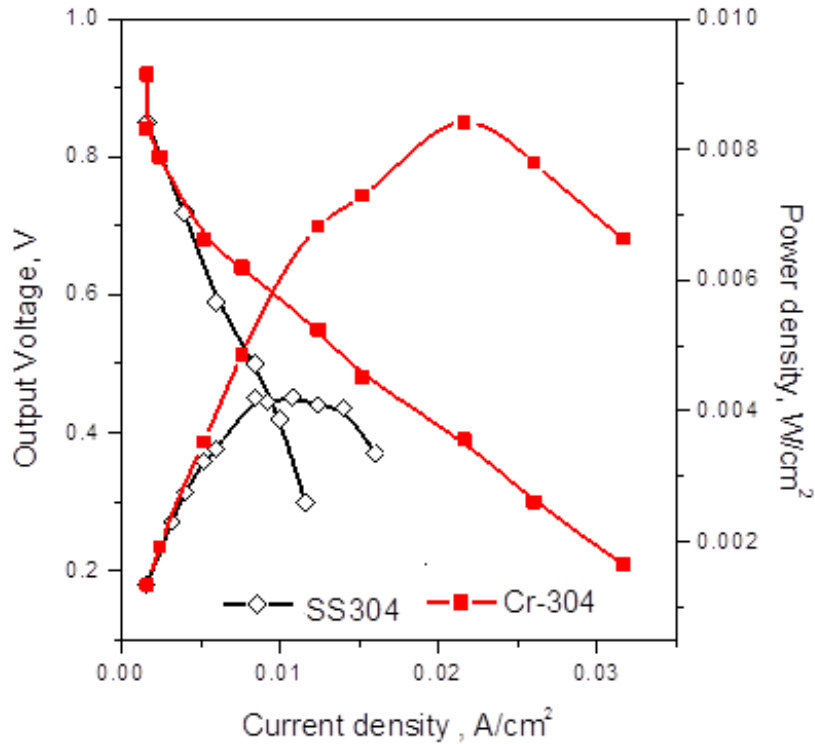


Figure 102 Single fuel cell performance of Cr-304 and SS304 bipolar plates

Table 27 Peak power data for the single cells with coated and uncoated stainless steel and the corresponding ICR at 125 N/cm².

Material	Maximum Power density (mW/cm ²)	Current density, mA/cm ²	ICR (mΩ.cm ²) @ 125 N/cm ²
SS304	4.21	10.00	163.7
Cr-304	8.47	21.60	29.0

It can also be seen in Table 27 that the performance of the single fuel cells with Cr-304 and SS304 bipolar plates was consistent with their ex-situ ICR values. This result is in agreement with the

literature, wherein it is reported that the performance of the single fuel cell is dependent on the ICR of the material for the bipolar plate [91, 112, 149]. Therefore, the improvement in the performance of the single fuel cell with Cr-304 bipolar plate over that of the single fuel cell with SS304 bipolar plates can be attributed to the lower contact resistance between the bipolar plates and the gas diffusion layer given that both single fuel cell were assembled with identical MEAs and operated under identical conditions.

6.4 SUMMARY

The influence of selected process parameters (time, activator content and temperature) on the corrosion current density of pack-chromised 304 stainless steel in simulated PEM fuel cell environment of 0.5 M H₂SO₄ + 2 ppm HF at 70 °C was systemically investigated using Box–Behnken design. The temperature, at which the coating was deposited, was found to be the most significant process parameter influencing the corrosion current density of pack-chromised 304 stainless steel in the investigated environment. However, an interaction effect exists between temperature and the activator content.

Optimisation of process parameters via numerical simulation and the desirability function revealed that the optimal process parameters to obtain chromised coatings with the minimum corrosion current density were time of ~3 hours, activator content of 6.84 wt.% and temperature of 1040°C. SEM/EDX, XPS and XRD characterisation of the chromised coatings indicated that the optimised coating consisted of a mixture of chromium-carbides, nitrides and oxides. Potentiodynamic and potentiostatic polarisation at typical cathodic and anodic PEM fuel cell operating potentials and environments indicated better corrosion resistance than the substrate in the selected PEM fuel cell environment. The optimised coating exhibited a low transient current density of ~2 μA/cm² and

$-6 \mu\text{A}/\text{cm}^2$ in the cathode and anode environments respectively, as well as about six fold decrease in ICR of the substrate at $150 \text{ N}/\text{cm}^2$ which was found to be $143.2 \text{ m}\Omega.\text{cm}^2$.

Performance evaluation of single fuel cells assembled with bipolar plates coated with the optimised process parameters and bare 304 stainless steel indicated that the single fuel cell with the optimised coated bipolar plates attained maximum power density of $8.47 \text{ mW}/\text{cm}^2$ at current density of $21.60 \text{ mA}/\text{cm}^2$. On the other hand, the single fuel cell with the uncoated plates attained maximum power density of $4.21 \text{ mW}/\text{cm}^2$ at current density of $10.00 \text{ mA}/\text{cm}^2$. The improvement in power out-put of the cell with the coated bipolar plates over that of the cell with the uncoated plates was attributed to the lower contact resistance of the optimised chromised coating compared to that of the substrate.

Chapter 7

Pre-carburised And Chromised Coatings

7.1 INTRODUCTION

This chapter reports preliminary attempts to improve the single fuel cell performance of the coatings produced at the optimised process parameters. As seen in the last chapter, the single fuel cell performance showed a correlation with the ex-situ ICR values, thereby suggesting that cell performance could be improved by reducing ICR. Furthermore, post-modification of CoBlast™ coated stainless steel also suggested that a carbon-rich layer deposited before or after could reduce the ICR of chromised coating. Hence, in this chapter, a carbon rich layer was deposited by pack carburisation prior to chromising at the optimised process conditions and its performance in simulated and real PEM fuel cell environments was reported. As indicated earlier in Chapter 3, pack carburising is no longer commercially viable as it has been replaced by more controllable techniques such as gas and plasma carburising; however, it was adopted in this study for ease of application.

7.2 PRE-CARBURISATION AND CHROMISING PROCESSING OVERVIEW

Table 28 presents an overview of the carbon mass uptake after pack-carburisation at 925 °C for 1-3 hours and subsequent chromium mass uptake after chromising treatments at the optimised processing parameters (i.e. activator content of 6.78 wt.%, time of ~3 hours and temperature of 1040 °C. The samples are hereafter named CPC-304-1, CPC-304-2, and CPC-304-3 with the last digit representing the time of carburisation. It can be inferred from Table 28 that increasing the carburising time resulted in a corresponding increase in carbon mass uptake. However, the concentration of diffused chromium into the carburised steel depended on the amount of carbon

content in the carburised steel. This observation is attributed to the formation of chromium carbides at chromising temperatures. It is reported that the chromium carbide layer formed during chromising treatment limits the diffusivity of chromium. Hence, the reduced thickness with higher carbon content as seen in Table 28 [246-248].

Table 28 Mass gain by SS304 after carburising for 1-3 hours and subsequently chromising at 1040 °C for ~ 3 hours

Material	Time of carburisation	Mass gain mg/cm² after carburisation	Time of chromising	mass gain after chromising (mg/ cm²)	*Average Thickness (µm)
CPC-304-1	1	6	3	19.8	16
CPC-304-2	2	14	3	12.6	11
CPC-304-3	3	18	3	12.1	10

*Thickness measured using SEM line measurement tools and EDX line scan

7.3 SURFACE CHARACTERISATION

(A) Carburised stainless steel

Figure 103 shows the locked coupled XRD pattern for 304 stainless steel pack carburised at 925 °C for 3 hours. The XRD pattern of the untreated stainless steel is also shown for reference. The XRD pattern for bare 304 stainless steel (SS304) indicates the presence of austenite and strain-induced martensite as commonly reported for 304 stainless steels [123, 249,250]. Strain induced

martensite in SS304 is related with processing or fabrication route for the 304 stainless steel sheet. After carburising, peaks due to cementite (Fe_3C) and thermal induced martensite can be observed. Martensite is attributed to fast cooling from austenitic temperatures while cementite is attributed to diffusion of carbon into the Fe matrix during carburising [204].

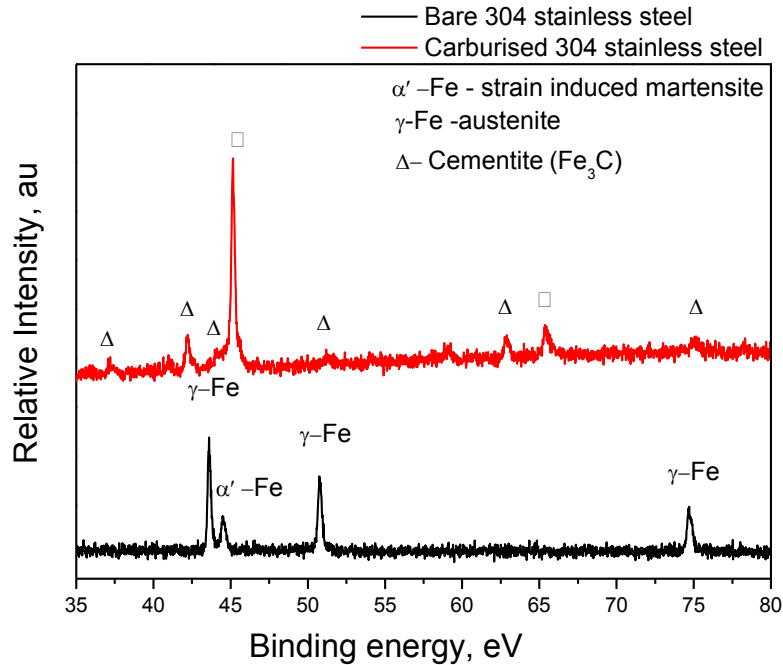


Figure 103 XRD of CPC-304-3 carburised at 925 °C for 3 hours.

Figure 104 shows the cross-section of 304 stainless steel pack carburised at 925 °C for 3 hours. EDX composition of the surface indicated that > 70% carbon, 24% oxygen and 5% iron were present. High oxygen content in the carburised surface is attributed to surface oxidation during carburisation as commonly reported for carburised steels [192,193]. Although carbon concentration measured by EDX may not be a true representation of the carbon content, the high carbon concentration compared to other elements and corresponding increase in mass after carburising as shown in Table 28, confirms a carbon enriched surface.

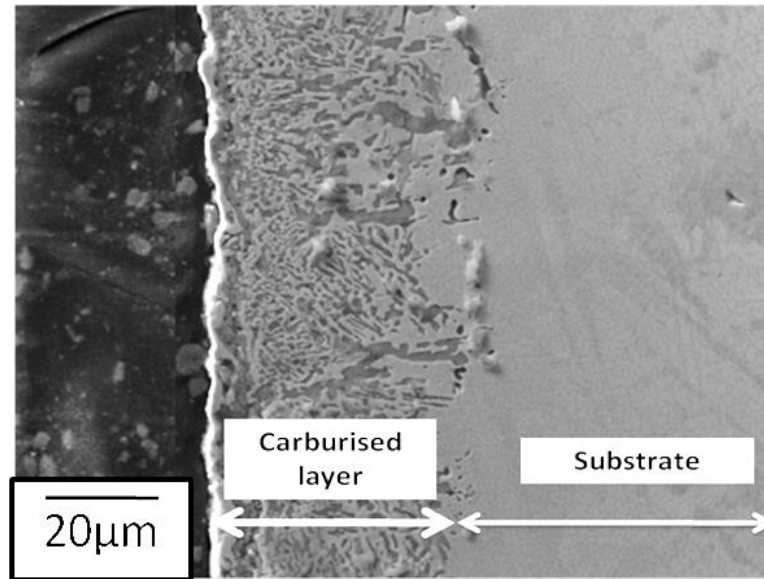


Figure 104 Cross-section of 304 stainless steel carburised at 925 °C for 3 hours

(B) Pre-carburised and chromised AISI304 stainless steel.

I. Surface morphology

Figure 105 (a) to (c) presents the surface morphologies of the CPC-304 samples. All samples irrespective of carburising time have similar morphologies consisting of discrete particles of Cr-N-C rich phase buried in a Cr-C rich matrix (Figure 106). The EDX spectrum of the surface shown in Figure 106 suggests that the discrete particles are either chromium nitrides or chromium carbo-nitrides. It is possible that the carbon content in the discrete particles is from the matrix given the limited depth of penetration of EDX. In any case, nitrogen is introduced into the system from the

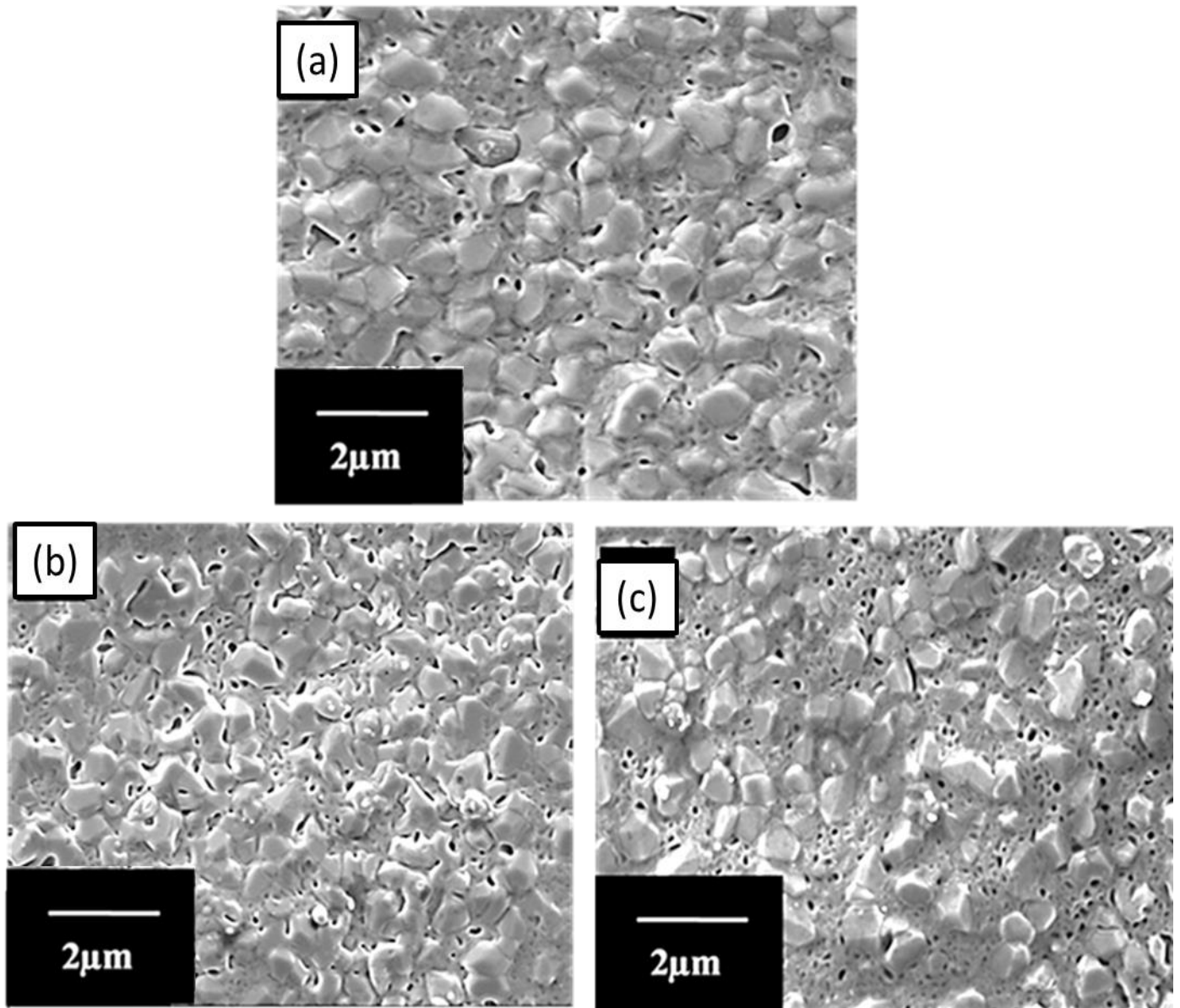


Figure 105 Surface morphology of (a) CPC-304-1(b) CPC-304-2 (c) CPC-304-3.

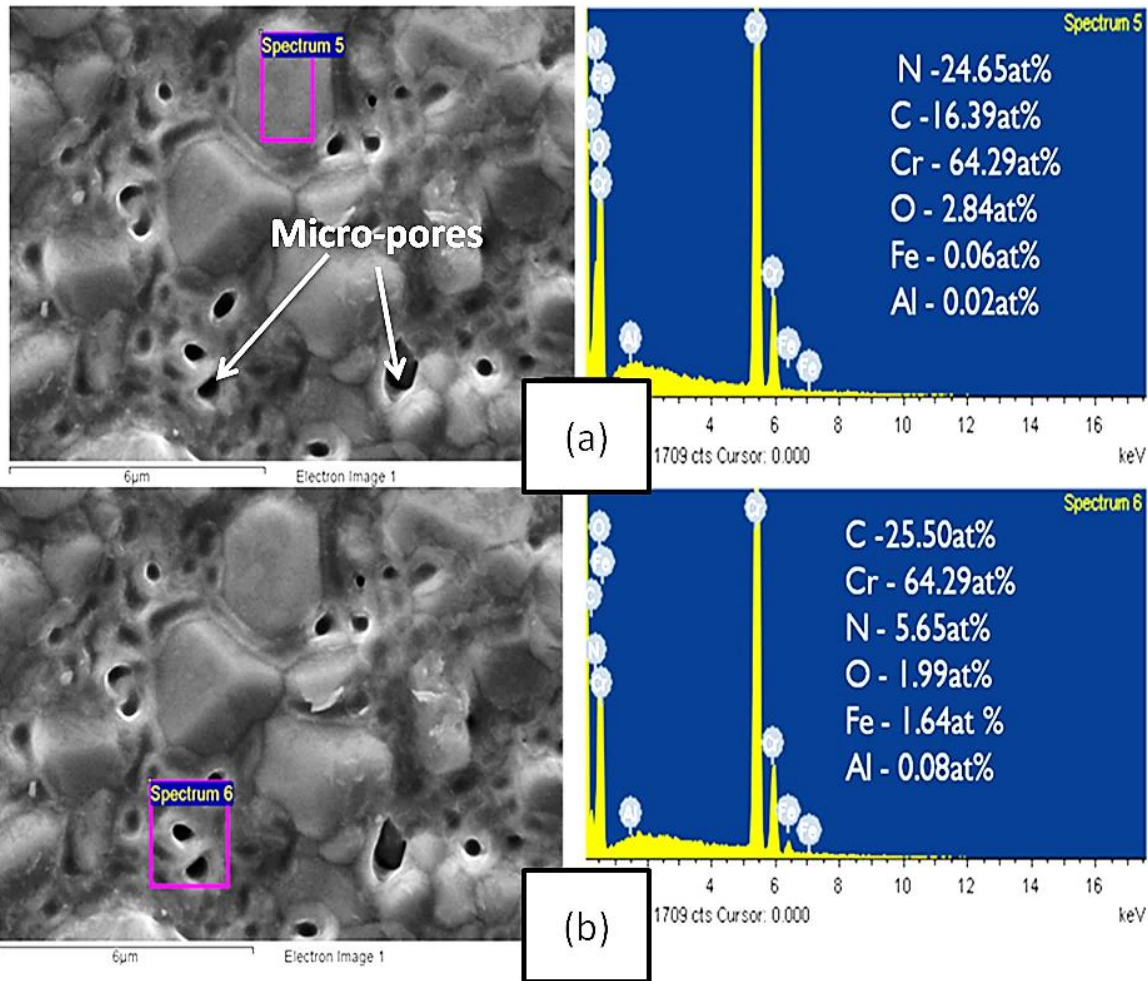


Figure 106 SEM image and EDX spectrum of CPC-304 (a) discrete particles (b) matrix.

decomposition of the ammonium chloride activator, thus, creating a favourable environment for formation of chromium nitrides or carbo-nitrides. Also noticeable in Figure 106 is the presence of micro-pores attributed to the Kirkendall effect during solid state diffusion of chromium into the carburised samples at high temperatures. The cross-sectional SEM images and EDX mapping of the pre-carburised and chromised samples are shown in Figure 107. The EDX maps showed that the surfaces of the coatings were enriched with chromium.

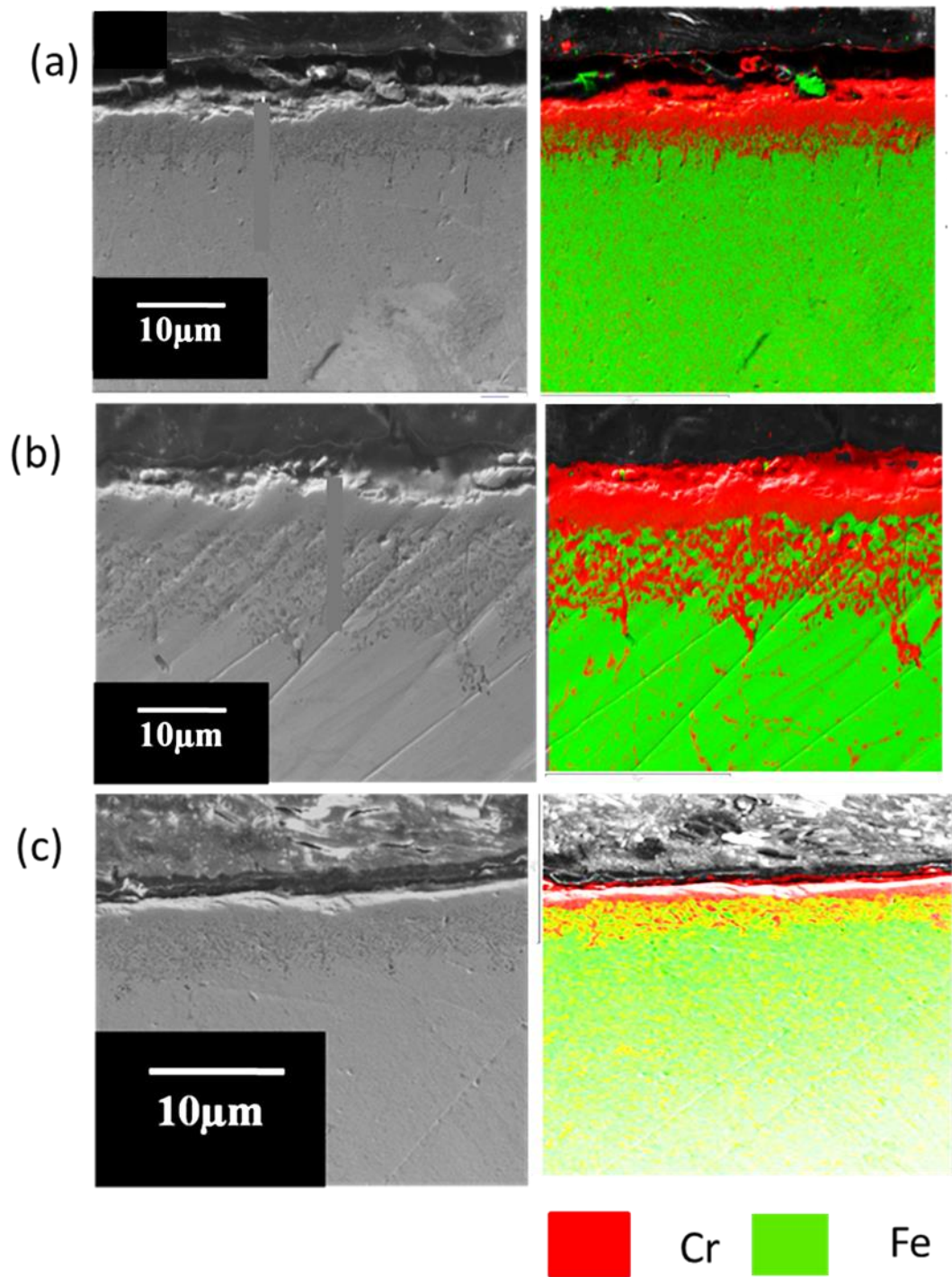


Figure 107 (a) Cross-section and EDX colour map of (a) CPC-304-1(b) CPC-304-2 (c) CPC-304-3.

II. XRD phase analysis

Figure 108 shows the glancing XRD patterns of CPC-304 samples at incidence angle of 5° . The XRD patterns at this depth of sampling show that similar phases were formed in the three samples irrespective of the carbon content. The phases formed chromium nitrides (Cr_2N), chromium carbide (Cr_2C_3 , Cr_{23}C_6 , and Cr_7C_3). Previous studies on pre-carburising and chromising of 316 sintered stainless steel had reported the absence of chromium nitrides [251] while Hosmani et al. [193] didn't indicated the existence of chromium nitride in the XRD pattern of pre-carburised and chromised low carbon steel. This observation in the literature could be attributed to the overlapping of chromium nitrides and chromium carbides peaks or a very small concentration of chromium nitrides making it difficult to detect by locked coupled XRD.

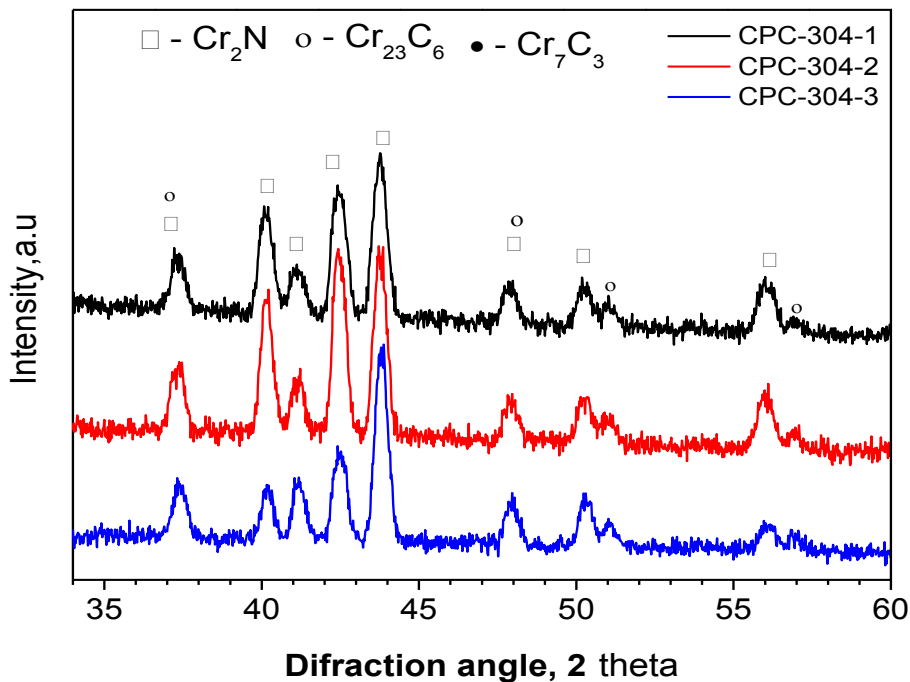


Figure 108 Glancing incidence XRD of CPC-304 stainless steels at 5° .

Also, Iorga et al. [251] had reported the presence of Fe_3C in pre-carburised and chromised sintered 316 stainless steels using conventional XRD which has a depth of penetration of about 10 μm . However, Fe_3C was not detected using grazing XRD, a surface sensitive XRD technique. Hence, it is possible that Fe_3C is buried at higher depths within the sample.

Comparing the phases formed in CPC-304 stainless steels to that formed in Cr-304 (Figure 97), it can be seen that the chromium carbides formed in Cr-304 were formed in solid solution of iron; hence, they are called chromium iron carbides. These types of carbides are formed due to the low carbon content of stainless steels. However, with increased carbon content as in the case of CPC-304 stainless steels, hard chromium carbides are formed.

(III) XPS

The XPS survey spectrum for CPC-304-1, CPC-304-2 and CPC-304-3 is presented in Figure 109. The spectrum indicates the presence of Cr, C, O, N and Al in all CPC-304-3 stainless steels irrespective of time of carburisation. It can also be seen in Figure 109 that Fe 2p peak was not detected on the outermost layers of the CPC-304 samples, thus, implying negligible concentration of iron on the CPC-304 stainless steels.

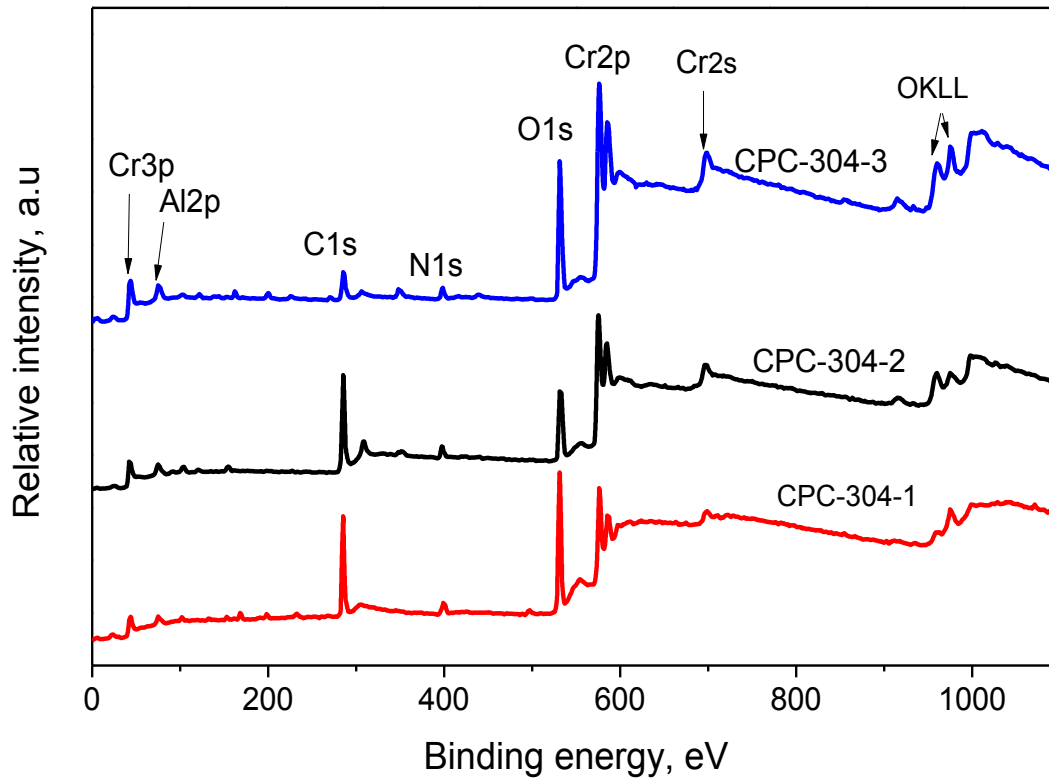


Figure 109 XPS survey spectrum for CPC-304 samples after 150 seconds of sputtering.

Figure 110 shows the core-level spectra of Cr2p, N1s, C1s and O1s for the outermost layer of CPC-304 samples after 150 seconds of sputtering. The Cr2p spectrum (Fig. 110 (a)) indicates the presence of Cr-C, Cr-N and Cr-O bonding in all samples irrespective of time of carburisation. The Cr2p_{3/2} shoulder centered at a binding energies of ~574.2 eV in CPC-304-1 and the Cr2p_{3/2} peak at ~574.6 eV in CPC-304-2 and CPC-304-3 are ascribed to chromium iron carbides and chromium carbides respectively [218, 235, 236]. The presence of chromium nitride is established by the Cr-N bond with Cr 2p_{3/2} shoulders at 575.5 eV [219, 220]. The broad nature of the Cr2p_{3/2} peak at 576.0-578.0 eV is indicative of chromium oxide in +3 and +4 oxidation state [219, 220, 244, 245]. The

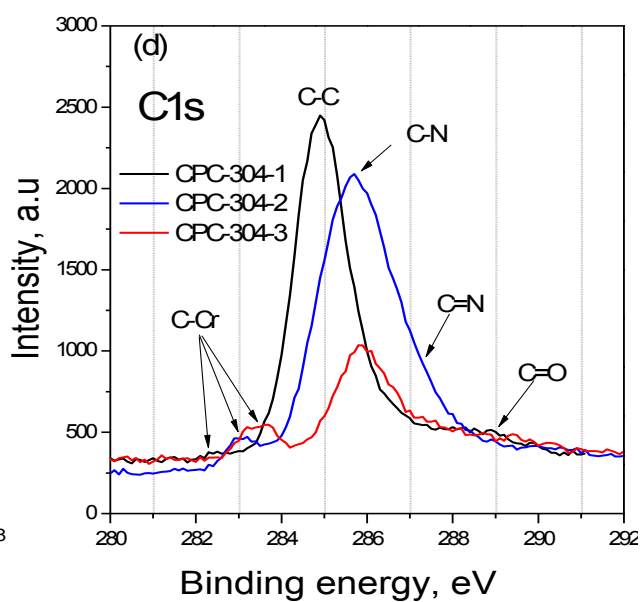
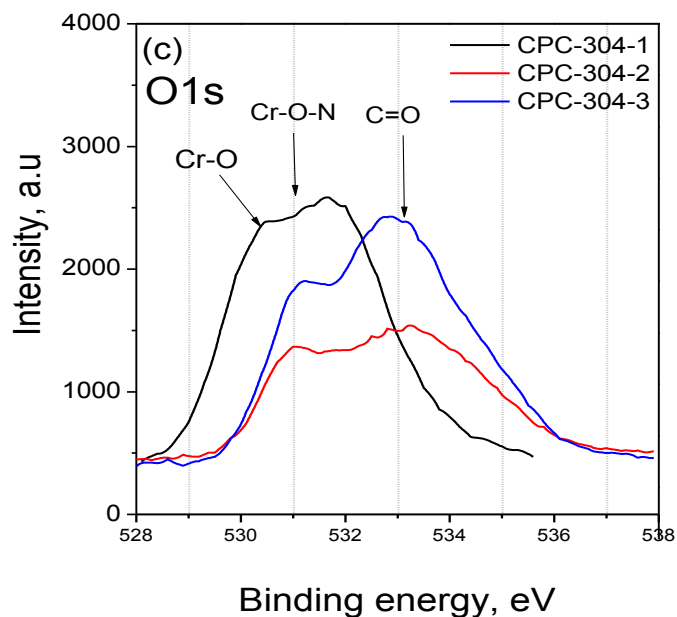
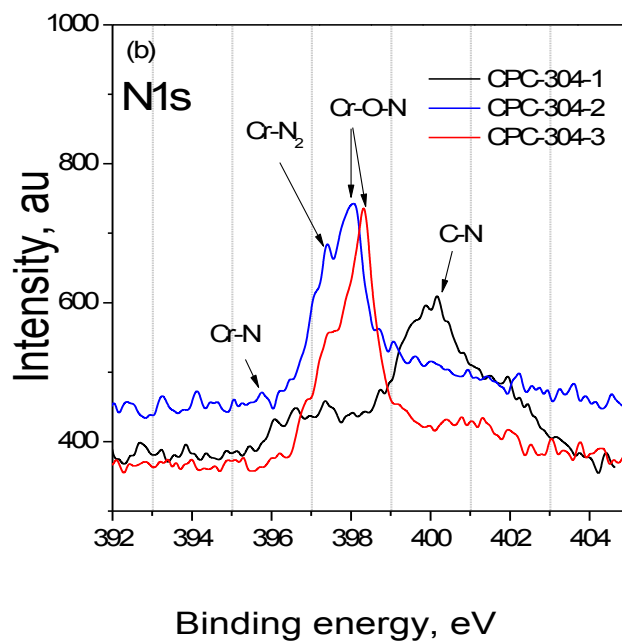
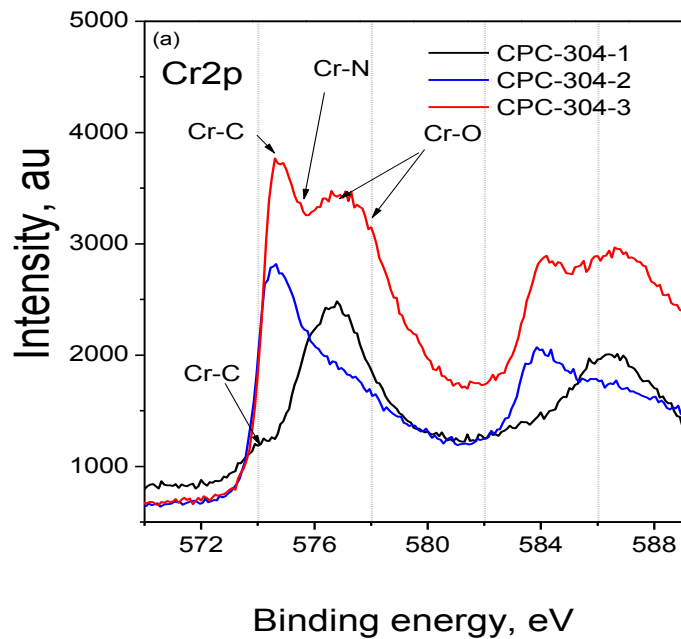


Figure 110 XPS analysis of CPC-304 samples (a) N1s (b) O1s spectrum.

possibility of co-existence of chromium oxide in different oxidation state is related to the small difference in their standard Gibbs free energy of formation per g-atom Cr – (Cr_2O_3 – 569 kJ/mol, CrO_3 - 589.9 kJ/mol) [245].

The N1s spectrum shown in Figure 110 (b) indicates the presence of three types of nitrides: CrN at binding energy of 396.75 eV, Cr_2N at binding energies of 397.45 eV and chromium oxy nitrides (CrO_xNy) at binding energy of (398.02 \pm 0.3 eV) [219, 220, 244, 245]. The broad nature of the N1s spectrum between 398.5-403.0 eV for CPC-304-1 stainless steel suggest the presence of different nitrogen bonding to carbon e.g. - pyrrolic N (398.8 eV), quaternary N (400.2 eV), and oxidised N (401.3 eV) [252, 253].

Figure 110 (c) shows the O1s spectrum of CPC-304 samples. The O1s spectrum establishes the presence of chromium oxide at binding energy of 530.5 \pm 0.3 eV, chromium oxy nitrides at binding energy of 531.4 \pm 0.2 eV and oxygen contribution from organic carbon at ~533.0 eV [219, 220, 244, 245].

The C1s spectrum shown in Figure 110 (d) indicates the presence of chromium carbides at binding energies of 282.3 eV and 283.6 eV for CPC-304-1, 282.8 – 283.2 eV for CPC-304-2, 282.8 - 283.7 eV for CPC-304 [218, 235, 236]. The broad nature of the C1s spectrum for CPC-304-2 and CPC-304-3 is indicative of different types of chromium carbides. It is noted that C-Fe bonding in iron carbide exist at a binding energy of ~283.6 eV [218]. However, the non- existence of iron carbide at the outermost layer is further established with the absence of Fe2p peak in Figure 111. The C1s peak at 284.9-285.7 eV in the CPC-304-samples is assigned to adventitious carbon while the peak at 286.2 eV and shoulders at ~287 eV and 299.0 eV is attributed to contributions from carbon nitrides and organic carbon respectively [218].

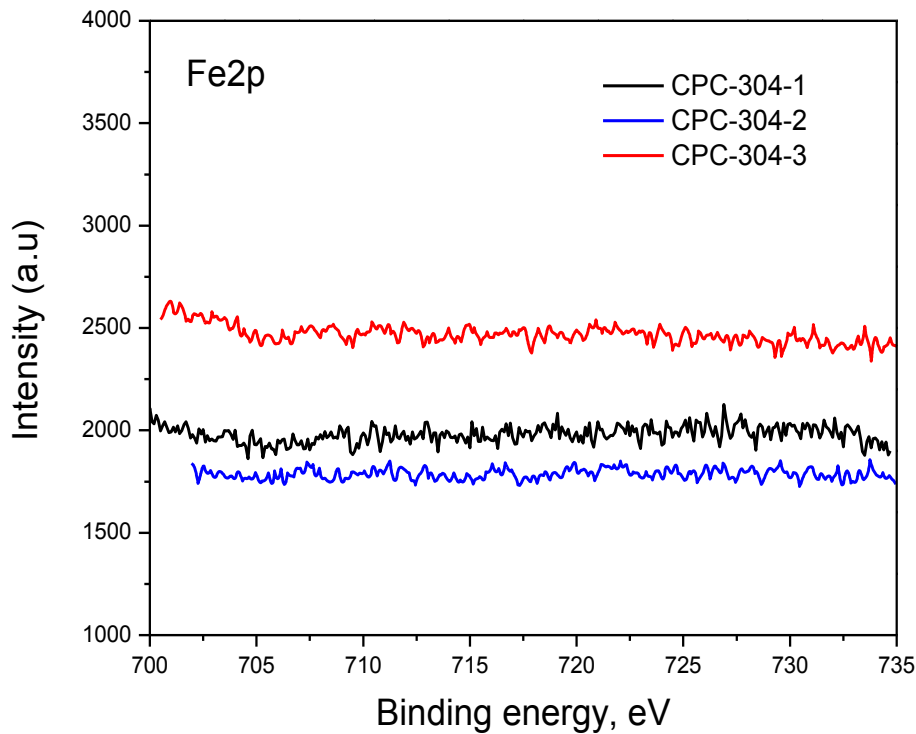


Figure 111 Fe2p core level spectra for pre-carburised and chromised CPC-304 samples

7.4 Interfacial contact resistance.

The interfacial contact resistance (ICR) of the CPC-304 stainless steel samples as a function of compaction pressure is presented in Figure 112. At typical compaction force of 150 N/cm^2 as marked in the inset of Figure 112, ICR of the CPC-304 samples is given as $20.35 \text{ m}\Omega\cdot\text{cm}^2$, $16.10 \text{ m}\Omega\cdot\text{cm}^2$ and $10.85 \text{ m}\Omega\cdot\text{cm}^2$ for CPC-304-1, CPC-304-2 and CPC-304-3 respectively. This trend is consistent with the carbon content of the samples presented in Table 28 i.e. the higher the carbon content of the CPC-304 stainless steels, the lower the ICR values. The decrease in ICR values of CPC-304 samples as carbon content decreased can be attributed to increasing concentration of chromium carbide and nitride on the outermost layer evidenced by increasing intensity of these compounds as time of carburisation increased from 1-3 hours Figure 110 (b) and (d).

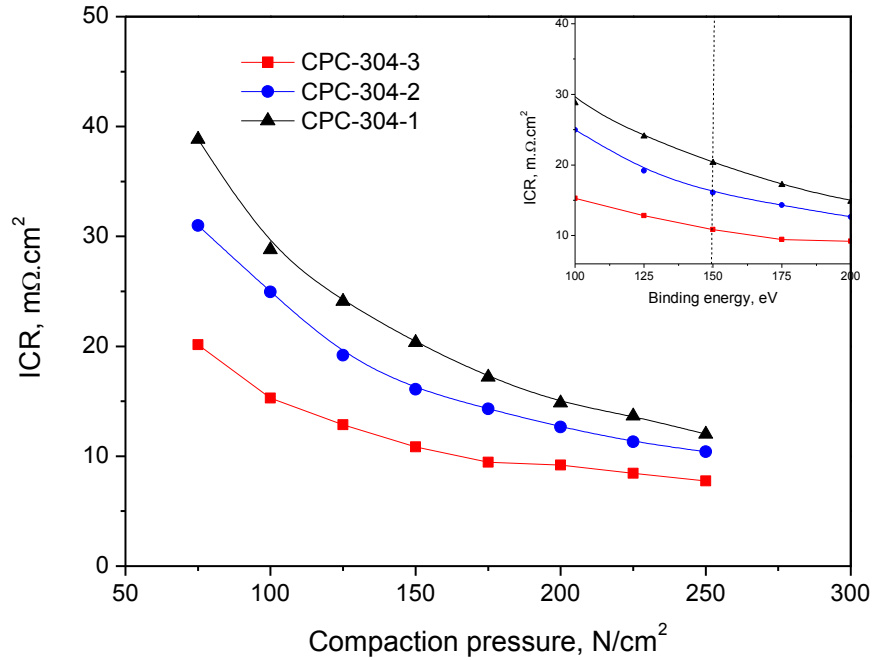


Figure 112 Interfacial contact resistance of CPC-304 stainless steels as a function of compaction pressure.

Comparison of the ICR values of the CPC-304 samples to that of Cr-304 suggest that increasing the carbon content of chromised coatings could decrease ICR of chromised coatings. This observation is consistent with recent reports by Wang et al. [135, 136]. The authors demonstrated that increasing the carbon content of chromium electroplated coatings by decreasing the current density at which the coatings were deposited resulted in a corresponding decrease in ICR.

7.5 CORROSION BEHAVIOUR EVALUATION

Figure 113 (a) and (b) shows the potentiodynamic polarisation curves of CPC-304 samples in 0.5 M H₂SO₄ + 2 ppm HF at 70 °C with hydrogen and air bubbled through the electrolyte to simulate

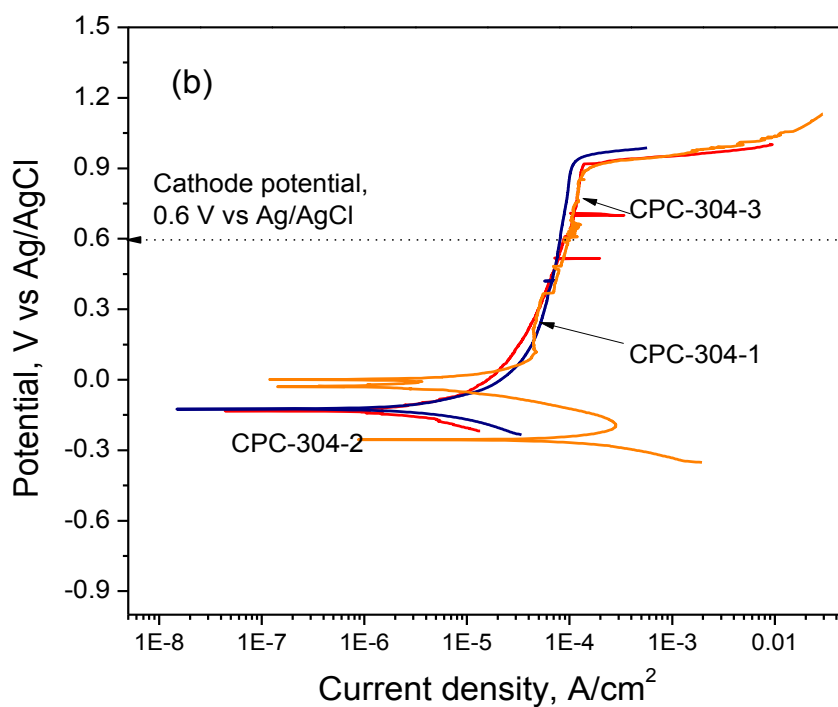
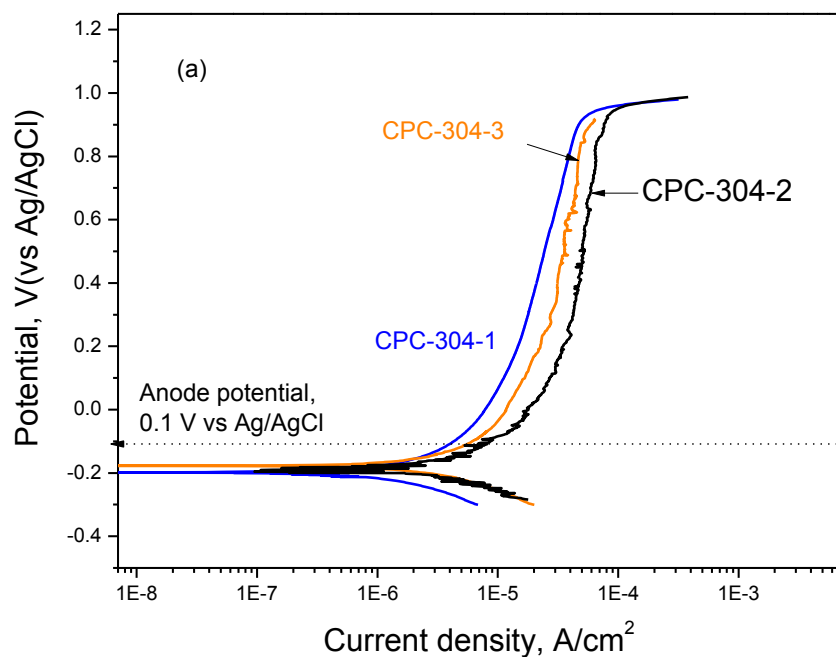


Figure 113 Potentiodynamic curves for CPC-304 samples in simulated PEM fuel cell (a) anodic and (b) cathodic environment.

PEM fuel cell anodic and cathodic conditions respectively. The corrosion parameters derived from these curves are presented in Table 29. It can be seen from the polarisation curves and corrosion parameters that the CPC-304 samples exhibited similar corrosion potentials, corrosion currents and passive-transpassive behaviour in simulated PEM fuel cell anodic environment.

Table 29: Corrosion parameters of CPC-304 samples in 0.5 M H₂SO₄ + 2 ppm HF at 70 °C

Material	E_{corr}		i_{corr}	
	(V vs Ag/AgCl)		$(\mu\text{A}/\text{cm}^2)$	
	Anode	Cathode	Anode	Cathode
CPC-304-1	0.19	-0.12	2.46	3.33
CPC-304-2	-0.20	-0.26	1.08	94.60
CPC-304-3	-0.18	-0.12	1.37	3.74

A similar trend was observed in the cathodic environment with the exception of the CPC-304-2 sample which exhibited double anodic nose, probably due to instability at open circuit potential or different reduction processes occurring at different potentials [212]. At typical cathodic and anodic PEM fuel cell working potential which are marked in Figure 113, it can also be seen that the CPC-

304 stainless steels exhibited similar performance, signifying that the carbon content had a negligible influence on the corrosion performance of the stainless steels.

Comparing these results to those obtained for Cr-304 in Table 23, it can be seen that pre-carburising prior to chromising adversely degraded the corrosion resistance of Cr-304 which can be explained by:

- a) Pack carburising of austenitic stainless steel at temperatures >550 °C promoted the formation of chromium carbides at the grain boundaries. Consequently the Fe matrix was devoid of chromium and corrosion resistance was degraded i.e. the steel was sensitised. However, a subsequent chromising treatment could potentially restore chromium to the Fe matrix such that the CPC-304 samples will essentially behave like the original stainless steel as seen in this study and reported in Iorga et al. [251]. However, because diffusion of chromium is restricted by the carbon rich surface when chromium carbide is formed. Hence, the post-chromising process may not adequately restore the steel to its former corrosion resistance state depending on the chromising process parameters.
- b) The presence of micro-pores in CPC-304 samples could also contribute to its lower corrosion resistance compared with Cr-304. Defects such as micro-pores, which serve as channels for environment-substrate interaction in the corrosive environment, are unavoidable in diffusion coatings due to the diffusion gradient created by the slow diffusion of chromium compared to carbon otherwise known as the Kirkendall effect.
- c) Defects such as micro-pores in CPC-304 stainless steels would also contribute to its lower corrosion resistance. Defects in coatings are well known to facilitate environment-substrate interaction in corrosive environments. However, defects such as micro pores are

unavoidable in diffusion coatings due to the diffusion gradient created by the slow diffusion of chromium compared to carbon otherwise known as the Kirkendall effect.

- d) Loss of corrosion resistance of CPC-304 stainless steels compared to chromised stainless steel could also be attributed to the presence of discrete chromium nitride particles, untransformed iron carbide and buried martensite in the CPC-304 stainless steels. These features in the coatings can facilitate galvanic corrosion between the substrate and the coatings [109, 115, 251].

Nevertheless, the corrosion resistance of CPC-304 stainless steels could potentially be alleviated by:

(a) Carburising at low temperatures via gas and/or plasma carburising.

It is reported that low temperature carburisation at $< 500\text{ }^{\circ}\text{C}$ by gas and plasma carburisation can facilitate the formation of carbon expanded austenitic structure with improved corrosion resistance compared to that of the substrate [192, 254]. For instance, Nikam et al. [254] reported that carburised 316L stainless steel produced by gas carburising within temperature range of $465\text{--}475^{\circ}\text{C}$ by Swagelok Company, USA exhibited better corrosion performance in simulated PEM fuel cell environment of $1\text{ M H}_2\text{SO}_4 + 2\text{ ppm HF}$ at $80\text{ }^{\circ}\text{C}$. The carburised stainless steel exhibited low transient current density of $1.5\text{ }\mu\text{A}/\text{cm}^2$, which was about one order of magnitude lower than that of the substrate ($50\text{ }\mu\text{A}/\text{cm}^2$) after 25 hours of potentiostatic polarisation in $1\text{ M H}_2\text{SO}_4 + 2\text{ ppm HF}$ at $80\text{ }^{\circ}\text{C}$ with oxygen bubbling. However, the ICR of the carburised steel ($95\text{ m}\Omega\cdot\text{cm}^2$ at $250\text{ N}/\text{cm}^2$) was significantly higher than the targeted $10\text{ m}\Omega\cdot\text{cm}^2$ due to surface oxidation during carburisation. Post chromising treatment of such carburised stainless steel could possibly reduce its ICR as seen in the case of post chromising of CoBlast™ stainless steel.

(b) Use of non-nitrogen based halide activators.

Corrosion resistance of the CPC-304 stainless steels could also be improved by preventing the formation of discrete chromium nitride particles via the use of other non-nitrogen based halide activators such as AlF_3 , AlCl_3 and NaCl .

7.6 SINGLE FUEL CELL PERFORMANCE

Among the CPC-304 stainless steels, CPC-304-3 was selected for single fuel cell evaluation based on its ICR values, which was the lowest among the stainless steels examined. Figure 114 (a) and (b) presents the initial polarisation and power density curve of the single fuel cell assembled with CPC-304-3 bipolar plates. The polarisation and power density curves for Cr-304 and SS304 are also

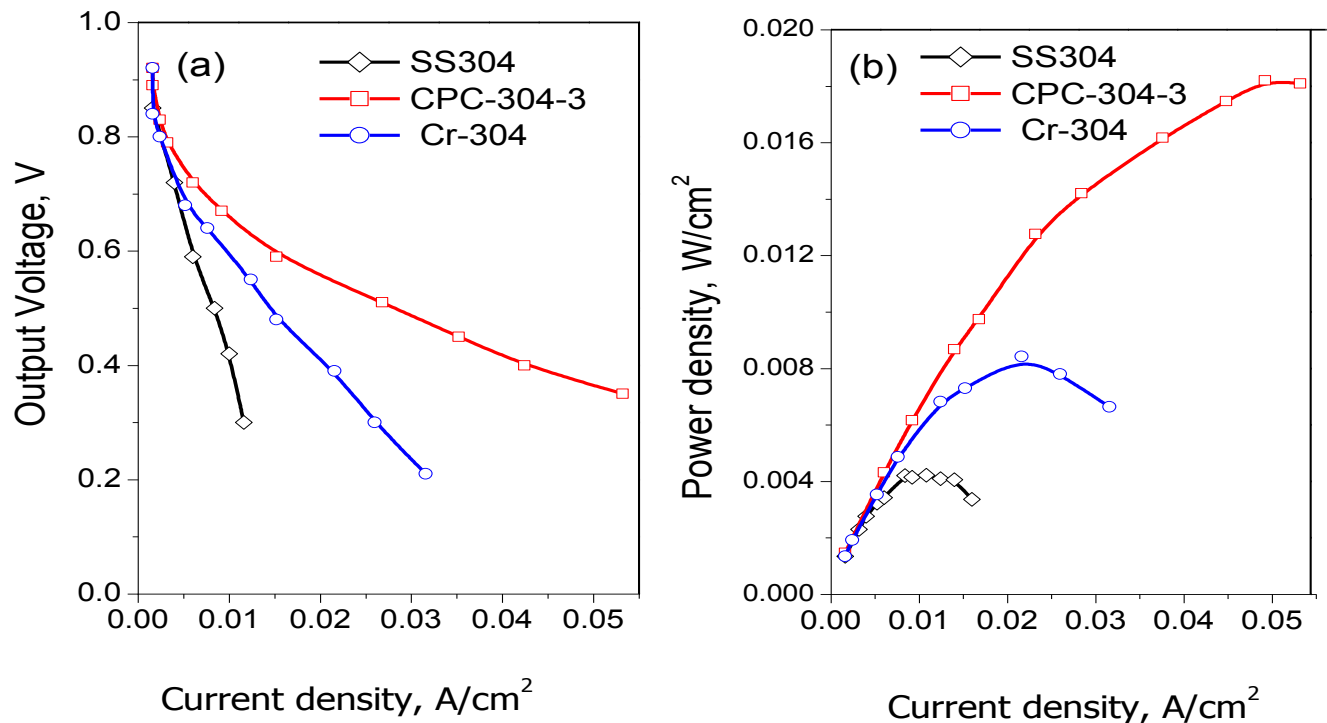


Figure 114 Polarisation curves and power density curves for single fuel cells with CPC-304, Cr-304 and SS304 bipolar plates.

plotted for reference. The single fuel cell with the CPC-304-3 bipolar plates exhibited an OCV of 0.92 V (Figure 114 (b)) and a peak power density of 18.20 mW/cm² at a current density of 53.2 mA/cm² (Figure 114 (b)). Comparing these values with the OCV and peak power density obtained for the single fuel cell with Cr-304 and SS304 (Table 27), it can be seen that the single fuel cell with the CPC-304-3 bipolar plate exhibited a similar OCV to the cell with Cr-304 bipolar plates and a higher OCV than the cell with SS304 bipolar plates. On the other hand, the single cell with CPC-304-3 bipolar plate attained a maximum power density which was approximately twice and thrice the peak power output of the single fuel cells with Cr-304 and SS304 bipolar plates respectively. The improvement in cell performance of the cell with the CPC-304-3 bipolar plate is attributed to its ICR given that the cells were tested under similar conditions in agreement with previously published works [89, 91,112,149].

Figure 115 presents the current –time profile of the single fuel cells with CPC-304, Cr-304 and SS304 bipolar plates. The cells were tested for 10 hours at 0.6 V. As shown in Figure 115, the performance of the fuel cells in descending order was: CPC-304-3 > Cr-304 > S304 in agreement with the initial polarisation and power curves (Figure 114). At the end of the 10-hour test, current densities for the single fuel cells were found to be : 203 mA/cm² for the single cell with CPC -304-3 plates, 75 mA/cm² for the cell with Cr-304 plate and 35 mA/cm² for the cell with SS304 bipolar plates.

After the 10 hours test, the cells were dismantled and GDLs were characterised with SEM/EDX to evaluate the effect of corrosion. On dismantling the cells, a brownish corrosion product was observed on the cathode side GDL of the cell for the CPC-304-3 bipolar plates. The corrosion product is ascribed to chunk effect, i.e. the loss of the metal pieces from the bulk alloy when anodically polarised [255, 256].

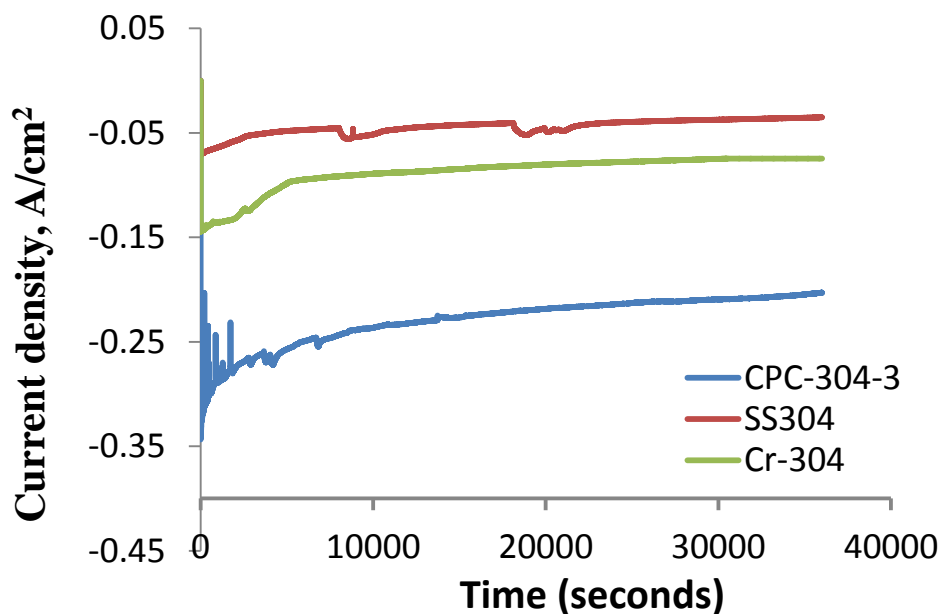


Figure 115 Current density–time profile for single fuel cells with CPC-304-3, Cr-304 and SS304 bipolar plate at 0.6 V.

Figure 116–118 presents the SEM images and EDX spectrum of the cathode side GDLs of the single fuel cells with CPC-304-3, Cr-304 and SS304 bipolar plate. It can be seen that the SEM image of the GDL for the single fuel cell with CPC-304-3 bipolar plates showed a damaged GDL with corrosion product particles (Figure 116 (a)). It is also possible that the damage could be due to the compaction force given that traces of the channels on the bipolar plate can be seen on the SEM images. The EDX spectrum (Figure 116 (b)) showed the presence of Fe, Cr, Ni and Mn. On the other hand, the GDL of the single fuel cell with Cr-304 and SS304 bipolar plates ((Figure 117 (a) and Figure 118 (a)) showed no damage, while the EDX spectrum of the respective GDLs showed traces of Fe, Ni, Mn and Cr compared to that of the cell with the CPC-304-3 bipolar plates.

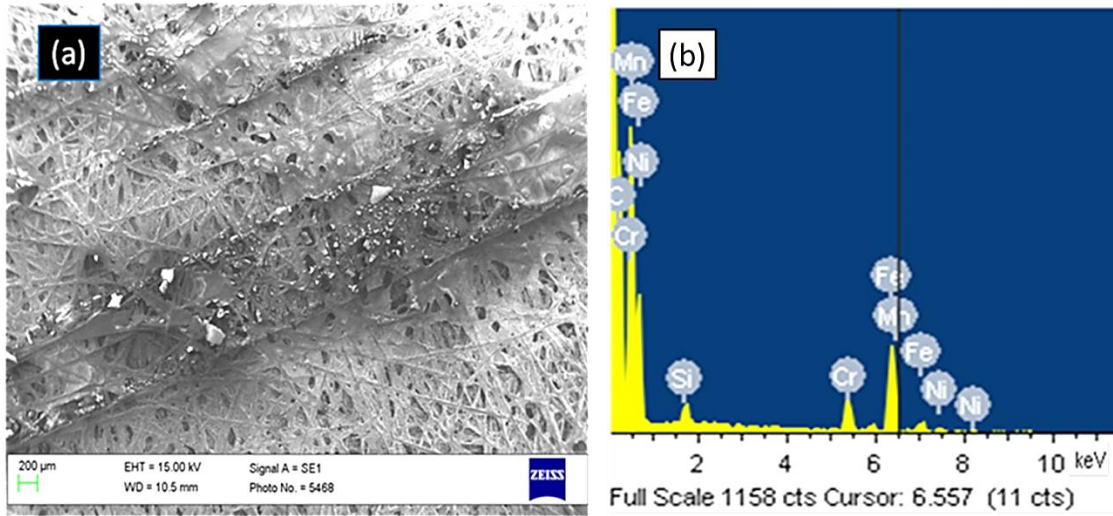


Figure 116 Cathode side GDL of single fuel cell with CPC-304-3 bipolar plates after 10 hours of testing (a) surface morphology (b) EDX spectrum.

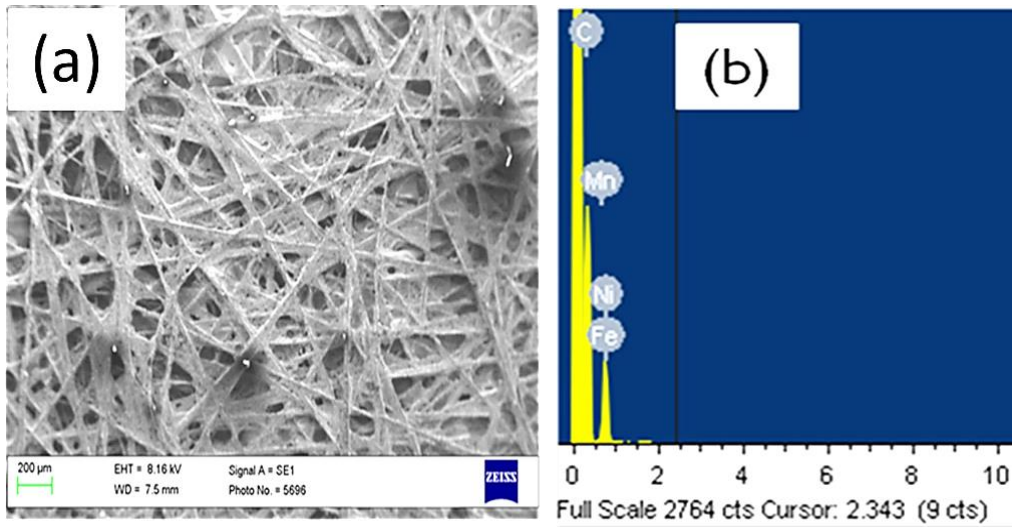


Figure 117 Cathode side GDL of single fuel cell with Cr-304 bipolar plates after 10 hours of testing (a) surface morphology (b) EDX spectrum.

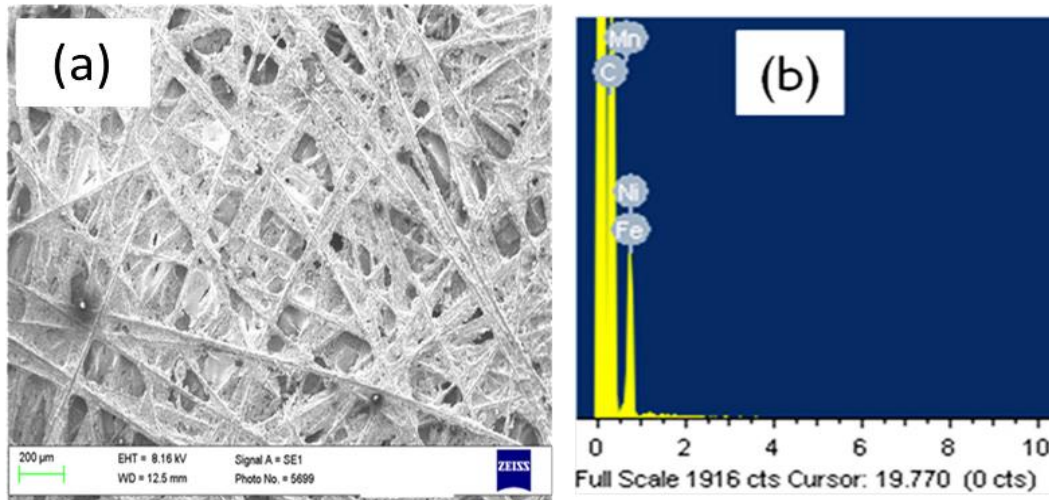


Figure 118 (a) SEM image (b) EDX spectrum of the cathode side GDL of single cell with SS304 bipolar plates after 10 hours of testing.

7.7 SUMMARY

The influence of pre-carburising prior to chromising on the ex-situ and in-situ performance of Cr-304 was investigated. Pre-carburising prior to chromising enhanced the surface conductivity of chromised 304 stainless steel (Cr-304) via the formation of conductive chromium carbides and nitrides. Hence, ICR of Cr-304 stainless steel was reduced by ~15%, ~33%, ~55% as carburising time increased from 1 to 3 hours respectively. On the other hand, corrosion properties of the pre-carburised-chromised stainless steel (CPC-304) was degraded compared to that of that of Cr-304 at typical cathodic PEM fuel cell working potentials. However, the corrosion properties of the CPC-304 were comparable to that of the substrate. The loss of corrosion resistance was attributed to the sensitisation of the stainless steel via high temperature pack carburisation amongst other factors.

Single fuel cell evaluation of the CPC-304 sample carburised for 3 hours (CPC-304-3) indicated that the cell attained a peak power density of 18.20 mW/cm² at 53.2 mA/cm². This result

represented a two and three fold improvement in the peak output power of the single fuel cells with Cr-304 and SS304 bipolar plates. This trend was also sustained in the durability studies. However, SEM/EDX characterisation of the cathode side GDL after the 10 hour test indicated that the corrosion resistance of CPC-304-3 needed to be further improved by adopting low temperature carburisation techniques.

Chapter 8

Conclusions, Contributions and Future work

8.1 CONCLUSIONS

Proton exchange membrane (PEM) fuel cells are potential alternative power sources for automobiles and other transportation devices. However, PEM fuel cells are expensive and not as durable as conventional power sources. Replacement of conventional graphite bipolar plates with metallic bipolar plates is widely considered as one of the promising routes to cost reduction of PEM fuel cells. Metals are, however, prone to corrosion in the PEM fuel cell environments and exhibit unacceptable contact resistance with the gas diffusion layer. Hence, metals require surface modification to be viable materials for bipolar plates. In the present study, the performance of CoBlast™ coated metals and pack chromised stainless steels in PEM fuel cell environments was investigated. The summary and conclusions drawn from the performance evaluation of the coatings are given as follows:

(A) CoBlast™ deposited graphite coatings

Graphite based coatings were deposited on 316 stainless steel and Ti grade V alloys by the CoBlast™ process, a surface modification process which deposits coatings via blasting of powders on the substrate. Surface characterisation of the coated metals revealed a rough and discontinuous layer of coatings composed of isolated pockets of graphite or alumina mixed with graphite embedded in the substrate oxide layer. Hence, the coated layer did not protect the substrate from corrosion in simulated PEM fuel cell environment of 0.5 M H₂SO₄ + 2 ppm HF at room

temperature or at typical PEM fuel cell operating temperature. The interfacial contact resistance (ICR) of the coated metals at typical PEM fuel cell compaction pressure of 100-200 N/cm² were slightly lower than that of the substrates but significantly higher than the ICR of graphite and the targeted 10 mΩ.cm². The reduction in ICR values was attributed to the doping effect of graphite on the surface oxide layer of the substrates.

In order to improve the continuity and thickness of the coatings, CoBlast™ treated stainless steel was pack chromised at 900 °C for 3 hours. Post chromising treatment of CoBlast™ coated stainless steel indicated the formation of a multiphase coating comprising of graphite, alumina and chromium based coatings, which yielded ICR values significantly lower than that of CoBlast™ coated and chromised stainless steel at typical PEM fuel cell compaction pressure. However, the graphite and alumina inclusions in the modified coatings promoted corrosion of the matrix in preference to the graphite/alumina coating in simulated PEM fuel cell environment. Hence, neither CoBlast™ deposited graphite based coating nor the modified graphite/chromised coatings can be considered suitable coatings for surface modification of metallic bipolar plate application.

(B) Chromium diffusion coatings.

The influence of time, activator content and temperature on the corrosion current density of pack-chromised 304 stainless steel in simulated PEM fuel cell environment of 0.5 M H₂SO₄ + 2 ppm HF at 70 °C was systemically investigated using Box Behnken Box designs, a design of experiment (DoE) technique. The temperature at which the coating was deposited was found to be the most significant process parameter affecting the corrosion current density of pack-chromised 304 stainless steel in simulated PEM fuel cell environment of aerated 0.5 M H₂SO₄ + 2 ppm HF at

70 °C. The interaction effect existed between temperature and the activator content was also found to be statistically significant.

Optimisation of the process parameters via numerical simulation and use of the desirability function revealed that the optimal process parameters were: time of ~3 hours, activator content of 6.78 wt. % and temperature of 1040 °C. Surface characterisation of the chromised coatings produced at these parameters revealed a mixture of chromium iron carbides, chromium iron nitrides and chromium oxides. Performance evaluation of the chromised coatings deposited at the optimised process parameters (Cr-304) in simulated PEM fuel cell environment indicated good corrosion resistance and about six fold reductions in the ICR of the substrate at 150N/cm². Based on these results, the performance of 5cm² active area single fuel cells assembled with Cr-304 and bare 304 stainless steel was evaluated. The polarisation results indicated that Cr-304 bipolar plates attained a maximum power density of 8.47 mW/cm² at a current density of 21.60 mA/cm², while the cell with the uncoated plates only attained a maximum power density of 4.21 mW/cm² at 10.00 mA/cm². Thus, it can be concluded that chromised 304 stainless steels are promising materials for PEM fuel cell bipolar plates.

Attempts to improve single fuel cell performance of the single fuel with Cr-304 stainless steel by pre-carburising prior to chromising were also conducted. The duplex surface treatment enhanced the surface conductivity of chromised 304 stainless steel via the formation of conductive chromium carbides and nitrides. Hence, ICR of chromised 304 stainless steel was reduced by ~15%, ~33%, ~55% as carburising time increased from 1-3 hours respectively. On the other hand, corrosion properties of chromised 304 stainless steel deteriorated at typical PEM fuel cell working potentials, but were comparable to that of the substrate, which was about an order of magnitude higher than the targeted 1µA/cm² for bipolar plate applications. The loss of corrosion resistance of

the chromised coating was attributed to sensitisation via high temperature pack carburisation process. Considering the fact that corrosion resistance of the pre-carburised and chromised samples could be improved by low temperature carburisation techniques such as gas and plasma carburising, the single fuel cell performance of the 3 hour pre-carburised -chromised 304 stainless steel samples was evaluated and compared with that of chromised 304 stainless steel and the substrate. The initial cell polarisation results indicated that the single cell with the pre-carburised-chromised bipolar plate attained maximum power density of 18.20 mW/cm^2 at a current density of 53.2 mA/cm^2 representing a doubling and tripling increase in the maximum power density of the single fuel cell with Cr-304 and bare stainless steel bipolar plates respectively. The result of short term durability test of the single fuel cells conducted for 10 hours was consistent with the initial polarisation result. SEM/EDX characterisation of the cathode side GDL of the single fuel cells after the test established the need to improve the corrosion resistance of the pre-carburised and chromised 304 stainless steel by adopting low temperature carburisation techniques such as gas-, plasma or electrochemical carburisation. It can be concluded from these results that duplex treatment of pre-carburisation prior to chromising should be considered promising for surface modification of metallic bipolar plate.

8.2 CONTRIBUTION TO KNOWLEDGE

Key contributions of this research to knowledge in the field of surface modification of metallic bipolar plate for PEM fuel cells are:

1. Optimisation of process parameters via experimental design is an effective route to improving the performance of surface coatings for metallic bipolar plates. Adopting this method, chromised coatings which showed comparable performance to previously reported

pre-treated and chromised stainless steels in simulated PEM fuel cells environment were achieved. More importantly, it was shown that an interaction effect exist between chromising temperature and activator content. This finding will be helpful in tailoring the surface morphologies of chromised coatings for the desired application.

2. Duplex treatment of carburisation and chromising has the potential to enhance the performance of chromised stainless steel bipolar plate in PEM fuel cells environments provided carburisation is conducted with low temperature carburising processes.

8.3 FUTURE WORK.

The following tasks are proposed for future work:

- Enhancing the corrosion resistance of pre-carburisation and chromised stainless steel by employing low temperature carburisation technique such as gas or the use of plasma carburising.
- Long term lifetime assessment of single fuel cells assembled with chromised stainless, pre-carburised and chromised stainless steel bipolar plates produced in (1) above up to 1000 hours using graphite bipolar plate as reference.
- Exploring the influence of other duplex surface treatments such as pre-oxidation, pre-nitridation prior to chromising treatment on the corrosion, interfacial contact resistance of chromised stainless steel and single cell performance of chromised stainless steel bipolar plates.
- In-depth XPS analysis of pre-carburised and chromised stainless steels.
- Corrosion behaviour evaluation by electrochemical impedance spectroscopy (EIS).

REFERENCES

- [1] British Petroleum Statistical Review of World Energy June 2015. [Online] Available: www.bp.com/content/dam/bp/pdf/energy-economics/statistical-review-2015/bp-statistical-review-of-world-energy-2015-full-report.pdf. (Last accessed on 02/01/2016)
- [2] 2015 Key world Energy statistics. International energy Agency 2015. [online] Available: www.iea.org/publications/freepublications/publication/KeyWorld_Statistics_2015.pdf. (Last accessed on 02/01/2016)
- [3] CO₂ emissions from fuel consumption highlight 2014. International Energy Agency [online] Available: www.ourenergypolicy.org/co2-emissions-from-fuel-combustion-highlights-2014-edition (Last accessed on 02/01/2016).
- [4] M. Balat, Potential importance of hydrogen as a future solution to environmental and transportation problems. *Inter. J. Hydrogen Energy* 2008; 33: 4013 – 4029.
- [5] S. Sharma, S. K. Ghoshal, Hydrogen the future transportation fuel: From production to applications, *Renewable and Sustainable Energy Reviews* 2015; 43: pp. 1151-1158.
- [6] S. McWhorter, C. Read, G. Ordaz, N. Stetson Material based hydrogen storage: attributes for near- term, early market PEM fuel cells. *Current opinion in solid state and materials science* 2011; 15: pp. 29-38.
- [7] Energy in Transport 2014 report. Sustainable Energy Authority of Ireland. [Online] Available:http://www.seai.ie/Publications/Statistics_Publications/Energy_in_Transport/Energy-in-Transport-2014-report.pdf. (Last accessed on 02/01/2016)
- [8] Reducing emissions from transport. [online] Available: www.ec.europa.eu/clima/policies/transport/transport/index_en.html. (Last accessed on 02/01/2016)

- [9] O.Z Sharaf, M F. Orhan, An overview of fuel cell technology: Fundamentals and applications, *Renewable and Sustainable Energy Reviews* 2014; 32: pp. 810-853.
- [10] S. Srinivasan, *Fuel cells: from fundamentals to applications*. New York: Springer science and Business media; 2006.
- [11] B. G. Pollet, I. Staffell, J. L. Shang, Current status of hybrid, battery and fuel cell electric vehicles: From electrochemistry to market prospects, *Electrochimica Acta* 2012; 84: pp. 235-249.
- [12] R. O`Hayre, S-W. Cha, W. Colella, F. B. Prinz, *Fuel cell fundamentals*, New York: John Wiley & Sons, Inc. 2006.
- [13] J. Larminie, A. Dicks, *Fuel cell systems explained*, England, John Wiley & Sons Ltd. 2002.
- [14] P.S Greenwood, ‘‘Polymeric bipolar plates for PEM fuel cells: experimental and modelling approach to assess factors influencing performance’’, PhD thesis, Loughborough University, United Kingdom, (2010), pp. 20.
- [15] G. Merle, M. Wessling, K. Nijmeijer, Anion exchange membranes for alkaline fuel cells: A review, *J. Membrane Science* 2011; 377: pp. 1–35.
- [16] F. Barbir, *PEM fuel cells theory and practice*, USA Eleviser 2013, 2nd edition.
- [17] Y. Wang, K. S. Chen, J. Mishler, S. C. Cho, X. C. Adroher, A review of polymer electrolyte membrane fuel cells: Technology, applications, and needs on fundamental research , *Applied Energy* 2011; 88; pp. 981-1007.
- [18] J. C Yang, Y.S. Park, S.H. Seo, H.J. Lee, J.S. Noh, Development of a 50 kW PAFC power generation system. *J. Power Sources* 2002; 106, (1-2): pp. 68-75.

- [19] A.L Dicks, Molten carbonate fuel cells, *Current Opinion in Solid State and Materials Science*, 2004; 8: pp. 379–383.
- [20] T. A. Adams, J. Nease, D. Tucker, P. I. Barton, *Energy Conversion with Solid Oxide Fuel Cell Systems: A Review of Concepts and Outlooks for the Short- and Long-Term Ind. Eng. Chem. Res.* 2013;52: pp. 3089-3111.
- [21] D. Brett and N. Brandon, Review of materials and characterization method for polymer electrolyte fuel cell flow-field plates, *J. Fuel Cell Sci.& Tech.* 2007; 4: pp. 29-44.
- [22] H. Tawfik, Y. Hung, D. Mahajan, Metal bipolar plates for PEM fuel cell- review *J. Power Sources* 2007; 163 (2): pp. 755-767.
- [23] N. Heras, E.P Roberts, R. Langton, D.R Hodgson, A review of metal separator plate materials suitable for automotive PEM fuel cells. *Energy & Environment Sci.* 2009; 2: pp. 206-214.
- [24] R. A. Antunes, M. C.L. de Oliveira, G. Ett, V.Ett, Carbon materials in composite bipolar plates for polymer electrolyte membrane fuel cells: A review of the main challenges to improve electrical performance, *J. Power Sources* 2011; 196 (6): pp. 2945-2961.
- [25] K.H. Cho, W.G. Lee, S.B. Lee, H. Jang, Corrosion resistance of chromized 316L stainless steel for PEMFC bipolar plates, *J. Power Sources* 2008; 178 : pp. 671–676.
- [26] S.B. Lee, K.H. Cho, W.G. Lee, H. Jang, Improved corrosion resistance and interfacial contact resistance of 316L stainless-steel for proton exchange membrane fuel cell bipolar plates by chromizing surface treatment, *J. Power Sources* 2009; 187: pp. 318–323.

- [27] L. Yang, H. Yu, L. Jiang, L. Zhu, X. Jian, Z. Wang, Improved anticorrosion properties and electrical conductivity of 316L stainless steel as bipolar plate for PEM fuel cell by lower temperature chromizing treatment, *J. Power Sources* 2010; 195: pp. 2810–2814.
- [28] T-M. Wen, K-H Hou, C-Y Bai, M-D. Ger, P-H Chien, S-J Lee, Corrosion behaviour and characteristics of reforming chromized coatings on SS 420 steel in the simulated environment of proton exchange membrane fuel cells, *Corros. Sci.* 2010; 52: pp. 3599–3608.
- [29] C-Y. Bai, T-M Wen, M-S Huang, K-H Hou, M-D Ger, S-J Lee, Surface modification and performance of inexpensive Fe-based bipolar plates for proton exchange membrane fuel cells, *J. Power Sources* 2010;195: pp. 5686–5691.
- [30] N. Guo , M. C. Leu, Performance investigation of polymer electrolyte membrane fuel cells using graphite composite plates fabricated by selective laser sintering, *J. Fuel Cell Sci. Tech.* 2014; 11(1); :011003-011003-8. doi:10.1115/1.4025520.
- [31] S-P Jung, C-I Lee, C-C Chen, W-S Chang, C-C Yang, Development of novel proton exchange membrane fuel cells using stamped metallic bipolar plates, *J. Power Sources* 2015; 283: pp. 429-442.
- [32] M. Rikukawa, K. Sanui, Proton-conducting polymer electrolyte membranes based on hydrocarbon polymers, *Progress in Polymer Sci.* 2000 (25): pp. 1463-1502
- [33] S.M J. Zaidi, T. Matsuura, *Polymer Membranes for Fuel Cells*, Springer Science and Business Media, LLC 2009. doi: 10.1007/978-0-387-73532-0.
- [34] J. Zhang, *PEM fuel cell electrocatalyst and catalyst layers: Fundamentals and application* edited by, Springer Verlag, London, 2008

- [35] J. Benziger, J. Nehlsen, D. Blackwell, T. Brennan, J. Itescu, Water flow in the gas diffusion layer of PEM fuel cells, *J. Membrane Sci.* 2005; 261: pp. 98–106.
- [36] L. Peng, P. Yi, X. Lai, Design and manufacturing of stainless steel bipolar plates for proton exchange membrane fuel cells, *Inter. J. Hydrogen Energy* 2014;39 (36): pp. 21127–21153.
- [37] S. Karimi, N. Fraser, B. Roberts, F.R. A Foulkes, Review of Metallic Bipolar Plates for Proton Exchange Membrane Fuel Cells: Materials and Fabrication Methods, *Advances in Materials Sci. & Engr.* 2012, Article ID 828070, <http://dx.doi.org/10.1155/2012/828070>.
- [38] R. A. Antunes, M. Cristina, L. Oliveira G. Ett, V. Ett, Corrosion of metal bipolar plates for PEM fuel cells: A review, *Int. J. Hydrogen energy* 2010; 35: pp. 3632–3647.
- [39] E. Planes, L. Flandin, N. Alberola, Polymer composites bipolar plates for PEMFCs, *Energy Procedia* 2012; 20: pp. 311 – 323.
- [40] G. Upreti, D. L. Greene, K. G. Duleep, R.Sawhney, Fuel cells for non-automotive uses: Status and prospects, *Inter. J. Hydrogen Energy* 2012; 37 (8): pp. 6339-6348.
- [41] US DOE Office of energy efficiency and renewable energy: Hydrogen fuel Cells and infrastructures technologies program: Multi-Year research, Development and Development, and Demonstration, Plan. pp. 25-29. [Online] Available: <http://www.nrel.gov/docs/fy05osti/34289.pdf>. Last accessed on 05/01/2016.
- [42] A. Martin, L. Jörissen, AutoStack – CORE – Industry Led European Consortium to Develop Next Generation Automotive Stack Hardware, *ECS Transactions* 2015; 69 : (17) pp. 957-961.
- [43] A. Martin, L. Jörissen, Auto-Stack - Implementing a European Automotive Fuel Cell Stack Cluster Fuel Cell Applications, *ECS Transactions* 2012: 42 (1): pp. 31-38.

- [44] H. Tsuchiya, O. Kobayashi, Mass production cost of PEM fuel cell by learning curve, *Int. J. Hydrogen Energy* 2004; 29: pp. 985-990.
- [45] I. Bar-On, R. Kirchain, R. Roth, Technical cost analysis for PEM fuel cells, *J. Power Sources* 2002; 109(1), pp.71-75.
- [46] B.D. James, J.A. Kalinoski, K.N. Baum, Mass Production Cost Estimation for Direct H₂ PEM Fuel Cell Systems for Automotive Applications: 2010 Update, Directed Technologies, Arlington,VA. [Online] Available: https://www1.eere.energy.gov/hydrogenandfuelcells/pdfs/mass_production_cost_estimation_report.pdf. (Last accessed on 06/01/2016).
- [47] R. Taherian, A review of composite and metallic bipolar plates in proton exchange membrane fuel cell: Materials, fabrication, and material selection, *J. Power Sources* 2014; 265: pp. 370-390.
- [48] F. A. de Bruijn, V.A.T. Dam, G.J.M. Janssen, Review: Durability and degradation issues of PEM fuel cell components, *Fuel cells* 2008; 1: pp. 3-22.
- [49] H.L. Wang, J.A. Turner, The influence of metal ions on the conductivity of Nafion 112 in polymer electrolyte membrane fuel cell, *J. Power Sources* 2008; 183 (2) : pp. 576–5809.
- [50] M. Sulek, J. Adams, S. Kaberline, M. Ricketts, J.R. Waldecker, In situ metal ion contamination and the effects on proton exchange membrane fuel cell performance, *J. Power Sources* 2011;196 : pp. 8967–8972.
- [51] K.D. Baik, B. K. Hong , M. S. Kim, Novel technique for measuring oxygen crossover through the membrane in polymer electrolyte membrane fuel cells, *Inter. J. Hydrogen Energy* 2013; 38 : pp. 8927 – 8933.

- [52] Fuel cell theory, http://www.fuelcell.no/principle_fctheory_eng.htm (accessed on 01/07/2016).
- [53] C. J. Netwall, B. D. Gould, J.A. Rodgers, N.J Nasello, K.E. Swider-Lyons, Decreasing contact resistance in proton-exchange membrane fuel cells with metal bipolar plates. *J. Power sources* 2013; 227: pp. 137-144.
- [54] [http://bama.ua.edu/~rreddy/projects/fuel cells.htm](http://bama.ua.edu/~rreddy/projects/fuel%20cells.htm). (Last accessed on 05/05/2016)
- [55] B. Avasarala, P. Haldar, Effect of surface roughness of composite bipolar plates on the contact resistance of a proton exchange membrane fuel cell, *J. Power Sources* 2009; 188 (1), pp. 225-229.
- [56] A. Kraysberg, M. Auinat, Y. Ein-Eli, Reduced contact resistance of PEM fuel cell's bipolar plates via surface texturing, *J. Power Sources* 2007; 164: pp. 697–703
- [57] T. J. Mason, J. Millichamp , T. P. Neville, A. El-kharouf ,B. G. Pollet, D. J. L. Brett, Effect of clamping pressure on ohmic resistance and compression of gas diffusion layers for polymer electrolyte fuel cells , *J. Power Sources* 2012; 219: pp. 52-59.
- [58] S-D. Yim, B-J. Kim, Y-J. Sohn, Y-G Yoon, G-G Park, W-Y Lee, C-S. Kim, Y. C. Kim The influence of stack clamping pressure on the performance of PEM fuel cell stack *Current Applied Physics* 2010; 10: pp. 59–61.
- [59] M.S. Ismail, T. Damjanovic, D.B. Ingham, M. Pourkashanian, A. Westwood, Effect of polytetrafluoroethylene-treatment and microporous layer-coating on the electrical conductivity of gas diffusion layers used in proton exchange membrane fuel cells, *J. Power Sources* 2010; 195: pp. 2700–2708.

- [60] A. El-kharouf, T. J. Mason, Dan J.L. Brett, Bruno G. Pollet, Ex-situ characterisation of gas diffusion layers for proton exchange membrane fuel cells, *J. Power Sources* 2012; 218: pp. 393–404.
- [61] Stainless steels, ASM speciality handbook edited by J.R Davis ASM Material Park, OH 1999
- [62] K.H. Lo, C.H. Shek , J.K.L. Lai, Recent developments in stainless steels, *Materials Science and Engineering R* 2009; 65: pp. 39–104.
- [63] J. J Kim, Y. M. Young, Study on the passive film of type 316 stainless steel, *Int. J. Electrochem. Sci.* 2013; 8, pp. 11847 – 11859
- [64] H. Wang, J. A. Turner. Reviewing metallic PEMFC bipolar plates, *Fuel Cells* 2010; 10(4): pp. 510–519.
- [65] H. Wang, M.A. Sweikart, J.A. Turner, Stainless steel as bipolar plate material for polymer electrolyte membrane fuel cells. *J. Power sources* 2003, 115 (2), pp.243-251.
- [66] H. Wang, J. A. Turner, Ferritic stainless steels as bipolar plate material for polymer electrolyte membrane fuel cells, *J. Power Sources* 2004; 128: pp. 193-200.
- [67] D.P. Davies, P.L. Adcock, M. Turpin and S.J. Rowen, Bipolar plate materials for solid polymer fuel cells, *J. Applied Electrochemistry* 2000; 30: pp. 101-105.
- [68] L. Ma, S. Warthesen, D.A. Shores, Evaluation of materials for bipolar plates in PEMFCs, *J. New Materials for Electrochemical Systems* 2000: pp. 221-228.
- [69] D. D. Papadias, R. K. Ahluwalia, J. K. Thomson, H. M. Meyer III, M. P., H. Wang, J. A. Turner, R. M, R. Borup, Degradation of SS316L bipolar plates in simulated fuel cell environment: Corrosion rate, barrier film formation kinetic and contact resistance, *J. Power sources* 2015; 273: pp. 1237-1249.

- [70] M. C. Li, C. L. Zeng, S. Z. Luo, J. N. Shen, H. C. Lin, C. N. Cao, Electrochemical corrosion characteristics of type 316 stainless steel in simulated anode environment for PEMFC. *Electrochimica Acta* 2003; 48:pp. 1735-1741.
- [71] R. C Makkus, A. H.H Janssen, F. A de Bruijn, R. K. Mallant, Use of stainless steel for cost competitive bipolar plates in the SPFC, *J. Power Sources* 2000; 86 (1–2):pp. 274-282.
- [72] Y. Wang and D. Northwood, Effects of O₂ and H₂ on the corrosion of SS316L metallic bipolar plate materials in simulated anode and cathode environments of PEM fuel cells. *Electrochimica Acta* 2007; 52: pp. 6793–6798.
- [73] Y. Soma, I. Muto, N. Hara, Electrochemical Properties of Titanium in PEFC Bipolar Plate Environments. *Materials Transactions* 2010; 51 (5):pp. 939 - 947.
- [74] Y. Wang and D. Northwood, An Investigation of Commercial Grade 2 Titanium as a bipolar plate material for PEM fuel cells. *Electrochemical Soc. Trans.* 2008; 11 (18): pp. 53-60.
- [75] D.R. Hodgson, B. May, P. L. Adcock, D, P. Davies. New lightweight bipolar plate system for polymer electrolyte membrane fuel cells. *J. Power sources* 2001; 96(1): pp. 233-235.
- [76] C. K. Jin, M. G. Jeong, C. G. Kang, Fabrication of titanium bipolar plates by rubber forming and performance of single cell using TiN-coated titanium bipolar plates, *Inter. J. Hydrogen Energy* 2014; 39 (36): pp. 21480-21488.
- [77] P. L. Hentall, J. B.Lakeman, G. O. Mepsted, P. L. Adcock, J. M. Moore, New materials for polymer electrolyte membrane fuel cell current collectors, *J. Power Sources* 1999; 80: pp. 235-241.

- [78] A.S. Woodman, E.B. Anderson, K.D. Jayne, and M.C. Kimble, "Development of Corrosion-Resistant Coatings for Fuel Cell Bipolar Plates," in American Electroplaters and Surface Finishers Society 1999, AESF SUR/FIN '99 Proceedings, June 1999.
- [79] S-J. Lee, C-H. Huang, Y-P Chen, Investigation of PVD coating on corrosion resistance of metallic bipolar plates in PEM fuel cell, *J. Materials Processing Technology* 2003;140: pp. 688–693.
- [80] V. V. Nikam, R. G. Reddy, Corrosion studies of a copper–beryllium alloy in a simulated polymer electrolyte membrane fuel cell environment, *J. Power Sources* 2005;152: pp. 146-155
- [81] V. V. Nikam, R. G. Reddy, Copper alloy bipolar plates for polymer electrolyte membrane fuel cell, *Electrochimica Acta* 2006; 51 (28): pp. 6338-6345.
- [82] P. Costamagna, S. Srinivasan, Quantum jumps in the PEMFC science &Technology from the 1960s to the year 2000.Part II Engineering technology development and application aspect, *J. Power Sources* 2001; 102: 253-269.
- [83] S-S. Hsieh, C-F. Huang, C-L. Feng, A novel design and micro-fabrication for copper (Cu) electroforming bipolar plates, *Micron* 2008; 39 (3): pp. 263-268.
- [84] T.J. Pan, X.W. Zuo, T. Wang, J. Hu, Z.D. Chen, Y.J. Ren, Electrodeposited conductive polypyrrole/polyaniline composite film for the corrosion protection of copper bipolar plates in proton exchange membrane fuel cells, *J. Power Sources* 2016; 302: pp. 180-188.
- [85] J. Wind, R. Spah, W. Kaiser, G. Bohm, Metallic bipolar plates for PEM fuel cells, *J. Power Sources* 2002; 105: pp. 256-260.
- [86] S-H. Wang, J. Peng, W-B Lui, J.S Zhang Performance of the gold-plated titanium bipolar plates for the light weight PEM fuel cells. *J. Power Sources* 2006; 162 (1):pp. 486-491

- [87] S-H. Wang, J. Peng, W-B Lui, Surface modification and development of titanium bipolar plates for PEM fuel cells. *J. of Power Sources* 2006; 160 (1): pp. 485–489.
- [88] A. Kumar, M. Ricketts, S. Hirano, Ex situ evaluation of nano-meter range gold coating on stainless steel substrate for automotive polymer electrolyte membrane fuel cell bipolar plate, *J. Power Sources* 2010; 195 (5): pp. 1401-1407.
- [89] D. Zhang, L. Duan, L. Guo, Z. Wang, J. Zhao, W.H Tuan, K. Niihara, TiN-coated titanium as the bipolar plate for PEMFC by multi-arc ion plating. *Int. J. Hydrogen Energy* 2011; 36: pp. 9155-9161.
- [90] Z. Ren, D. Zhang, Z. Wang, Stacks with TiN/titanium as the bipolar plate for PEMFCs. *Energy* 2012; 48 (1): pp. 577 -581.
- [91] E.A. Cho, U.-S.Jeon, S.-A.Hong, I.-H. Oh, S.-G. Kang, Performance of a 1kW-class PEMFC stack using TiN-coated 316 stainless steel bipolar plates, *J. Power Sources* 2005; 142: pp. 177-183.
- [92] Y. Wang and D. O. Northwood An investigation into TiN-coated 316L stainless steel as a bipolar plate material for PEM fuel cells, *J. Power Sources* 2007; 165(1): pp. 293-298.
- [93] R. Tian, J. Sun, L. Wang, Plasma-nitrided austenitic stainless steel 316L as bipolar plate for PEMFC, *Int. J. Hydrogen Energy* 2006, 31(13): pp. 1874-1878.
- [94] N.D Nam, Jung Gu Kim, W.-S. Hwang, Effect of bias voltage on the electrochemical properties of TiN coating for polymer electrolyte membrane fuel cell, *Thin Solid Films* 2009; 517 (17): pp. 4772-4776
- [95] W-S. Jeon, J.-G.Kim, Y.-J.Kim, J.G. Han Electrochemical properties of TiN coatings on 316L stainless steel separator for polymer electrolyte membrane fuel cell *Thin Solid Films* 2008 ; 516 (11): pp. 3669-3672.

- [96] K. Feng, D.T.K. Kwok, D. Liu, Z. Li ,X. Cai, P.K. Chu, Nitrogen plasma-implanted titanium as bipolar plates in polymer electrolyte membrane fuel cells. *J. Power sources* 2010; 195 (19): pp. 6798-6804.
- [97] M. Omrani, M. Habibi, R. Amrollahi, A. Khosravi, Improvement of corrosion and electrical conductivity of 316L stainless steel as bipolar plate by TiN nanoparticle implantation using plasma focus, *Inter. J. Hydrogen Energy* 2012; 37(19): pp. 14676-14686.
- [98] D. Zhang , L. Duan , L. Guo , Z. Wang , J. Zhao , W.H Tuan , K. Niihara , TiN-coated titanium as the bipolar plate for PEMFC by multi-arc ion plating, *Int. J. Hydrogen Energy* 2011; 36: pp. 9155-9161.
- [99] S.H. Lee, N. Kakati, J. Maiti, S.H. Jee, D.J. Kalita, Y.S. Yoon, Corrosion and electrical properties of CrN- and TiN-coated 316L stainless steel used as bipolar plates for polymer electrolyte membrane fuel cells, *Thin Solid Films* 2013; 529 (1): pp. 374-379.
- [100] B. Wu, Y. Fu, J. Xu, G. Lin, M. Hou, Chromium nitride films on stainless steel as bipolar plate for proton exchange membrane fuel cell, *J. Power Sources* 2009; 194 (2): pp. 976-980.
- [101] O. Lavigne, C. Alemany-Dumont, B. Normand, S. Berthon-Fabry, R. Metkemeije, Thin chromium nitride PVD coatings on stainless steel for conductive component as bipolar plates of PEM fuel cells: Ex-situ and in-situ performances evaluation, *Inter. J. Hydrogen Energy* 2012; 37(14): pp. 10789-10797.
- [102] K. Feng, Z. Li, H. Sun, L. Yu, X. Cai, Y. Wu, P. K. Chu, C/CrN multilayer coating for polymer electrolyte membrane fuel cell metallic bipolar plates, *J. Power Sources* 2013; 222: pp. 351-358.

- [103] C. K. Jin, K. H. Lee, C. G. Kang, Performance and characteristics of titanium nitride, chromium nitride, multi-coated stainless steel 304 bipolar plates fabricated through a rubber forming process, *Inter. J. Hydrogen Energy* 2015; 40 (20): 6681-6688.
- [104] R. Tian, Chromium nitride/Cr coated 316L stainless steel as bipolar plate for proton exchange membrane fuel cell, *J. Power Sources* 2011; 196 (3): pp. 1258-1263.
- [105] H. Zhang, G. Lin, M. Hou, L. Hu, Z. Han, Y. Fu, Z. Shao, B. Yi, CrN/Cr multilayer coating on 316L stainless steel as bipolar plates for proton exchange membrane fuel cells, *J. Power Sources* 2012; 198: pp. 176–181.
- [106] N. D. Nam, D. S. Jo, J. G. Kim, D. H. Yoon, Corrosion protection of CrN/TiN multi-coating for bipolar plate of polymer electrolyte membrane fuel cell, *Thin Solid Films* 2011; 519 (20):pp. 6787-6791.
- [107] F. Bi, P. Yi, T. Zhou, L. Peng, X. Lai, Effects of Al incorporation on the interfacial conductivity and corrosion resistance of CrN film on SS316L as bipolar plates for proton exchange membrane fuel cells, *Inter. J. Hydrogen Energy* 2015; 40 (31): pp. 9790-9802.
- [108] M.P. Brady, K. Weisbrod, I. Paulauskas, R.A. Buchanan, K.L. More, H. Wang, M. Wilson, F. Garzon, L.R. Walker, Preferential thermal nitridation to form pin-hole free Cr-nitrides to protect proton exchange membrane fuel cell metallic bipolar plates, *Scripta Materialia* 2004; 50 (7): pp. 1017-1022.
- [109] B. Yang, M.P. Brady, H. Wang, J.A. Turner, K.L. More, D.J. Young, P.F. Tortorelli, E.A. Payzant, L.R. Walker, Protective nitride formation on stainless steel alloys for proton exchange membrane fuel cell bipolar plates, *J. Power Sources* 2007;174(1): pp. 228-236.

- [110] M.P. Brady, B. Yang, H. Wang, J.A. Turner, K.L. More, M. Wilson, F. Garzon, The formation of protective nitride surfaces for PEM Fuel Cell Metallic Bipolar Plates. TMS, J. materials (JOM) 2006: pp. 50-57.
- [111] M.Brady, H. Wang, J. Turner, H. Meyer III ,K. More,P.Tortorelli ,B. McCarthy , Pre-oxidized and nitrated stainless steel alloy foil for proton exchange membrane fuel cell bipolar plates: Part 1. Corrosion, interfacial contact resistance, and surface structure J. Power Sources 2010; 195 (17) : pp. 5610-5618.
- [112] T. Toops, M. Brady , P. Tortorelli , J. Pihl, F. Estevez , D. Connors , F. Garzon, T. Rockward, T. Gervasio, W. Mylan, H. Kosaraju, Pre-oxidized and nitrated stainless steel alloy foil for proton exchange membrane fuel cell bipolar plates. Part 2: Single-cell fuel cell evaluation of stamped plates. J. Power Sources 2010; 195 (17): pp. 5619-5627.
- [113] M.P. Brady, M. Abd Elhamid, G. Dadheech, J. Bradley, T.J. Toops, H.M. Meyer III, P.F. Tortorelli, Manufacturing and performance assessment of stamped, laser welded, and nitrated FeCrV stainless steel bipolar plates for proton exchange membrane fuel cells, Inter. J. Hydrogen Energy 2013; 38 (11) : pp. 4734-4739.
- [114] K-H. Lee, S-H. Lee, J-H Kim, Y-Y. Lee, Y-H. Kim, M-C. Kim, D-M Wee, Effects of thermal oxi-nitridation on the corrosion resistance and electrical conductivity of 446M stainless steel for PEMFC bipolar plates, Inter. J. Hydrogen Energy 2009; 34 (3): pp. 1515-1521.
- [115] S-H Lee, T-H Yang, S-H Hyun, Y-S Yoon, Corrosion behaviour of pre-oxidized and thermally nitrated stainless steel for polymer electrolyte membrane fuel cell bipolar plate Corros. Sci. 2012; 58: pp. 79-85.

- [116] H. Wang, J. A. Turner, Electrochemical nitridation of a stainless steel for PEMFC bipolar plates, *Inter. J. Hydrogen Energy* 2011; 36 (20): pp. 13008-13013.
- [117] H. Wang, J. A. Turner, Modifying a stainless steel for PEMFC bipolar plate via electrochemical nitration, *Fuel cells* 2013; 13 (5): pp. 917-921
- [118] L. Jinlong, L. Tongxiang, L. Hongyun, Effect of grain refinement and electrochemical nitridation on corrosion resistance of the 316L stainless steel for bipolar plates in PEMFCs environment, *J. Power Sources* 2015; 293: pp. 692-697.
- [119] J. Barranco, F. Barreras, A. Lozano, A. M. Lopez, V. Roda, J. Martin, M. Maza, Gonzalo G. Fuentes, E. Almandoz, Cr and Zr/Cr nitride CAE-PVD coated aluminium bipolar plates for polymer electrolyte membrane fuel cells, *Inter. J. Hydrogen Energy* 2010, 35; 20: pp. 11489 -11498.
- [120] J. Barranco, F. Barreras, A. Lozano, M. Maza, Influence of CrN-coating thickness on the corrosion resistance behaviour of aluminium-based bipolar plates, *J. Power Sources* 2011: 196, (9), pp. 4283-4289.
- [121] Z. Li, K. Feng, Z. Wang, X. Cai, C. Yao, Y. Wu, Investigation of single-layer and multilayer coatings for aluminium bipolar plate in polymer electrolyte membrane fuel cell, *Inter. J. Hydrogen Energy* 2014; 39 (16): pp.8421-8430.
- [122] L. Wang, J. Sun, J. Sun, Y. Lv, S. Li, S. Ji, Z. Wen, Niobium nitride modified AISI 304 stainless steel bipolar plate for proton exchange membrane fuel cell, *J. Power Sources* 2012; 199: pp. 195-200.
- [123] L. Wang, J. Sun, J. Sun, Y. Lv, S. Li, S. Ji, Z. Wen, Molybdenum nitride modified AISI 304 stainless steel bipolar plate for proton exchange membrane fuel cell, *Inter. J. Hydrogen Energy* 2012; 37(7): pp. 5876-5883.

- [124] C. Choe, H. Choi, W. Hong, J-J Lee, Tantalum nitride coated AISI 316L as bipolar plate for polymer electrolyte membrane fuel cell, *Inter. J. Hydrogen Energy*, 2012, 37 (1): pp. 405-411.
- [125] R.J. Tian, J.C. Sun, L. Wang, Effect of plasma nitriding on behaviour of austenitic stainless steel 304L bipolar plate in proton exchange membrane fuel cell, *J. Power Sources* 2007: 163 (2): pp.719-724.
- [126] R.J. Tian, J.C. Sun, L. Wang, Plasma-nitrided austenitic stainless steel 316L as bipolar plate for PEMFC, *Inter. J. Hydrogen Energy* 2006; 31 (13): pp. 1874-1878.
- [127] W. Hong, D-H Han, H Choi, M-W Kim, J-J Lee, High-density plasma nitriding of AISI 316L for bipolar plate in proton exchange membrane fuel cell, *Inter. J. Hydrogen Energy* 2011; 36(3): pp. 2207-2212.
- [128] K. Lin, X. Li, L. Tian, H, Active screen plasma nitriding of 316 stainless steel for the application of bipolar plates in proton exchange membrane fuel cells. *Inter. J. Hydrogen Energy* 2014; 39 (36): pp. 21470-21479.
- [129] K. Lin, X. Li, L. Tian, H. Dong, Active screen plasma surface co-alloying treatments of 316 stainless steel with nitrogen and silver for fuel cell bipolar plates, *Surface & Coatings Techn.* 2015; 283: pp. 122-128.
- [130] K. Lin, X. Li, L. Tian, H. Dong, Active screen plasma surface co-alloying of 316 austenitic stainless steel with both nitrogen and niobium for the application of bipolar plates in proton exchange membrane fuel cells. *Inter. J. Hydrogen Energy* 2015; 40 (32): pp. 10281-10292.
- [131] Y. Hung, H. Tawfik, D. Mahajan, Durability and characterization studies of polymer electrolyte membrane fuel cell's coated aluminium bipolar plates and membrane electrode assembly, *J. Power Sources* 2009; 186 (1): pp. 123-127.

- [132] L. Wang, J. Sun, B. Kang, S. Li, S. Ji, Z. Wen, X. Wang, Electrochemical behaviour and surface conductivity of niobium carbide-modified austenitic stainless steel bipolar plate, *J. Power Sources* 2014; 246: pp. 775-782.
- [133] C-Y Bai, M-D Ger, M-S Wu, Corrosion behaviors and contact resistances of the low-carbon steel bipolar plate with a chromized coating containing carbides and nitrides. *Inter. J. Hydrogen Energy* 2009; 34 (16): pp. 6778-6789.
- [134] C-Y Bai, T-S Wen, K-H Hou, N-W Pu, M-D Ger, The characteristics and performance of AISI 1045 steel bipolar plates with chromized coatings for proton exchange membrane fuel cells , *Inter. J. Hydrogen Energy* 2011; 36 (6): pp. 3975-3983.
- [135] H-C Wang, H-H Sheu, C-E Lu, K-H Hou, M-D Ger, Preparation of corrosion-resistant and conductive trivalent Cr-C coatings on 304 stainless steel for use as bipolar plates in proton exchange membrane fuel cells by electrodeposition, *J. Power Sources* 2015; 293: pp. 475-483.
- [136] H-C Wang, H-H Sheu, C-E Lu, K-H Hou, M-D Ger ,The study of electroplating trivalent CrC alloy coatings with different current densities on stainless steel 304 as bipolar plate of proton exchange membrane fuel cells, *Thin Solid Films* 2014; 570: pp. 209-214.
- [137] B. Wu, G. Lin, Y. Fu, M. Hou, B. Yi, Y. Zhao, L. Wei, P. Yi, L. Peng, Chromium-containing carbon film on stainless steel as bipolar plates for proton exchange membrane fuel cells, *Inter. J. Hydrogen Energy* 2010; 35 (24): pp. 13255-13261.
- [138] H. Wang, J. A. Turner, SnO₂: F, coated ferritic stainless steels for PEM fuel cell bipolar plates, *J. Power Sources* 2007; 70 (2): pp. 387-394.
- [139] H. Wang, J. A. Turner, X. Li, R. Bhattacharya, SnO₂:F coated austenite stainless steels for PEM fuel cell bipolar plates , *J. Power Sources* 2007; 171(2): pp. 567-574.

- [140] H. Wang, J.A. Turner, X. Li, G. Teeter, Process modification for coating SnO₂:F on stainless steels for PEM fuel cell bipolar plates, *J. Power Sources* 2008 ; 178(1): pp. 238-247.
- [141] J. H. Park, B. J. Jeon, J. K. Lee, Electrochemical characteristics of fluorine-doped tin oxide film coated on stainless steel bipolar plates, *Surface & Coatings Techn.*, 2015; 277: pp. 1-6.
- [142] A. E. Fetohi, R.M. A. Hameed, K.M. El-Khatib, Ni–P and Ni–Mo–P modified aluminium alloy 6061 as bipolar plate material for proton exchange membrane fuel cells, *J. Power Sources* 2013; 240: pp. 589-597.
- [143] A. E. Fetohi, R.M. A. Hameed, K.M. El-Khatib, Development of electroless Ni–P modified aluminium substrates in a simulated fuel cell environment, *J. Industrial & Engineering Chemistry* 2015; 30: pp. 239-248.
- [144] A. E. Fetohi , R.M. A. Hameed , K.M. El-Khatib , E. R. Souaya, Study of different aluminium alloy substrates coated with N-C0-P as metallic bipolar plates for PEM fuel cell applications, *Inter. J. Hydrogen Energy* , 2012 ; 37: pp. 10807- 10817.
- [145] C-K Lee, Electroless Ni–Cu–P/nano-graphite composite coatings for bipolar plates of proton exchange membrane fuel cells, *J. Power Sources*, 2012 220: pp. 130-137.
- [146] T. Fukutsuka, T. Yamaguchi, S-I Miyano, Y. Matsuo, Y. Sugie, Z. Ogumi, Carbon-coated stainless steel as PEFC bipolar plate material , *J. Power Sources* 2007; 174 (1) : pp. 199-205.
- [147] K. Feng, X. Cai, H. Sun, Z. Li, P. K. Chu, Carbon coated stainless steel bipolar plates in polymer electrolyte membrane fuel cells, *Diamond and Related Materials*, 2010;19 (11): pp. 1354-1361

- [148] Y. Show, Electrically conductive amorphous carbon coating on metal bipolar plates for PEFC. *Surface and Coatings Techn.* 2007; 202 (4–7) : pp. 1252-1255.
- [149] P. Yi, L. Peng, L. Feng, P. Gan, X. Lai, Performance of a proton exchange membrane fuel cell stack using conductive amorphous carbon-coated 304 stainless steel bipolar plates, *J. Power Sources* 2010; 195(20): pp. 7061-7066.
- [150] W-L. Wang, S-M He, C-H Lan, Protective graphite coating on metallic bipolar plates for PEMFC applications, *Electrochimica Acta* 2012; 62: pp. 30-35.
- [151] H. Husby, O.E. Kongstein, A. Oedegaard, F. Seland, Carbon-polymer composite coatings for PEM fuel cell bipolar plates, *Inter Journal of Hydrogen Energy* 2014; 39 (2): pp. 951-957.
- [152] C-Y Chung, S-K Chen, P-J Chiu, M-H Chang, T-T Hung, T-H Ko, Carbon film-coated 304 stainless steel as PEMFC bipolar plate, *J. Power Sources* 2008; 176 (1): pp. 276-281.
- [153] N-W Pu, G-N. Shi, Y-M. Liu, X. Sun, J-K. Chang, C-L Sun, M-D Ger, C-Y. Chen, P-C. Wang, Y-Y. Peng, C-H. Wu, S. Lawes, Graphene grown on stainless steel as a high-performance and ecofriendly anti-corrosion coating for polymer electrolyte membrane fuel cell bipolar plates, *J. Power Sources* 2015; 282: pp. 248-256.
- [154] A. C. Stoot, L. Camilli, S-A Spiegelhauer, F. Yu, P. Bøggil, Multilayer graphene for long-term corrosion protection of stainless steel bipolar plates for polymer electrolyte membrane fuel cells, *J. Power Sources* 2015; 293: pp. 846-851.
- [155] S-J. Lee, C-H. Huang, Y-P. Chen, Investigation of PVD coating on corrosion resistance of metallic bipolar plates in PEM fuel cell, *J. Materials Processing Techn.* 2003; 140: pp. 688–693.

- [156] Y. Suzuki, M. Watanabe, T. Toda and T. Fujii, Development of electrically conductive DLC coated stainless steel separators for polymer electrolyte membrane fuel cell , J. Phys. : Conf. Ser. 2013; 441 012027: pp1-6.
- [157] S. Joseph, J.C. McClure, R. Chianelli, P. Pich, P.J. Sebastian, Conducting polymer- coated stainless steel bipolar plates for proton exchange membrane fuel cells (PEMFC), Inter. J. Hydrogen Energy 2005; 30: pp. 1337-1344.
- [158] S. Joseph, J.C. McClure, R. Chianelli, P. Pich, P.J. Sebastian, J. Moreira, E. Valenzuela Polyaniline and polypyrrole coatings on aluminium for PEM fuel cell bipolar plates, J. Power Sources 2008;77 (1): pp. 161-166.
- [159] Y. Wang and D. Northwood, An investigation into polypyrrole-coated 316L stainless steel as a bipolar plate material for PEM fuel cells, J. Power Sources 2006; 163 (1): pp. 500-508.
- [160] W.J. Pech-Rodríguez, D. González-Quijano, G. Vargas-Gutiérrez, F.J. Rodríguez-Varela, Electrophoretic deposition of polypyrrole/Vulcan XC-72 corrosion protection coatings on SS-304 bipolar plates by asymmetric alternating current for PEM fuel cells, Inter. J. Hydrogen Energy 2014;39 (29): pp. 16740-16749.
- [161] L-J Yang, H-J Yu, L. Jiang, L. Zhu , X-Y Jian, Z. Wang, Graphite –polypyrrole coated 316L stainless steel as bipolar plates for proton exchange membrane fuel cells. Inter .J. Minerals, Metallurgy and Materials 2011; 18 (1): pp. 53-58.

- [162] Y. Wang and D. Northwood, Optimization of the polypyrrole-coating parameters for proton exchange membrane fuel cell bipolar plates using the Taguchi method, *J. Power Sources* 2008; 185 (1): pp. 226–232
- [163] Y-B Lee, C-H Lee, D-S Lim, The electrical and corrosion properties of carbon nanotube coated 304 stainless steel/polymer composite as PEM fuel cell bipolar plates, *Inter. J. Hydrogen Energy* 2009; 34 (24) : pp. 9781-9787.
- [164] J.R. Mawdsley, J.D. Carter, X. Wang, S. Niyogi, C.Q.Fan, R. Koc, G.Osterhout, Composite-coated aluminium bipolar plates for PEM fuel cells. *J. Power Sources* 2013; 231: pp. 106-112.
- [165] Y. Fu, M. Hou, H. Xu, Z. Hou, P. Ming, Z. Shao, B. Yi, Ag–polytetrafluoroethylene composite coating on stainless steel as bipolar plate of proton exchange membrane fuel cell, *J. Power Sources* 2008; 182 (2): pp. 580 - 584.
- [166] Y. Show, K. Takahashi, Stainless steel bipolar plate coated with carbon nanotubes (CNT)/polytetrafluoroethylene (PTFE) composite film for proton exchange membrane fuel cell (PEMFC), *J. Power Sources* 2009; 190 (2): pp. 322-325.
- [167] W. Yuan, Y. Tang, X. Yang, Z. Wan, Porous metal materials for polymer electrolyte membrane fuel cells – A review .*Applied Energy* 2012; 94: pp. 309-329.
- [168] A. Kumar, R. G. Reddy , Materials and design development for bipolar/end plates in fuel cells. *J. Power Sources* 2004; 129 (1) : pp. 62-67.

- [169] B-T. Tsai, C-J. Tseng, Z-S.Liu, C-H.Wang, C-I Lee, C-C.Yang, S-K.Lo, Effects of flow field design on the performance of a PEM fuel cell with metal foam as the flow distributor, *Inter. J. Hydrogen Energy* 2012; 37 (17): pp. 13060-13066.
- [170] O. J. Murphy, A. Cisar, E.Clarke, Low-cost light weight high power density PEM fuel cell stack, *Electrochimica Acta* 1998; 43 (24) : pp. 3829-3840.
- [171] C-J. Tseng, B. T. Tsai, Z-S. Liu, T-C. Cheng, W-C. Chang, S-K Lo, A PEM fuel cell with metal foam as flow distributor , *Energy Conversion and Management* 2012; 62 : pp. 14-21.
- [172] A. Kumar, R.G Reddy Modelling of polymer electrolyte membrane fuel cell with metal foam in the flow-field of the bipolar/end plates, *J. Power Sources* 2003; 114 (1) : pp. 54-62.
- [173] J. O'Donoghue, D. Haverty, Method of Doping Surfaces, *PCT Application: WO2008/033867*, (2008).
- [174] F. Tan, M. Nasiri, M. Al-Rubeai, In vitro osteoblastic cell activity on Bioglass-derived bioceramic surfaces deposited by a novel CoBlast™ technique, *J. Biotechnology* 2012;150: pp. 454 - 456.
- [175] F. Tan, M. Naciri, D. Dowling, M. Al-Rubeai, In vitro and in vivo bioactivity of CoBlast™ hydroxyapatite coating and the effect of impaction on its osteoconductivity, *Biotechnology Advances* 2012; 30 (1): pp. 352-362.
- [176] J.N. Barry, B. Twomey, A. Cowley, L. O'Neill, P.J. McNally, D.P. Dowling, Evaluation and comparison of hydroxyapatite coatings deposited using both thermal and non-thermal techniques, *Surface & Coatings Techn.* 2013; 226: pp. 82-91.

- [177] D. Fleming, L. O'Neill, G. Byrne, N. Barry, D. P. Dowling, Wear resistance enhancement of the titanium alloy Ti-6Al-4V via a novel co-incident microblasting process, *Surface & Coatings Techn.* 2011; 205(21-22): pp 4941-4947.
- [178] J. G. Carton, N. Cobbe, J. O'Donoghue, L. Pambaguian, A. Norman, V. Liedtke, T. McCaul, Aerospace material and process: making next generation design possible (AEROMAT Conference and Exposition, USA,). June 18-21, 2012.
- [179] M. Saxena, B. K. Prasad, T. K. Dan, Corrosion characteristics of aluminium alloy graphite particulate composite in various environments, *J. of Materials science* 1992; 27(17), pp 4805-4812.
- [180] E. M. Sherif, A. A. Almajid, F. H. Latif, H. Junaedi, Effects of Graphite on the Corrosion Behavior of Aluminum Graphite Composite in Sodium Chloride Solutions, *Int. J. Electrochem. Sci.* 2011; 6, pp. 1085 - 1099
- [181] M. C. Galetz, *Coatings for Superalloys*, Superalloys, Dr. M. Aliofkhazraei (Ed.), (2015). InTech, DOI: 10.5772/61141. Available from: <http://www.intechopen.com/books/superalloys/coatings-for-superalloys> (last accessed 07/05/2016)
- [182] R. Bianco, R. A. Rapp, *Pack cementation diffusion coatings*, Metallurgical and Ceramic Protective Coatings Netherlands: Springer Science & Business Media; 978-94-009-1501-5, 1996, pp. 236-260.
- [183] A.R. Castle, D.R. Gabe, Chromium diffusion coatings, *Int. Mat. Rev.* 1999; 44 (2): pp. 37-59.

- [184] E. Kasprzycka, Chromizing, Encyclopedia of Tribology New York, Springer Science & Business Media 978-0-387-92897-5, 2013, pp. 382-387.
- [185] Z.D. Xiang, P.K. Datta, Relationship between pack chemistry and aluminide coating formation for low-temperature aluminisation of alloy steels, Acta Materialia 2006; 54, pp. 4453–4463.
- [186] K.D. Ralston, D. Fabijani, R.T. Jones, N. Birbilis, Achieving a chromium rich surface upon steels via FBR-CVD chromising treatments, Corros. Sci. 2011; 5: pp. 2835–2842.
- [187] Y-W Chung, Introduction to Materials Science for Engineers, Taylor and francis group, florida,USA
- [188] N. V. Bangaru, R. C. Krutenat, Diffusion Coatings of Steels: Formation Mechanism and Microstructure of Aluminized Heat-Resistant Stainless Steels, J. Vac. Sci. Techn. 1984; 2: pp. 806-815.
- [189] C. Lopez, A. Kvryan, S. Kasnakjian, A. Coronado, S. Sujittosakul, O. Villalpando, V. Rav, Effect of Austenite Stability on Pack Aluminizing of Austenitic Stainless Steels, JOM 2015; 67: pp. 61-67.
- [190] Iron-carbon diagram. [Online]. Available:http://www.tf.uni-kiel.de/matwis/amat/mw1_ge/kap_8/illustr/i8_4_1.html(Last accessed on 21/01/2016).
- [191] H.S. Khatak, B. Rav, Corrosion of Austenitic Stainless Steels: Mechanism, Mitigation and Monitoring, 2002, Alpha Science International Ltd, UK.

- [192] S.R. Collins, P.C. Williams, and S.V. Marx, A. Heuer, F. Ernst, and H. Kahn, Low-Temperature Carburization of Austenitic Stainless Steels, ASM Handbook, Volume 4D, Heat Treating of Irons and Steels, ASM International 2014: pp. 451 – 460.
- [193] S.S. Hosmani, P. Kuppusami, R.K. Goyal, An Introduction To Surface Alloying of Metals India , Springer Briefs in Applied Sciences and Technology 978-81-322-1888-3. 2014.
- [194] S.L.C. Ferreira, R.E. Bruns, H.S. Ferreira, G.D. Matos, J.M. David, G.C. Brandao, E.G.P. da Silva, L.A. Portugal, P.S. dos Reis, A.S. Souza, W.N.L. dos Santos, Box-Behnken design: An alternative for the optimization of analytical methods, *Analytica Chimica Acta* 2007; 597, pp. 179–186.
- [195] D.C. Montgomery, Design and analysis of experiments, John Wiley & Sons Inc 2013.
- [190] R.H. Myers and D.C. Montgomery, Response surface methodology, Wiley, 2002.
- [197] M. Mourabet, A. El Rhilassi, M. Bennani-Ziatni, A. Taitai, Comparative Study of Artificial Neural Network and Response Surface Methodology for Modelling and Optimization the Adsorption Capacity of Fluoride onto Apatitic Tricalcium Phosphate, *Universal J. Applied Mathematics* 2014; 2 (2), pp. 84-91.
- [198] H. Ebrahimifar, M. Zandrahimi, B. Nikrooz, M. Sedighi, Production of cobalt anti-corrosion coating on AISI 430 steel-Optimization using Box-Behnken experimental designs, *Indian J. Chemical Techn.* 2013; 20: pp.40-45.

- [199] B. Nikrooz, M. Zandrahimi, Optimization of process variables and corrosion properties of a multi-layer silica sol gel coating on AZ91D using the Box–Behnken design, *J. Sol-Gel Sci. Techn.* 2011; 59: pp. 640–649.
- [200] R. Soleimani, F. Mahboubi, S.Y. Arman, M. Kazemi, A. Maniee, Development of mathematical model to evaluate microstructure and corrosion behaviour of electroless Ni–P/nano-SiC coating deposited on 6061Al alloy, *J. Industrial & Engr. Chemistry* 2015; 23:pp. 328–337.
- [201] L. Naiming, X. Faqin, W. Xiangqing, T. Wei, Influence of process parameters on thickness and wear resistance of rare earth modified chromium coatings on P110 steel synthesized by pack cementation, *J. of Rare earths* 2011, 29 (4): pp. 396-400.
- [202] Scanning Electron Microscopy. [Online], Available: www.purdue.edu/ehts/rem/rs/sem.htm (Last accessed on 04/01/2016).
- [203] Scanning Electron Microscopy & Energy Dispersive X-Ray Spectroscopy. [Online]. Available: <http://www.surfgroup.be/semedx>. (Last accessed on 04/01/2016)
- [204] M. Ohring, *Engineering Material science*, Academic press, London 1995 pp 96.
- [205] X-ray photoelectron spectroscopy. [Online] Available: https://en.wikipedia.org/wiki/X-ray_photoelectron_spectroscopy. (Last accessed on 04/01/2016).
- [206] J. Conolly “On the use of atmospheric and laser plasmas for biomedical applications” PhD thesis, Dublin City University, 2012.

- [207] N. Perez, *Electrochemistry and corrosion science*, Kluwer academic publishers Boston 2004.
- [208] E. McCafferty, Validation of corrosion rates measured by the Tafel extrapolation method, *Corrosion Science* 2005; 47: pp. 3202–3215.
- [209] J.R Davis, *Corrosion: understanding the basic* ASM international Material Park, Ohio.
- [210] D.A. Jones, *Principles and prevention of corrosion*, second edition, Prentice-Hall, Inc. 1996.
- [211] Y. Tan, *Heterogeneous electrode process and localised corrosion*, John Wiley and Son Inc. 2013.
- [212] E.E. Stansbury, R.A. Buchanan, *Fundamentals of Electrochemical Corrosion*, ASM International, Ohio, 2000
- [213] R. L. Borup and N. E. Vanderborgh, Design and Testing Criteria for Bipolar Plate Materials for PEM Fuel Cell Applications. *Materials Research Society Proceedings*, USA 1995; 393, 151 doi:10.1557/PROC-393-151.
- [214] G. Hinds, E. Brightman, Towards more representative test methods for corrosion resistance of PEMFC metallic bipolar plates, *Inter. J. Hydrogen Energy* 40 (2015) 2785 -2791.

- [215] Th. Uelzen, J. Müller, Wettability enhancement by rough surfaces generated by thin film technology *Thin Solid Films* 2003; 434 (1–2) : pp. 311-315.
- [216] R. N. Wenzel, Surface Roughness and Contact Angle, *J. Phys. Chem.* 1949; 53 (9): pp. 1466–1467.
- [217] H. Nakaea, R. Inui, Y. Hirata, H. Saito, Effects of surface roughness on wettability *Acta Materialia* 1998; 46 (7):pp. 2313-2318.
- [218] NIST X-ray Photo spectroscopy Database 20 version 4.1 [online] Available: http://srdata.nist.gov/xps/main_search_menu.aspx (last accessed 04/01/2016).
- [219] A. Lippitz, Th. Hübert, XPS investigations of chromium nitride thin films, *Surface & Coatings Techn.* 2005; 200 (1–4): pp.250-253.
- [220] A. Conde, A.B. Cristóbal, G. Fuentes, T. Tate, J. de Damborenea, Surface analysis of electrochemically stripped CrN coatings, *Surface & Coatings Techn.* 2006; 201 (6-4): pp.3588-3595.
- [221] C. Pirlot, J. Delhalle, J.J. Pireaux, Z. Mekhalif, Surface modification of polycrystalline iron surfaces by n-dodecanethiol: an XPS investigation, *Surface & Coatings Techn.* 2001; 138 (2-3): pp. 166-172.
- [222] W.H. Lee, C.Y. Hyun, XPS study of porous dental implants fabricated by electro-discharge-sintering of spherical Ti–6Al–4V powders in a vacuum atmosphere, *Applied Surface Science* 2006; 252 (12) : pp. 4250-4256.

- [223] M. Multigner, S. Ferreira-Barragáns, E. Frutos, M. Jaafar, J. Ibáñez, P. Marín, M.T. Pérez-Prado, G. González-Doncel, A. Asenjo, J.L. González-Carrasco, Superficial severe plastic deformation of 316 LVM stainless steel through grit blasting : Effects on its microstructure and subsurface mechanical properties , *Surface & Coatings Techn.* 2010; 205 (7): pp. 1830-1837.
- [224] O. Unal, R. Varol, Surface severe plastic deformation of AISI 304 via conventional shot peening, severe shot peening and re-peening, *Applied Surface Science* 2015; 351: pp. 289-295.
- [225] T. Balusamy, T.S.N. Narayanan, K. Ravichandran, Il S. Park, M. H. Lee, Influence of surface mechanical attrition treatment (SMAT) on the corrosion behaviour of AISI 304 stainless steel, *Corros. Sci.* 2013; 74: pp.332-344.
- [226] W. Li, D. Y. Li, Influence of surface morphology on corrosion and electronic behavior, *Acta Materialia* 2006; 54: pp. 445-452.
- [227] M. Browne, P.J Gregson, Effect of mechanical surface pre-treatment on metal ion release, *Biomaterials* 2000; 21 (4): pp. 385-392.
- [228] H. Dong, Y. Sun, T. Bell, Enhanced corrosion resistance of duplex coatings, *Surface & Coatings Techn.* 1997; 90 (1-2): pp. 91-101.
- [229] J. Munemasa, T. Kumakiri, Effect of the surface roughness of substrates on the corrosion properties of films coated by physical vapour deposition, *Surface & Coatings Techn.* 1991; 49 (1-3): pp. 496-499.

- [230] C. Liu, A. Leyland, S. Lyon, and A. Matthews, An a.c. impedance study on PVD CrN-coated mild steel with different surface roughness, *Surface and Coatings Techn.* 1995; 76–77: pp. 623-631.
- [231] S.D. Lu, Z.B. Wang, K. Lu, Enhanced chromizing kinetics of tool steel by means of surface mechanical attrition treatment, *Materials Science and Engineering: A* 2010; 527 (4–5): pp. 995-1002.
- [232] Z.B. Wang, J. Lu, K. Lu, Wear and corrosion properties of a low carbon steel processed by means of SMAT followed by lower temperature chromizing treatment, *Surface and Coatings Techn.* 2006; 201 (6): pp. 2796-2801.
- [233] W. Li, D.Y. Liu, Variations of work function and corrosion behaviors of deformed copper surfaces, *Applied Surface Science* 2005; 240 (1- 4): pp. 388-395.
- [234] S.M. Alvarez, A. Bautista, F. Velasco, Influence of strain-induced martensite in the anodic dissolution of austenitic stainless steels in acid medium, *Corros Sci.* 2013; 69: pp.130-138.
- [235] M. Detroye, F. Reniers, C. Buess-Herman, J. Vereecken, AES–XPS study of chromium carbides and chromium iron carbides, *Applied Surface Sci.* 1999;144–145: pp. 78–82.
- [236] N. Tabet , I. Allam , R.C, Yin, X-ray photoelectron spectroscopy investigation of the carburization of 310 stainless steel , *Applied Surface Science* 2002; 195 : pp. 166–174.

- [237] F. Otsubo, K. Kishitake, T. Akiyama, T. Terasaki, Characterization of blasted austenitic stainless steel and its corrosion resistance, *J. Thermal Spray Techn.* 2003; 12 (4) : pp. 555-559.
- [238] C. Galván, L. Saldaña, M. Multigner, A. Calzado-Martín, M. Larrea, C. Serra, N. Vilaboa, J. L. González-Carrasco , Grit blasting of medical stainless steel: implications on its corrosion behavior, ion release and biocompatibility, *J. of Materials Science: Materials in Medicine* 2012; 23(3): pp. 657-666.
- [239] E. Çelik, A.Ş. Demirkıran, E. Avcı, Effect of grit blasting of substrate on the corrosion behaviour of plasma-sprayed Al₂O₃ coatings, *Surface & Coatings Techn.* 1999; 116–119: pp. 1061-1064.
- [240] J. Bhandari, F. Khan, R. Abbassi, V. Garaniya, R. Ojeda, Modelling of pitting corrosion in marine and offshore steel structures – A technical review, *J. Loss prevention in the process industries* 2015; 37: pp. 39-62.
- [241] F. A. P. Fernandes, S. C. Heck, C. A. Picon, G. E. Totten , L. C. Casteletti, Wear and corrosion resistance of pack chromised carbon steel, *Surface Engineering*, 2012; 28 (5) : pp. 313-317.
- [242] J. Creus, H. Mazille, H. Idrissi, Porosity evaluation of protective coatings onto steel, through electrochemical techniques, *Surf. Coat. Technol.* 2000; 130, pp. 224–232.
- [243] H. Dong, Y. Sun, T. Bell, Enhanced corrosion resistance of duplex coatings, *Surface and Coatings Technol.* 1997; 90, pp. 91-101.

- [244] L. Castaldi, D. Kurapov, A. Reiter, V. Shklover, J. Patscheide, Tuning the crystallographic and electronic properties of chromium oxynitride films, *J. Appl. Phys.* 2011; **109**, pp. 053720-1 – 053720-7.
- [245] I. Milošev, H.-H. Strehblow, B. Navinšek, XPS in the study of high-temperature oxidation of CrN and TiN hard coatings, *Surface and Coatings Techn.* 1995;74–75: pp. 897-902.
- [246] J-W Lee, J-G Duh, S-Y Tsai, Corrosion resistance and microstructural evaluation of the chromized coating process in a dual phase Fe-Mn-Al-Cr alloy, *Surface & Coatings Techn.* 2002; 153 (1): pp. 59-66.
- [247] G.H. Meier, C. Cheng, R.A. Perkins, W. Bakker, Diffusion chromizing of ferrous alloys, *Surface and Coatings Techn.* 1989; 39–40(1): pp. 53-64.
- [248] J-W Lee, J-G Duh, Evaluation of microstructures and mechanical properties of chromized steels with different carbon contents, *Surface and Coatings Technology* 2004; 177–178: pp. 525-531.
- [249] C. C. Mohan, A. Prabhath, A. M Cherian, S. Vadukumpully, S. V. Nair, K. Chennazhi, D. Menon, Nanotextured stainless steel for improved corrosion resistance and biological response in coronary stenting, *Nanoscale* 2015; 7, pp. 832–841.

- [250] Y. Peng, J. Gong , Y. Jiang, M. Fu, D. Rong, The effect of plastic pre-strain on low-temperature surface carburization of AISI 304 austenitic stainless steel, *Surface & Coatings Technol.* 2016; 304 : pp. 16–22.
- [251] S. Iorga, M. Cojocaru, A. Chivu, S. Ciuca, M. Burdusel, P. Badica, C. D. Leuvrey, G. Schmerber, C. Ulhaq-Bouillet, S. Colis, Influence of the Carbo-Chromization Process on the Microstructural, Hardness, and Corrosion Properties of 316L Sintered Stainless Steel, *Metallurgical & Materials transaction A* 2014: pp. 3089-3096.
- [252] H. Huang, X. Feng, C. Du, S. Wu and W. Song, One-step pyrolytic synthesis of small iron carbide nanoparticles/3D porous nitrogen-rich graphene for efficient electro-catalysis, *J. Mater. Chem. A* 2015; 3: pp. 4976–4982.
- [253] N. A. Kumar, H. Nolan, N. McEvoy, E. Rezvani., R. L. Doyle, M. E. G. Lyons, G. S. Duesberg, Plasma-assisted simultaneous reduction and nitrogen doping of graphene oxide nanosheets, *J. Mater. Chem. A* 2013; 1, pp.4431–4435
- [254] V. V. Nikam, R. G. Reddy, S. R. Collins, P. C. Williams, G. H. Schiroky, G. W. Henrich, Corrosion resistant low temperature carburized SS 316 as bipolar plate material for PEMFC application, *Electrochimica Acta* 2008; 53 (6): pp. 2743-2750.
- [255] M. Andrei, F. di Gabriele, P. L. Bonora, D. Scantlebury, Corrosion behaviour of magnesium sacrificial anodes in tap water, *Materials and corrosion* 2003 ;54: pp. 5-11.

[256] E. McCafferty, Introduction to Corrosion Science, Springer Science + Business Media, New York, 2010: pp. 49.

APPENDIX I

The value range of the selected process parameters for the design of experiments for chromised coatings was selected based on values reported in the literature as explained below:

I. Temperature

Temperature range for pack chromisation is commonly reported to be conducted at temperatures above 1000 °C because the coating growth mechanism is limited by diffusion and chemical reaction kinetics [3]. Lin et al. [4] reported that temperatures ≤ 900 °C were unsuitable for diffusion coatings as the coating had a high volume of pores. As temperature increased to 950 °C porosity was reduced but increased at 1000 °C with finer grains. However, substrate composition affects chromised coating characteristics. Hence, experiments to confirm if 900 °C was suitable for stainless steel were also performed, porous coatings were obtained as shown in Figure 119 (a) below. The coatings obtained at 1000 °C had a lower porosity (Figure 119 (b)). The coatings obtained at 1000 °C also exhibited a higher thickness than that obtained at 900 °C. Therefore, the lower level of the temperature range was chosen to be 1000°C as the lower the volume of the defects the better will be the corrosion performance of the surface.

Researchers at the Korea University, South Korea [1, 2, 5] had reported chromised stainless steel produced at 1050 °C and 1100 °C for PEM fuel cell bipolar plate applications. Temperatures above 1100 °C are possible. However, it is known that as temperature increases grain size of diffusion coating increases and corrosion resistance decreases with increase in grain size [6, 7], hence, temperature higher than 1100°C was not considered.

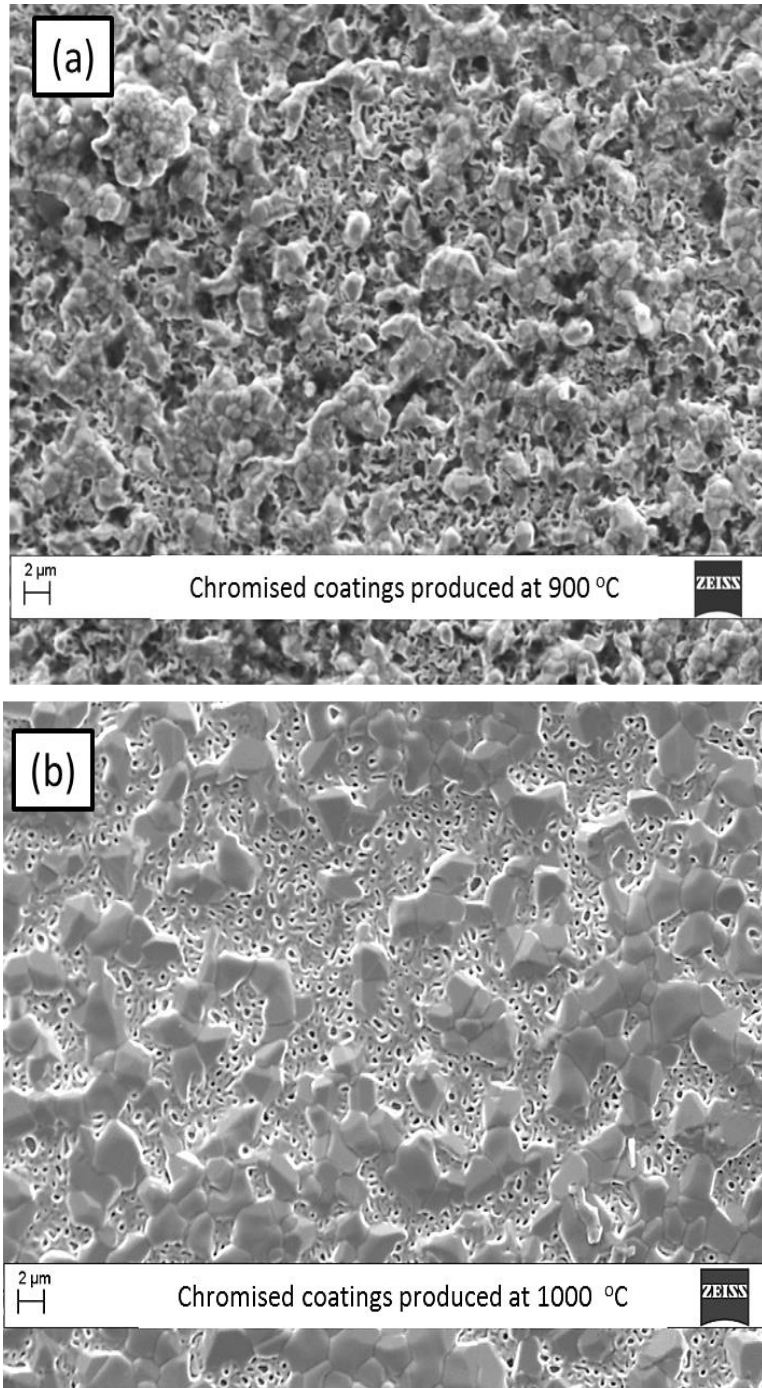


Figure 119 Surface morphology of chromised 304 stainless steel produced at (a) 1000 °C and (b) 1100 °C for 3 hours

II. Time

The lower end of the time range was selected to be 3 hours based on the following work in the literature:

Table 30 Time range reported for pack chromising process in the literature.

Material	Duration/ temperature	References
Chromised 316 stainless steel	2.5 hours /1100 °C	1
Chromised 316 stainless steel	2.5 hours / 1050 °C	2
Chromised 316 stainless steel	3 hours / 1100 °C	5
Chromised 316, 304, 409 stainless steel	3 hours / 1000 °C	8

In order to obtain a reasonable thickness and good surface morphology, 2 hours was not considered. Also, 2.5 hours was rounded to 3 hours in order to avoid fractions.

Time of 9 hours was chosen at the upper limit based on Cho et al [1] work wherein chromised stainless steel was produced at 10 hours. However, 9 hour was considered instead of 10 hours because:

1. Ralston et al. [8] had shown that the thickness achieved with chromising 304 stainless steel at 1000 °C for 3 hours was twice that achieved with 316 stainless steel at the same processing conditions. Hence, it may be possible to achieve the same or higher thickness achieved at 10 hours with 316 stainless steel at 9 hours given that Ref. 9 and 10 have

shown that the thickness of diffusion coatings in austenitic stainless steels is related to its austenite stability, which is related to the Ni content of the austenitic stainless steel. Hence, diffusion coatings formed with 304 stainless can achieve higher thickness than 316 stainless steels under similar processing conditions.

2. Health and safety regulation of the School of Mechanical & Manufacturing Engineering, Dublin City University, Ireland does not permit the use of the furnace beyond working hours. Hence, the maximum time that could be achieved was 9 hours.

III. Activator content

The literature on pack cemented coatings have indicated that insufficient or excess activator content can yield defective chromised coatings [11-13] , hence, 1 and 2 wt. % were not considered. 3-7 wt. % activator content was chosen based on the activator content reported in Ref. [1], [2] and [5].

References

1. K.H. Cho, W.G. Lee, S.B. Lee, H. Jang, Corrosion resistance of chromized 316L stainless steel for PEMFC bipolar plates, *J. Power Sources* 2008; 178: pp. 671–676.
2. S.B. Lee, K.H. Cho, W.G. Lee, H. Jang, Improved corrosion resistance and interfacial contact resistance of 316L stainless-steel for proton exchange membrane fuel cell bipolar plates by chromizing surface treatment, *J. Power Sources* 2009; 187: pp. 318–323.
3. Z.B. Wang , J. Lu, K. Lu, Wear and corrosion properties of a low carbon steel processed by means of SMAT followed by lower temperature chromizing treatment, *Surface & Coatings Technology* 2006; 201: pp. 2796–2801

4. N. Lin, F. Xie, T. Zhong, X. WU , W. Tian, influence of process parameters on thickness and wear resistance of rare earth modified chromium coatings on P110 steel synthesized by pack cementation, *J. Rare Earths* 2010; 28: pp. 301-304.
5. L. Yang, H. Yu, L. Jiang, L. Zhu, X. Jian, Z. Wang, Improved anticorrosion properties and electrical conductivity of 316L stainless steel as bipolar plate for PEM fuel cell by lower temperature chromizing treatment, *J. Power Sources* 2010; 195: pp. 2810–2814.
6. K.D. Ralston, N. Birbilis and C.H.J. Davies, Revealing the relationship between grain size and corrosion rate of metals, *Scripta Materialia* 2010; 63: pp. 1201–1204.
7. K.D. Ralston, N. Birbilis, Effect of grain size on corrosion: a review, *Corrosion* 2010; 66: pp. 075005-0750013.
8. K.D. Ralston, D. Fabijanic, R.T. Jones, N. Birbilis, Achieving a chromium rich surface upon steels via FBR-CVD chromising treatments, *Corro. Sci.* 2011, 53 (9): pp. 2835–2842.
9. N. V. Bangaru, R. C. Krutenat, Diffusion Coatings of Steels: Formation Mechanism and Microstructure of Aluminized Heat-Resistant Stainless Steels, *J. Vac. Sci. Techn.* 1984; 2: pp. 806-815.
10. C. Lopez, A. Kvryan, S. Kasnakjian, A. Coronado, S. Sujittosakul, O. Villalpando, V. Rav, Effect of Austenite Stability on Pack Aluminizing of Austenitic Stainless Steels, *JOM* 2015; 67: pp. 61-67.
11. H. Ebrahimifar, M. Zandrahimi, B. Nikrooz, M. Sedighi, Production of cobalt anti-corrosion coating on AISI 430 steel-Optimization using Box-Behnken experimental designs, *Indian J. Chemical Techn.* 2013; 20: pp. 40 -45.

12. D. Chaliampalias, G. Stergioudis, S. Skolianos, G. Vourlias, The effect of the deposition temperature and activator concentration on the structure of NiCrBSi coatings deposited on low carbon steels by pack cementation process, *Material letters* 2008; 62: pp. 4091–4093.
13. H. Ebrahimifar, M. Zandrahimi, Mn coating on AISI 430 ferritic stainless steel by pack cementation method for SOFC interconnect applications, *Solid State Ionics* 2011; 183: pp. 71–79.

APPENDIX II

(A) Safety procedures for Acid preparation

The following precautionary measures were taken during the acid preparation;

- An acid preparation zone was cut off to prevent entry of other persons in the area with warning signs of 'H₂SO₄ + HF in use' in place. At least one other person was around when the acids were prepared.
- Acid preparation was conducted in a fume hood to avoid inhalation of toxic acidic vapor. Calcium gluconate gel (antidote for HF) was kept in the vicinity of the fume hood where the acids were prepared.
- Nearest phone and emergency response number were kept closed to the working area.
- The following personal protective equipment (PPE) were used in the course of acids preparation:
 - Eye goggles and face shield were worn during acid preparation.
 - A laboratory coat with a chemical splash apron and a shoe cover made from natural rubber was used during the acid preparation.
 - Gloves - A pair of medium weight natural rubber gloves and nitrile gloves were worn during acid preparation to prevent body contact with both dilute and concentrated acids
- The prepared acids were stored in polyethylene containers and kept in designated cabinets.

- All hardware used for acid preparation were immediately rinsed with water and soaked in soapy solution for some days after which it was washed, rinsed and stored in designated places.

(B) Safety procedures for experiments with HF acid

The following safety procedures were observed in running experiments involving HF acid:

1. Standard laboratory PPE (a pairs of neoprene gloves, goggles, nose cover and a fully buttoned lab coat) were worn before commencement of experiment.
2. All experiments involving acid mixture containing 2 ppm HF was carried out in designated fume hood or extraction hood. Appropriate signs: “ DANGER – H₂SO₄ & HF ACID IN USE” signs were displayed on the fume hood and cabinet door throughout the experiments.
3. The fume hood sash was open to a maximum of 25cm to prevent inhalation while, secondary containers were used to contain spillage.
4. Calcium gluconate gel (antidote for HF acid) was kept in the vicinity of the fume hood or extractor where the experiments were conducted. Other people in the laboratory were also notified of the location of the gel.
5. Nearest phone and emergency response number were kept closed to the working area.
6. Everyone in the laboratory was notified of the use of hazardous chemicals (i.e. HF and H₂SO₄). Experiments involving these chemicals were conducted during working hours only with at least one other person present in the laboratory.

7. All equipment used were specifically designed for use with acids and washed thoroughly with soap and rinsed in running water after use.
8. Nearest water source, safety shower and eye wash were identified before commencement of the experiments.

(C) Safety procedures for experiments with hydrogen gas

1. Personal protective equipment: Pair of neoprene gloves, goggles, nose shield and a fully buttoned laboratory coat was worn before commencement of experiments. Danger signs: “HYDROGEN GAS IN USE” was displayed on fume hood and designated areas.
2. Hydrogen gas cylinder was chained down as shown in Figure 120 to prevent toppling.

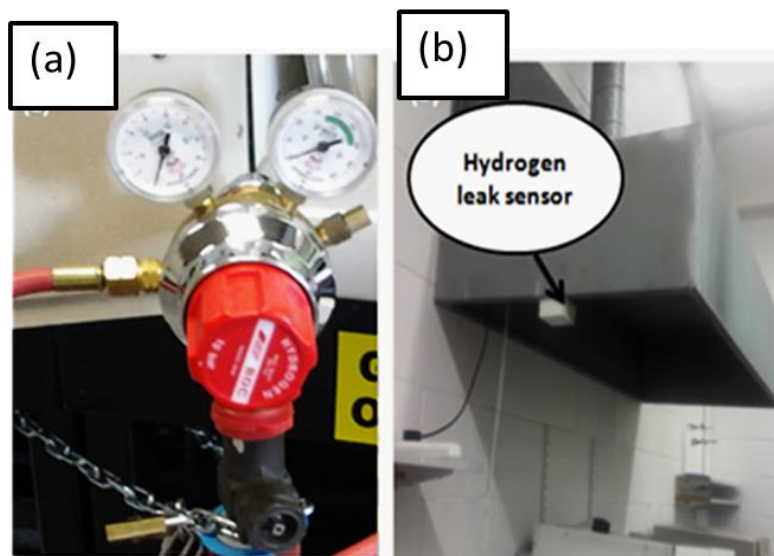


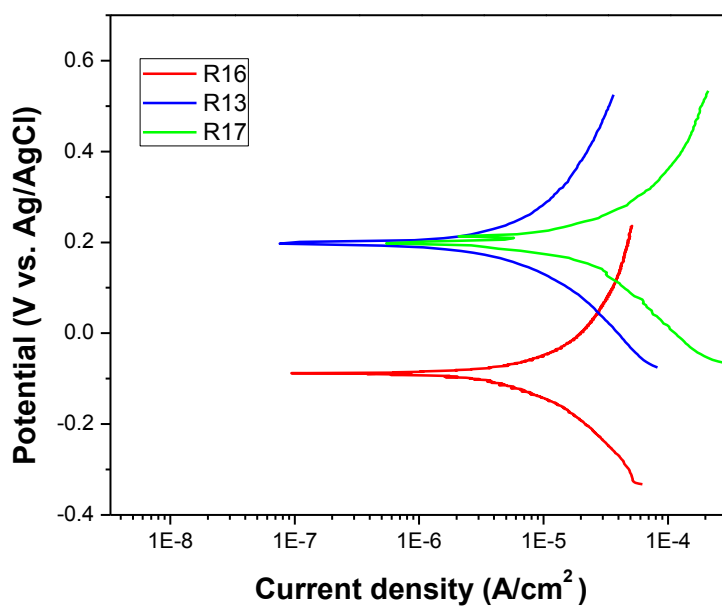
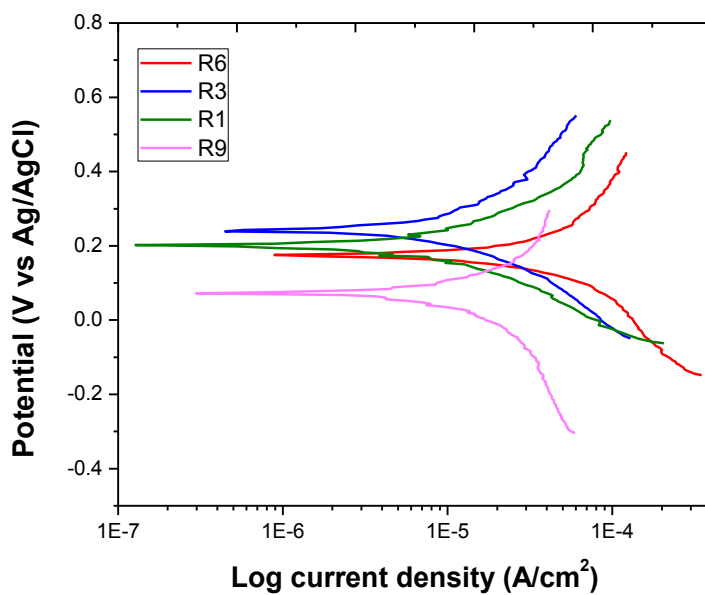
Figure 120 (a) Hydrogen gas regulator b) hydrogen leak sensor and extraction hood

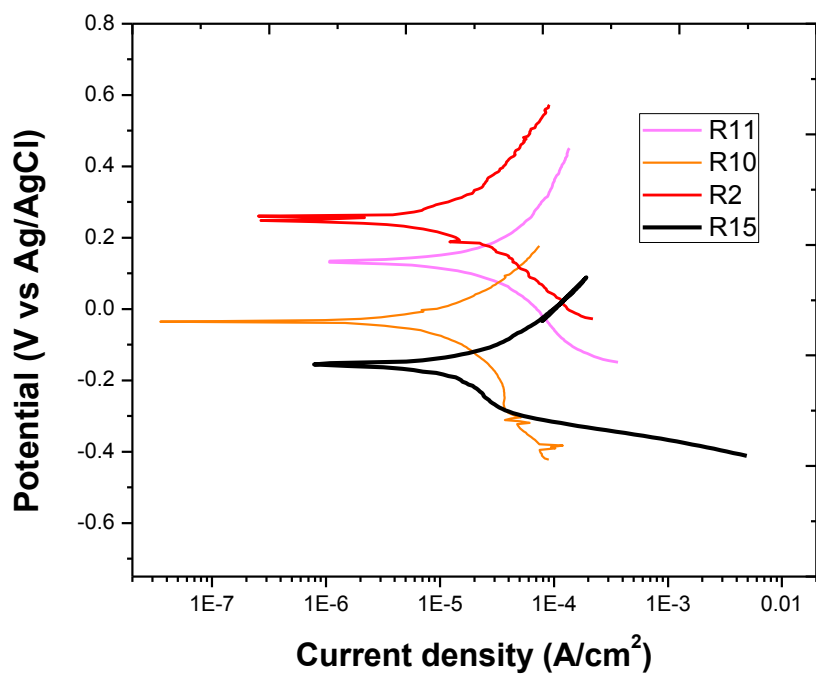
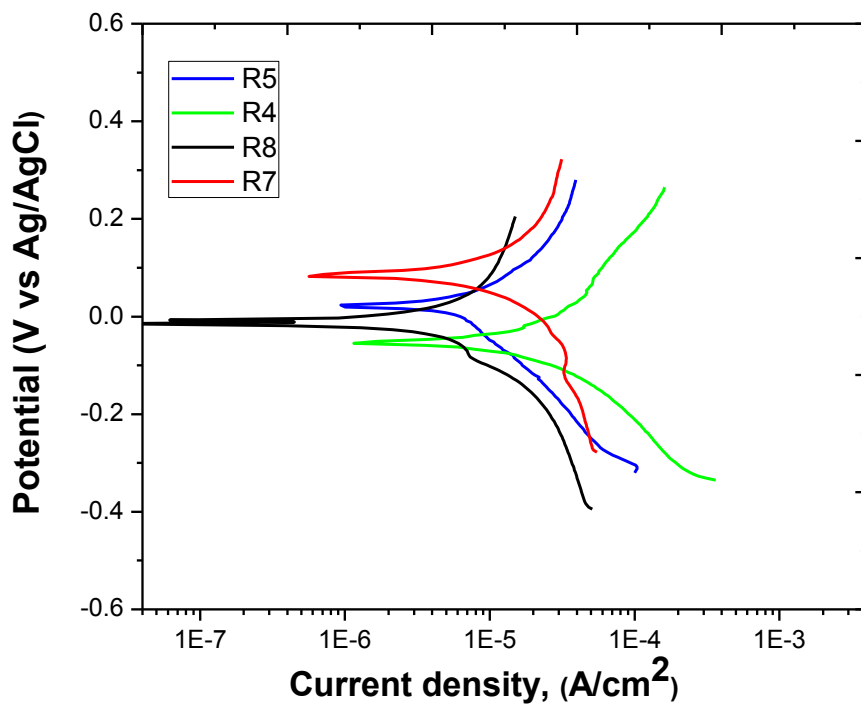
3. All experiments involving hydrogen gas were conducted in designated fume or extraction hoods used. Hydrogen leak sensors were also in place in case of leakage.

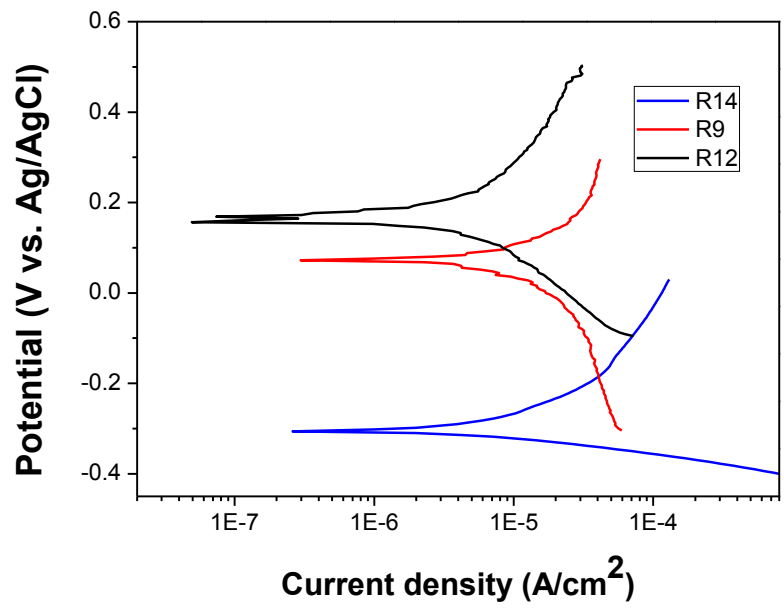
4. Low pressures (1 to 3 bar gauge) and extremely low flow rates (20 - 50 ml/min) were used in the experiments.
5. Hydrogen rated, fittings, piping, gauges were used as flow controllers and pressure fittings were used throughout the experimental apparatus.
6. Fire extinguishers and fire blankets were readily available in the laboratory.

APPENDIX III

I. Tafel plots for chromised 304 stainless steels in 0.5 M H₂SO₄ + 2 ppm at 70 °C







II. Cross sectional SEM images of chromised 304 stainless steel.

